Universität Rostock

Traditio et Innovatio

Structure-reactivity relationships in plasmonic metal-semiconductor nanocomposites for photocatalytic hydrogen generation assessed by *in situ* spectroscopy

Dissertation

zur Erlangung des akademischen Grades

doctor rerum naturalium (Dr. rer. nat.)

an der Mathematisch-Naturwissenschaftlichen Fakultät

der Universität Rostock

vorgelegt von

Jacqueline Bettina Priebe, geb. am 17.09.1985 in Berlin

aus Rostock

Rostock, 23.04.2015

urn:nbn:de:gbv:28-diss2015-0154-7

1. Gutachter Prof. Dr. Angelika Brückner
Leibniz-Institut für Katalyse e.V. an der Universität Rostock

2. Gutachter Prof. Dr. Michael Wark
Institut für Chemie, Carl von Ossietzky Universität Oldenburg

3. Gutachter Prof. Dr. Matthias Bauer
Department Chemie, Universität Paderborn

Tag der Einreichung: 24.04.2015

Tag der mündlichen Aussprache: 14.07.2015

Erklärung

Hiermit erkläre ich, die vorliegende Arbeit selbstständig verfasst und keine anderen als die angegebenen Quellen und Hilfsmittel benutzt zu haben.

Rostock, 23. April 2015

Jacqueline Bettina Priebe

Kurzfassung

Wasserstoff wird aufgrund seiner hohen Energiedichte und umweltschonenden Verbrennung als Energieträger der Zukunft angesehen. Dessen nachhaltige Herstellung im groSSen MaSSstab aus Wasser und Sonnenlicht erfordert die Entwicklung von Photokatalysatoren, die unter Bestrahlung mit sichtbarem Licht arbeiten. Aus technologischer Sicht bietet hierbei die Anwendung heterogener Halbleiterkatalysatoren diverse Vorteile. Um die schnelle Rekombination der lichtgenerierten Ladungsträger im reinen Halbleiter zu unterdrücken, werden diese gewöhnlich mit Metallpartikeln beladen, welche als Elektronenfänger fungieren. Da konventionelle Systeme wie TiO_2 ausschlieSSlich UV-Licht absorbieren, behandelt diese Arbeit deren Kombination mit Münzmetallpartikeln, wie Au, Ag und Cu, für die photokatalytische Wasserstofferzeugung aus Wasser und Methanol als Opferagenz. Es wurde bereits vorab gezeigt, dass diese Nanopartikel aufgrund ihrer Oberflächenplasmonenresonanz-Absorption die Protonenreduktion unter Bestrahlung mit sichtbarem Licht ermöglichen. Der mechanistische Ursprung dieser Aktivität wird jedoch kontrovers diskutiert. Angeregt durch diese Erkenntnisse, zielte die vorliegende Arbeit insbesondere auf mechanistische Studien an plasmonischen Metall/Halbleiter-Katalysatoren ab, welche zum Einen den Einfluss der Halbleitersynthese und dessen Modifikation (z.B. durch Dotierungsverfahren) auf die Natur und Reaktivität der Ladungsträger untersuchten. Auf der anderen Seite wurde analysiert, wie sich verschiedene Methoden zur Metallpartikelabscheidung und die Partikelzusammensetzung auf die strukturellen, elektronischen und katalytischen Eigenschaften auswirken. Hierfür wurden geeignete *in situ*-spektroskopische Techniken (EPR, XANES, UV-vis und FTIR) angewandt, um die Katalysatorfunktion unter reaktionsnahen Bedingungen zu beobachten und somit wertvolle Struktur-Eigenschaftsbeziehungen zu erschlieSSen. Diese können eine Grundlage bilden, katalytische Systeme hinsichtlich ihrer Aktivität, Stabilität und ökonomischen Effizienz zu optimieren.

Zunächst wurde am Beispiel des bewährten Halbleitersystems $NaTaO_3$ demonstriert, dass dessen Aktivität stark durch die gewählte Synthesemethode beeinflusst werden kann. Eine besondere Exotemplatmethode führte im Vergleich zur herkömmlichen Festphasenreaktion zu deutlich höheren Wasserstoffraten unter UV-vis-Licht. *In situ*-EPR-Daten belegen, dass dies auf einer effizienteren Ladungsträgerverwertung beruht, da deren Rekombination womöglich durch die gröSSere Oberfläche vermindert wird. EPR- sowie katalytische Messungen zeigten auSSerdem, dass eine Beladung mit Au diesen Effekt verstärkte, vermutlich

aufgrund eines Elektronentransfers von $NaTaO_3$ auf die Metallpartikel.

Darüber hinaus wurde für den Modellkatalysator Au-TiO_2 *in situ*-spektroskopisch ermittelt, dass die TiO_2-Trägerzusammensetzung sowie die Au-Abscheidungsmethode maSSgeblich die Effizienz von Elektronentransferprozessen über die Au/TiO_2-Grenzfläche bestimmen. Die *deposition-precipitation*-Methode zur Beladung mit Au war hierbei überlegen gegenüber anderen Methoden, da hierdurch kleine und einheitliche Au-Partikel unter Reaktionsbedingungen gebildet und auSSerdem oberflächengebundene reaktive Hydroxylspezies generiert werden. Diese begünstigen die beschleunigte indirekte Methanoloxidation, weshalb deutlich höhere H_2-Bildungsraten resultierten. Längere Abscheidungszeiten führten bei dieser Methode jeodch zu einer starken TiO_2-Defektbildung, wodurch Elektronentransferprozesse und damit die photokatalytische Aktivität verringert wurden.

Weiterhin konnte durch wellenlängenabhängige *in situ*-EPR-Messungen bestätigt werden, dass der plasmoneninduzierte Transfer von Au-Elektronen auf TiO_2 der initiierende Schritt für die Protonenreduktion über Au-TiO_2 unter Anregung mit sichtbarem Licht ist. Während Anatas/Rutil-Mischphasen als Trägermaterial diesen Transfer erlaubten, war er hingegen nicht möglich, wenn EPR-aktive intrinsische TiO_2-Defekte vorlagen. Diese wurden in Anatas und einem Anatas/Brookit-Gemisch detektiert und resultieren vermutlich aus der TiO_2-Synthese. Die Aktivität von Au-beladenem Anatas unter sichtbarem Licht konnte auch nicht durch N-Dotierung erhöht werden, obwohl dies zu einer erheblichen Absorptionssteigerung führte. *In situ*-EPR-Daten deuten darauf hin, dass die angeregten N-Elektronen eher durch Sauerstoffvakanzen abgefangen werden, anstatt auf die Goldpartikel überzugehen. Dadurch wird die Zahl der reaktiven Au-Elektronen und auch die Aktivität unter UV-vis-Licht vermindert gegenüber dem undotierten System. Allerdings stellte sich eine Reduktion mit H_2 als gewinnbringend für metallfreies TiO_2 heraus. Hierbei wurden mithilfe der *in situ*-EPR-Spektroskopie zusätzlich Beiträge von lichtaktiven N-Spezies ermittelt, die offenbar von eingeschlossenen NO-Molekülen stammen und durch die Reduktion in das TiO_2-Gitter eingebaut worden sind.

Wasserstoff wurde auch über Cu-TiO_2 aus Wasser und Methanol gebildet. Wie durch *in situ*-XANES, *in situ*-UV-vis und *in situ*-EPR demonstriert werden konnte, war hierfür vor allem eine *in situ*-Reduktion der Cu^{2+}-Spezies zu Cu^0-Partikeln verantwortlich. Dieser Prozess hing für monometallische Systeme von der Cu-Abscheidungsmethode ab, wobei die reduktive Abscheidung mit $NaBH_4$ diese Reduktion auch mit sichtbarem Licht ermöglichte. Dies galt auch für bimetallische Cu/Au-Katalysatoren, welche mit sichtbarem Licht sehr aktiv waren, sofern Cu und Au in gemischten Partikeln vorlagen. Dahingegen bildeten solche, in denen Cu und Au getrennt voneinander auf TiO_2 verteilt waren, kaum Wasserstoff mit sichtbarem Licht.

Abstract

Hydrogen is regarded as major energy carrier of the future, due to its high energy density and environmentally friendly combustion. Its sustainable high-scale generation from water and sunlight necessitates photocatalysts working under visible light. From a technical point of view, the application of heterogeneous semiconductor catalysts provides valuable advantages. In order to suppress the fast recombination of light-generated charge carriers in pristine semiconductors, they are usually loaded with noble-metal nanoparticles acting as efficient electron traps. Since conventional semiconducting systems such as TiO_2 can only absorb UV light, this work addresses their combination with coinage metal particles such as Au, Ag, and Cu for the photocatalytic hydrogen generation from water and methanol as sacrifical agent. It has been shown previously that these particles allow proton reduction under visible light, the mechanistic origin of which, however, is still controversially discussed. Inspired by these works, the present study aims especially at mechanistic investigations on plasmonic metal/semiconductor nanocomposites, which examine the impact of the semiconductor-preparation method and its modification (*e.g.* by doping procedures) on the nature and reactivity of charge carriers. Moreover, the influence of the metal-deposition method and the particle composition on the structural, electronic, and catalytic properties was analyzed. To this end, suitable *in situ* spectroscopic techniques (EPR, XANES, UV-vis and FTIR) were applied for monitoring the catalyst's function under reaction-like conditions, whereby valuable structure-reactivity relationships could be revealed.

First, the photocatalatyic performance of the well-established system $NaTaO_3$ was demonstrated to be strongly affected by the synthesis method applied. An advanced exotemplate method led to markedly higher hydrogen evolutions under UV-vis light than a conventional solid-state reaction. *In situ* EPR data visualized that this is due to a more efficient utilization of charge carriers, since their recombination is probably reduced by the larger surface area. Furthermore, EPR and catalytic measurements showed that this effect was further enhanced by loading with Au, most likely due to an electron transfer from $NaTaO_3$ to the metal particles.

Beyond that, from *in situ* spectroscopic analysis on the model catalyst Au-TiO_2, it was inferred that the TiO_2-support composition as well as the Au-deposition method crucially determine the efficiency of charge transfer across the Au/TiO_2 interface. The deposition-precipitation method for loading with Au was superior to other methods, since thereby

small and uniform particles were formed under reaction conditions, and, moreover, reactive hydroxyl species were efficiently generated at the TiO_2 surface. The latter favor the more effective indirect methanol oxidation and, thus, led to remarkably higher H_2-evolution rates. However, for this method, prolonged deposition times provoked a strong formation of TiO_2-lattice defects, which reduced electron-transfer processes and, thus, the photocatalytic activity.

In this context, it was confirmed by wavelength-dependent *in situ* EPR experiments that the plasmon-induced transfer of Au electrons into the conduction band of TiO_2 is most probably the initial step in proton reduction over Au-TiO_2 under visible light. While this transfer was enabled in catalysts with anatase/rutile-mixed phases as support material, it was inhibited in materials exhibiting EPR-active intrinsic TiO_2 defects. These were detected in anatase and in an anatase/brookite mixture and most probably result from the TiO_2 synthesis. The visible-light activity of anatase could not be improved by N doping either, although it led to a markedly increased absorption of visible wavelengths. *In situ* EPR data suggest that this might be due to the preferential trapping of excited N electrons by oxygen vacancies instead of their transfer into the metal sphere. Thereby, the number of reactive Au electrons and, thus, the activity under UV-vis light decreased compared to the undoped counterparts. On the other hand, reduction with hydrogen was shown to be advantageous for metal-free TiO_2. However, *in situ* EPR spectroscopy indicates that additional N species that have been incorporated during the reduction treatment contributed to the enhanced performance of this catalyst. These visible-light-active N centers most likely stem from initially enclosed NO molecules.

Hydrogen was evolved from water and methanol over Cu-TiO_2 as well. As evidenced by *in situ* XANES, UV-vis and EPR, this required a fast *in situ* of Cu^{2+} species to Cu^0 particles. For monometallic catalysts, this process was dependent on the Cu-deposition method, since in contrast to the preparation by impregnation, the reductive precipitation using $NaBH_4$ enabled this reduction even under visible light. This, too, applied to bimetallic Cu/Au catalysts. These were proven to be highly active under visible light when Cu and Au formed mixed particles on TiO_2, whereas catalysts in which Cu and Au were separated from each other, barely evolved H_2 under pure visible light.

Contents

Scientific publications

Parts of this thesis have been or will be published:

Journal articles fully or partially related to this work

1. **J.B. Priebe**, A.J.J. Lennox, J. Radnik, M. Adam, H. Junge, M. Beller, and A. Brückner, *"On the Origin of Visible-light Activity of (Mixed) Metal Particles Deposited on TiO_2 in Photocatalytic Hydrogen Generation – An in situ Spectroscopic Study"*, *in preparation*

2. M. Cargnello, T. Montini, S.Y. Smolin, **J.B. Priebe**, J.J. Delgado Jaén, V.N. Doan-Nguyen, M.-M. Pohl, T.R. Gordon, Y. Lu, J. Baxter, A. Brückner, P. Fornasiero, and C.B. Murray, *"Length-Dependent Photoreactivity in Highly Active Brookite Titania Nanorods"*, *in preparation*

3. **J.B. Priebe**, J. Radnik, A.J.J. Lennox, M.-M. Pohl, M. Karnahl, D. Hollmann, K. Grabow, U. Bentrup, H. Junge, M. Beller, and A. Brückner, *"Solar Hydrogen Production by Plasmonic Au-TiO_2 Catalysts: Impact of Synthesis Protocol and TiO_2 Phase on Charge Transfer Efficiency and H_2 Evolution Rates"*, *ACS Catal.* **5**, 2137–2148 (2015).

4. T. Meyer*, **J.B. Priebe***, R.O. da Silva*, T. Peppel, H. Junge, M. Beller, A. Brückner, and S. Wohlrab, *"Advanced Charge Utilization from $NaTaO_3$ Photocatalysts by Multilayer Reduced Graphene Oxide"*, *Chem. Mater.* **26**, 4705–4711 (2014).
(* These authors contributed equally.)

5. A. Cybula, **J.B. Priebe**, M.M. Pohl, J.W. Sobczak, M. Schneider, A. Zielińska-Jurak, A. Brückner, and A. Zaleska, *"The Effect of Calcination Temperature on Structure and Photocatalytic Properties of Au/Pd Nanoparticles Supported on TiO_2"*, *Appl. Catal. B* **152–153**, 202–211 (2014).

6. **J.B. Priebe**, M. Karnahl, H. Junge, M. Beller, D. Hollmann, and A. Brückner, *"Water Reduction with Visible Light: Synergy between Optical Transitions and Electron Transfer in Au-TiO_2 Catalysts Visualized by in situ EPR Spectroscopy"*, *Angew. Chem. Int. Ed.* **52**, 11420–11424 (2013).

Additional peer-reviewed journal articles

1. A. Brückner, A. Hinz, **J.B. Priebe**, A. Schulz, and A. Villinger, *"Cyclic Group 15 Radical Cations"*, *Angew. Chem. Int. Ed.*, **54**, 7426–7430 (2015).

2. M. Haehnel, **J.B. Priebe**, J.C.H. Yim, A. Spannenberg, A. Brückner, L.L. Schafer, and U. Rosenthal, *"Four-membered Heterometallacyclic d^0 and d^1 Complexes of Group 4 Metallocenes with Amidato Ligands"*, *Chem. Eur. J.* **20**, 7752–7758 (2014).

3. J. Fritsch, E. Siebert, **J.B. Priebe**, I. Zebger, F. Lendzian, C. Teutloff, B. Friedrich, and O. Lenz *"Rubredoxin-related Maturation Factor Guarantees Metal Cofactor Integrity during Aerobic Biosynthesis of Membrane-bound [NiFe]-Hydrogenase"*, *J. Biol. Chem.* **289**, 7982–7993 (2014)

4. M. Haehnel, S. Hansen, **J.B. Priebe**, A. Spannenberg, P. Arndt, A. Brückner, and U. Rosenthal, *"Highly Strained Heterometallacycles of Group 4 Metallocenes with Bis(diphenylphosphino)methanide Ligands"*, *Chem. Eur. J.* **19**, 7568–7574 (2013).

Contributions in conferences

Oral presentations

Invited lecture

1. **J.B. Priebe**, *"In situ Spectroscopic Tools for Elucidating Electron-transfer Mechanisms and Structure-reactivity Relationships in Photocatalytic Hydrogen Generation over Supported Metal Catalysts"*, 4^{th} International Symposium on Surface Imaging/Spectroscopy at the Solid/Liquid Interface, Krakow (Poland), September 2–4, 2015.

Other lectures

1. **J.B. Priebe**, A. Brückner, *"In situ spectroscopy: A "must-have" for monitoring light-generated charge carriers in supported metal catalysts for hydrogen generation"*, 5^{th} International Conference on Semiconductor Photochemistry (SP5), Saint-Petersburg (Russia), July 27–31, 2015.

2. **J.B. Priebe**, J. Radnik, H. Junge, M. Beller, A. Brückner, *"All Eyes on Catalysis - Katalysatoren in der Wasserspaltung live und in Aktion"* 17^{th} Northern German PhD Student Colloquium of Inorganic Chemistry (NDDK), Rostock (Germany), September 11–12, 2014.

3. **J.B. Priebe**, J. Radnik, H. Junge, M. Beller, A. Brückner, *"Revealing Structure-reactivity Relationships in Solar Water Reduction over Plasmonic Photocatalysts by Spectroscopic in situ Techniques"*, 20^{th} International Conference on Photochemical Conversion and Storage of Solar Energy (IPS-20), Berlin (Germany), July 27 – August 1, 2014.
4. **J.B. Priebe**, *"All Eyes on Catalysis – Torlinien-Kameras in der Katalyse"*, Science Communication Workshop "Rostock's Eleven", Rostock (Germany), June 11–13, 2014.
5. **J.B. Priebe**, M. Karnahl, H. Junge, M. Beller, A. Brückner, *"Higher Visible-Light Response for Water Reduction by Plasmonic (mixed) Metal Particles: A Spectroscopic in situ Study"*, 18^{th} International Conference on Semiconductor Photocatalysis and Solar Energy Conversion (SPASEC-18), San Diego (USA), November 17–21, 2013.
6. **J.B. Priebe**, K. Grabow, U. Bentrup, A. Brückner, *"Opportunities and Limitations of Spectroscopic in situ Techniques for Monitoring Working Plasmonic Water-splitting Photocatalysts"*, DFG SPP 1613 Summer School, Ellwangen (Germany), October 06–09, 2013.
7. **J.B. Priebe**, M. Karnahl, H. Junge, M. Beller, A. Brückner, *"In situ EPR Spectroscopy as a Useful Tool for Investigating Visible-light-activity Enhancement Mechanisms of Plasmonic Photocatalysts for Water Reduction"*, 16^{th} Northern German PhD Student Colloquium of Inorganic Chemistry (NDDK), Bremen (Germany), September 19–20, 2013.
8. **J.B. Priebe**, M. Karnahl, H. Junge, M. Beller, A. Brückner, *"Au-TiO_2 for Solar H_2 Production from Water: Obtaining Structure-reactivity Relationships by in situ EPR Spectroscopy"*, Workshop "Catalysis for Sustainable Synthesis (CaSuS)", Rostock (Germany), September 16–18, 2013.
9. **J.B. Priebe**, K. Grabow, M. Karnahl, U. Bentrup, H. Junge, M. Beller, A. Brückner, *"Water Reduction over Plasmonic Photocatalysts: Impact of Catalyst Modification on Performance and Stability Studied by in situ Techniques"*, 11^{th} European Congress on Catalysis (EuropaCat), Lyon (France), September 01–06, 2013.

Poster presentations

1. **J.B. Priebe**, J. Radnik, M. Karnahl, D. Hollmann, H. Junge, M. Beller, A. Brückner, *"On the Origin of Visible-Light Activity in Water Reduction of Plasmonic (Mixed) Metal Photocatalysts"*, 8^{th} European Meeting on Solar Chemistry and Photocatalysis: Environmental Applications (SPEA-8), Thessaloniki (Greece), June 25–28, 2014.

2. **J.B. Priebe**, M. Karnahl, H. Junge, M. Beller, D. Hollmann, A. Brückner, *"In situ EPR Spectroscopy in Photocatalytic Water Splitting over Au-TiO_2 Catalysts"*, 2^{nd} Summer School Spectroelectrochemistry, Dresden (Germany), August 23–30, 2013.

3. **J.B. Priebe**, M. Karnahl, H. Junge, M. Beller, D. Hollmann, A. Brückner*, *"Electron-Transfer Pathways in Plasmonic Au-TiO_2 for Photocatalytic Water Reduction Depending on Excitation Wavelength and Catalyst Structure"*, Workshop "Spins as Functional Probes in Solar Energy Research", Berlin (Germany), April 10–12, 2013.

4. **J.B. Priebe**, D. Hollmann, K. Grabow, U. Bentrup, M. Karnahl, H. Junge, M. Beller, A. Brückner, *"Photocatalytic Water Reduction on Plasmonic Au-TiO_2: Impact of Excitation Wavelength and Catalyst Structure on Charge Transfer and Activity"*, 46. Jahrestreffen Deutscher Katalytiker, Weimar (Germany), March 13–15, 2013.

5. **J.B. Priebe**, D. Hollmann, A. Brückner, *"Activity Enhancement in Photocatalytic Water Splitting by Plasmonic Metal Particles Deposited on Semiconductors: An in situ EPR Study"*, 15^{th} Northern German PhD Student Colloquium of Inorganic Chemistry (NDDK), Krelingen (Germany), September 24–25, 2012.

6. **J.B. Priebe**, D. Hollmann, S. Schüler, A. Brückner, *"Spectroscopic Insights into the Mechanism of Photocatalytic Water Reduction by Plasmonic Gold Catalysts supported on Titania"*, S2B Eco2 Colloquium "Photocatalytic Water Splitting", Evonik Industries, Marl (Germany), June 26, 2012.

7. **J.B. Priebe**, D. Hollmann, S. Schüler, A. Brückner, *"EPR Spectroscopic Investigation of Plasmonic Metal Catalysts in Photocatalytic Water Splitting"*, Leibniz PhD student colloquium, Berlin (Germany), June 07–08, 2012.

List of tables

List of figures

List of abbreviations

a.u. ..... Arbitrary units
at.-% ..... Atomic percentage (with respect to the material's surface)
ATR ..... Attenuated total reflexion
BET ..... Brunauer-Emmet-Teller
CB ..... Conduction band
CP ..... Co-precipitation
cw ..... Continuous wave
DP ..... Deposition-precipitation
DR ..... Diffuse reflectance
EDXS ..... Energy dispersive X-ray spectroscopy
EM ..... Exotemplate method
EPR ..... Electron paramagnetic resonance
EXAFS ..... Extended X-ray absorption fine structure
FTIR ..... Fourier transform infrared
GC ..... Gas chromatography
HAADF ..... High-angle annular dark field
hfs ..... Hyperfine structure
ICDD ..... International Centre for Diffraction Data
ICP-OES ..... Inductively coupled plasma optical emission spectrometry
IM ..... Impregnation
lw ..... Line width
m-rGO ..... Multilayer reduced graphene oxide
MeOH ..... Methanol
n.d. ..... Not determined
NP ..... Nanoparticle
PD ..... Photo-deposition
PDF ..... Powder diffraction file
PVA ..... Polyvinyl alcohol
RP ..... Reductive precipitation
SC ..... Semiconductor
SEM ..... Scanning electron microscopy

SHC ..... Solar-to-hydrogen conversion
SIM ..... Sol-immobilization
SKM ..... Schuster-Kubelka-Munk
SMSI ..... Strong metal-support interaction
SP ..... Stepwise precipitation
SPR ..... Surface plasmon resonance
SR ..... Sacrificial reagent
SSR ..... Solid-state reaction
TCD ..... Thermal conductivity detector
TEM ..... Transmission electron microscopy
UV-vis ..... Ultraviolet-visible
VB ..... Valence band
wt.-% ..... Weight percentage
XANES ..... X-ray absorption near edge structure
XAS ..... X-ray absorption spectroscopy
XPS ..... X-ray photoelectron spectroscopy
XRD ..... X-ray diffraction

1 Introduction

1.1 Motivation and Objective

In 2013, the average global energy consumption reached 16.9 TW, which was predominantly (>85 %) extracted from fossil fuels.[1] There is no doubt that this rate will dramatically increase as the world population is expected to hover around 9.5 billion people by 2050.[2] Even though the fossil reserves may not be depleted within the next decades, their consumption is for sure accompanied with high levels of detrimental CO_2 emissions causing accelerated global warming.[3] Therefore, in order to provide *ca.* 30–40 TW of ecologically produced energy in 2050, significant contributions from carbon-free resources are needed. Besides clean and renewable alternatives such as geothermal or wind energy, the most abundant sustainable energy stems from solar radiation, powering the planet with *ca.* $1.65 \cdot 10^5$ TW,[4] which is far beyond the expected energy consumption. However, from an economical and technological point of view, the direct conversion of sunlight into electricity, *e.g.* by photovoltaic solar cells, is still unsatisfactory due to its fluctuating availability. Therefore, artificial photosynthesis, the conversion of solar energy, CO_2 and water into storable and transportable carbon-based fuels, gains increasing importance and attention in recent research.[5–9] A feasible alternative to that challenging multi-electron involving CO_2-reduction chemistry is the generation of hydrogen from protons, which could be provided by worldwide abundant water molecules. Since the combustion of H_2, *e.g.* within a fuel cell, releases high amounts of energy ($\Delta H^\circ = -286\,\mathrm{kJ\,mol^{-1}}$) and does not include other (detrimental) emissions than water, sustainable H_2 is considered one of the key fuels to cover the future energy demand.

$$2\,H_2O(l) \xrightarrow{h\nu,\,\mathrm{cat.}} 2\,H_2(g) + O_2(g) \qquad \Delta G^\circ = +237\,\mathrm{kJ\,mol^{-1}} \tag{1.1}$$

The conversion of solar light into chemical energy *via* the thermodynamically "uphill" water splitting reaction (Eq. 1.1) requires suitable photocatalysts. Honda and Fujishima were the first who described the photo-electrolysis of water into O_2 at a titanium dioxide (TiO_2) photoanode and H_2 at a Pt cathode.[10] Since then, extensive research has been carried out to develop highly efficient semiconductor (SC) water-splitting photocatalysts working best under solar radiation, which contains about 50 % visible light along with a

small UV contribution (*ca.* 5 %).[11–13] Most of these approaches gained limited success, which may be, among other reasons, due to a lack of mechanistic understanding of the material's particular function.

On the other hand, the oxidation of organic compounds, such as alcohols, saccharides, amino acids, polymers or biomass derivatives (glycerol or carbohydrates), instead of water was found to accelerate the H_2-production rate due to less positive changes of Gibbs free energy.[14] Therefore, the usage of "sacrificial reagents" (SR) as hole scavengers can effectively improve the photo-evolution of H_2, due to its easier oxidation compared to the formation of O_2 (two-electron process *vs.* four-electron process), which suppresses the recombination of charge carriers as well as the favored back reaction between H_2 and O_2. For that purpose, methanol (MeOH) is frequently employed as SR in a test reaction in order to explore a photocatalyst's potential for H_2 generation. As proposed by Kawai *et al.*, the decomposition of MeOH occurs with water as net oxidant in multiple steps according to Eq. 1.2–1.4.[15]

$$\mathrm{CH_3OH(l)} \xrightarrow{h\nu,\,\mathrm{cat.}} \mathrm{HCHO(g)} + \mathrm{H_2(g)} \qquad \Delta G^\circ = +64.1\,\mathrm{kJ\,mol^{-1}} \qquad (1.2)$$

$$\mathrm{HCHO(g)} + \mathrm{H_2O(l)} \xrightarrow{h\nu,\,\mathrm{cat.}} \mathrm{HCOOH(l)} + \mathrm{H_2(g)} \qquad \Delta G^\circ = +47.8\,\mathrm{kJ\,mol^{-1}} \qquad (1.3)$$

$$\mathrm{HCOOH(l)} \xrightarrow{h\nu,\,\mathrm{cat.}} \mathrm{CO_2(g)} + \mathrm{H_2(g)} \qquad \Delta G^\circ = -95.8\,\mathrm{kJ\,mol^{-1}} \qquad (1.4)$$

In contrast to the first two reactions, the last conversion process, Eq. 1.4, is thermodynamically favorable at room temperature and thus provides an intrinsic barrier for the undesired H_2 uptake. The overall equation can be expressed by

$$\mathrm{CH_3OH(l)} + \mathrm{H_2O(l)} \xrightarrow{h\nu,\,\mathrm{cat.}} \mathrm{CO_2(g)} + 3\,\mathrm{H_2(g)} \qquad \Delta G^\circ = +16.1\,\mathrm{kJ\,mol^{-1}} \qquad (1.5)$$

In order to produce economical value out of Eq. 1.5, photocatalysts are needed that are capable of converting sunlight efficiently into H_2 by proton reduction. This requires systems that are able to work especially with visible light, *i.e.* the major part of solar radiation. As pointed out below, the emphasis in current research lies more in the screening of a wide range of new materials than in understanding their mode of action. This may be insufficient, as designing new photocatalysts with optimum band gap and high activity requires detailed insights into the behavior of materials already available. Especially conventional semiconducting systems deposited with visible-light-active coinage metals such as Au, Ag and Cu recently emerged as promising candidates, due to their unique optical absorption known as surface plasmon resonance (SPR). However, the detailed mechanistic background of the SPR-mediated activity enhancement is still controversially discussed, though its complete understanding is inevitable in order to tune the structure of plas-

monic photocatalysts towards an optimum performance. A rational design of tailored photocatalysts should therefore imply a fundamental analysis of inherent structure-function relationships, which are generally well accessible by way of suitable *in situ* spectroscopic investigations. Visualizing the nature of light-induced species, their stability and consumption by the reactants is of particular interest for photocatalytic reactions. A study on how these parameters are affected by the synthesis protocol, the reaction conditions, such as the applied excitation source, and the modification of catalytic materials would shine light on the detailed function of the working catalyst.

In view of the urgent need for novel photocatalysts in H_2 generation, the present work aims at a detailed mechanistic insight into the function of semiconductors loaded with plasmonic metal particles. Particular attention is dedicated to a systematic study of the influence of:

- the synthesis method for $NaTaO_3$ semiconductors (Chapter 3)
- the method of gold deposition onto TiO_2 (Chapter 4)
- modifications of the TiO_2-based support, including doping strategies (Chapter 5)
- the nature and composition of the metal particles (Chapter 6)

on the ability to generate and separate reactive charges as well as on the photocatalytic performance. Especially, *in situ* electron paramagnetic resonance (EPR) spectroscopy has been applied to visualize light-generated catalytically active species within the catalyst and their interaction with reactants during hydrogen generation. Additionally, *in situ* X-ray absorption spectroscopy (XAS) and *in situ* ultraviolet-visible (UV-vis) spectroscopy were applied to follow changes in the metal-oxidation state during the lifespan of the catalyst. *In situ* infrared (IR) spectroscopy was used to monitor directly the stepwise consumption of the sacrificial reactant MeOH. In combination with standard characterization methods in heterogeneous catalysis, such as transmission electron microscopy (TEM), X-ray photoelectron spectroscopy (XPS), and X-ray diffraction (XRD), a comprehensive picture of the catalysts in each step of their lifespan was drawn, which could serve as a basis for improvements of the catalytic systems towards better performance, stability and higher economic efficiency.

1.2 State of the Art

Similar to the above mentioned photo-electrochemical cell introduced by Honda and Fujishima, particulate semiconductors can function as a large set of microcells, built by the individual nano-sized particles of the suspended powder. Especially for the use of SR, powder photocatalysts exhibit the advantage of being much simpler and less expensive. TiO_2 is by far the most investigated SC photocatalyst due to its low cost, non-toxicity and high stability.[16] Furthermore, its band-gap position fulfills the requirements for a water-splitting photocatalyst, since the potential of its conduction band (CB, the empty Ti t_{2g} band) is more negative ($E_{\mathrm{cb}} = -0.47\,\mathrm{V}$ *vs.* NHE at pH 7 for anatase) than the reduction potential $E(\mathrm{H^+/H_2}) = -0.41\,\mathrm{V}$, and the valence band (VB, the fully occupied p band) is located more positively ($E_{\mathrm{vb}} = 2.66\,\mathrm{V}$) than the water-oxidation potential ($E(\mathrm{O_2/H_2O}) = 0.82\,\mathrm{V}$).[17,18] Therefore, TiO_2 is a suitable model catalyst for mechanistic investigations in photocatalytic H_2-evolution reactions.[19–22]

1.2.1 Primary light-induced processes within semiconductor photocatalysts for H_2 generation

Figure 1.1 depicts the fundamental processes occurring in metal-loaded (*e.g.* commonly used Pt) TiO_2 upon interaction with photons of energy equal to or greater than the TiO_2 band gap ($E_g = 3.1\,\mathrm{eV} \equiv 400\,\mathrm{nm}$). The photocatalytic reaction is initiated by electron excitation with UV light from the valence band into the conduction band of TiO_2 (1):

$$\mathrm{TiO_2} \quad \xrightarrow{h\nu_{\mathrm{UV}}} \quad \mathrm{TiO_2}(\mathrm{h^+_{vb}}) \quad + \quad \mathrm{TiO_2}(\mathrm{e^-_{cb}}) \tag{1.6}$$

These excited CB-electrons, $\mathrm{e^-_{cb}}$, can be trapped at lattice-Ti^{4+} sites:

$$\mathrm{Ti^{4+}} \quad + \quad \mathrm{e^-_{cb}} \quad \rightarrow \quad \mathrm{Ti^{3+}} \tag{1.7}$$

Ti^{3+} is paramagnetic and thus detectable by EPR spectroscopy in UV-light-irradiated TiO_2.[23] However, in the presence of electron-trapping metal particles such as Pt or Au, possessing a lower Fermi level than the TiO_2-CB, these electrons are quickly transferred into the metal sphere (2) leading to a lower intensity of the Ti^{3+} signal in the EPR spectra.[24] The extend to which electrons and holes are thus prevented from recombination depends on the height of the Schottky barrier, ϕ_B, formed at the metal/SC interface.[25] The Schottky barrier can be estimated by

$$\phi_B = \phi_M - X_S \tag{1.8}$$

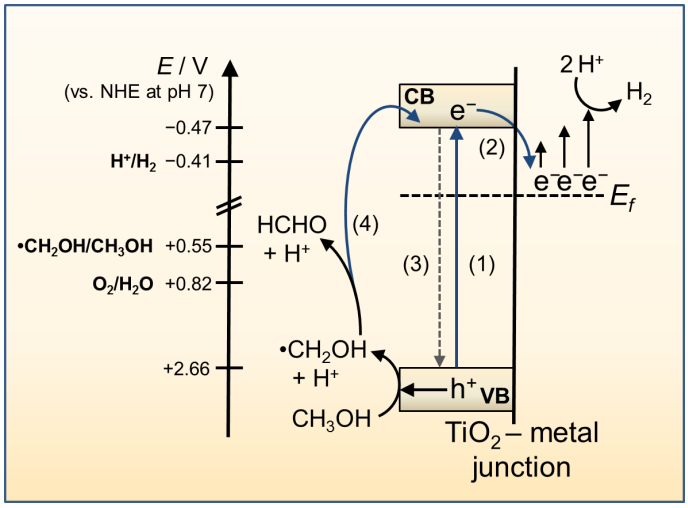

Figure 1.1: UV-light-induced processes and electron-transfer pathways (blue arrows) in metal-loaded TiO_2. VB-electrons are excited into the TiO_2-CB (1) and quickly transferred into the metal due to its lower Fermi level (2). Thereby, the recombination of e^-_{cb} and h^+_{vb} (3) is suppressed. The remaining positive holes oxidize MeOH to hydroxymethyl radicals, which then inject another electron into the TiO_2-CB (4).

where ϕ_M is the work function of the metal, which is defined as the energy required to excite an electron from the metallic Fermi level into the vacuum, and X_S is the electron affinity of the SC being *ca.* 3.9 eV for TiO_2.[25] As the work function of Au is 5 eV, the Schottky barrier at the Au/TiO_2 interface becomes *ca.* 1.1 eV.[26] Hence, the electrons are hindered from back transfer into the TiO_2-CB and instead accumulate in the metal, whereby the Fermi level is shifted negatively.[27] Once the potential has exceeded $E(H^+/H_2)$, the protons are reduced to H_2. On the other side, strongly oxidizing positive holes, h^+_{vb}, remain in the valence band, which can easily oxidize MeOH as its oxidation potential is equal to 0.55 V.[28] Depending on the nature of adsorbed species, the MeOH oxidation occurs either directly or indirectly.[29] The latter happens in assistance of hydroxyl radicals primarily formed upon hole-trapping at surface-hydroxyl groups ($E(OH^\bullet/OH^-)$= 1.90 V at pH 7)[28] according to Eq. 1.9.

$$OH^- \quad + \quad h^+_{vb} \quad \rightarrow \quad {}^\bullet OH \tag{1.9}$$

Asmus *et al.*[30] showed that $^\bullet$OH radicals react with MeOH rather through the abstraction of a hydrogen from a C–H bond (93 %) resulting in hydroxymethyl radicals ($^\bullet CH_2OH$, also identified by EPR spin trapping)[31,32] instead of forming methoxy radicals, $CH_3O^\bullet$. The $^\bullet CH_2OH$ radicals exhibit a large negative potential ($E(HCHO, H^+/^\bullet CH_2OH) = -0.74$ V), [33] and therefore quickly inject an electron into the TiO_2-CB producing formaldehyde (Figure 1.1 (4), current doubling effect).[34] In analogous manner, HCHO could be further oxidized to HCOOH and finally to CO_2 (Eq. 1.3–1.4).[35,36] Although at least half of the produced H_2 might be attributed to the hole-mediated oxidation process due to the current doubling effect,[37] Bahnemann *et al.* showed by isotope experiments that D_2 was detected as main product from a CH_3OH/D_2O mixture over Pt-TiO_2 and concluded that most likely the evolved H_2 originates from water, while MeOH solely acts as SR.[38]

1.2.2 Progress in semiconductor photocatalysis for H_2 generation

Since the oil crisis in 1973, rapid progress was made in the development of SC-based photocatalysts for H_2 production.[13] Figure 1.2 depicts the different generations of SC photocatalysts ranked by their performance in solar fuel production. TiO_2 was chosen as exemplary main component due to its popularity in photocatalysis.

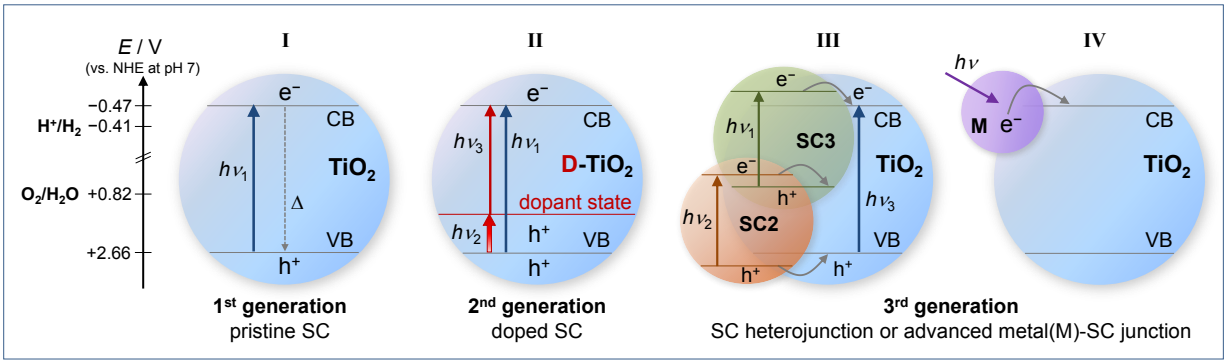

Figure 1.2: Development of SC-based photocatalysts for H_2 generation.[13]

Pristine semiconductors

The application of pristine SCs (1^{st} generation) was shown to be of limited efficiency due to several reasons. Besides the well-known TiO_2 (E_g = 3.0–3.2 eV)[39], other pristine SCs were investigated, such as ZnO (E_g = 3.2 eV),[40, 41] $NaTaO_3$ (E_g = 4.0 eV),[42] and $SrTiO_3$ (E_g = 3.4 eV),[43] all of them characterized by suitable band positions for overall water splitting. By employing these bare SCs as photocatalysts, generally the rapid recombination of charge carriers resulted in low H_2 yields. As explained above, this could be suppressed by addition of metal particles or carbon-based conducting materials such as graphene.[44–47] Moreover, it has been shown that the photoactivity of pristine semiconductors is governed by their structural and electronic properties,[48, 49] which can be mainly influenced by the chosen synthesis route. For TiO_2, it was reported that an optimum particle size exists in photocatalytic reactions, which has been ascribed to the two competing recombination processes in the bulk and at the surface of the catalyst.[48] The SC-particle size can be effectively tuned *e.g.* by variation of the reaction time and calcination processes,[48] the reaction conditions such as pH,[50] or the type of preparation itself.[51]

However, due to their large band gaps (> 3 eV), only UV light can be absorbed by the most common materials, which limits the solar-to-hydrogen-conversion (SHC) efficiency even in the presence of electron-trapping noble metals. In view of practical applications, the SHC should reach values of 10 % corresponding to a band gap of about 2.5 eV (without

any losses). Hence, the conversion of visible light by the photocatalyst is indispensable for a feasible H_2 economy. Visible-light-responding pristine SCs, however, either evinced a high sensitivity to photo-corrosion (CdS, CdSe) or possess unsuitable band positions for H_2 generation such as WO_3 or Fe_2O_3.[52, 53] Furthermore, low-band-gap materials demonstrated generally lower photoactivities in surface-chemical reactions. This has been attributed to insufficient flat-band potentials for the initiation of photocatalytic processes compared to wide-band-gap SCs.[54]

Doped semiconductors

Many approaches have been established for narrowing the band gap of promising SCs that showed high H_2 evolutions under UV light. Doping with (non-)metal cations or anions emerged as a promising route to enhance visible-light absorption. The substitution of lattice metal ions or anions of these wide-band-gap materials creates certain intraband levels (localized or delocalized, depending on the dopant concentration)[55] in the forbidden band (Figure 1.2, II). Choi *et al.* showed that doping of TiO_2 with 21 different metal ions led to a red shift of the absorption edge, which was attributed to charge transitions between the metal-ion *d* electrons and the TiO_2 conduction band.[56] However, visible-light absorption caused by doping can only produce H_2 when the created charge carriers can supply adequate redox potentials for proton reduction. Karakitsou *et al.* reported about improved H_2 rates by doping TiO_2 with cations of a valence higher than that of the parent cation (Ti^{4+}), whereas the introduction of lower-valence cations reduced the H_2-evolution rate.[57] This was attributed to the resulting electronic alterations upon either *n*- or *p*-type doping, respectively. Co-doping with two suitable metal ions can also increase the photoactivity due to synergistic effects. While mono-doping of $SrTiO_3$ with Cr increased the number of recombination centers (Cr^{6+} formation) leading to lower activities, co-doping with Cr/Nb, Cr/Ta, Cr/W or Cr/Sb enabled H_2 production from H_2O/MeOH even under visible light, since the second metal component maintained the charge balance by preventing Cr^{6+} formation.[58, 59] It was further shown that metal-ion doping also affects the charge recombination rates. Introducing metal ions near the surface enhanced the charge-carrier transfer by fast trapping and detrapping processes, whereas bulk doping apparently hindered their migration to the photocatalyst's surface resulting in lower H_2 evolutions compared to the undoped TiO_2.[60]

Perturbation of the SC valence band by anion doping (N, F, S, C *etc.*) may be more promising for enhancing visible-light H_2 evolution,[61] as it was reported to be less associated with the formation of recombination centers compared to metal-ion doping.[20] N-doped TiO_2 is by far the most investigated photocatalytic system in this connection (an overview is given in Ref. [62, 63]). Nitrogen has been incorporated into the TiO_2 lattice

through several methods, *e.g.* the reduction-nitridation procedure *via* nonthermal plasma treatment,[64] sputtering and subsequent calcination of TiO_2 in N_2,[61] wet methods using urea or aqueous NH_3 solution,[65,66] and annealing in NH_3(g) flow.[67] There exist different opinions about the effect of N incorporation on the TiO_2 band gap. The increased visible-light response of TiO_2:N was either attributed to a band-gap narrowing upon mixing the N 2*p* orbitals with the O 2*p* states,[61] or to the excitation of electrons from localized N 2*p* states located slightly above the TiO_2-VB (Figure 1.2, II),[67] the existence of which has been confirmed by recent theoretical calculations on this system.[68,69] The photoactivity of the N-doped catalysts, however, did not always correlate with the observed absorptions.[62] Yuan *et al.* reported about the effect of N content and calcination temperature of urea-prepared TiO_2:N for H_2 generation from H_2O/Na_2SO_3 solution. Interestingly, a significant increase in visible-light (>400 nm) H_2 evolution was observed for high N contents (urea/$TiO_2 \geq 3$) and upon high-temperature treatment, the latter of which led to a partial phase transformation from anatase to rutile.[65] The authors inferred that due to the thus created TiO_2:N phase mixture, visible-light-excited charges were separated more efficiently similar as in the case of well-known P25 leading to enhanced photoactivity as explained below.

Recently, Sayed *et al.* reported that N doping of reduced TiO_2 further increased the H_2 evolutions under visible light.[70] In addition to the N-introduced states above the valence band, the reduced TiO_2:N contained high amounts of Ti^{3+} as evident from EPR spectroscopy, which must be associated with oxygen vacancies creating discrete levels below the TiO_2-CB. When their concentration is high enough, the authors inferred an overlap of these states with the CB, whereby the band gap is narrowed. Reduced pristine TiO_2 is also known as "self-doped" TiO_2. Although it was once claimed to be photoinactive for H_2 evolution due to lower electron mobility and decreased reduction potential of the vacancy states,[71] many groups recently reported about the development of highly efficient self-doped TiO_2 for photocatalytic H_2 generation.[72–74] Possible methods to obtain reduced TiO_2 materials are *e.g.* anodization[73,74], the pulsed-laser ablation method,[75] and chemical reduction with 2-ethylimidazole or diethylene glycol.[72,76] Especially, "blue" or "black TiO_2" prepared by hydrogenation of stoichiometric TiO_2 have attracted considerable attention in the last years, due to their enhanced performance in water splitting under visible light.[77–82] In this regard, Liu *et al.* showed that a remarkable activation upon a specific high-pressure H_2-treatment was observed for anatase-containing TiO_2.[81] However, structural and/or electronic reasons explaining this observation from an *in situ* spectroscopic point of view have been barely provided for these systems.

Semiconductor composites

One major limitation of SC doping is that thereby the oxidation and reduction potentials of the excited charge carriers can be reduced as well. Moreover, in order to avoid increased recombination rates due to higher defect concentrations in doped SCs, another route has been followed for the development of visible-light-active photocatalysts, *i.e.* the constitution of multisemiconductor composite systems (Figure 1.2, III). In principle, one can distinguish between "multiphase" heterojunctions, consisting of different phases of the same compound, and "multicomponent" heterojunctions, which are composed of different SC materials.

The most prominent example of a multiphase composite is a TiO_2 anatase/rutile mixture, *e.g.* the commercial P25 of Evonik Industries. Since both TiO_2 phases exhibit different crystal structures, the band positions in anatase and rutile are different as well. It is generally accepted that the band gaps of rutile and anatase exhibit values of 3.03 and 3.20 eV, respectively.[39] However, the particular positions of the CB and VB in both TiO_2 polymorphs are still a matter of debate. While in 1996, the CB of anatase was determined by electrochemical impedance analysis to lie 0.2 eV above the CB of rutile,[84] recent studies using DFT and XPS indicate that the CB of rutile is positioned 0.2 eV more negatively than the CB of anatase and that the rutile-VB lies *ca.* 0.4 eV above the VB of anatase.[83,85] Hence, photo-excited electrons in an anatase/rutile composite are most likely transferred from rutile to anatase, while positive holes travel in the opposite direction. This is supported by former EPR investigations of TiO_2 mixed phases[86–88] and is proposed to be the main reason for the improved photocatalytic activity in *e.g.* H_2 generation compared to pure-phase TiO_2 catalysts.[32] Brookite/anatase composites were also reported to improve H_2 evolution from aqueous MeOH solutions,[89,90] though brookite-containing heterojunctions were less investigated from a mechanistic point of view. The brookite phase has a more cathodic CB potential than anatase, therefore electron transfer from brookite to anatase was proposed to occur in these composites confirmed by transient absorption measurements.[90]

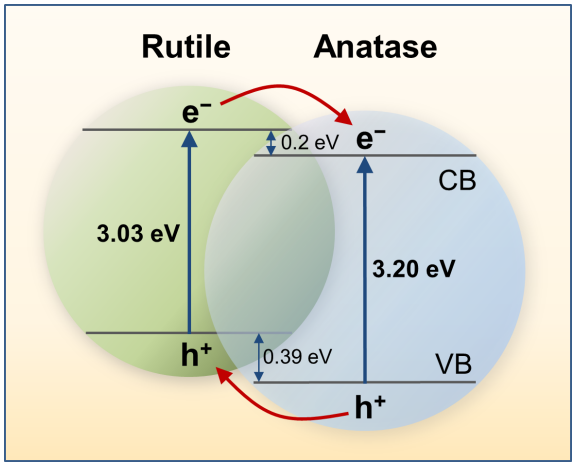

Figure 1.3: Band alignment in an anatase/ rutile heterojunction.[83] Excited electrons are transferred from rutile to anatase, whereas holes travel in the opposite direction.

In order to enhance visible-light photoactivities, multicomponent heterojunctions composed of low- and wide-band-gap materials were developed. Many of these composite systems have been investigated for solar H_2 production as well (for an overview see [91]). The CdS/TiO_2 composite belongs to the most investigated systems since 1984. Electrons in CdS

($E_g = 2.4\,\text{eV}$)[91] can be excited by visible light and are then transferred to TiO_2 due to its lower CB.[92] Recently, this system gained attention again, since very high SHC efficiencies were observed by decorating one-dimensional TiO_2 nanostructures, such as nanowires and nanotubes, with CdS quantum dots.[93–95] Serpone suggested that multiphoton excitation may be successful using a heterojunction composed of two low-band-gap materials and TiO_2 (Figure 1.2, III) as 3rd generation photocatalysts, whereby appropriate positioning of VB and CB could occur through the quantum size effect.[13]

Plasmonic metal loading

Utilizing the surface plasmon resonance (SPR) phenomena of noble metal nanoparticles (NPs), such as Au, Ag, and Cu, has attracted tremendous interest in heterogeneous photocatalysis over the past 20 years (Figure 1.4). This is due to the fact that, on the one hand, SPR-metal-loaded SCs exhibit the advantages of a typical metal-SC junction, *i.e.* an improved charge-carrier separation resulting from the Schottky barrier. On the other hand, SPR of coinage metals leads to light-absorption in the visible region, *e.g.* around 520 nm for 10 nm spherical Au particles.[96] Hence, the SPR effect improves the catalytic rates under visible light for many reactions as demonstrated in numerous studies (for an overview see [97, 98]). For example, the selective oxidation of alcohols over supported Au NPs, *e.g.* the conversion of benzyl alcohol to benzaldehyde, was shown to be promoted under visible-light irradiation, which was attributed to the Au-SPR absorption.[99, 100] Similar effects were observed in imine synthesis.[101, 102] In photocatalysis, the SPR properties of Au were reported to enhance *e.g.* the degradation of organic pollutants,[103–105] the reduction of CO_2 to hydrocarbon fuels,[106] photoelectrochemical water splitting,[107–109] and hydrogen generation from aqueous organic solutions under visible light.[110–117] Therefore, Serpone *et al.* considered improved systems consisting of SPR-NP-decorated photoactive materials as next (3rd) generation photocatalysts, whereby the SPR-NPs act as antennae in nanocomposites for enhanced multi-photon excitation (Figure 1.2, IV).[13]

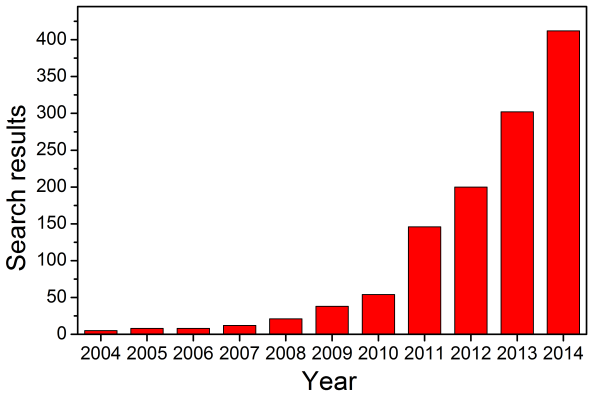

Figure 1.4: Number of publications per year related to the SPR effect in photocatalysis. Data collected by topic search (plasmon* AND photocatal*) in ISI Web of Science [v5.16].

The fundamental principle of the SPR effect is described by Mie's theory.[118] It is based on the interaction of the Au *sp* electrons with the incident light leading to coherent

oscillations of charges at the metal-dielectric interface (Figure 1.5a), *i.e.* the plasmon. Light is absorbed by the NP when the frequency of the surface electrons matches the photon frequency. For Au, Ag and Cu, this absorption occurs usually at 530, 400, and 580 nm, respectively. The spectral position of the plasmon resonance is, however, dependent on the surrounding medium as well as on the NP size and shape.[119] In general, SPR only starts to be detectable at a cluster size above 2 nm,[120] since then the localized molecular orbitals of the metal cluster overlap and form a conduction band, in which the electrons can move quasi-free. The absorption maximum of the SPR band typically shifts to higher wavelengths with increasing particle size. Due to the SPR properties, the NPs exhibit very large absorption and scattering cross sections as well as a strong resonant enhancement of the local electromagnetic field near the NP surface. The excited plasmon can decay through two competing channels (Figure 1.5b). The probability for radiative decay, *i.e.* the re-emission of photons (scattered light), is directly proportional to the NP volume and dominates for particles larger than 40 nm.[121] Non-radiative decay is the dominating channel for small particles and results in the formation of electron-hole pairs. Electrons in the NP are then excited to energy levels above the Fermi level ("hot states") and are, thus, no longer in thermal equilibrium with the remaining cold electron sea. As depicted in Figure 1.5b, this electron excitation can either occur within the *sp* band (*intra*band transitions) or through *inter*band excitation resulting from the transition of *d* electrons into the *sp* band. The latter transition occurs in both, NPs and bulk metals of $d^{10}s^1$ configuration. Whereas the contribution of interband transitions to the absorption cross section is negligible for Ag NPs, Au and Cu show an overlap between $d \rightarrow sp$ excitations at $E \approx 2.4$ eV with the intraband SPR transitions.[122]

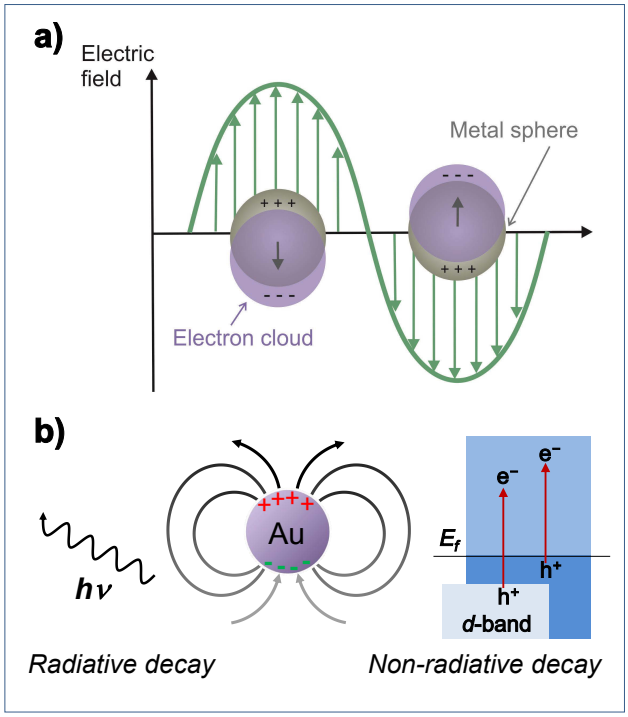

Figure 1.5: a) Schematic description of the SPR effect in noble-metal NPs upon interaction with light. b) Decay processes for excited surface plasmons.

The mechanism of SPR-enhancement in photocatalysis is still controversially discussed. The SPR-driven decomposition of organic compounds under visible light for example has been ascribed to a direct electron transfer (DET),[123–125], the local electric-field enhancement (LEFE), [126–128], and the local heating effect (LHE).[129,130] Especially the Au-NP size was reported to play a crucial role in photocatalytic H_2 generation over Au-TiO_2 cata-

lysts, as it was demonstrated to be more effective by use of larger Au particles.[115,131,132] The different mechanisms are illustrated in Figure 1.6 for photocatalytic H_2 evolution from H_2O/MeOH.

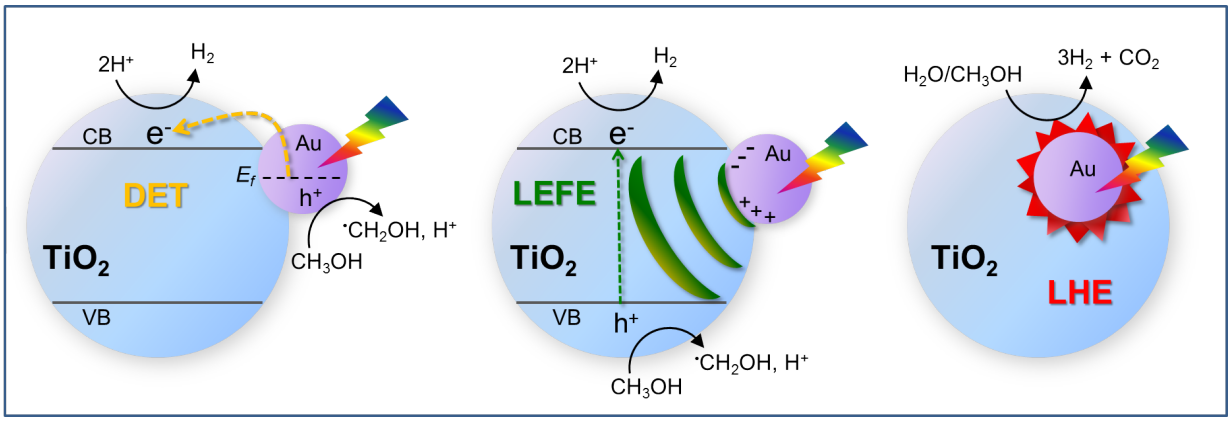

Figure 1.6: Possible mechanisms of SPR enhancement in photocatalytic H_2 generation from H_2O/MeOH over Au-TiO_2. Visible-light activity can be caused by direct electron transfer (DET) from Au to TiO_2, electron-hole pair formation in TiO_2 *via* local electric field enhancement (LEFE), and an SPR-induced local heating effect (LHE).

Direct electron transfer Tian and Tatsuma were the first who proposed a direct charge transfer of excited Au electrons into the TiO_2 support, which explains their observations of increased photocurrent upon visible-light excitation of an Au-TiO_2 photoelectrode.[124] DET is assumed to occur when the SPR-excited "hot" electrons reach energy levels higher than the Schottky barrier (Figure 1.6, left). Nishijima *et al.* even observed a photocurrent by irradiating Au-TiO_2 with light of 1300 nm,[133] which corresponds to *ca.* 0.95 eV and is, thus, of sufficient energy to inject Au electrons from the Fermi level into the TiO_2-CB, the gap between which was estimated by 0.96 eV.[97] The transferred electrons then accumulate in the conduction band, whereby their reduction potential increases. Finally, the electrons possess enough reductive power to reduce adsorbed protons and evolve hydrogen. At the same time, positive holes formed in the Au NP are proposed to be consumed by the sacrificial electron donator, *e.g.* methanol. Since this DET mechanism is similar to that in dye-sensitized semiconductors introduced first by Grätzel *et al.*,[134] the effect is often called *SPR sensitization*. An increased photocurrent alone, however, may not be taken as evidence for this ultrafast electron-transfer phenomenon, as such improvements have also been explained by changes in light scattering or reflection.[135] Besides interesting approaches using transient absorption spectroscopy,[136–139] rarely any spectroscopic evidence has been provided so far for the DET mechanism.

Local electric-field enhancement Other groups claim that the DET mechanism is unfavorable as the individual electrons would not carry enough energy to overcome the Schot-

tky barrier, since SPR is a collective phenomenon and, thus, the photon energy should be shared by a multitude of electrons.[140] Furthermore, SPR enhancement was also observed when the semiconductor and the metal NPs were separated by insulating layers inhibiting DET.[141] This was explained by a strongly enhanced local electromagnetic field near the surface of the NPs, which in turn enhances the generation of electron-hole pairs within the semiconductor (Figure 1.6, middle). Visible-light excitation of Au-TiO_2 was demonstrated to enhance the incident electric-field intensity at the TiO_2 surface by up to 1000 times, which led to an increased water-splitting activity by factors 5 and 66 using 532 nm and 633 nm as excitation wavelength, respectively.[108]

Local heating effect Upon excitation, the "hot" electrons can also thermalize through electron-electron scattering, which produces a hot-electron sea of several thousands of degrees Celsius.[142] By reaching a thermal equilibrium in the metal NP, a temperature increase of the semiconductor and the reaction medium in the close surrounding of the NP can be observed. This LHE was proposed to enhance the thermochemical and thermocatalytical degradation of organic compounds at a relatively low external temperature.[143, 144] Hydrogen generation by ethanol reforming was also reported to be improved by plasmon-induced localized heating.[130] In general, smaller particles show a higher light-absorption efficiency as explained above and are thus more efficient in converting light into heat than larger particles.[143, 145]

2 Methods and experimental protocols

In this chapter all of the investigated materials and their preparation procedures are listed. Furthermore, a fundamental theoretical background of applied characterization methods is provided. Thereby, this chapter is the basis necessary to follow the deep analytical investigation and interpretation presented in the next chapters. After describing the detailed synthesis protocols for the photocatalysts in the first section, the standard photocatalytic testing procedure is introduced, by which the evolved hydrogen under UV and visible light from H_2O/MeOH mixtures was determined. Finally, the value of specific standard ex situ characterization techniques in photocatalysis is explained and their fundamentals are introduced. The main focus lies on the application of spectroscopic in situ methods, the relevance of which is stressed in this chapter as well. In situ UV-vis, FTIR, XANES, and EPR spectroscopies are explained in more detail due to their uncontroversial pertinence in photocatalysis research.

2.1 Catalyst preparations

2.1.1 Synthesis of $NaTaO_3$ photocatalysts

All $NaTaO_3$-based materials studied in this thesis (Chapter 3) were synthesized in the lab of Dr. S. Wohlrab at LIKAT Rostock. Two different methods were applied to prepare $NaTaO_3$: a standard solid-state reaction (SSR) introduced by Kato *et al.*,[146] and an exotemplate method (EM) described by Wohlrab *et al.*[147] Briefly, for obtaining catalyst **$NaTaO_3$(SSR)**, a stoichiometric mixture of Ta_2O_5 (4.40 g, 9.96 mmol, 99.99 %, ChemPur) and Na_2CO_3 (1.06 g, 9.6 mmol, Merck) was suspended in 20 mL of ethanol and well ground in an agate ball mill (200 rpm) for 24 h. After drying at 50 řC, the mixture was thermally treated in a Pt crucible at 1150 řC (10 řC min^{-1}) for 10 h. **$NaTaO_3$(EM)** was obtained by dissolving $NaNO_3$ (0.75 g, 8.80 mmol, Merck) in 50 mL deionized water and adding subsequently a $Ta_2(C_2O_4)_5$ solution (11.4 mL, 8.80 mmol, c_{Ta} = 0.77 mmol mL^{-1}, H.C. Starck), polyvinyl alcohol (3.0 g, 98 %, M_n = 72000 g mol^{-1}, Roth) and D-sucrose (30.0 g, 99.7 %, Roth) under continuous stirring at 95 řC. After complete dissolution, the viscous mixture was heated at 220 řC for 1 h to produce a carbonaceous foam. $NaTaO_3$ NPs were obtained by calcination at 500 řC for 20 h.

Multilayered reduced graphene oxide (m-rGO) was synthesized by slowly adding graphite powder (3.0 g, particle size <20 µm, Sigma-Aldrich) and $KMnO_4$ (18.0 g, 0.11 mol, Sigma-Aldrich) to a solution of H_2SO_4 (360 mL, 98 %) and H_3PO_4 (40 mL, 85 %) at T = 40 řC. The suspension was kept at 50 řC for 12 h before cooling down to room temperature. Then, the mixture was added to 400 mL ice, containing H_2O_2 (3.0 mL, 30 %). After sifting it two times through a metal sieve (250 µm), the filtrate was centrifuged (15 min, 8000 rpm). The precipitate was washed two times consecutively with deionized water, 30 % HCl solution, and ethanol. Finally, the remaining solid was washed with water, centrifuged, and vacuum-dried overnight at 60 řC. For the reduction step, the material was dispersed in ethanol and kept in a Teflon-lined stainless-steel autoclave at 150 řC for 12 h. Au- and/or m-rGO-loaded $NaTaO_3$ were generated *in situ* by adding 10 wt.-% m-rGO and/or $HAuCl_4 \cdot 3H_2O$ corresponding to 0.2 wt.-% Au (related to the mass of the semiconductor) into the reaction vessel during the photocatalytic H_2-evolution measurements, whereby the additives were deposited *via* a photo-deposition mechanism.

2.1.2 Metal deposition onto TiO_2

Au-deposition techniques for Au-TiO_2 synthesis

The impact of the Au-deposition procedure on the catalytic performance (Chapter 4) was investigated by depositing the nominal amount of 1 wt.-% Au onto TiO_2 (P25, Evonik)

by use of different synthesis protocols. Unless otherwise stated, each method ended with filtering the solid, washing with 500 mL distilled water and drying for 12 h at 100 řC in air.

For **sol-immobilization (SIM)**,[148] an aqueous solution of polyvinyl alcohol (PVA) (1.2 mL, 1 wt.-% solution, Merck Chemicals) was slowly added to an aqueous solution of $HAuCl_4 \cdot 3H_2O$ (5 mL, 10.1 mM, Aldrich). The sol was formed by dropwise addition of a freshly prepared $NaBH_4$ solution (2.5 mL, 0.1 M, Aldrich). After stirring for 30 min at 25 řC, 1.0 g of the TiO_2 support (*e.g.* P25, Evonik) was added and the suspension was stirred for further 12 h.

A carbon-free **reductive precipitation (RP)** method similar to SIM was carried out by first suspending 1.0 mg TiO_2 in 20 mL distilled H_2O. Then, an aqueous solution of $HAuCl_4 \cdot 3H_2O$ (5 mL, 10.1 mM) was slowly added and the suspension was stirred for 10 min. A freshly prepared $NaBH_4$ solution (2.5 mL, 0.1 M) was dropped into the mixture and stirred further 30 min at 25 řC prior to filtration.

For **photo-deposition (PD)**, 1.0 g TiO_2 was added into a Schlenk tube containing 100 mL methanol. The suspension was flushed with argon in order to remove oxygen as a potential electron acceptor. TiO_2 was pre-reduced by irradiation with a 300 W Xe lamp (LOT Oriel) for 20 min, whereby a color change from white to blue was observed, indicating the formation of Ti^{3+}. An aqueous solution of $HAuCl_4 \cdot 3H_2O$ (0.53 mL, 0.1 M) was dropped into the suspension, which was then stirred for 2 h at 25 řC.

Deposition-precipitation (DP) occurred by heating a suspension of $HAuCl_4 \cdot 3H_2O$ (50 mL, 5 mM) to 70 řC under continuous stirring. A NaOH solution (10.5 mL, 0.1 M) was added dropwise to adjust the pH to around 7. 10.8 mL of the Au-containing solution were added to 96.8 mL distilled H_2O and stirred for 15 min. Then 1.0 g of TiO_2 were added and the suspension was stirred for 1 h at 70 řC and for a further 1 h at 25 řC. A **prolonged deposition-precipitation (DP12)** procedure was carried out by extending the stirring time at 25 řC from 1 h to 12 h. The **effect of calcination** on the properties of catalysts prepared by DP was investigated as well. To this end, the dried DP catalyst was calcined at 200, 400 or 600 řC (5 řC min^{-1}, 2 h) in flowing air (denotation: **DP200**, **DP400** and **DP600**, respectively).

Deposition of Cu-based (mixed-)metal particles onto TiO_2

P25 (Evonik) was used as TiO_2 support material in order to study the impact of the nature of the metal particle and its composition (Chapter 6). Two pure Cu-loaded TiO_2 catalysts were synthesized applying different protocols. **Impregnation method (IM)** was carried out by suspending 1.0 g TiO_2 in 300 mL absolute alcohol. An aqueous solution of $Cu(NO_3)_2 \cdot 3H_2O$ (0.15 mM, 25 mL, Aldrich) was added dropwise. The mixture was stirred for 10 h at 80 řC, filtered and washed with 500 mL distilled water. The material was dried

at 100 řC for 12 h and subsequently calcined at 500 řC (3 řC min^{-1}, 3 h) in flowing air. The **RP** method was carried out as described above for Au deposition using 1.0 g TiO_2, an aqueous solution of $Cu(NO_3)_2{\cdot}3H_2O$ (0.15 mM, 5 mL), and a freshly prepared solution of $NaBH_4$ (0.1 M, 4 mL).

Mixed metal particles (Cu/Au and Cu/Ag) were also deposited *via* RP method. For that purpose, either a **stepwise precipitation (SP**) or a simultaneous **co-precipitation (CP**) procedure was applied. SP was carried out by first dropping an aqueous $NaBH_4$ solution (0.1 M, 4 mL) into 20 mL of an aqueous suspension containing 1 g TiO_2 and 36 mg $Cu(NO_3)_2{\cdot}3H_2O$. After 20 min of reduction time, 4.0 mg $HAuCl_4{\cdot}3H_2O$ (or accordingly 3.1 mg $AgNO_3$) in 10 mL H_2O were added dropwise. $NaBH_4$ solution (0.1 M, 1 mL) was dropped into the solution again, which was then stirred for further 10 min. For Cu/Au-CP, an aqueous $NaBH_4$ solution (0.1 M, 5 mL) was added dropwise to a suspension containing 1 g TiO2, 36 mg $Cu(NO_3)_2{\cdot}3H_2O$, and 4.0 mg $HAuCl_4{\cdot}3H_2O$ in 50 mL H_2O. The mixture was stirred for 30 min prior to filtration, washing and drying at 100 řC.

2.1.3 Preparation and modification of TiO_2-based supports

Pristine TiO_2 materials

In order to explore the effect of the TiO_2-phase composition (Section 5.1), commercial and self-prepared materials were used: two different mixtures of anatase and rutile (**P25**, Evonik, and Hombikat, **Hom**, Aldrich), a pure anatase phase (**Ana**, Sachtleben E3-588-321-006), a pure rutile phase (**Rut**, Sachtleben E3-583-141-005).

An anatase/brookite mixture (**Bro**) was prepared as described elsewhere.[149] Briefly, titanium powder (10 mmol, Aldrich) was dissolved in 30 % H_2O_2 (40 mL, Roth) and 25 % NH_3 (11.2 mL, VWR). The mixture was stored for 16 h at 5 řC. Glycolic acid (27 mmol, Aldrich) was added at 25 řC and the solution was slowly heated to 95 řC under continuous stirring. After 7 h of water evaporation, a yellow titanium glycolate complex was obtained. This complex (5 mmol) was dissolved in H_2O (10 mL) and 25 % NH_3 (10 mL) in order to adjust pH 10.8. The solution was filled in a hydrothermal Teflon reactor (Parr Instruments, 75 mL) and heated to 260 řC for 24 h. The resulting white TiO_2 powder was washed repetitively and dried at 40 řC.

Modification of the TiO_2 supports by reduction

Reduced TiO_2 (**Hy-An**) was provided by the group of Prof. P. Schmuki, University of Erlangen. Commercial anatase (**An**, Aldrich, 99.8 %, particle size: 25–25 nm) was used as precursors for high-pressure H_2 reduction. The reduction procedure has been reported elsewere.[81] Briefly, the TiO_2 powder was annealed in H_2 atmosphere (99.999 %, Linde)

at 20 bar and 500 řC for 20 h in an autoclave (1 L, 70 mm inner diameter). Au deposition (0.6 wt.-%) onto the An support as reference material has been carried out by *in situ* photo-deposition.

Modification of the TiO_2 supports by N doping

Commercial TiO_2 anatase (**Ana**, Sachtleben) and an anatase/rutile mixture (**P25**, Evonik) were heat-treated in an NH_3 flow (99.98 %, Air Liquide) in a tubular furnace (HTM Reetz, type LOBA 1000-58-220-QW) equipped with gas-flow and temperature controllers (JUMO dTRON 308). The TiO_2 sample (3 g) was filled into the glass tube, which was placed on a shaker (200 rpm, IKA VXR basic Vibrax). After setting a certain NH_3 flow (10–15 L h^{-1}), the temperature was raised within 1 h to 500–650 řC and kept for 3–6 h before cooling down to room temperature (see Table 2.1). The sample code consists of the respective support (Ana or P25) followed by the nitridation conditions (NH_3 flow, temperature, time). Au deposition (1.0 wt.-%) was carried out onto Ana:N15-600-5 (**Au-Ana:N**) and P25:N15-550-3 (**Au-P25:N**) using the DP method described in Section 2.1.2 without calcination.

Table 2.1: Preparation conditions of several TiO_2:N catalysts investigated in Section 5.3.

Catalyst	TiO_2 material	NH_3 flow / L h^{-1}	Temperature / řC	Nitriding time / h
Ana:N10-500-6	anatase	10	500	6
Ana:N15-600-5	anatase	15	600	5
Ana:N15-650-5	anatase	15	650	5
Ana:N10-650-5	anatase	10	650	5
P25:N15-600-5	P25	15	600	5
P25:N15-550-5	P25	15	550	5
P25:N15-550-3	P25	15	550	3

For comparison, one sample, **TiO_2:N-Urea**, was synthesized *via* sol-gel approach with urea as nitrogen source. Briefly, urea (40 g, >99 %, Aldrich) was dissolved in distilled water (200 mL) under stirring at room temperature. Titanium(IV) isopropoxide (10 mL, >97 %, Aldrich) was added dropwise and the resulting suspension was stirred for 2 h. Then the solid was isolated by vacuum filtration and dried at 60 řC for 12 h. The yellow material was finally calcined at 400 řC (10 řC min^{-1}) in flowing air for 4 h.

2.2 Catalytic testing

Unless otherwise stated, the photocatalytic tests were performed in the group of Dr. H. Junge (Beller group) at LIKAT, Rostock. The H_2-evolution measurements were carried out under argon atmosphere with freshly distilled solvents. Details about the equipment and the experimental set-up are described in [150]. Typically, a double-walled and thermostatically controlled reaction vessel was connected to an automatic gas burette. 50 mg of the catalyst in 10 mL in H_2O/MeOH (volume ratio 1 : 1) were irradiated with a Hg vapor lamp (Lumatec Superlite 400, 7.2 W output) at 25 řC. Two different internal lamp-filter settings were used: a UV-vis-light filter (320–500 nm, denoted by UV-vis light) and a visible-light filter (400–700 nm, denoted by vis light), the radiation spectra of which are presented in Figure 2.1a and b, respectively. In the majority of cases, gas evolution was recorded under UV-vis light for 3 h and under visible light for further 3 or 21 h. After the reaction was completed, a gas sample was taken for gas chromatographic (GC) analysis using a GC HP 6890N (external calibration). The H_2-evolution rate, r_{H_2} given in mmol g^{-1} h^{-1}, was calculated according to Eq. 2.1 by assuming ideal gas behavior of H_2 with a molar volume of $V_m = 24.48$ L mol^{-1}.

$$r_{H_2} = \frac{V_{exp}}{V_m \, m \, t} \tag{2.1}$$

where V_{exp} is the experimentally determined gas volume evolved after a certain reaction time, t, and m is the sample mass.

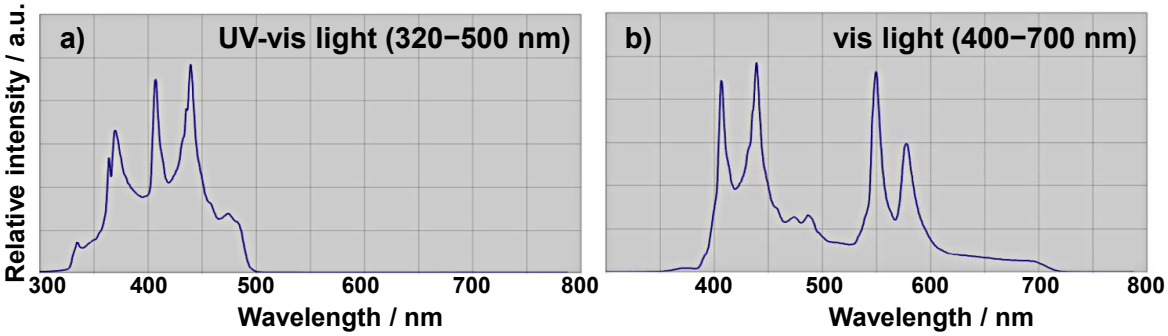

Figure 2.1: Radiation spectra recorded by Lumatec of the Lumatec Superlite 400 for two different internal optical filter settings: a) UV-vis-light filter (320–500 nm) and b) visible-light filter (400–700 nm).

2.3 Techniques for catalyst characterization

In order to shine light on the principles of the catalyst's function, detailed insights into the constitution of bulk and surface are required. These properties may change during the catalytic process. Therefore, standard characterization techniques have to be complemented by advanced methods that are able to characterize each step of the catalyst's

lifespan, especially the catalytic event itself. Not only *ex situ*, but also suitable *in situ* spectroscopic investigations have been carried out in order to reach a deeper understanding of the basic mechanistic steps during photocatalytic proton reduction over metal-loaded semiconductors.

2.3.1 Inductively coupled plasma optical emission spectrometry (ICP-OES)

The knowledge about metal contents and the elemental composition of the semiconducting support material is fundamental for a comparative study of photocatalysts. By ICP-OES analysis, the weight percentages (wt.-%) of metal ions can be determined simultaneously or sequentially. To this end, a plasma source produced by electromagnetic induction excites the elements electronically, whereby characteristic electromagnetic radiation is emitted subsequently by each atom upon the relaxation process.[151] The emission at the different wavelengths is usually recorded by semiconductor photo-detectors, such as charge coupled devices, allowing a quantitative elemental determination by comparing the element-specific radiation intensity with that of a calibration standard.

Experimental description In a typical procedure, the sample (10 mg) was dissolved in 5 mL aqua regia and 3 mL hydrofluoric acid by treatment with the microwave-assisted sample preparation system "MULTI WAVE" (Anton Paar/Perkin-Elmer) at *ca.* 200 řC and 60 bar. The solution was filled up to 100 mL with distilled water and analyzed using a Varian 715-ES ICP-emission spectrometer and the ICP Expert software.

2.3.2 Elemental (CHN) analysis

CHN analysis was applied to determine ion-doping concentrations or impurity levels (mainly carbon and nitrogen) within the photocatalysts. In general, the solid catalyst is burned in an excess of oxygen at temperatures of 1700–1800 řC, which produces typical combustion products such as carbon dioxide (C), water (H) and nitric oxide (N). The product gases flow through a GC separation column and are detected sequentially by a thermal conductivity detector (TCD), which was calibrated against pre-analyzed standards.

Experimental description A CHNS multianalyzer TruSpec (Leco) was used for the quantitative analysis of C, H and N. The catalyst (10 mg) was mixed with V_2O_5 as oxidation reagent and packed into a tin container, which is easily oxidizable. The reactor is heated to 1050 řC and the combustion products were quantified by the TCD at 290 řC.

2.3.3 Brunauer-Emmett-Teller (BET) surface area analysis

As heterogeneous photocatalytic reactions happen at the catalyst surface, the number of photoactive sites usually depends on the surface area of the catalyst. Its dimension is critically affected by the particle size, particle morphology, surface texturing and porosity. It can be determined using the approach developed by Brunauer, Emmett and Teller.[152] The BET theory extends the Langmuir theory of a monolayer physisorption of gases on a solid surface to an infinite multilayer adsorption (Figure 2.2a) and results in the BET adsorption isotherm:

$$\frac{p}{W\left(p_0 - p\right)} = \frac{c-1}{W_m c}\left(\frac{p}{p_0}\right) + \frac{1}{W_m c} \tag{2.2}$$

where p/p_0 represents the relative pressure of the adsorbate at the temperature of adsorption, W is the weight of adsorbed gas, W_m the weight of adsorbate as monolayer and c the BET constant. For small relative pressures ($0.05 < \frac{p}{p_0} < 0.3$) the BET isotherm can be depicted as straight line by plotting $\frac{p}{W(p_0-p)}$ against $\frac{p}{p_0}$ (BET plot, Figure 2.2b). The BET plot allows the determination of W_m and c from the values of the slope ($s = (c-1)(W_m c)^{-1}$) and the y-intercept ($i = (W_m c)^{-1}$). The specific surface area, S_{BET}, can be derived from

$$S_{\mathrm{BET}} = \frac{W_m N_A A_{cs}}{mM} \tag{2.3}$$

where $N_A = 6.023 \cdot 10^{23}$ is the Avogadro constant, A_{cs} is the adsorbate cross sectional area (16.2 Å^2), M is the molar mass of the adsorbate, and m is the sample weight.

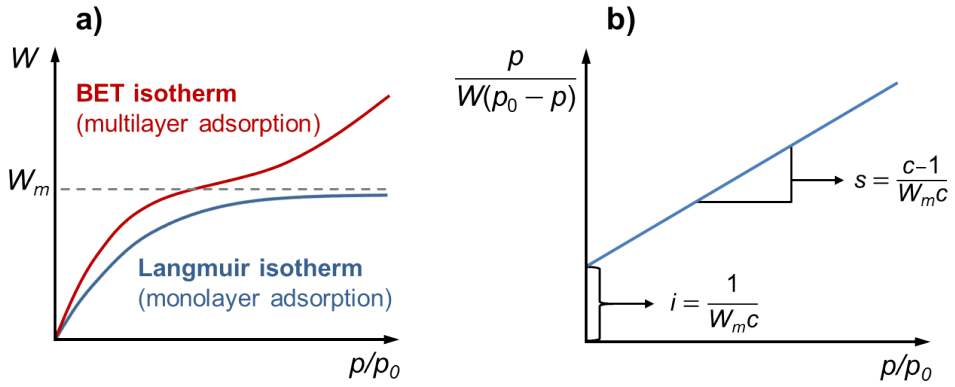

Figure 2.2: a) Comparison between the physisorption isotherms based on Langmuir and BET theory. b) Exemplary BET plot by which W_m and c can be derived.

Experimental description The BET surface area was determined by analyzing the physisorption properties of N_2 on a defined sample weight (200–600 mg) with a BELSORP mini device in the range $0.05 < \frac{p}{p_0} < 0.3$ by multipoint analysis. Prior to measurement, the catalyst was evacuated for 2 h at 150 řC in order to remove physisorbed water molecules.

2.3.4 Transmission electron microscopy (TEM)

The imaging of nanostructured photocatalysts by high-resolution microscopic techniques provides insights into the size distribution, morphology and composition of each nanoparticle species. TEM imaging is based on the elastic scattering of electrons in an high-energy electron beam (100–300 kV) upon interacting with the atoms of a solid thin sample (<100 nm), whereby much higher resolutions (atomic scale) are obtained than by light microscopes due to the small de Broglie wavelength of the electron. Figure 2.3 illustrates the schematic diagram of a conventional TEM. It comprises an illumination system (containing the electron gun), a specimen stage, the magnification system and the data recording system.[153] After transmission through the thin specimen, the scattered electron beam is focused by the objective lens and propagates through several image-forming lenses. The image of the specimen is formed when the fluorescent screen is located in the image plane of the objective lens. In general, there are three different modes of operation defined by the alignment of the objective aperture allowing the creation of contrast (Figure 2.3b). For *bright-field imaging*, only the forward scattered wave is used to form the image, whereby darker parts of the image correspond to more strongly scattering parts (thick areas in which heavy atoms are enriched) of the sample. In contrast, these regions appear brighter in the *dark-field mode* when the objective aperture allows only diffracted beams to pass. High-angle annular dark field (HAADF) images are formed by beams that have strongly interacted with the specimen and reveal useful information, *e.g.* about planar defects or stacking faults. Lattice images are obtained by *high-resolution TEM* which uses a large objective aperture that allows many beams, including the direct beam, to pass (Figure 2.3, bottom).

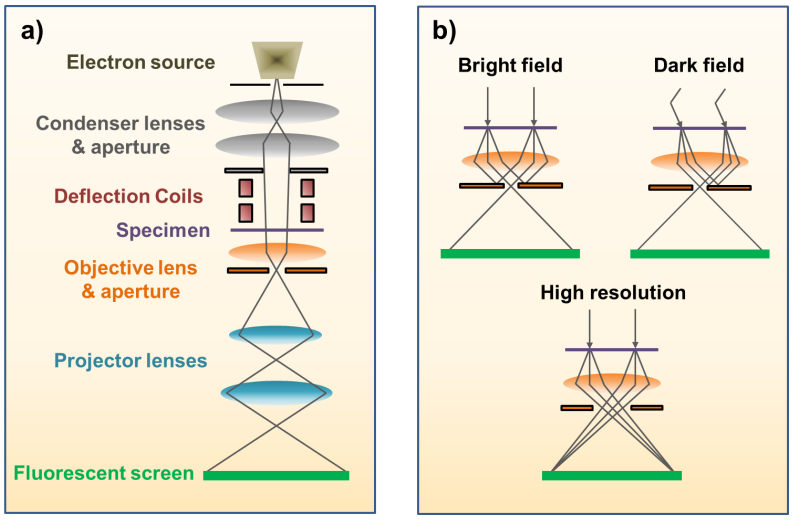

Figure 2.3: a) Scheme of a conventional TEM. b) Optic ray diagrams for bright-field, dark-field and high-resolution TEM.

In addition to the elastic scattering forming TEM images, the interaction of the electron beam with the specimen also comprises inelastic scattering phenomena. The impinging

electron beam may transfer enough energy to an inner-shell electron of an atom that it gets excited into the vacuum level. Consequently, an emission of X-ray photons occurs by the transition of outer-shell electrons to the vacant site. The energy of the emitted photons is characteristic of the emitting atom. Therefore, TEM can be directly coupled with an energy-dispersive X-ray (EDX) spectroscopic device for local elemental analysis, which counts the X-rays emitted from the illuminated specimen region as a function of the photon energy.

Experimental description Transmission electron microscopy investigations were conducted at 200 kV by using a JEM-ARM200F (JEOL) instrument. The microscope is equipped with a JED-2300 (JEOL) energy-dispersive X-ray spectrometer (EDXS) for chemical analysis. HAADF imaging was operated with a spot size of 5 c (*ca.* 0.15 nm) and a 30 µm condenser aperture. Prior to TEM analysis, the sample was deposited onto a carbon-supported Cu grid (mesh 300). For Cu-containing samples, Ni grids were used. Size distributions of the metal components were determined by measuring the diameters of at least 50 particles using the ImageJ software.

2.3.5 X-ray diffraction (XRD)

As explained above, crystallinity and crystal structure of semiconductor photocatalysts can highly influence the photocatalytic performance. Therefore, the nonambiguous determination of the interatomic distances and bond angles by X-ray diffraction analysis is highly desirable. This technique is based on the interaction of lattice atoms with a monochromatic beam of incident X-rays (of wavelengths similar to the spacing of planes in the crystal lattice) causing its diffraction, constructive and destructive interference, into many specific directions (Figure 2.4). The condition for constructive interference is expressed by Bragg's law:[154]

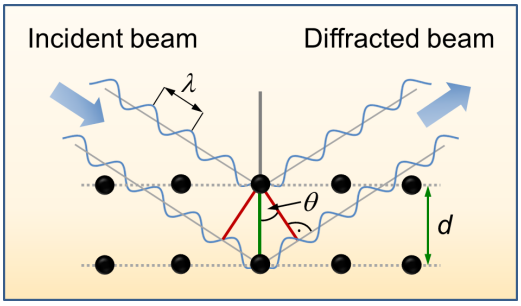

Figure 2.4: Scheme of the Bragg diffraction of X-rays at atoms in a crystal lattice.

$$n\lambda = 2d\sin\theta \tag{2.4}$$

where n is an integer (order of reflection), λ is the wavelength of the incident X-ray beam (1.5406 Åfor Cu K_α), d is the distance between parallel lattice planes, and θ is the angle between the incident beam and the lattice plane. For each lattice distance, Eq. 2.4 predicts a maximum at a specific diffraction angle. These powder-diffracted X-rays are detected and counted for each value of 2θ in a certain range so that all possible diffraction directions

are attained. By plotting the intensity of detected X-rays as a function of 2θ, an X-ray diffraction pattern is obtained, which represents the structure of the unit cells within the investigated sample. Furthermore, the crystallite sizes can be obtained by X-ray line broadening analysis. This method was developed by Scherrer,[155] who showed that the line broadening (full width at half maximum) of the diffraction peak, β, is related to the mean crystallite diameter, D_c, as:

$$D_c = \frac{K\lambda}{\beta \cos\theta} \tag{2.5}$$

Experimental description X-ray diffraction powder patterns at ambient conditions were recorded in transmission geometry with Cu K_α radiation in the 2θ range of 10–70 ř (step width = 0.25 ř) on a Stoe STADI P diffractometer, equipped with a linear position sensitive detector. For quantitative determination of phase ratios, Rietveld method was applied on the XRD patterns. Mean crystallite sizes were estimated using the Scherrer equation with $K = 0.95$ and $\lambda = 1.54$ Å.

2.3.6 X-ray photoelectron spectroscopy (XPS)

XPS is a powerful technique for determining surface-sensitively (usually in 1–10 nm depth) the elemental composition as well as the chemical and electronic state of the elements in a solid catalyst. It is based on Einstein's photoelectric effect. This phenomenon occurs when high-energy photons (*e.g.* X-rays) impinge on a sample and lead to the ionization of atoms. Thereby, valence and tightly-bound core-level electrons absorb the photons, which leads to their ejection into the continuum with a certain amount of kinetic energy, E_{kin}. Using monochromatic X-rays of known energy (*e.g.* Al K_α with a photon energy of $E_p = 1486.6$ eV) the electron binding energy, E_b, of the emitted electrons (with respect to the Fermi level of the spectrometer) can be determined by detecting their kinetic energy based on the following equation:

$$E_b = E_p - (E_{kin} + \phi) \tag{2.6}$$

where ϕ is the work function of the spectrometer, which is equal to the energy released by the photoelectron as it becomes absorbed by the detector of the spectrometer. E_b is the energy difference between the electron's original level, E_i (initial state), to a state of rest outside the atom, E_f (final state). Thus, a shift of peak position in a XP spectrum can be due to final-state and initial-state effects, the latter of which are closely associated to changes in the oxidation state of the atom. Such change in the charge of an atom can, however, also arise from changes in the surroundings (*e.g.* ligand alterations). Changes

of an atom's core-level structure may be also dominated by effects of the positive charge (core hole) remaining on the atom cluster in the photoemission final state.[156] *I.e.* smaller metal particles exhibit more discrete conduction bands and more coordinatively unsaturated surface atoms. Therefore, the screening of a created core hole will be much smaller as the particle size decreases, so that the photoelectron will experience a higher E_b.[157]

The photoelectron peak intensity, I_j, for an element j depends on the average atomic concentration of element j in the surface, N_j, by

$$I_j = N_j \sigma_j \lambda_j K \tag{2.7}$$

where σ_j is the photoelectron cross-section (Scofield factor) for element j, λ_j is the inelastic mean free path of a photoelectron from element j, and K is a constant expressing all other factors related to quantitative detection of an XPS signal. Hence, by measuring standards of known surface concentration, it is possible to determine surface contributions of elements in the material, which account for the catalytic active sites in a heterogeneous catalyst.

Experimental description XP spectra were recorded using a VG ESCALAB 220iXL instrument with monochromatic Al K_α radiation. Peaks were fitted by Gaussian-Lorentzian curves after Shirley background subtraction. The electron binding energy was referenced to the adventitious carbon with C 1*s* peak at 284.8 eV. For quantitative analysis, the peak areas were determined and divided by the element-specific Scofield factor and the analyzer-depending transmission function.

2.3.7 X-ray absorption spectroscopy (XAS)

While in XPS monochromatic X-rays are used to create core holes by photo-ionization, X-ray absorption spectroscopy measures the absorption of photons as a function of the incident X-ray energy, near and at energies above the specific electron binding energy of a known core level of the considered atom. Therefore, these experiments are conducted at synchrotron facilities, which are able to generate a tunable high-energy (10^4 eV) X-ray excitation. When the X-ray energy equals the binding energy of a core shell, there is a abrupt increase in absorption, the so-called absorption edge. The edges are denoted according to the principle quantum number of the excited electron: K

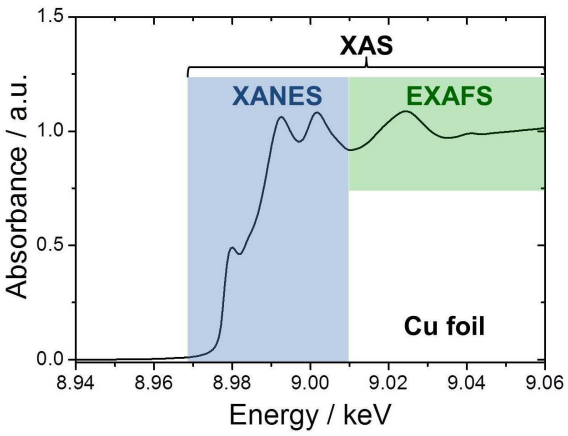

Figure 2.5: Exemplary XAS spectrum of Cu foil.

for $n = 1$, L for $n = 2$, M for $n = 3$ etc.

A typical X-ray absorption spectrum of Cu foil at the K edge is displayed in Figure 2.5. Basically, two regimes can be distinguished, XANES and EXAFS. The EXAFS region arises when the absorption of X-rays provokes an ejection of a core electron into the continuum with high kinetic energy (Figure 2.6, right). These high-energy electrons are weakly back-scattered by only a single atom in the surrounding. In contrast, XANES is the region within 50 eV of the absorption edge (Figure 2.6, left), which contains the absorption of photons that either excite the photoelectrons into the continuum with low kinetic energy or into unoccupied orbitals controlled by dipolar selection rules (Figure 2.6 middle, left). The appearance of a weak pre-edge peak in XANES measured at the K edge as typically found for transition metal ions such as Cu^{2+} is due to dipol-forbidden transitions of s electrons into empty valence d orbitals (quadrupole transitions). Analysis of the EXAFS region allows the determination of interatomic distances, coordination numbers and species of the neighbors, while XANES is strongly sensitive to oxidation states and the site symmetry.

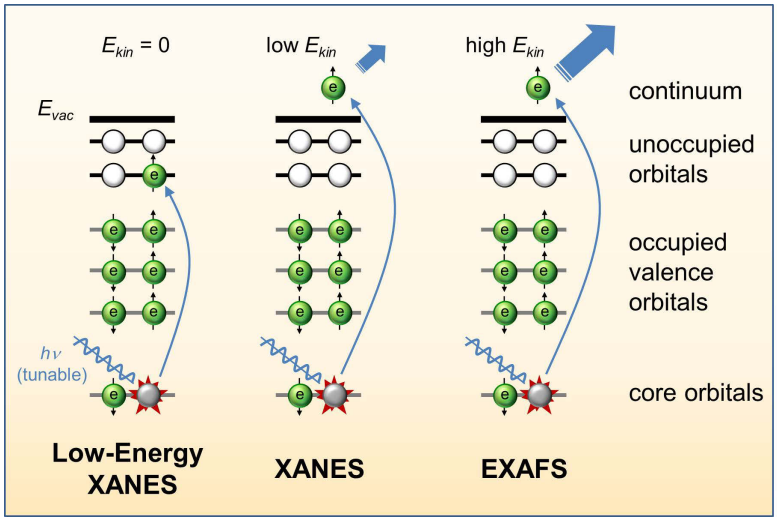

Figure 2.6: Electron transition processes contributing to the regimes of an XAS spectrum.[158]

Due to experimental reasons, it is often advantageous not to measure the attenuated X-ray intensity after transmitting the sample for recording the absorption spectrum. Instead, the processes that follow the excited state (decay happens within a few femtoseconds) can be counted as well. Two main mechanisms occur upon filling the empty core hole with an electron from a higher shell: i) the emission of a fluorescent photon of well-defined energy, and ii) an Auger process, in which the excess of energy is lost by ejecting a second electron into the continuum. Either of these processes can be used to measure the absorption. Although at low energies the Auger process is more likely than the fluorescence, the electron yield predominantly contains Auger electrons emitted by surface atoms. Since they quickly lose their kinetic energy in a solid (within 1 nm), bulk-produced Auger electrons are not

likely to emit the sample.

Experimental description The X-ray absorption experiments were carried out at the μ-spot beamline of the synchrotron storage ring BESSY II (Helmholtz Center for Materials and Energy) in Berlin, Germany, and at the European Synchrotron Radiation Facility (ESRF) in Grenoble, France. All samples were filled into quartz-glass capillaries with 1 mm diameter and a wall thickness of 0.01 mm. The fluorescence of the Au L_α or the Cu K_α was detected using a silicon drift detector.

2.3.8 Fourier transform infrared (FTIR) spectroscopy

As mentioned above, heterogeneous photocatalytic reactions are strongly affected by the surface properties of the catalytic material. A direct monitoring of the interaction between adsorbed molecules and the catalyst is enabled by suitable vibrational spectroscopic methods such as FTIR spectroscopy.[159] Moreover, *in situ* FTIR approaches provide information about the nature of adsorbed intermediates and reaction products, which contributes to an understanding of the catalytic reaction. Transitions between two vibrational states of a molecule are induced by the electric field component of light in the infrared region (mid IR: 4000–200 cm^{-1}). As the resonance frequency of a distinct vibration depends on the reduced mass of the atoms of the vibrating group, μ, and on the strength of the bonds (expressed by the force constant, f) according to Eq. 2.8, one observes IR bands at the highest frequencies for light atoms and for groups with high bond energies.

$$\nu_{vib} = \frac{1}{2\pi}\sqrt{\frac{f}{\mu}} \tag{2.8}$$

A non-linear molecule with N vibrating atoms gives rise to $3N - 6$ different fundamental vibrations, whereas $3N - 5$ vibrational modes are discernible for linear molecules such as CO_2 ($3 \cdot 3 - 5 = 4$ modes). The intensity of an IR band, however, is proportional to the change in the dipole moment during the vibration (selection rule). Thus, there are IR-active as well as IR-inactive vibrations (see Figure 2.7 for CO_2).

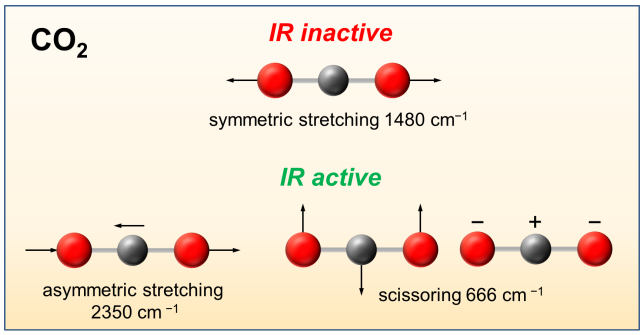

Figure 2.7: The four vibrational modes of a linear three-atomic molecule (CO_2).

For investigating the surface chemistry of a catalyst by IR spectroscopy, one can choose different sampling techniques depending on the properties of the sample or on the purpose of analysis. Transmission and attenuated total reflexion (ATR) IR are among the most frequently used methods. In transmission mode, the IR beam transmits a self-supported sample wafer (Figure 2.8a), which is formed by pressing the sample pure or diluted in KBr. This method can be applied for routine characterization of the catalyst surface. Moreover, it allows the determination of surface-acidic sites and of surface-metal oxidation and coordination states by using specific probe molecules such as pyridine or carbon monoxide, respectively. However, ATR sampling has proved valuable as *in situ* technique for analyzing the consumption of the sacrificial reactant methanol during photocatalytic H_2 generation. The thin-film solid catalyst is in strong contact to the ATR crystal (generally ZnSe allowing the detection of vibrations from 650 to 15000 cm^{-1}). Passing through the crystal, the incoming IR beam penetrates the catalyst on top of it, so that the attenuated radiation is finally reflected (Figure 2.8b). The intensity of an ATR-FTIR signal strongly depends on the number of reflections in the crystal as well as on the depth of penetration, which itself increases with higher wavelengths.

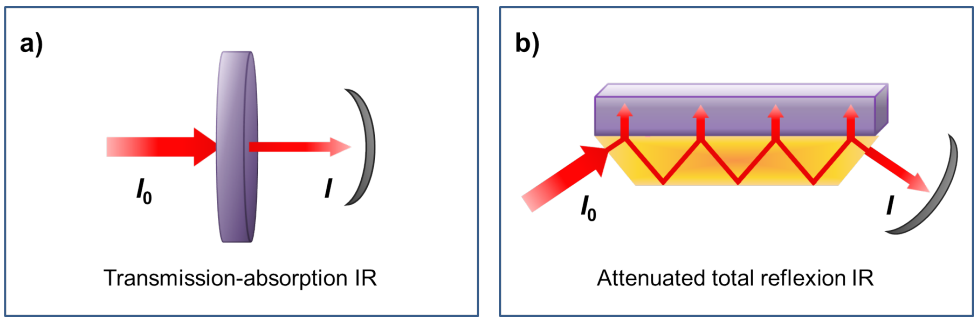

Figure 2.8: Principles of the IR sampling techniques a) transmission-absorption and b) attenuated total reflexion.

Experimental description The FTIR measurements and band assignments were carried out in the lab of Dr. U. Bentrup at LIKAT. Spectra in transmission mode were recorded on a Thermo Scientific Nicolet 6700 spectrometer equipped with a heatable and evacuable homemade reaction cell with CaF_2 windows connected to a gas-dosing system. The sample powders were pressed into self-supporting wafers with a diameter of 20 mm and a weight of 50 mg. All spectra were recorded at room temperature with a resolution of 4 cm^{-1} and 64 scans. Before measurement, the samples were pretreated by heating in He up to 100 řC for 30 min and then cooled to room temperature.

The scheme of the experimental set-up for *in situ* ATR-IR measurements is depicted in Figure 2.9. Spectra were recorded on a Nicolet Avatar 370 (Thermo Electron) FTIR spectrometer equipped with a MCT detector. A Specac Gateway multi reflection horizontal

accessory, coupled to a custom-made 2 mL flow-through cell with quartz window containing a ZnSe crystal on the bottom plate. The 45 ř internal reflection element of $72 \times 10 \times 6$ mm enables 6 infrared bounces. All spectra were recorded with 64 scans at $4\,cm^{-1}$ resolution. Before measurement, the ZnSe crystal was coated with the catalyst. The catalyst was suspended in distilled water ($c = 1.47\,g\,L^{-1}$) and the suspension was treated for 30 min in an ultrasonic bath. Then, 3 mL of this suspension was spread on the ZnSe crystal and dried in vacuum overnight. For the experiment, a He stream ($20\,mL\,min^{-1}$) saturated with a mixture of Methanol/H_2O (1:1) was flushed through the ATR-IR cell. After 10 min He flush ($20\,mL\,min^{-1}$), a spectrum was recorded, which was subtracted from the spectra measured under irradiation. Then, the ATR-IR cell was irradiated with a Xe lamp (300 W, LOT-Oriel GmbH & Co. KG) for 30 min without filter or for 120 min with a 420 nm cut-off filter.

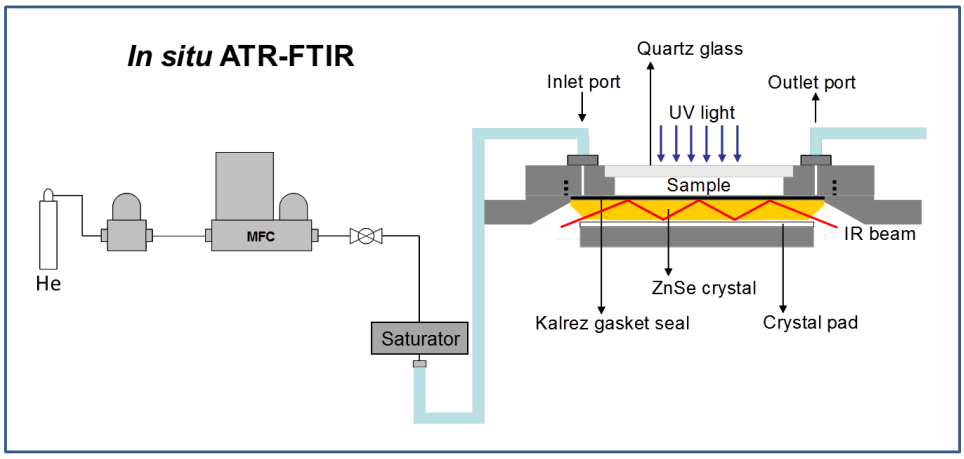

Figure 2.9: *In situ* ATR-IR set-up for investigations on photocatalytic H_2 generation from H_2O/MeOH.

2.3.9 Ultraviolet-visible (UV-vis) spectroscopy

Semiconductor photocatalysis is initiated by electronic transitions induced by absorption of light in the UV-vis range. Therefore, an electronic and optical characterization of photocatalysts by UV-vis spectroscopy opens up access for an understanding of the light-conversion properties of the investigated materials. The transition of an electron in the highest-energy state in the valence band, E_{vb}, to the lowest-energy state in the conduction band, E_{cb}, both characterized by a certain crystal momentum (k-vector), requires a minimum of energy: the band-gap energy, E_g. Band-gap transitions of electrons in a semiconductor can be either direct or indirect, depending on whether the momentum of electrons in the conduction band and that of holes in the valence band is the same or not, respectively.[160]

In contrast to direct transitions, the transition of the electron in indirect band-gap semiconductors occurs with assistance of a phonon providing the required momentum (Figure

2.10, gray arrow), while almost all of the energy stems from the photon (green arrow). Since indirect transitions always involve the absorption or emission of phonons (non-radiative processes), they occur much slower than the direct equivalents. Therefore, the efficiency of light harvesting and conversion is strongly affected by the type of the highest transition present in the semiconductor. E_g can be calculated from UV-vis absorption measurements. The strong increase in the absorbance at a certain wavelength, λ_g, in the UV-vis spectrum (absorption edge) gives evidence for the excitation of a valence-band electron into the conduction band. Hence, E_g (given in eV) can be easily calculated by using Planck's equation

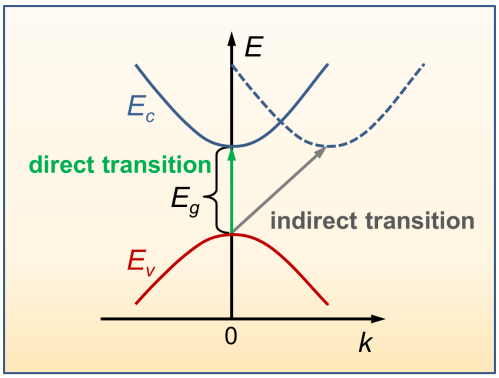

Figure 2.10: Direct and indirect band-gap transitions of electrons in a semiconductor.

$$E_g = h\frac{c}{\lambda_g} \tag{2.9}$$

where $h = 4.135 \cdot 10^{-15}$ eVs is the Planck constant and $c = 2.998 \cdot 10^{8}\,\mathrm{m\,s^{-1}}$ the speed of light in vacuum. However, in order to consider the different types of transitions (direct or indirect) other approaches such as the Schuster-Kubelka-Munk (SKM) method are more applicable. Since UV-vis spectra of powder catalysts are recorded in diffuse-reflexion (DR) mode, the diffuse reflectance, R, is directly obtained from the output of the spectrometer. Its relation to the absorption coefficient, K, and the scattering coefficient, S, is given by the SKM function:

$$F(R) = \frac{(1-R)^2}{2R_\infty} = \frac{K}{S} \tag{2.10}$$

Hence, if S remains constant and is thus not dependent on the wavelength, the SKM function represents the absorbance.

For calculations of E_g, the Tauc plot[161] can be applied which is expressed by

$$(h\nu K)^{\frac{1}{n}} \propto (h\nu F(R))^{\frac{1}{n}} = A\,(h\nu - E_g) \tag{2.11}$$

where A is a proportional constant. It is $n = 1/2$ for direct allowed transitions and $n = 2$ for indirect allowed transitions. Hence, for a direct band gap, plotting of $h\nu$ *vs.* $[F(R)h\nu]^2$ gives rise to a straight line, whereas the plot of $h\nu$ *vs.* $[F(R)h\nu]^{1/2}$ forms a straight line for an indirect band gap, the value of which can be measured by extrapolating the straight line to $F(R) = 0$.

Experimental description UV-vis diffuse reflectance spectra were recorded with an Avantes 45 ř optical probe connected to an Avantes AvaSpec-2048 UV-vis spectrometer using $BaSO_4$

as a standard. The catalyst was measured either pure or in a suspension containing 20 mg of the sample in 2 mL H_2O/MeOH under UV-vis irradiation *via* the optical probe.

2.3.10 Electron paramagnetic resonance (EPR) spectroscopy

As the nature and lifetime of a catalyst's photo-excited state strongly influence its photocatalytic performance, spectroscopic tools are required that are capable of monitoring light-induced electron-transfer pathways. Since *in situ* EPR spectroscopy allows a selective detection of paramagnetic centers formed and consumed during the reaction, it exhibits outstanding advantages in unraveling the mechanisms of photocatalytic processes. In the present thesis, this powerful technique was therefore primarily applied in order to visualize the efficiency of charge generation and transfer.

Free organic or inorganic radicals, triplet states of molecules, and transition metals with unpaired d or f electrons may be EPR-active as their total spin quantum number, S, is non-zero and a multiple of 1/2. This gives rise to a non-zero rotational angular momentum, $\vec{S}$, of the electron, the z-component of which can only assume two different values for a system with $S = 1/2$, expressed by the secondary spin quantum number, M_S, ranging from $-S$ to $+S$.[162]

$$S_z = \cos\left|\vec{S}\right| = \pm\frac{1}{2}\hbar = M_S\hbar \qquad (2.12)$$

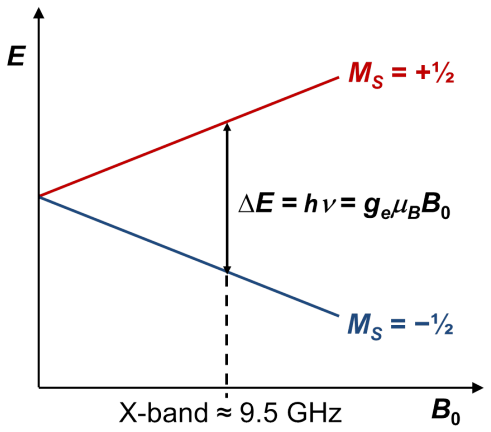

Figure 2.11: Electron Zeeman interaction of a free electron with $S = 1/2$.

The most important physical consequence of the electron spin is the associated magnetic moment, $\vec{\mu}_e$, which is proportional to $\vec{S}$ and interacts with an external magnetic field, $\vec{B}$ (electron Zeeman interaction, Figure 2.11). The energy of this interaction for a free electron with $M_S = \pm 1/2$ is given by

$$E = \vec{\mu}_e \bullet \vec{B} = -g_e\mu_B\vec{S} \bullet \vec{B} = \pm\frac{1}{2}g_e\mu_B B_0 \qquad (2.13)$$

where $\bullet$ describes a scalar product, $\mu_B = 9.274 \cdot 10^{-24}\,\mathrm{J\,T^{-1}}$ is the Bohr magneton, and $g_e = 2.0023$ is a constant of proportionality known as the *Landé factor*. Since there is an increasing energy difference between both spin states, transitions can be induced by electromagnetic radiation, the energy of which is equal to the energy difference, ΔE. Absorption

occurs when the selection rule $\Delta M_S = 1$ is fulfilled:

$$\Delta E = g_e \mu_B B_0 = h\nu \tag{2.14}$$

Typically, the resonance energy is in the range of microwaves, *e.g.* 9.5 GHz in the X-band working mode. Due to technical reasons, the frequency is held constant and the magnetic field is varied (*continuous wave* (cw) mode).

As the spin magnetic moment may be affected by the environment interacting with the spin, resonant absorption energies of bound electrons in atoms and molecules shift with respect to the free electron. These interactions are quantum mechanically characterized by the static spin Hamiltonian, $\mathcal{H}^S$, which acts on the orbital wavefunction.[163] The energies corresponding to each interaction are given by the eigenvalues of $\mathcal{H}^S$. The Hamiltonian, which describes the main interactions of the paramagnetic species in the investigated materials of the present study, can be reduced to

$$\mathcal{H}^S = \mathcal{H}^{eZ} + \mathcal{H}^{hf} + \mathcal{H}^{nZ} \tag{2.15}$$

where $\mathcal{H}^{eZ}$ is the electron Zeeman interaction, $\mathcal{H}^{hf}$ is the electron-nuclear hyperfine interaction, and $\mathcal{H}^{nZ}$ describes the nuclear Zeeman interaction. In general, due to the much larger mass of the nucleus than that of an electron, the energetic contribution of the latter is small compared to the former two interactions and will therefore not be considered here. $\mathcal{H}^{eZ}$ for an unpaired electron in a bound state, *e.g.* in a molecule, includes the interaction of the spin with its orbit expressed by $\mathcal{H}^{so}$.

$$\mathcal{H}^{so} = \lambda \vec{L} \bullet \vec{S} \tag{2.16}$$

where $\vec{L}$ is the angular momentum and λ is the spin-orbit coupling constant, which increases with the atomic number. The interaction according to Eq. 2.16 leads to characteristic deviations of the g-value from the Landé factor, so that the electron Zeeman term becomes

$$\mathcal{H}^{eZ} = \mu_B \vec{B} \bullet \tilde{\mathrm{g}} \bullet \vec{S} = \lambda \vec{L} \bullet \vec{S} + \mu_B \vec{B} \bullet (\vec{L} + g_e \bullet \vec{S}) \tag{2.17}$$

The electron Zeeman term depends on the symmetry of the corresponding orbitals or ligands. This means that the interaction with the magnetic field is anisotropic and varies along the x-, y and z-direction in the molecule. This anisotropy is expressed by the g-tensor, $\tilde{\mathrm{g}}$, which is given as

$$\tilde{\mathrm{g}} = \begin{pmatrix} g_x & 0 & 0 \\ 0 & g_y & 0 \\ 0 & 0 & g_z \end{pmatrix} \tag{2.18}$$

where g_x, g_y and g_z are the principle values of $\tilde{\mathrm{g}}$. For paramagnetic species in solution, the anisotropy represented by the three g-values is averaged to an isotropic value, g_{iso}, due to the fast rotation of the molecules.

$$g_{iso} = \frac{g_x + g_y + g_z}{3} \tag{2.19}$$

For solid samples such as powder catalysts, however, the resonance frequency depends on the orientation of the spins relative to the magnetic field, whereby the different absorption signals of all orientations overlap. The resulting shapes of the EPR signals for a spin system with rhombic, axial, and isotropic symmetry, respectively, are displayed in Figure 2.12.

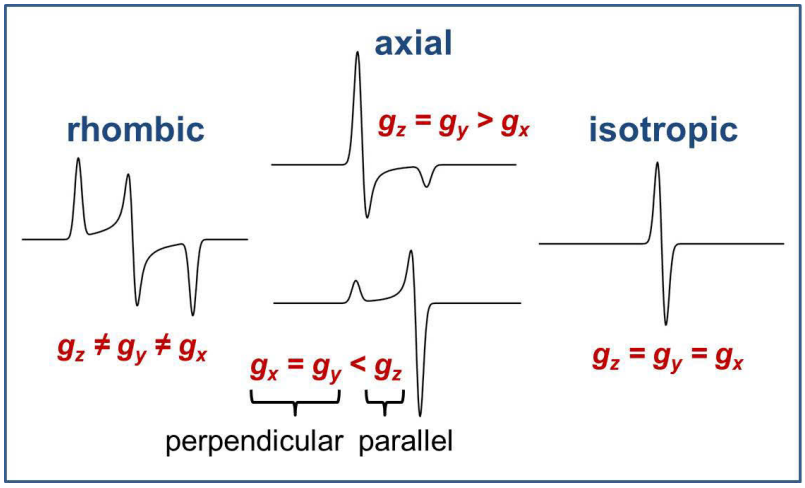

Figure 2.12: Exemplary simulated EPR signals of spin systems with rhombic, axial, and isotropic symmetry, respectively.

When n nuclei with a non-zero nuclear spin moment, $\vec{I}$, are present in the surrounding of the electron spin, additional terms contributing to the spin Hamiltonian (Eq. 2.15) have to be considered. The interaction between the magnetic moment of a nucleus with the magnetic moment of the electron is expressed by the electron-nuclear hyperfine interaction:

$$\mathcal{H}^{hf} = \sum_{i=1}^{n} \mathcal{H}_i^{hf,iso} + \sum_{i=1}^{n} \mathcal{H}_i^{hf,dip} = \vec{S} \bullet \tilde{\mathrm{A}}_i \bullet \vec{I}_i \tag{2.20}$$

where $\tilde{\mathrm{A}}_i$ is the hyperfine tensor, which consists of an isotropic contribution (Fermi-contact part) and an anisotropic (dipolar) part. The magnitude of the isotropic contribution is proportional to the spin density at the nucleus, $|\psi(0)|^2$, and is given by

$$\mathcal{H}_i^{hf,iso} = a_{iso}\vec{S} \bullet \vec{I} = \frac{8\pi}{3} g_e \mu_B g_N \mu_N |\psi(0)|^2 \vec{S} \bullet \vec{I} \tag{2.21}$$

where a_{iso} is the isotropic hyperfine coupling constant. Therefore, isotropic hyperfine interaction is only observed for spins located in s orbitals. However, for unpaired electrons

in transition metal complexes or in organic radicals, in which the spin density is usually located in d or p orbitals, respectively, isotropic hyperfine coupling can contribute as well due to spin polarization effects. For an electron with $S = 1/2$, the coupling to every nucleus i leads to a splitting of the spin levels into $2I_i + 1$ sublevels, with I_i being the respective nuclear spin quantum number. Due to the selection rules $\Delta M_S = \pm 1$ and $\Delta M_I = 0$ the number of spin transitions and, thus, hfs coupling lines in an EPR spectrum is given by

$$N_e = \prod_i (2I_i + 1) \tag{2.22}$$

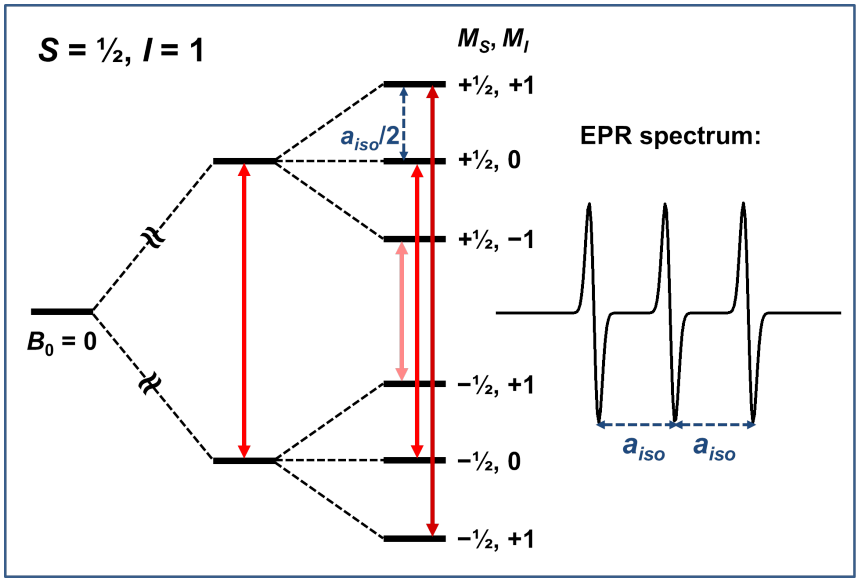

Figure 2.13: Energy-level diagram and simulated EPR spectrum for an electron with $S = 1/2$ coupling to a nucleus with $I = 1$. Displayed are the main energetic contributions, *i.e.* electron Zeeman and isotropic hyperfine interaction. Red arrows visualize the allowed transitions, which lead to the characteristic line pattern of the EPR spectrum.

The intensity of an EPR spectrum is directly dependent on the population difference between the two spin states, energetically separated by ΔE, prior to microwave absorption, which is given by the Boltzmann distribution:

$$\frac{N_+}{N_-} = \exp\left(-\frac{\Delta E}{kT}\right) \tag{2.23}$$

where N_+ and N_- are the populations of electrons with $M_S = +1/2$ and $M_S = -1/2$, respectively, $k = 1.381 \cdot 10^{-23}\,\mathrm{J\,K^{-1}}$ is the Boltzmann constant, and T is the absolute temperature. For an EPR experiment at X-band (9.5 GHz), the population ratio is about 0.999. Cooling with liquid nitrogen can thus increase the population difference and accordingly the EPR signal intensity. In order to enhance the signal-to-noise ratio, cw-EPR spectra are

usually recorded with phase-sensitive detection by an lock-in amplifier. Therefore, EPR signals appear as the first derivative of the corresponding absorption signal. Whether or not one can observe an EPR signal of a paramagnetic species at a certain temperature also depends on the line width (lw), ΔB, which is crucially influenced by the relaxation times according to the Heisenberg uncertainty principle. In general, two relaxation processes take place in order to return to the thermodynamic equilibrium, the spin-lattice relaxation (characterized by T_1) and the spin-spin relaxation (characterized by T_2). The enthalpic process (T_1) refers to the restoration of the Boltzmann distribution (Eq. 2.23) by dissipating the energy (heat) into the surrounding structure, which leads to an exponential decay of the energy. The equilibrium is also rebuilt by an entropic relaxation process (T_2), when the spins gradually lose their phase alignment upon direct spin-spin interaction (without energy transfer to the lattice). Both relaxation processes may contribute to the EPR lw by

$$\Delta B \propto \left(\frac{1}{T_1} + \frac{1}{T_2}\right) \tag{2.24}$$

In case of organic radicals in solutions, where $T_1 > T_2$, the EPR lw is mainly affected by T_2. In contrast, for metal centers in solid samples, where $T_1 \ll T_2$, the spin-lattice relaxation dominates. If the relaxation is too fast, the signal may be broadened beyond detection due to the shorter lifetime of the excited state. On the other hand, very slow relaxation times can lead to saturation phenomena. If the microwave power is too high, a return of the spin to the ground state is hindered. This causes a fast decrease in the population difference, so that no more absorption processes and, thus, EPR signals are observed.

The EPR signal intensity is also dependent on the magnetic susceptibility, which is itself inverse proportional to the temperature according to the Curie-Weiss law:

$$\chi_m = \frac{C}{T - T_c} \tag{2.25}$$

where C is a material-specific Curie constant, T is the absolute temperature and T_c is the Curie temperature, which can be determined experimentally by plotting the inverse signal intensity against the temperature. Then the x-axis intercept represents T_c, the value of which increases with stronger dipolar interaction between the spins.

Experimental description X-band EPR spectra were recorded by a Bruker EMX CW-microspectrometer with an ER 4119HS-WI high-sensitivity optical resonator. A grid on the front side of the resonator enabled irradiation with a 300 W Xe-arc lamp (LOT Oriel) equipped with different optical filters (LOT Oriel 282/532HT10 band-pass and GG420/515 cut-off filters). For low-temperature (T = 90 K) experiments, the samples (15 mg) were filled into commercial X-band EPR tubes (Wilmad, 4 mm outer diameter) and measured

under liquid nitrogen stream.

In situ EPR spectra at room temperature ($T = 290\,\mathrm{K}$) were carried out with special "home-made" flow cells allowing water and methanol saturated carrier gas (He 30 mL min^{-1}, 5 % H_2O/ MeOH = 1:1) to pass through the catalyst during spectra recording (Figure 2.14). Experimental g-values were determined by calibration with a 2,2-diphenyl-1-picrylhydrazyl (DPPH) standard ($g = 2.0036 \pm 0.00004$) according to

$$g = 2.0036 \frac{B_{0,\mathrm{DPPH}}}{B_{0,\mathrm{sample}}} \tag{2.26}$$

The EPR spectra were simulated using the SIM32 software elaborated by Prof. Z. Sojka (Jagellonian University, Cracow, Poland).[164, 165]

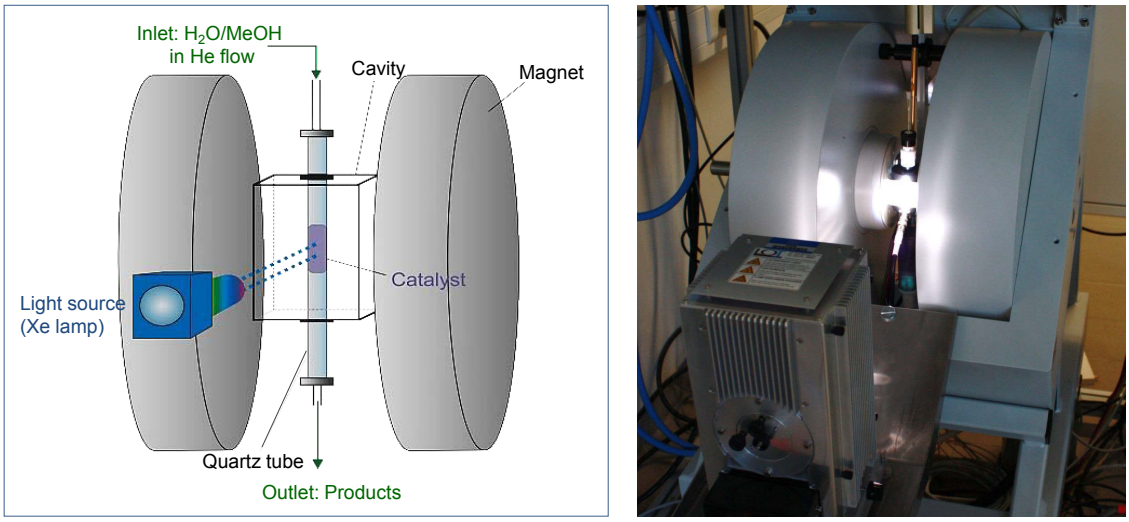

Figure 2.14: Set-up of *in situ* EPR experiments during photocatalytic H_2 production from H_2O/MeOH mixtures.

3 $NaTaO_3$ photocatalysts for hydrogen generation

$NaTaO_3$ is a prominent example for a pristine H_2-evolution catalyst, since it exhibits a strong cathodic conduction-band potential (1.1 eV above the H^+/H_2 redox level).[146] As mentioned in Section 1.2, the photoactivity of a pristine semiconductor such as $NaTaO_3$ is highly affected by its specific structural and electronic properties, which can be tuned by the synthesis conditions. However, comparative studies on the photoactivities of differently prepared semiconductors alone often do not directly allow to explore what factor(s) dominates the activity, since heterogeneous photocatalytic reactions occur through a sequence of multistep processes.[11] Therefore, dedicated mechanistic studies on the impact of the semiconductor-preparation method by suitable in situ spectroscopic approaches may shine light on the relevant rate-determining properties. For example, the activity of $NaTaO_3$ photocatalysts has been shown to be highly sensitive against the preparation method, but only few mechanistic explanations have been provided for this well-established photocatalytic material. Hu et al. showed that sol-gel method led to $NaTaO_3$ showing higher H_2 evolutions than that prepared by solid-state reaction,[166] which could be either explained by the differences in particle size or crystal structure (monoclinic vs. orthorhombic phase). Unambiguous conclusions drawn from in situ spectroscopic analysis that visualize the capability of charge-carrier formation and their reaction, however, have been neglected so far. This chapter presents in Section 3.1 a comparative study on $NaTaO_3$ prepared by a standard solid-state reaction and an advanced exotemplate method for application in photocatalytic H_2 generation. For the first time, in situ EPR spectroscopy has been successfully applied on $NaTaO_3$ catalysts to follow the light-induced formation of paramagnetic species and their consumption by water and methanol. In Section 3.2, the impact of additives such as Au and/or multilayer reduced graphene oxide on the nature of charge carriers and their mechanistic origin are discussed.

3.1 Solid-state reaction *vs.* exotemplate method

To explore the impact of the synthesis protocol on the catalyst structure, charge-carrier formation and photocatalytic properties of $NaTaO_3$, an advanced exotemplate method (EM) has been applied in comparison to a conventionally used solid-state reaction (SSR).[a] Both preparation methods led to crystalline phases of orthorhombic structure as seen from the XRD patterns in comparison to ICDD PDF 73-878 (Figure A.1). The mean crystallite size was determined by 25 nm for sample $NaTaO_3$(EM) using the Scherrer equation, whereas the reflections in the XRD pattern of $NaTaO_3$(SSR) were too sharp for line-broadening analysis. Scanning electron microscopy (SEM) revealed particle sizes >1 µm of roundish shape for $NaTaO_3$(SSR), whereas $NaTaO_3$(EM) consists of differently shaped aggregates in the nanometer range (Figure A.1). This trend is consistent with BET surface area measurements, which revealed 1.4 $m^2\ g^{-1}$ and 22.4 $m^2\ g^{-1}$ for $NaTaO_3$(SSR) and $NaTaO_3$(EM), respectively.

Figure 3.1a depicts the optical absorption spectra of $NaTaO_3$ prepared by EM (blue) and SSR (red), exhibiting both an absorption edge around 320 nm. As orthorhombic $NaTaO_3$ was shown to possess a direct band gap,[168] the values of E_g were determined by Tauc-plot analysis with $n = 1/2$ (Figure 3.1b). For catalyst $NaTaO_3$(SSR), a slightly lower band gap (E_g = 4.06 eV) was determined compared to $NaTaO_3$(EM) (E_g = 4.10 eV). This may be related to the smaller particle size of the latter catalyst as previously demonstrated *e.g.* for TiO_2 photocatalysts.[169] In both catalysts, valence-band electrons can thus only be excited into the conduction band upon UV-light irradiation. These excited electrons are

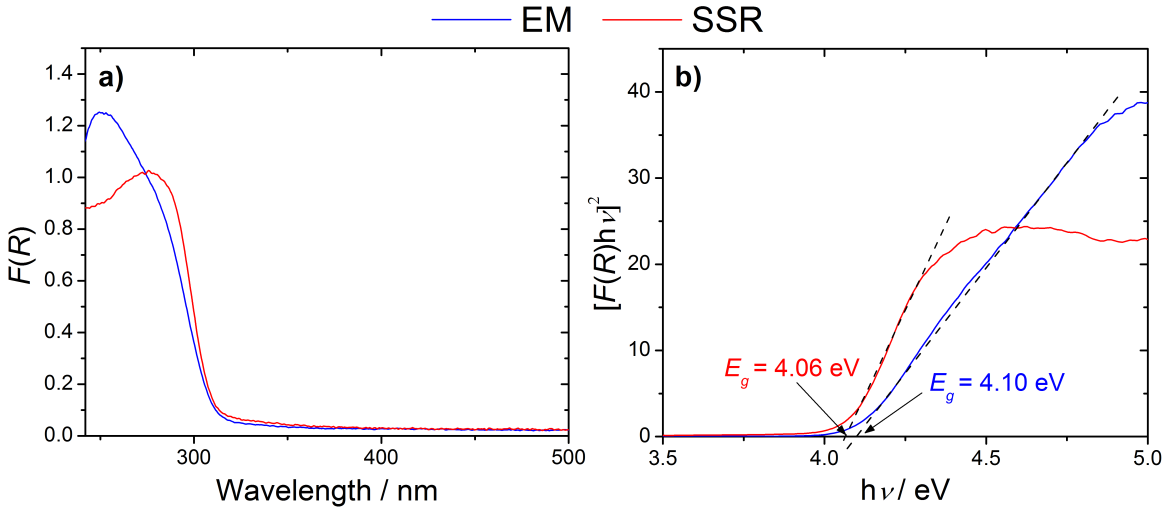

Figure 3.1: a) Diffuse reflectance spectra and b) Tauc plots according to Eq. 2.11 with $n = 1/2$ for a direct band gap of $NaTaO_3$ catalysts prepared by EM (blue) and SSR (red).

[a]The syntheses of $NaTaO_3$ catalysts and their structural characterizations (SEM, TEM, XRD and BET analyses) were carried out by the group of Dr. S. Wohlrab, LIKAT. The data have been published in [167].

able to reduce adsorbed species, such as protons to hydrogen. Figure 3.2 displays the photocatalytic H_2-evolution rates for pristine and additive-loaded $NaTaO_3$ prepared by SSR and EM obtained from H_2O/MeOH mixtures under UV-light-irradiation, measured in the group of Dr. S. Wohlrab, LIKAT. It is clearly seen that all $NaTaO_3$(EM)-based catalysts show superior photoactivity compared to the samples based on the SSR-synthesized support. $NaTaO_3$ is known to evolve H_2 without any co-catalyst,[146] which is confirmed here as well. However, the amount of H_2 produced over catalyst $NaTaO_3$(EM) was 17.5 times higher than that measured for $NaTaO_3$(SSR), which must be related to the structural and electronic properties of both photocatalysts. Indeed, the BET surface area also differs by a factor of 16, thus correlating with the detected activities. In general, a larger BET surface area increases the probability of surface reactions of photo-generated electrons and holes with water molecules compared to that of charge-carrier recombination in the bulk. However, spectroscopic evidence for the increased charge-carrier formation and stability has not yet been provided for this specific photocatalytic system. Therefore, *in situ* EPR spectroscopic investigations have been conducted on these materials in order to provide insights into the nature of trapped charges, which might be affected by the semiconductor preparation protocol.

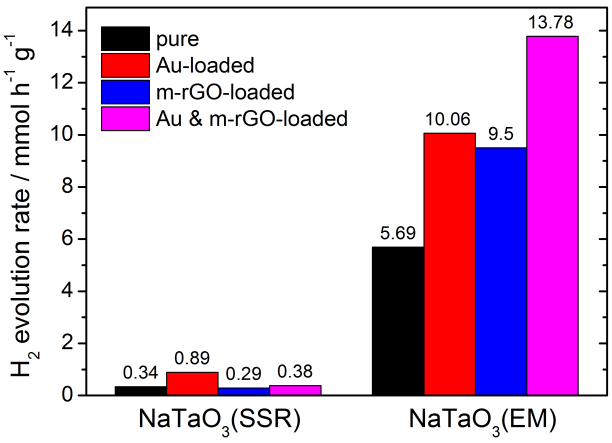

Figure 3.2: Photocatalytic H_2 production of the differently prepared $NaTaO_3$ photocatalysts. Conditions: 0.2 g catalyst in 100 mL H_2O/MeOH = 1:1, 150 W medium pressure mercury lamp (TQ 150, UV-Consulting Peschl). Data taken from [167].

3.1.1 Charge-carrier formation in $NaTaO_3$ visualized by EPR

Figure 3.3a displays the *in situ* EPR spectra of $NaTaO_3$ prepared by EM (blue) and SSR (red). The dark spectra show rarely any EPR-active species, except of a weak isotropic feature C1 at $g = 2.003$ for $NaTaO_3$(EM), which may be assigned to electrons trapped at oxygen vacancies known as F^+ centers (Table 3.1) as also observed in other metal oxides.[170] Signal C1 did not markedly increase upon UV-vis-light irradiation in air, but a second EPR signal C2 appeared under these conditions for the catalyst prepared by EM. In the presence of ambient air, containing paramagnetic dioxygen, surface-bound paramagnetic species can be broadened beyond detection due to their dipolar interaction with gas-phase oxygen. Therefore, signal C2 is most likely arising from a paramagnetic species in the subsurface region. As pointed out above, the UV-light-excited conduction

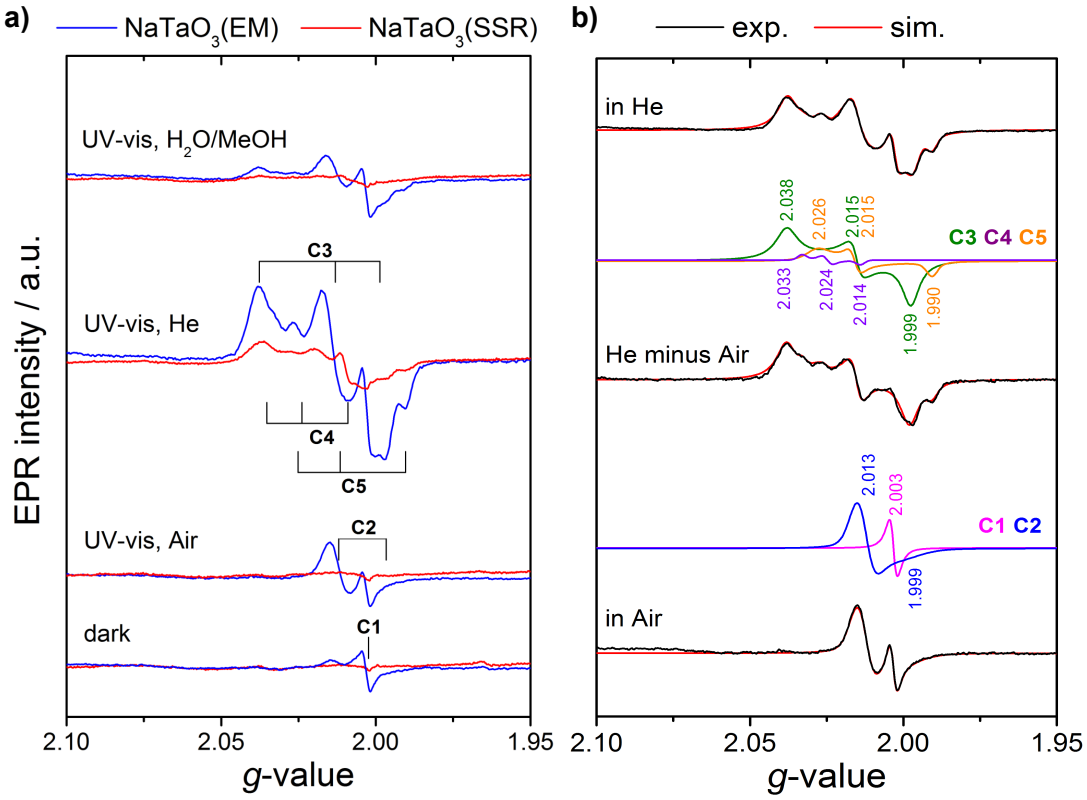

Figure 3.3: a) Comparison of the *in situ* EPR spectra of $NaTaO_3$ prepared by EM (blue) and SSR (red). Measurements started in air without irradiation, followed by 10 min UV-vis-light irradiation (Xe lamp, no filter) and subsequent introduction of helium under continuous illumination. Finally, the reactants H_2O/MeOH were introduced in helium under UV-vis light. b) Deconvolution of the experimental EPR spectra (black) for $NaTaO_3$(EM) by simulation (red and colored lines). C1 and C2 were obtained from the spectrum of irradiated $NaTaO_3$(EM) in air, whereas C3, C4 and C5 were simulated by subtracting the spectrum in air from that in He under UV-vis light. The sum of all simulated species C1–C5 produced the simulated spectrum of $NaTaO_3$(EM) irradiated in He.

electrons in $NaTaO_3$ can be trapped at metal centers such as Ta^{5+} according to:

$$Ta^{5+} + e^-_{cb} \rightarrow Ta^{4+} \tag{3.1}$$

At the same time, the remaining positive holes may be trapped at lattice oxide species leading to oxide radicals, which can be located in the surface and subsurface region.

$$O^{2-} + h^+_{vb} \rightarrow O^{\bullet -} \tag{3.2}$$

As demonstrated earlier, Ta^{4+} is not detectable at room temperature.[171,172] Hence, most likely signal C2 can be assigned to trapped holes ($O^{\bullet -}$ species) located in subsurface layers of $NaTaO_3$.

The concentration of paramagnetic species in the catalyst prepared by SSR, however, was much lower under irradiation in air compared to $NaTaO_3$(EM). This may be due to

Table 3.1: Simulation-derived EPR parameters of signals observed in $NaTaO_3$ catalysts prepared by EM and SSR and their species assignment. Table corresponds to Figures 3.3 and 3.4.

EPR signal	g_z	g_y	g_x	Signal assignment	Reference
C1	2.003	2.003	2.003	F^+ centers	a, [170]
C2	2.013	2.013	1.999	subsurface oxide radical $O^{\bullet-}$ in $NaTaO_3$	a
C3	2.038	2.015	1.999	surface superoxide radical $O_2^{\bullet-}$ on $NaTaO_3$	a
C4	2.033	2.024	2.014	surface oxygen species[b]	a
C5	2.026	2.015	1.990	surface oxygen species[b]	a
C6	2.003	2.003	2.003	conduction electrons in m-rGO	a, [173]

[a]This work. [b]Not specified.

the higher BET surface area of the latter catalyst, which leads to a larger surface exposition to the incident light. Furthermore, the larger particles in $NaTaO_3$(SSR) might favor bulk recombination of charge carriers rather than trapping at lattice atoms. The inability to stabilize charges in $NaTaO_3$(SSR) could also explain its lower activity in H_2 evolution. This is also demonstrated by the EPR spectra under irradiation in helium flow. Then, no more dipolar interaction with gas-phase oxygen occurs, which uncovers the adsorbed paramagnetic surface species. Both catalysts exhibit similar signals, but of very different intensity. Again, the EPR signals $NaTaO_3$(SSR) are much weaker, probably resulting from the faster recombination in that catalyst.

In order to extract the different EPR species from the complex spectrum of $NaTaO_3$, the EPR signals obtained in air were subtracted from the spectrum in helium prior to spectrum simulation (Figure 3.3b). Three additional species C3–C5 were obtained, which must be located at the outermost $NaTaO_3$ surface. To further explore their specific nature, 50 µL H_2O_2 were added to the EPR tube containing the pure $NaTaO_3$(EM) catalyst. This would produce superoxide species, $O_2^{\bullet-}$, under illumination upon the reaction sequence 3.3–3.5.[174]

$$H_2O_2 \xrightarrow{h\nu,\,\mathrm{cat.}} 2\,HO^{\bullet} \tag{3.3}$$

$$HO^{\bullet} + H_2O_2 \rightarrow HO_2^{\bullet} + H_2O \tag{3.4}$$

$$NaTaO_3\text{–}HO_2^{\bullet} \rightarrow NaTaO_3\text{–}O_2^{\bullet-} + H^+ \tag{3.5}$$

The corresponding EPR spectrum recorded at 220 K exhibits a signal with parameters similar to those of signal C3, apart from slight differences in line width and g_z (Figure A.2a). This is a clear indication that signal C3 is attributed to surface-bound $O_2^{\bullet-}$ species, since its line shape and g-values are also characteristic for such species bound at other metal oxides.[175] In the present case, the $O_2^{\bullet-}$ signal is most likely created upon trapping

of photo-excited electrons at surface-bound oxygen molecules acting as efficient electron traps:[176, 177]

$$O_2(ad) \quad + \quad e^-_{cb} \quad \rightarrow \quad O_2^{\bullet -}(ad) \tag{3.6}$$

For proper match of the simulated spectrum with the one obtained from the experiment, it was necessary to include two more rhombic EPR signals, C4 and C5. The nature of these species was not identified throughout the experiments. They are most probably related to surface-bound oxygen species, though bound at different sites.

Under H_2O/MeOH-saturated helium flow, the signals C3–C5 attributed to surface-bound oxygen species and even the subsurface $O^{\bullet -}$ species, C2, strongly lost intensity (Figure 3.3). Interestingly, signal C2 only slightly weakened upon adding the hole scavenger MeOH (Figure A.2b), which supports the assignment of the latter species to trapped holes. In contrast, C3–C5 already decreased upon addition of water alone. Thus, the photo-excited trapped electrons are either consumed by water molecules or the specific trapping sites are blocked by them, preventing the EPR-signal formation.

3.2 Impact of promoting additives on the EPR spectra

As shown in Figure 3.2, the photocatalytic activity of $NaTaO_3$(EM) was markedly improved upon loading with co-catalysts, such as 0.2 wt.-% Au and/or 10 wt.-% m-rGO. The co-loaded sample reached the highest activity of 17.78 mmol h^{-1} g^{-1}. While Au tends to act as primary H_2 evolution site, the conductive graphene sheets support electron-withdrawing from the $NaTaO_3$-CB. Therefore, synergistic effects can lead to enhanced photoactivity on such a co-loaded semiconductor. However, the effect for $NaTaO_3$(SSR) was only significant in case of Au loading, which doubled the evolved H_2. An additional loading with m-rGO decreased the photoactivity of Au-deposited $NaTaO_3$(SSR). As the Au particles were determined to be of similar size in the catalysts prepared by EM and SSR (Figure A.3), the latter effect may be again explained by the lower surface area of $NaTaO_3$(SSR). It is possible that a similar weight loading of m-rGO onto $NaTaO_3$(SSR) therefore results in a less effective transfer to the surface and/or to the co-catalytic Au particles compared to a material with large surface/bulk ratio, due to differences in layer thickness and surface coverage.

Since for $NaTaO_3$(EM), additive loading enhanced the H_2 generation, *in situ* EPR spectra were recorded for these samples, which are depicted in Figure 3.4a. Interestingly, none of the signals C2–C5 appeared in the spectra of the catalysts loaded with Au and/or m-rGO upon irradiation with UV-vis light in helium. A probable reason might be that the photo-excited electrons in $NaTaO_3$ are rather transferred to the Au particles possessing a lower Fermi level or respectively to the conducting m-rGO layers than being trapped at surface-bound

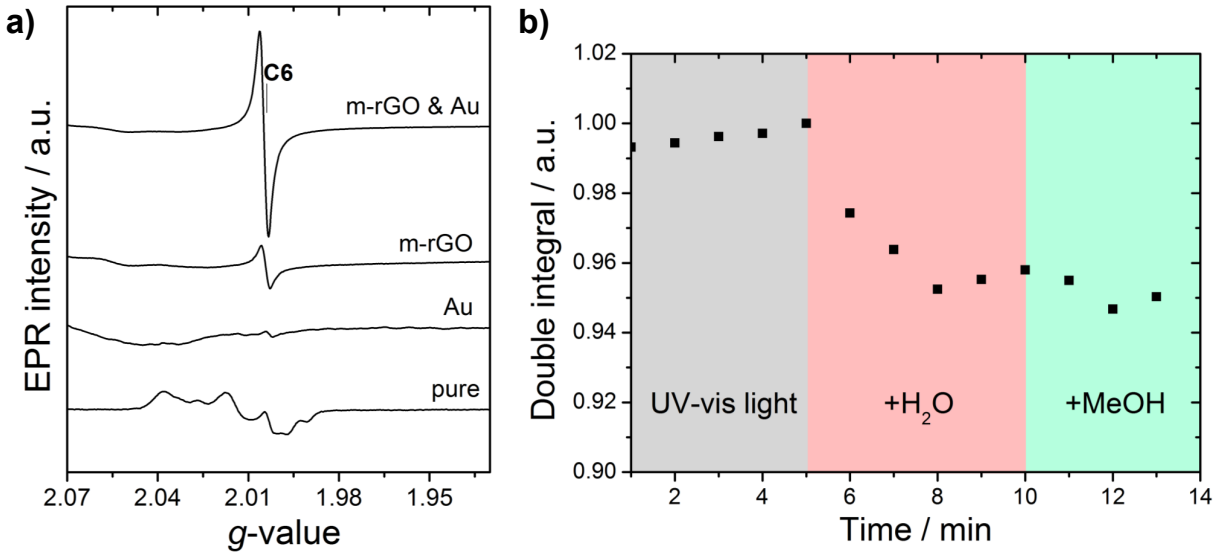

Figure 3.4: a) *In situ* EPR spectra in flowing He under irradiation with UV-vis light of $NaTaO_3$(EM) pure, loaded with 0.2 wt.-% Au, loaded with 10 wt.-% m-rGO and loaded with 0.2 wt.-% Au as well as 10 wt.-% m-rGO. b) Development of the normalized double integral of signal C6 observed in Au- and m-rGO-loaded $NaTaO_3$(EM) upon UV-vis-light irradiation and subsequent addition of H_2O and MeOH.

oxygen to form *e.g.* $O_2^{\bullet-}$ (C3). This is confirmed by the EPR spectrum of the Au-loaded sample, containing only a weak isotropic defect-related signal C1 (g = 2.003), which did not change upon irradiation or addition of the reactants. When photo-excited electrons are quickly transferred into the Au particle, they cannot be detected by EPR at ambient temperature.[178] In contrast, m-rGO-containing samples show a stronger isotropic signal C6 (Figure 3.4a, Table 3.1). This signal C6 can be assigned to carbon-based localized conduction electrons in m-rGO,[173] the number of which slightly increases upon UV-vis-light irradiation of the photocatalytic material as seen from the development of the corresponding double integral (Figure 3.4b, blue). This suggests a light-induced electron transfer similar to that proposed for the Au-loaded sample. The transferred electrons have then enough reductive potential to reduce the protons to form H_2, confirmed by the decrease of signal C6 upon addition of H_2O and MeOH (Figure 3.4b, red & green). The fact that for $NaTaO_3$(EM) co-loaded with Au and m-rGO, a much higher intensity of signal C6 was observed than for the catalyst loaded only with m-rGO indicates that Au might support the formation of carboneous conduction electrons. Thus, a synergistic effect of simultaneous Au and m-rGO-loading might further improve the photocatalytic performance. However, while the H_2 rate of Au/m-rGO-loaded $NaTaO_3$(EM) was shown to be indeed higher than by mono-loading with Au or m-rGO, they were still less than the sum of both mono-loaded catalyst.

3.3 Conclusion

This chapter on the one hand pointed out the importance of improved synthesis strategies for the semiconducting support material in order to obtain highly photoactive materials with enhanced charge utilization. As a chosen example, an advanced preparation of $NaTaO_3$ by EM revealed catalysts of much higher surface area than through the standard SSR protocol, despite the fact that both materials exhibit similar structures and electronic properties. The smaller particle size obtained by EM, however, cannot be taken as direct evidence for the better photocatalytic performance (factor 17), as it does not provide insights into the amount, nature, and reactivity of photo-excited species in both materials during the reaction. Therefore, *in situ* EPR spectroscopy was applied and proven to be a unique tool for monitoring bulk- and surface-located charge carriers under irradiation that react with water and methanol. It was thereby shown that $NaTaO_3$(EM) produced a much higher concentration of trapped charge carriers than $NaTaO_3$(SSR), not only at the surface, but also in the sub-surface region. Thus, the ability to generate stabilized charges in $NaTaO_3$ is enhanced by using the EM method. Hence, recombination of charge carriers dominates for SSR-prepared $NaTaO_3$ leading to much lower photocatalytic H_2 evolutions under UV light.

Moreover, the *in situ* EPR spectra of $NaTaO_3$(EM) mono- and co-loaded with additives such as Au and m-rGO strongly suggest that the improved activity of these samples compared to the pure catalyst are be most likely related to a UV-light-induced electron transfer from $NaTaO_3$ to Au and/or m-rGO. Synergistic effects due to simultaneous loading of Au and m-rGO are apparently reflected by the EPR data, but not clearly seen from the photocatalytic performance of the co-loaded materials. Variations of the additive contents should be explored in more detail in order to investigate a potential synergy-related improved photoactivity. This could also reveal positive effects of loading $NaTaO_3$(SSR) with m-rGO, which was shown to be detrimental in the present study for 10 wt.-% m-rGO.

4 Impact of Au-deposition method on structure and performance of Au-TiO_2

The previous chapter showed that Au deposited on semiconductors acts as efficient promoter in photocatalytic H_2 evolution, based on enhanced charge-carrier separation as introduced in Section 1.2. In this regard, Au-TiO_2 is one of the most investigated systems so far. It has been demonstrated earlier that the Au content as well as its particle size distribution are crucial parameters for high photocatalytic H_2-evolution rates over Au-TiO_2.[113] These factors are generally tunable through the chosen Au-TiO_2 synthesis conditions, such as calcination temperature[179] or the pH value during deposition.[180] It was further reported that the photocatalytic H_2 generation from water/ethanol mixtures is strongly dependent on the type of Au-deposition method itself at the same Au content.[181] Impregnation, photo-deposition, sol-immobilization, and deposition-precipitation are the most common techniques to deposit Au onto TiO_2.[182] However, in most of the studies concerning the dependence of photocatalytic H_2 production on the Au-deposition method, structural and electronic reasons are either neglected or inferred from ex situ analyses of the as-prepared catalyst. Therefore, this chapter addresses a detailed investigation on structure-reactivity relationships of differently prepared Au-TiO_2 catalysts for proton reduction from H_2O/MeOH mixtures. By using a combination of in situ spectroscopic techniques (UV-vis, XANES, EPR), the light-induced formation of active species and their reactivity upon addition of the reactants is studied. The results are interpreted with respect to the photocatalytic performance of the catalysts. As mentioned in Section 1.2, Au also exhibits unique optical properties (SPR effect) causing visible-light response of the materials. Therefore, wavelength-dependent catalytic and spectroscopic measurements are analyzed in this chapter in order to shine light on the mechanistic background of the SPR-induced H_2 evolution. Such information about the structural prerequisites allowing visible-light activity is essential for a future catalyst improvement.

4.1 Catalyst characterization and performance

A multiphase composite of TiO_2 (P25, 85 % anatase and 15 % rutile) was used as support material for investigations on how the chosen Au-deposition procedure affects the structure and photocatalytic performance of the resulting Au-TiO_2 catalysts. Impregnation is known to favor low Au-loading yields and pronounced agglomerations of Au particles on TiO_2.[182] Therefore, three other established procedures, sol-immobilization (SIM), photo-deposition (PD), and deposition-precipitation (DP), were applied for depositing a nominal amount of 1 wt.-% Au onto P25 (see Section 2.1.2). The main steps of these protocols are depicted in Figure 4.1. For SIM, an Au sol is formed by reducing Au^{3+} ions in an organic medium (PVA), which is subsequently immobilized onto the TiO_2 support. In the PD procedure, TiO_2 is pre-reduced by UV-light irradiation in MeOH (acting as hole scavenger), whereby afterward adsorbed Au^{3+} ions become reduced to Au^0 at these Ti^{3+} sites. For the DP method, gold hydroxide is initially deposited onto TiO_2, which finally leads to a precipitation of Au^0 particles upon subsequent dehydration and O_2 elimination processes.[183]

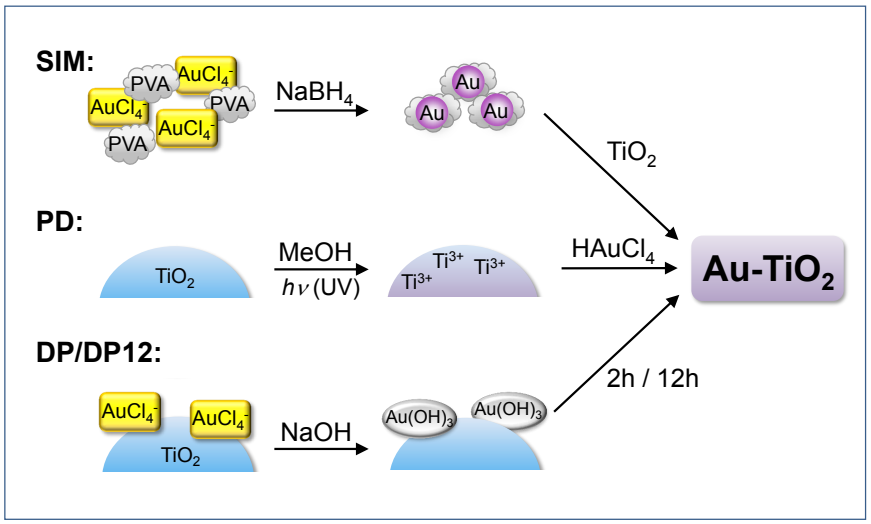

Figure 4.1: Schematic illustration of the elemental steps passed during Au deposition *via* sol-immobilization (SIM), photo-deposition (PD) as well as normal and prolonged deposition-precipitation (DP and DP12, respectively).

Table 4.1 summarizes the photocatalytic H_2 evolutions from H_2O/MeOH under UV (320–500 nm) and visible-light (400–700 nm) conditions, the mean Au diameter, d_m(Au), derived from TEM analysis, the overall Au content determined by ICP-OES, the surface-Au content obtained by XPS, and the binding energies of Au and Ti. Among the catalysts prepared by the three different methods (SIM, PD and DP), the lowest Au-loading yield was observed for AuP25-PD (0.46 wt.-% Au), which also led to the worst photoactivity under UV-vis- and visible-light conditions. In contrast, for catalysts AuP25-SIM and AuP25-DP the final

Table 4.1: Photocatalytic activities, mean Au-particle diameters, Au loadings and XPS parameters for Au and Ti of AuP25 catalysts prepared by different Au-deposition methods.

Catalyst	r_{H_2} / mmol g^{-1} h^{-1} UV-vis	vis	d_m(Au) / nm (TEM)	Au-wt.% (ICP-OES)	Au-at.-% (XPS)	E_b Au 4f / eV	E_b Ti 2p / eV
SIM	24	1.2	8.7	0.94	0.25	83.2 (Au^0-V_O) 83.7 (Au^0)	458.7 (Ti^{4+})
PD	5.1	0.42	41	0.46	0.08	84.0 (Au^0) 85.5 (Au^{3+})	457.3 (Ti^{3+}) 458.9 (Ti^{4+})
DP	33	2.4	1.1	0.93	0.57	84.3 ($Au^{\delta+}$)	459.4 (Ti^{4+})
DP12	3.4	0.25	–	0.35	0.11	83.7 (Au^0)	457.1 (Ti^{3+}) 458.8 (Ti^{4+})

Au loading was almost the anticipated amount of 1 wt.-%. The latter catalyst showed the highest H_2 production rates (followed by AuP25-SIM), but the DP method is apparently strongly sensitive towards preparation conditions. This is clearly demonstrated by comparison of catalysts AuP25-DP and AuP25-DP12, the latter of which was stirred for 12 h at 25 řC instead of 1 h. The prolongation of the deposition time led to only 0.35 % Au on P25 and the photocatalytic activity decreased by a factor of 10 to only 3.4 mmol g^{-1} h^{-1} under UV-vis light and 0.25 mmol g^{-1} h^{-1} with the visible-light filter (Table 4.1, Figure A.4). It must be emphasized that the visible-light filter (400–700 nm) contains small amounts of UV light (Figure 2.1), which might contribute to the "vis"-H_2 rates as well. However, UV-light radiation also accounts for a few percent in atmospheric sunlight and the overall goal should be to find catalysts working best under solar excitation.

As illustrated in Section 1.2, the generation of H_2 under UV light over metal-loaded semiconductors is based on a quick transfer of the photo-excited TiO_2-CB electrons into the metal sphere (Au) possessing a lower Fermi level. Thereby, the recombination of charge carriers (electrons and holes), which generally limits the photoactivity of bare semiconductors, is suppressed.[a] Thus, UV-light-stimulated H_2-evolution rates should be mainly governed by the number of active sites, *i.e.* Au particles acting as H_2-evolution centers, at the TiO_2 surface. At equal Au contents, smaller Au particles give rise to a higher number of potential electron traps at which the protons are reduced. Moreover, it was shown that the Fermi level of Au-TiO_2 catalysts is more negatively shifted by small Au particles than by large ones, which further enhances the separation of electrons and holes.[184] Therefore, it seems plausible that for AuP25-PD the lowest H_2 evolution was observed under UV-vis light, as it comprises only few large Au particles (d_m(Au) = 41 nm) determined by

[a]Bare P25 as reference material evolved 0.4 mmol g^{-1} h^{-1} H_2 with the 320–500 nm filter. No H_2 was detected for P25 using the 400–700 nm filter.

TEM analysis (Figure 4.2). This may arise from an unprotected particle growth during the PD procedure for Au deposition. While AuP25-SIM was prepared in the presence of the organic polymer PVA acting as particle stabilizer,[185] which led to smaller Au particles (d_m(Au) = 8.7 nm), the Au particles formed at the reduced Ti^{3+} sites during PD were not growth-protected. Hence, agglomeration with time is likely as the continuing light irradiation may also stimulate the Au particle movement.[186]

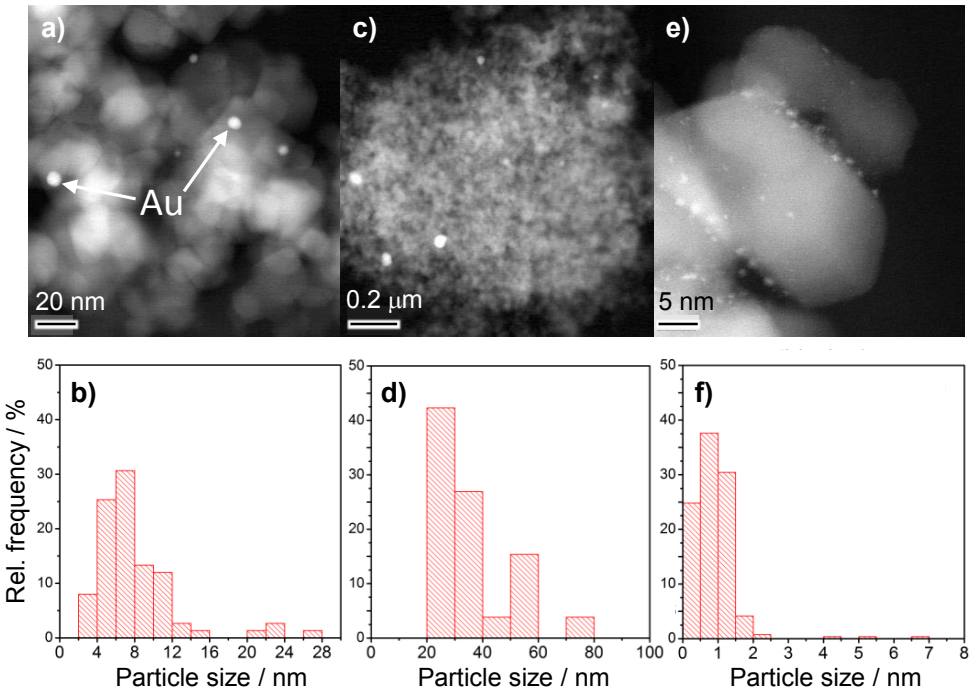

Figure 4.2: HAADF-TEM images and Au-particle-size distributions of as-synthesized AuP25-SIM (a, b), AuP25-PD (c, d), and AuP25-DP (e, f).

The difference in Au-particle size is also confirmed by the UV-vis absorbance spectra shown in Figure 4.3. In contrast to AuP25-DP and AuP25-DP12, intense Au-SPR absorption bands were observed for AuP25-SIM and AuP25-PD. In comparison with catalyst AuP25-SIM, the band maximum from AuP25-PD is shifted by 21 nm due to its larger mean Au-particle diameter. This Au-particle agglomeration in AuP25-PD consequently results in a lower surface content of Au (0.08 at.-%) determined by XPS (Table 4.1), compared to samples with higher Au-loading yields and smaller particle sizes such as AuP25-SIM (0.25 at.-%) and AuP25-DP (0.57 at.-%). Furthermore, the binding energies

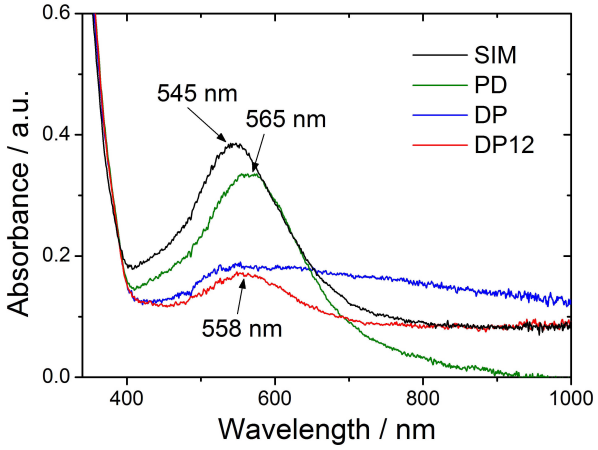

Figure 4.3: Au-SPR absorption of AuP25 catalysts prepared by different Au-deposition methods.

of Au and Ti in AuP25-PD point to an incomplete reduction of the Au^{3+} ions. The XPS Au $4f$ signal for AuP25-PD is composed of two different Au species (Table 4.1, Figure A.5a). The peak at 84.0 eV is in the range of reduced Au^0 (area marked green),[157, 187] while the signal component at 85.5 eV (Figure A.5a, pink) can be attributed to oxidized Au^{n+} with $n = 1, 2, 3$ depending on the strength of the metal-support interaction.[188] Note that for TiO_2 supports, large negative shifts were observed for binding energies of certain Au-oxidation states due to strong metal-support interactions (SMSI).[189] Therefore, an attribution to residual adsorbed Au^{3+} species ($n = 3$) is conceivable. On the other hand, a large amount of Ti^{3+} was observed in the Ti $2p$ region of the XP spectrum (Table 4.1, Figure A.5b, green), probably resulting from the pre-reduction step passed in the PD procedure (Figure 4.1). Such defect sites may hinder an efficient electron transfer of photo-excited TiO_2 electrons into the Au particles and, thus, can cause low activities as detected for AuP25-PD.

The XPS data in the Au $4f$ region for AuP25-SIM reveal two reduced Au species (Table 4.1). The peak at 83.7 eV (Figure A.5a, green) is slightly negatively shifted compared to bulk Au^0 (84.0 eV)[157] probably due to SMSI effects and can be therefore assigned to Au^0 nanoparticles strongly bound to TiO_2. The signal component at 83.2 eV (Figure A.5, blue) indicates the presence of another Au species partially negatively charged. This species may arise from Au particles bound at O^{2-} vacancies (Au-V_O).[190] These surface vacancies in TiO_2 formed in reducing environment such as $NaBH_4$ solution (Figure 4.1) likely act as Au nucleation sites, as their excess charge may be stabilized by the metal particle. Hence, the decrease in the Au-binding energy is likely caused by a partial contribution of the excess electrons to the bond formation between Au and the vacancy site.[190] Comparing the XPS data from catalysts AuP25-DP and AuP25-DP12 shows that the prolongation of the reaction time during DP method strongly affects the final Au-surface content, which is decreased for AuP25-DP12 by a factor of five (0.11 wt.%, Table 4.1). Although the Au-binding energy (83.7 eV) and the UV-vis spectrum (Figure 4.3, red) point to the presence of Au^0 particles, no Au species could be detected by TEM in AuP25-DP12 (not shown). Furthermore, a small surface contribution of Ti^{3+} is indicated by the XPS peak at 457.1 eV in the Ti $2p$ region (Figure A.5b, green). These results suggest that during the prolonged deposition procedure, either a considerable amount of Au may be incorporated into the TiO_2 matrix *via* interaction with those Ti^{3+} defect sites, or the Au particles strongly agglomerated and were thus not detected in TEM analysis by chance. In contrast, the Au $4f$ peak positions of the catalyst prepared by short-term DP, AuP25-DP, are slightly shifted to higher binding energies (84.3 eV, Table 4.1, Figure A.5a) compared to the values of reduced Au^0. This may be caused by either initial- or final-state effects as described in Section 2.3.6. Final-state effects could result from the very high dispersion (d_m(Au) = 1.1 nm) as

derived from TEM (Figure 4.2), which generally start to appear at sizes below 2 nm.[191] However, this peak might be also attributed to partly oxidized $Au^{\delta+}$ species[192] according to initial-state effects. As the DP procedure requires high temperatures for the precipitation of reduced Au^0 particles, the as-synthesized AuP25-DP catalysts (after drying at 100 řC) may still contain $Au(OH)_3$ oligomers (in $Au^{\delta+}$ state) bound at the TiO_2 surface.[193]

4.1.1 *In situ* monitoring of Au^0-particle formation in AuP25-DP

In order to clarify the origin of the positively shifted Au binding energy in AuP25-DP, *in situ* XAS measurements at the Au LIII absorption edge were conducted. Figure 4.4 displays the XANES region of the XA spectra for AuP25-SIM and AuP25-DP in their as-prepared state (red), after addition of H_2O/MeOH (blue) and under subsequent irradiation with UV-vis light (green). The XANES spectrum of as-prepared AuP25-SIM confirm the presence of reduced Au^0 species, as it is similar to that of Au foil (black dashed line) and did not change upon addition of H_2O/MeOH nor under UV-vis-light irradiation. In contrast, the as-prepared spectrum of AuP25-DP exhibits a weak peak *ca.* 4 eV above the Au LIII absorption edge ("white line", Figure 4.4b, orange), which is characteristic for oxidized $Au^{\delta+}$ species[194, 195] in accordance to the intial-state effects discussed above for the XPS data. Upon addition of H_2O/MeOH, this white line disappeared indicating the formation of Au^0 particles probably due to the reduction by electron-donating MeOH molecules. Further UV-vis-light irradiation did not lead to significant changes in the XANES spectrum.

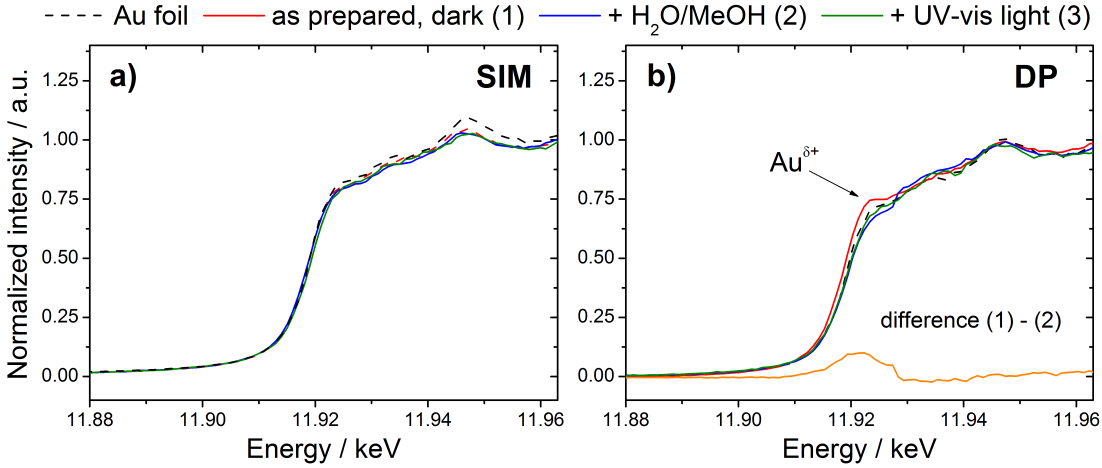

Figure 4.4: Changes in the XANES spectra at the Au LIII edge of as-prepared (red) AuP25-SIM (a) and AuP25-DP (b) and upon addition of H_2O/MeOH (blue) and subsequent UV-vis-light irradiation by a Xe lamp (green) compared to Au foil (dashed black). The subtraction spectrum (1) − (2) is displayed for AuP25-DP (orange).

Irradiation of AuP25-SIM in H_2O/MeOH did not markedly affect the SPR-band intensity or the position of the absorption maximum as well (Figure 4.5a), while the *in situ* UV-vis

spectra clearly illustrate the influence of radiation on the SPR-absorption band for AuP25-DP. The UV-vis spectrum of the as-prepared AuP25-DP catalyst exhibits a much lower SPR intensity compared to that of AuP25-SIM. This is most probably due to the initial $Au^{\delta+}$ state and the small Au diameter of 1.1 nm (Figure 4.2). In general, SPR absorption starts to be observable at a cluster size above 2 nm.[184] Upon addition of H_2O/MeOH and subsequent irradiation, the intensity of the band from the AuP25-DP catalyst clearly increases due to the ongoing *in situ* formation of Au^0 particles as demonstrated by XANES. Furthermore, the shift of the absorption maximum during irradiation visualizes the gradual particle growth. For AuP25-DP catalysts that have been isolated after the photocatalytic tests using the UV-vis-light filter for 3 h and the visible-light filter for 21 h (Figure 2.1), similar mean Au-particle sizes were observed (7.1 ± 2.8 nm and 8.8 ± 3.0 nm, respectively, Figure A.6). This *in situ* Au^0 formation might be one reason for the high photoactivity of AuP25-DP, since thereby very uniform and highly dispersed particles can be obtained, as the catalyst is prevented from Au agglomeration during synthesis.

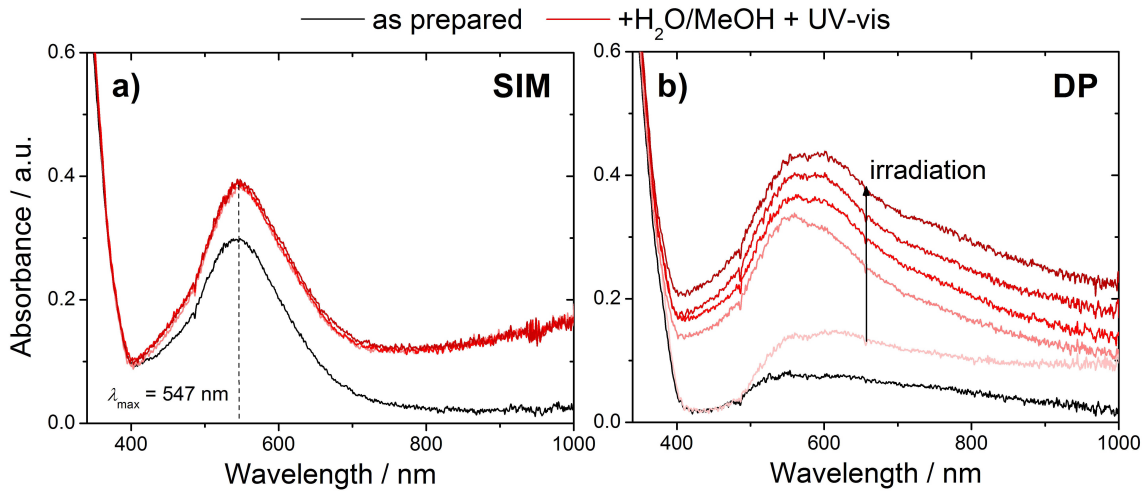

Figure 4.5: Changes of the Au-SPR absorption band of the as-synthesized catalyst (black) upon addition of H_2O/MeOH and subsequent irradiation (reddish) for AuP25-SIM (a) and AuP25-DP (b). Spectra were recorded each minute after addition of H_2O/MeOH.

4.1.2 The effect of calcination on AuP25-DP

A controlled thermal pre-treatment of the as-synthesized AuP25-DP catalysts can also generate well-defined reduced Au^0 particles loaded onto the TiO_2 support. The chosen calcination temperature is known to crucially affect particle growth and the extend of SMSI.[112, 196] Table 4.2 summarizes the photocatalytic H_2-production rates under UV-vis- and visible-light conditions, the mean Au-particle diameter derived from TEM, and the XPS data of Au and Ti for as-prepared AuP25-DP and calcined at 200, 400, and 600 řC.

Table 4.2: Photocatalytic activities, mean Au-particle sizes and XPS parameters (Au 4*f* and Ti 2*p*) of as-prepared AuP25-DP uncalcined and calcined at 200, 400 and 600 řC.

Catalyst	r_{H_2} / mmol g^{-1} h^{-1} UV-vis	vis	d_m(Au) / nm (TEM)	Au-at.-% (XPS)	E_b Au 4*f* / eV	E_b Ti 2*p* / eV
DP	33	2.4	1.1	0.57	84.3 ($Au^{\delta+}$)	459.4 (Ti^{4+})
DP200	9.0	0.3–1.2	16	0.23	84.5 ($Au^{\delta+}$)	458.8 (Ti^{4+})
DP400	20	1.1	10	--	--	--
DP600	31	1.8	11	0.13	83.6 (Au^0)	458.4 (Ti^{4+})

Surprisingly, the mean Au diameter was found to be the largest for the catalyst treated at the lowest temperature, while AuP25-DP400 and AuP25-DP600 exhibit similar particle sizes (Table 4.2, Figure A.7). However, the SPR-absorption maximum of AuP25-200 is located at the same position as for AuP25-DP400 (Figure 4.6), but extends to the higher wavelength range. The intensities of the Au-SPR absorption band indicate the presence of Au^0 particles for all calcined catalysts, whereas the Au-binding energy of the AuP25-DP200 catalyst is still in the range of partially oxidized $Au^{\delta+}$ species (84.5 eV) and is, thus, even higher than that observed for the as-prepared catalyst. This may indicate a lower SMSI, which could also explain the very low photoactivity (Table 4.2). Surprisingly, the catalyst treated at the highest temperature, AuP25-DP600, was almost as active under UV-vis light as the uncalcined catalyst. Its Au-binding energy is typical for reduced Au^0 particles (83.6 eV). In general, during the thermal precipitation of Au, the initially surface-bound $Au(OH)_3$ oligomers become dehydrated and agglomerate to Au_2O_3. At sufficiently high temperatures ($T > 300$ řC),[183] these oxide units are decomposed to Au^0 and O_2. Therefore, catalyst AuP25-DP200 might still contain such larger Au_2O_3 units along with reduced Au^0, which may lead to such a strong activity loss. Treatment at higher temperature ($T > 400$ řC), however, stimulates particle movement and rearrangement. Then the Au particles tend to preferentially precipitate at TiO_2-phase interfaces[179, 197] This effect plays an essential role for mixed-phase supports such as P25. As discussed below in detail (Chapter 5), the photo-excited electrons are thereby transferred across an additional phase, which further enhances the charge-carrier separation and, thus, the photoactivity.

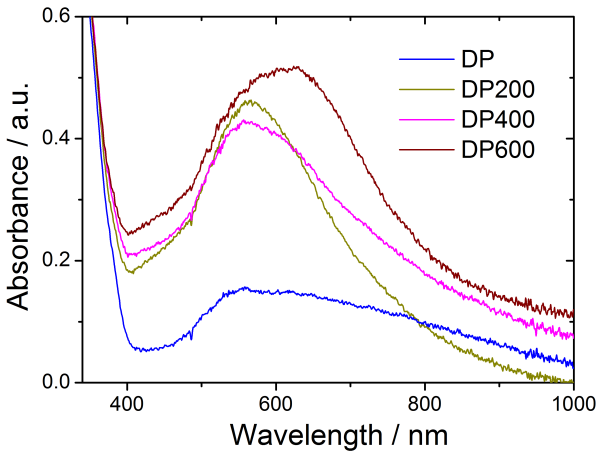

Figure 4.6: UV-vis spectra of AuP25-DP uncalcined (DP) and calcined at 200 (DP200), 400 (DP400) and 600 řC (DP600).

4.2 Light-induced charge-carrier formation and transfer

In situ EPR spectroscopy is the method of choice for visualizing light-induced electron-transfer processes as well as the formation and consumption of paramagnetic species during the photocatalytic reaction. Therefore, room-temperature EPR spectra of the AuP25 catalysts prepared by different methods were recorded in the dark, under irradiation with UV-vis light and under subsequent addition of H_2O and MeOH (Figure 4.7). The spectra demonstrate that the nature of the paramagnetic species is highly dependent on the chosen Au-deposition method. The catalysts prepared by PD and DP exhibited rarely any EPR-active species in the dark, while AuP25-SIM showed a weak isotropic feature at $g = 2.004$ (signal A3, Table 4.3), which most likely originates from electrons trapped at oxygen vacancies as discussed below. In contrast, a strong EPR signal A1 with axial symmetry was detected for AuP25-DP12 below $g = 2.0$ without any radiation. The g-values of this species are in the range of those observed for Ti^{3+} in TiO_2 (Table 4.3). Given the unusual fact that this signal was observed at room temperature indicates a variation in spin-lattice relaxation as explained in Section 2.3.10. This behavior may result from Ti^{3+} centers that are coordinatively unsaturated such as surface-located Ti sites [198] and/or Ti^{3+} in close vicinity to oxygen vacancies, for the latter of which, however, usually lower g-values were observed.[199] The assignment to surface-located Ti^{3+} species is supported by the signal decrease upon addition of H_2O and MeOH acting as scavengers of excess charges. Due to the longer reaction time in the DP12 procedure, the TiO_2 particles did presumably undergo a self-doping process, *i.e.* the creation of oxygen vacancies and Ti^{3+} interstitials as explained below in detail (Chapter 5). Thereby, high defect concentrations were obtained, which can result in a lower charge mobility and, thus, in an inhibited transfer to and from

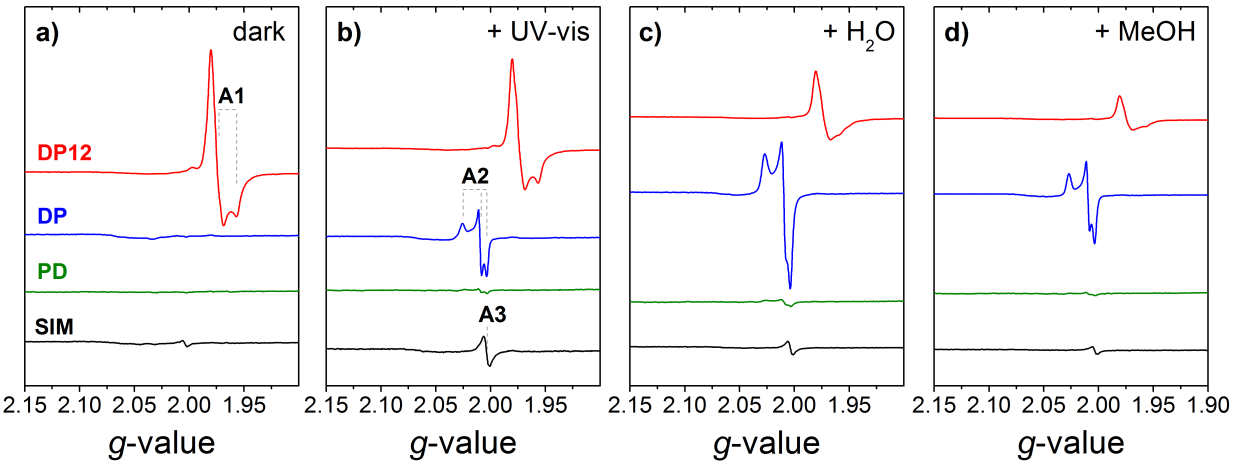

Figure 4.7: Room-temperature *in situ* EPR spectra of AuP25 catalysts prepared by different Au-deposition methods starting with the as-synthesized samples in the dark (a), under irradiation with UV-vis light (Xe lamp, no filter) (b), and with subsequent addition of water (c) and methanol (d).

Table 4.3: EPR parameters of observed signals in AuP25 catalysts prepared by different Au-deposition methods and their assignment based on literature.

EPR signal	g_z	g_y	g_x	Signal assignment	Reference
A1	1.978	1.978	1.957	Ti^{3+} in self-doped P25	a
	1.975	1.975	1.944	Ti^{3+} in self-doped anatase	[72]
	1.993	1.993	–	Ti^{3+} in self-doped anatase	[200]
A2	2.026	2.010	2.004	$O_2^{\bullet-}$ by irradiation of hydroxylated Au-P25 recorded at 290 K	a
	2.025	2.009	2.003	$O_2^{\bullet-}$ on hydrated anatase under UV-light radiation	[201]
	2.0243	2.0095	2.0036	$O_2^{\bullet-}$ on H_2O_2-treated rutile	[174]
	2.025	2.009	2.002	$O_2^{\bullet-}$ on Au-P25	[199]
A3	2.004	2.004	2.004	electrons trapped at O^{2-} vacancies ($e^-_{V_O}$) in Au-P25	a
	2.003	2.003	2.003	$e^-_{V_O}$ in Au-TiO_2	[199]
	2.005	2.005	2.005	$e^-_{V_O}$ in plasma-treated TiO_2	[202]
	2.0027	2.0027	2.0027	$e^-_{V_O}$ in outgassed TiO_2 aerogel	[203]
A4	2.026	2.015	2.004	Ti^{4+}–$O_s^{\bullet-}$ in Au-P25 recorded at 90 K	a
	2.026	2.015	2.005	Ti^{4+}–$O_s^{\bullet-}$ in calcined anatase	[204]
	2.026	2.017	2.008	Ti^{4+}–$O_s^{\bullet-}$ in calcined rutile	[204]
	2.024	2.014	2.007	Ti^{4+}–$O_s^{\bullet-}$ from aqueous anatase	[205]
A5	1.991	1.991	(1.961)[b]	bulk Ti^{3+} (anatase)	a
	1.992	1.992	1.962	bulk-located substitutional Ti^{3+} (anatase)	[206]
	1.990	1.990	1.957	bulk Ti^{3+} (anatase in P25)	[86]
A6	1.978	1.978	(1.944)[b]	bulk Ti^{3+} (rutile)	a
	1.9780	1.9746	1.9414	bulk interstitial Ti^{3+} (rutile single crystal)	[207]
	1.975	1.975	1.940	bulk Ti^{3+} (rutile in P25)	[86]
A7	2.035	–[b]	–[b]	Ti^{4+}–$O_2^{\bullet}H$	a
	2.034	2.009	2.002	Ti^{4+}–$O_2^{\bullet}H$	[176]
	2.034	2.008	2.002	Ti^{4+}–$O_2^{\bullet}H$	[208]

[a]This work. [b]Not resolved.

Au, leading to low H_2-evolution rates.

In contrast, the short-term DP procedure produced highly active catalysts, which did not show any EPR signal at room temperature in the dark, but under irradiation with UV-vis light. Then, a strong rhombic signal A2 is formed at typical g-values attributed to superoxide radicals, $O_2^{\bullet-}$, bound at the TiO_2 surface (Figure 4.7b, blue). Such $O_2^{\bullet-}$ species can be generated under irradiation *via* two different mechanisms. On the one hand, an electron-mediated process according to Eq. 4.1 could occur by trapping of the photo-excited electrons at surface-bound oxygen molecules, since the redox potential $E(O_2/O_2^{\bullet-})$

is slightly more positive (−0.33 V *vs.* NHE)[209] than the TiO_2 conduction-band potential ($E_{cb} = -0.47$ V at pH 7 for anatase).[17]

$$e^-_{cb} + O_2(ad) \rightarrow O_2^{\bullet -}(ad) \tag{4.1}$$

As the required oxygen may originate from traces in the helium flow, this signal should appear in all spectra of the different AuP25 catalysts. Thus, it is likely not the dominating process for the strong $O_2^{\bullet -}$ formation in AuP25-DP.

On the other hand, FTIR spectra of AuP25-DP compared to AuP25-SIM, the latter of which did not show such superoxide species under light irradiation, clearly illustrate that the DP method generates catalysts with specific surface-hydroxyl coverage (Figure A.8). Hence, the photo-generated positive holes are likely to be trapped by those surface-bound hydroxyl groups (Eq. 1.9). The hydroxyl radicals thus created may quickly recombine and form hydrogen peroxide (Eq. 4.2), which may be further converted to hydroperoxyl radicals ($E(H^+, HO_2^{\bullet}/H_2O_2) = 1.44$ V at pH 0)[210] upon oxidation by another trapped hole (Eq. 4.3). Bound at TiO_2, these radicals deprotonate at its basic centers to form $O_2^{\bullet -}$:[175]

$$2\,OH^{\bullet} \rightarrow H_2O_2 \tag{4.2}$$

$$H_2O_2 + OH^{\bullet} \rightarrow HO_2^{\bullet} + H_2O \tag{4.3}$$

$$TiO_2\text{–}HO_2^{\bullet} \rightarrow TiO_2\text{–}O_2^{\bullet -} + H^+ \tag{4.4}$$

Such a hole-mediated mechanism for the formation of $O_2^{\bullet -}$ at TiO_2 was first proposed by Howe *et al.* for hydrated anatase.[201] It is supported by the increase of the corresponding EPR signal upon adding H_2O, whereby probably more surface-hydroxyl groups are created and, thus, more trapping sites for h^+_{vb} at the TiO_2 surface. Moreover, the decrease in signal intensity after addition of the hole scavenger MeOH indicates a consumption of these trapped holes, so that the formation of $O_2^{\bullet -}$ is inhibited.

For the less active sample AuP25-PD, this $O_2^{\bullet -}$ signal was poorly formed upon irradiation with UV-vis light or addition of H_2O (Figure 4.7b and c, green). This may either indicate a less effective charge separation by transfer of CB electrons to Au resulting from the defect-rich structure, or a lack of specific surface-hydroxyl groups. The latter effect may also lead to lower activities, since the oxidation of MeOH was found to proceed faster indirectly *via* hydroxyl radicals.[211, 212] The FTIR study by Carneiro *et al.* provided further evidence for the crucial role of surface-OH groups in the photocatalytic oxidation of cyclohexane. This might also explain the lower H_2 evolution over AuP25-SIM compared to AuP25-DP, as the Au-particle size in AuP25-DP created *in situ* was similar to that in AuP25-SIM (Figure A.6) and therefore cannot be the crucial parameter for the difference in activity.

Wang *et al.* showed by sum frequency generation spectroscopy that the indirect oxidation by $^{\bullet}$OH can only become the dominant mechanism at a critical H_2O/MeOH molar ratio of *ca.* 300, due to the stronger adsorption properties of MeOH compared to H_2O.[29] Hence, these specific OH groups on AuP25-DP, allowing the favored indirect MeOH oxidation, are not likely to be formed for the other catalysts upon addition of H_2O/MeOH (volume ratio 1:1). However, by applying the DP method for Au deposition, hydroxyl species are probably tightly surface-bound at the as-synthesized catalyst and, thus, during the reaction. The photo-generated h^+_{vb} in AuP25-DP are, due to the less defective structure, highly mobile within AuP25-DP and, thus, trapped at its specific surface-hydroxyl groups, which presumably makes them more accessible for the hole scavenger MeOH and leads to higher H_2 evolutions compared to AuP25-SIM and AuP25-PD.

A similar effect was observed for the *in situ* EPR spectra of the calcined AuP25-DP catalysts as well. The room-temperature EPR signal A2, corresponding to hole-mediated $O_2^{\bullet-}$, was much more intense under irradiation for the more active catalysts AuP25-DP and AuP25-DP600 (Figure A.9). Moreover, the low-temperature EPR spectra shown in Figure 4.8 also illustrate the different capabilities of charge-carrier formation and separation in these catalysts. At $T = 90$ K, the reaction sequence 4.2–4.4 is slowed down. Without metal loading (bare P25), the very mobile photo-generated holes migrate to lattice-O^{2-} ions near the surface and react to Ti^{4+}–$O_s^{\bullet-}$ (A4, Table 4.3),[213] whereas the electrons tend to localize in the interior of the nanoparticle forming bulk-located Ti^{3+} species in anatase

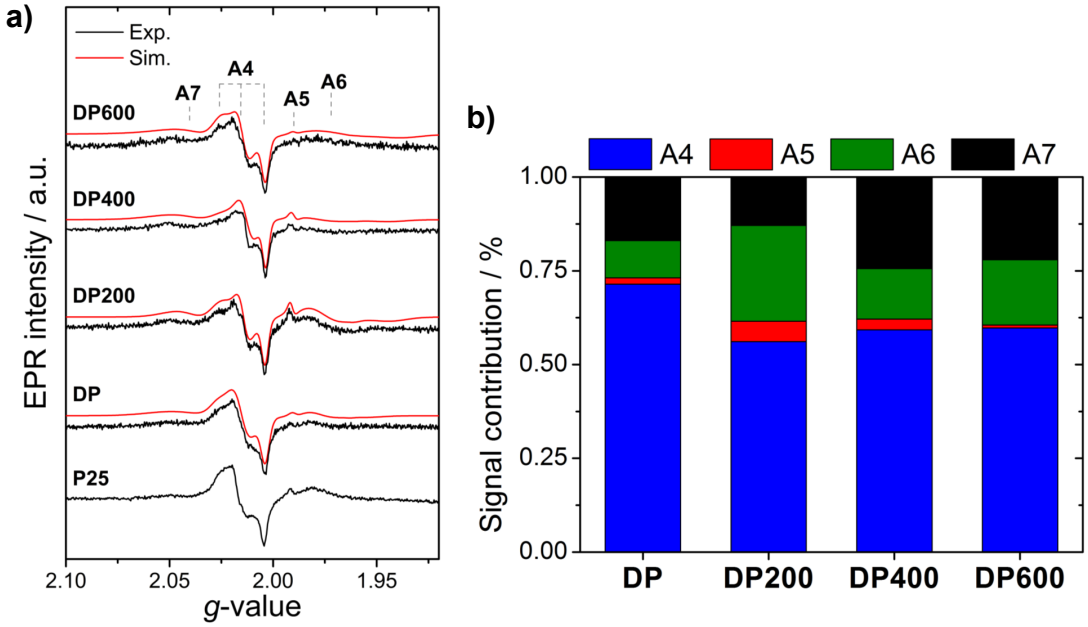

Figure 4.8: a) Low-temperature difference EPR spectra (black: UV-vis-light irradiated minus dark) and the corresponding signal simulations (red) of uncalcined AuP25-DP and calcined at 200, 400 and 600 řC in comparison to bare P25. b) Signal contributions of signals A4–A5 to the total double integrals.

(A5) and in rutile (A6). For the Au-loaded catalysts, however, the photo-excited electrons should be quickly transferred into the Au particles. Thus, higher Ti^{3+} concentrations in the EPR spectra indicate low charge-transfer capabilities, likely due to less SMSI and/or a lower number of active electron-trapping sites (Au). This is clearly seen by the corresponding spectra simulations revealing the highest Ti^{3+} contribution (signals A5 and A6) for catalyst AuP25-DP200 (Figure 4.8b), which also showed the lowest photoactivity (Table 4.2).

4.2.1 Visible-light-mediated electron transfer in Au-TiO_2

As mentioned in Section 1.2, Au-TiO_2 catalysts were also reported to generate H_2 solely by Au-SPR excitation with pure visible light,[111, 114] the detailed mechanism of which still remained unclear. Photocatalytic tests on selected AuP25 samples using an additional external filter ($\lambda > 420$ nm) revealed a significant amount of H_2 for catalyst AuP25-SIM (15 µmol H_2 in 26 h, Table A.1, experiment II), while other samples such as AuP25-DP12 (experiment III) did not show any visible-light-induced activity or, as in case of AuP25-DP, had to be pre-treated with UV light in order to generate SPR-active Au particles (experiments V–VII). Therefore, the origin and mechanism of the visible-light activity observed for AuP25-SIM was investigated by wavelength-dependent *in situ* FTIR and EPR measurements.

Figure 4.9 depicts the *in situ* FTIR spectra for UV-vis-light-irradiated AuP25-SIM in H_2O/ MeOH (purple) and for the same experiment using an cut-off filter ($\lambda > 420$ nm, green). The spectra exhibit similar negative (according to the consumption of adsor-

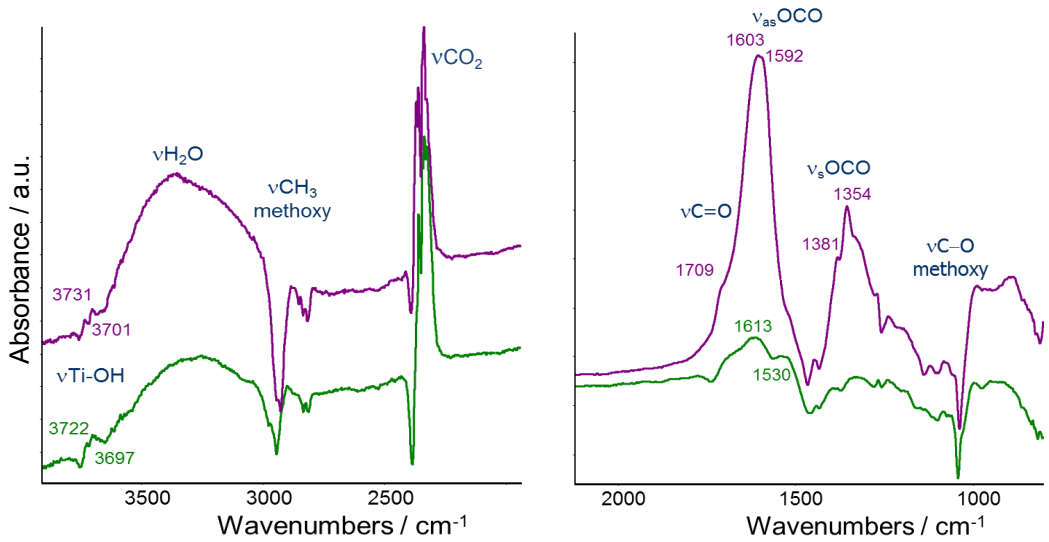

Figure 4.9: *In situ* ATR-IR spectra for AuP25-SIM in H_2O/MeOH. Depicted are the difference spectra obtained by subtracting the respective dark spectrum from the spectrum after 30 min UV-vis-light irradiation (Xe lamp without filter, purple) or from that after 120 min visible-light irradiation (Xe lamp, >420 nm filter, green).

bates) and positive (according to the formation of adsorbed products) bands under both wavelength ranges for excitation, though with much lower intensity for the experiment under pure visible light. This finding strongly suggests that the weak H_2 evolution of AuP25-SIM is solely caused by Au-SPR absorption. The negative bands observed at 2950–2830 cm^{-1} (stretching of CH_3 of molecularly and dissociatively chemisorbed MeOH)[214] and at 1050 cm^{-1} (C–O stretching of methoxy group)[215] are due to the consumption of adsorbed MeOH during irradiation. New bands appear at 1354, 1603 and 1709 cm^{-1} (symmetric and asymmetric stretching of OCO and C=O stretching of adsorbed formate species, respectively) as well as in the region of CO_2(g) (2250–2500 cm^{-1}), H_2O(g) (3000–3500 cm^{-1}) and OH(ad) (3500–3800 cm^{-1}). These bands indicate the stepwise oxidation of MeOH to formaldehyde and formic acid. The resulting formate species can be further converted photocatalytically into CO_2 and H_2O,[216] so that the corresponding gas-phase vibrations appear in the FTIR spectrum. However, the observation of increasing water bands can be either explained by an O_2-involving process (O_2 could be present in traces in the helium flow) for MeOH decomposition proposed by Chuang *et al.*,[217] or more likely by the involvement of lattice oxygen as confirmed by Muggli *et al.*[218, 219]

The EPR spectrum of AuP25-SIM under flowing helium contained an isotropic EPR signal A3 with a g-value close to that of a free electron (Table 4.3, Figure 4.7, black), which was not observed in pure P25 (Figure A.11, black). Such a signal could either arise from electrons trapped at TiO_2 oxygen vacancies (F^+ centers) or from the carbon residues in AuP25-SIM as detected by CHN analysis (C content: 0.4 wt.-%) and FTIR spectroscopy (ν(CH) in Figure A.8).[220] However, as shown in Figure A.11, this species was also observed with similar intensity for an AuP25 catalyst prepared by reductive precipitation using $NaBH_4$ without PVA as particle stabilizer (AuP25-RP, C content: 0.04 wt.-%). Moreover, XPS on AuP25-SIM revealed a high amount of Au in direct vicinity to TiO_2 surface-oxygen vacancies (Table 4.1), which supports the assignment of signal A3 to electrons trapped at oxygen vacancies ($e^-_{V_O}$). In contact with O_2, these electrons became trapped forming $O_2^{\bullet -}$ (Figure A.12), which would not be observed for carbon-based radical species. As the intensity of A3 strongly increased under irradiation (Figure 4.7b, black), the signal formation under excitation with certain wavelengths was investigated in order to clarify the origin of these electrons. As seen from Figure 4.10a, signal A3 was formed under irradiation with light in the visible region (532 ± 10 nm), whereas pure UV-light excitation (280 ± 10 nm) hardly affected the double integral of the EPR spectrum (Figure 4.10b). Since the pure TiO_2 support does not respond to light excitation above its absorption edge at *ca.* 400 nm, these trapped electrons reflected by signal A3 most likely do not originate from the TiO_2 valance band, but from the excited Au particles. Contrary to TiO_2, the Au particles absorb visible light due to their $d \rightarrow sp$ interband transitions ($E > 2.5$ eV $\equiv$ 495 nm)[221]

and surface plasmon resonance absorption (Figure 4.11a). For both experiments depicted in Figure 4.10, in which the sample was kept either in the dark (a) or under UV light (b) before switching to visible light, the formation of signal A3 occurred at similar rates ($\tau_f = 6.5$ min and $\tau_f = 6.0$ min, respectively). In contrast, the decay constant determined for the signal decay upon switching from 532 nm to UV light (a, $\tau_{dec} = 5.5$ min) differed strongly from that for shutting off the light (b, $\tau_{dec} = 10.9$ min). This might indicate a UV-light-stimulated back transfer of the trapped electrons into the adjacent Au particle (where they are not detectable by EPR) for the first conditions, instead of a slow relaxation as observed in the second experiment.

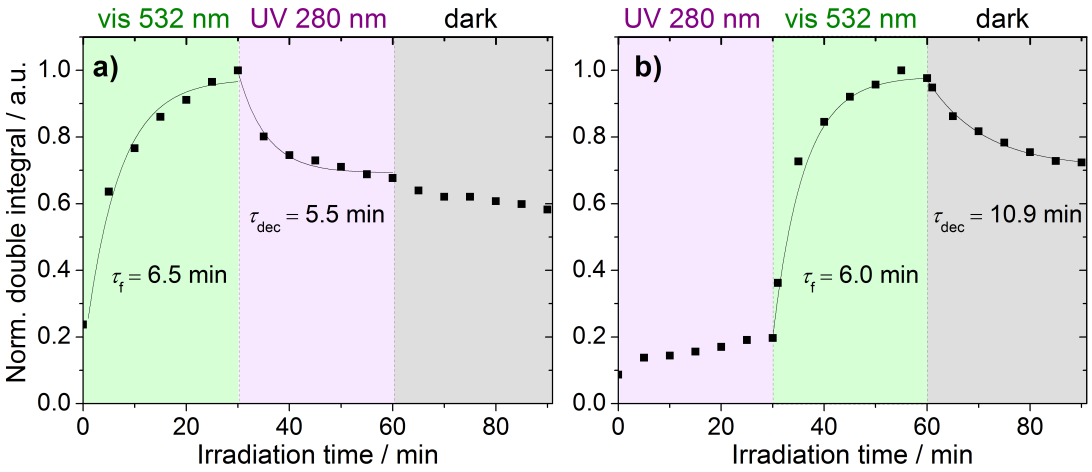

Figure 4.10: Double integrals of the EPR signal A3 (symbols) as a function of irradiation time starting with visible (532 ± 10 nm) and switching to UV light (280 ± 10 nm) after 30 min (a) and *vice versa* (b). The corresponding EPR spectra are depicted in Figure A.13. Time constants τ_f and τ_{dec} have been derived for the formation and decay processes, respectively, by fitting the time dependence of the EPR double integrals using exponential approximation equations (lines).

These findings strongly suggest an injection of "hot" Au electrons into the TiO_2 conduction band upon visible-light excitation. In order to explore whether the visible-light-induced electron trapping at TiO_2-oxygen vacancies is related to the Au-SPR phenomenon, a set of band-pass filters was used to select distinct excitation wavelengths in the range of 300–700 nm (Figure 4.11b). One experiment started at 300 nm, which was held constant for 15 min irradiation before switching to the next higher wavelength (blue line), whereas the second begun at 700 nm and run *vice versa* (red line). The double integrals for both experiments are plotted together with the UV-vis absorption spectrum of AuP25-SIM (black line). Both curves exhibit a maximum value of signal A3 at wavelengths of 450–500 nm, which is in good agreement with the maximum value of the electron-injection yield derived from transient absorption spectroscopy by Du *et al.*[139] Apparently, direct electron-hole pair generation by Au-interband ($d \rightarrow sp$) transition ($\lambda < 500$ nm, Figure 4.11a) accounts for the most electron injection into the TiO_2-CB. However, the clear increase of the double

integral at high wavelengths (red line) cannot be explained by Au-interband transitions and indicates that the SPR-enhanced electromagnetic fields lead to "hot" Au electrons of sufficient energy to overcome the Schottky barrier at the Au/TiO_2 interface. Hence, the pure visible-light activity observed for AuP25-SIM (Table A.1, experiments I and II) can be most likely attributed to these two Au-electron injection processes into the TiO_2 conduction band, where they accumulate to levels above the proton reduction potential and are thus able to reduce protons.

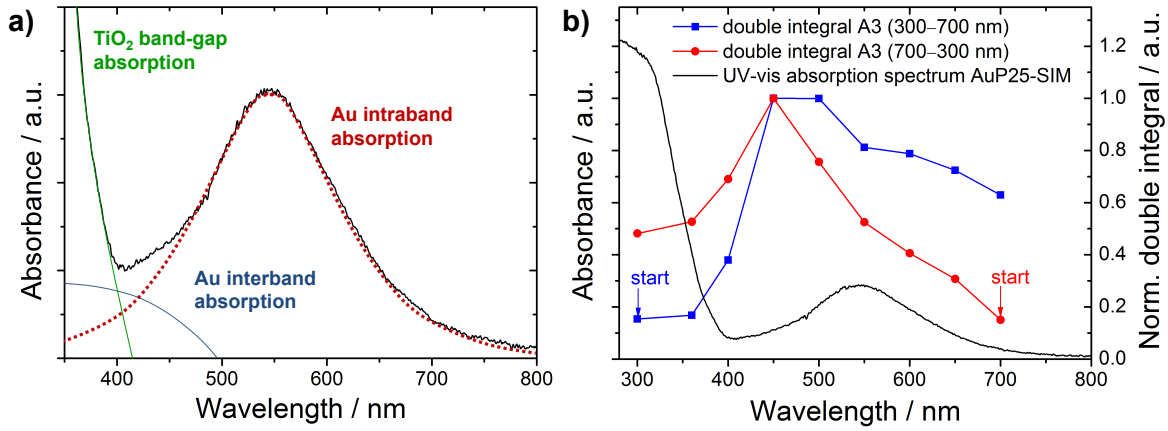

Figure 4.11: a) Deconvolution of the UV-vis absorption spectrum of AuP25-SIM. While the TiO_2 absorption (green) extends to *ca.* 400 nm, the Au-SPR band is centered at 547 nm (red). The contribution of Au-interband transitions ($d \rightarrow sp$) is clearly seen below 500 nm (blue). b) Double integrals of the EPR signal A3 (symbols) as a function of irradiation wavelength starting at 300 nm (blue) or at 700 nm (red) in comparison to the UV-vis absorption spectrum of AuP25-SIM (black). The excitation wavelength was kept for 15 min before switching to the next higher (or lower) wavelength. The corresponding EPR spectra are depicted in Figure A.14.

4.3 Conclusion

It has been demonstrated that the Au-deposition method crucially influences the resulting catalyst structure and, thus, its catalytic performance in H_2 generation from H_2O/MeOH. Deposition-precipitation exhibits unique advantages due to the generation of small and uniform Au particles in the early stages of the photocatalytic reaction. Thereby, cost-intensive high-temperature treatment in an additional calcination step becomes needless, as it merely leads to a loss of activity due to particle agglomerations. Otherwise, temperatures above 400 řC are required to rearrange Au particles towards their locations at phase boundaries and Au dimensions that are advantageous for efficient light-driven H_2 production. This was confirmed by *in situ* EPR spectroscopy revealing larger amounts of non-transferred photoexcited electrons for less active catalysts. Furthermore, EPR points out the important role of surface-hydroxyl species formed by the DP method. They act as initial trapping sites for the positive holes making them more accessible for the sacrificial reductant MeOH and

thereby promote its oxidation rate. However, the DP procedure was found to be highly sensitive to the reaction time. A longer exposition to the reaction mixture led to strongly decreased activities, which is most likely due to a modification of the TiO_2 support. EPR spectroscopy detected a high concentration of surface-Ti^{3+} defects for that catalyst, which apparently hinders an efficient electron transfer to Au. For catalyst AuP25-PD, an incomplete Au^{3+} reduction during the PD method was observed leading to low charge-transfer efficiencies as well.

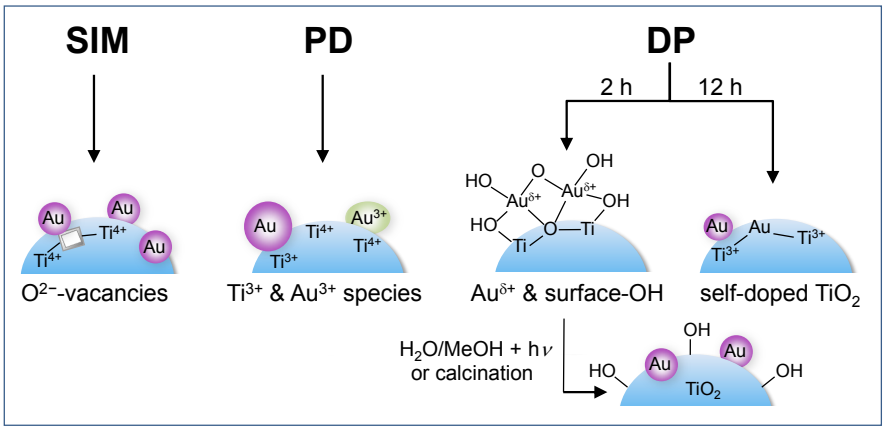

Figure 4.12: Surface-structural properties of AuP25 prepared by different Au-deposition protocols.

In contrast, sol-immobilization generates highly active catalysts due to efficient SMSI and well-distributed Au particles. Moreover, pure visible-light activity (>420 nm) was observed for AuP25-SIM. The spectroscopic results strongly suggest that this H_2 evolution is initiated by a direct electron transfer from Au into the TiO_2-CB. TiO_2-oxygen vacancies, at which Au tends to nucleate, act as trapping sites for these transferred Au electrons, so that this transfer process can be visualized by EPR. Both Au-absorption processes, $d \rightarrow sp$ interband and *sp*-intraband transitions due to SPR absorption, are likely to contribute to the electron injection. However, EPR signals of markedly higher intensity were observed in the region where inter- and intraband transitions overlap, which indicates a synergistic effect of the two Au absorptions, improving the capability of hot-electron transfer from Au into the TiO_2 conduction band.

Figure 4.13: *In situ* EPR spectroscopy visualized the transfer of Au-conduction electrons into TiO_2 vacancy sites, where they might be taken up by the protons to produce H_2.

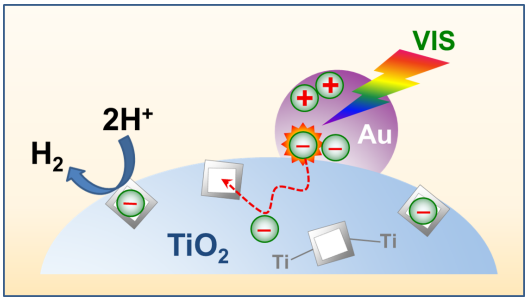

5 Modification of the support towards enhanced performance of Au-TiO_2

It has been shown in Chapter 4 that the method of Au deposition onto TiO_2 highly affects the photoactivity of Au-TiO_2 catalysts. However, modification of the TiO_2 support may be one major route for enhancing light response and charge-carrier lifetimes as well. This cannot only be done by improving the synthesis method as described in Chapter 3, but also by modifying TiO_2 either through doping procedures or by varying the phase composition. For example, anatase was often reported to exhibit better photocatalytic performances than rutile. This was attributed e.g. to a different nature of the band gap (indirect and direct, respectively),[222] or to a higher bulk mobility of charges in anatase.[49] Moreover, a TiO_2-phase composite, which is constituted by at least two different lattice modifications, can decrease the recombination of charge carriers by electron (and hole) transfer across the phases as described in Section 1.2. Therefore, the first part of this chapter addresses the role of the TiO_2-phase composition in Au-TiO_2 catalysts for their performance in H_2 production. Different TiO_2 single phases as well as phase composites were studied by in situ EPR spectroscopy in view of charge-carrier formation and the capability of electron transfer to (under UV light) and from (under visible light) the Au particles.

Intrinsic and extrinsic defects created upon doping of TiO_2 (e.g. self-doping or N doping, respectively) can shift the absorption edge towards visible light. Since H_2-reduced TiO_2 also led to enhanced solar H_2 evolution over the metal-free catalyst,[81] in situ EPR measurements on such a self-doped TiO_2 are discussed in the second part of this chapter in order to shine light on the mechanistic background for its improved activity. N doping of TiO_2 has been widely investigated in photocatalysis, though only few works focused on potential synergistic effects with the SPR absorption of Au NPs.[223–225] The nature of visible-light-active N species in TiO_2:N has been extensively studied by Giamello et al. using EPR spectroscopy.[226–229] However, most of these catalysts were prepared by sol-gel methods, which can lead to N species that are different from those created by e.g. thermal treatment in ammonia. A comparative in situ EPR study of metal-free N-doped TiO_2 and the corresponding SPR-active Au-loaded catalysts is presented in the third part of this chapter. Based on the catalytic results, plausible electron-transfer pathways are drawn.

5.1 Variation of the TiO_2 phase

Three different TiO_2 phases are naturally occurring: rutile, brookite and anatase, the structures of which are depicted in Figure 5.1. The tetragonal rutile phase (PDF 21-1276) is thermodynamically stable, whereas the orthorhombic brookite (PDF 29-1360) and tetragonal anatase (PDF 21-1272) phases are metastable. The stability of the different structures decreases in the order rutile > brookite > anatase due to the rising number of shared octahedron edges, whereby the inter-cation distances decrease (Pauling rule).[230]

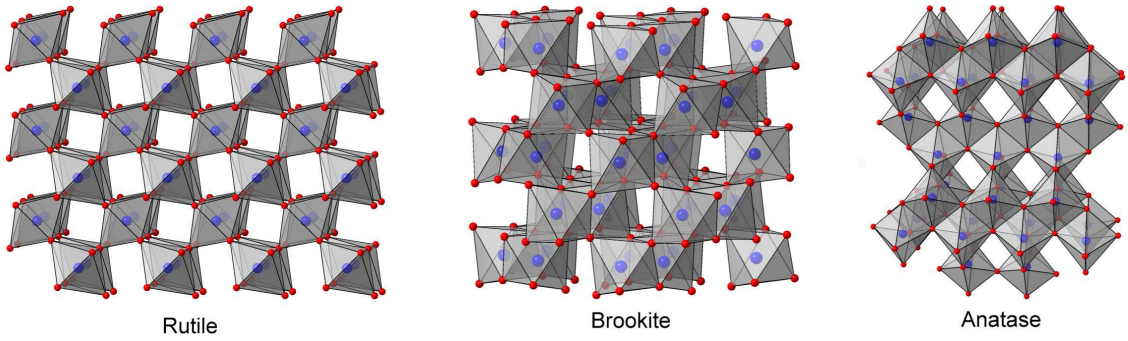

Figure 5.1: Crystal structures of the three naturally occurring TiO_2 phases rutile, brookite and anatase (red: O^{2-}, blue: Ti^{4+}).

Table 5.1 summarizes the structural and electronic properties of the five TiO_2-based materials used in this study: two mixed anatase/rutile composites (P25 and Hom), a pure rutile (Rut) and a pure anatase (Ana) phase as well as an anatase/brookite mixture (Bro). The crystallite sizes, determined by line-broadening analysis of the XRD patterns in Figure 5.2a using the Scherrer equation, were the smallest for Ana, Rut, and Bro. This is in accordance with the large BET surface areas observed for these supports. As demonstrated in Chapter 3, the surface area can be a crucial property in photocatalysis and may have a high impact on the H_2 evolution, since it can govern recombination rates of charge carriers.

Table 5.1: TiO_2-support phases used for Au-TiO_2 synthesis, their BET surface areas, composition (A: anatase, R: rutile, B: brookite) and crystallite sizes, D_c, determined by XRD peak analysis (Figure 5.2a) as well as the band-gap energies calculated from the absorption edge (Figure 5.2b).

Support	S_{BET} / $m^2\ g^{-1}$	Composition	$D_c(TiO_2)$ / nm	E_g / eV (absorption edge)
P25	50	A/R = 85:15	23(A), 38(R)	3.18
Hom	55	A/R = 87:13	21(A), 30(R)	3.20
Rut	96	R	15	3.05
Ana	70	A	14	3.21
Bro	77	A/B = 85:15	16(A), 28(B)	3.19

On the other hand, the TiO_2 semiconductors are also characterized by different optical properties as seen from the UV-vis spectra depicted in Figure 5.2b. The nature of the band gap (direct or indirect) and the corresponding energy for transition are known to play a key role in photocatalytic reactions. TiO_2 is supposed to be an indirect semiconductor,[231] though recent studies indicate that direct transitions dominate in the rutile phase.[222, 232] Since for TiO_2-phase composites such as P25, Hom, and Bro, two different band-gap transitions of the composed phases must be distinguished, the experimentally determined value for the band gap, E_g, is considered as indicator for the absorption limit of the present materials. Therefore, this minimum energy for the VB-electron excitation was calculated from the absorption edge (Figure 5.2b, dashed lines) and listed in Table 5.1 for the different supports. The band-gap energies $E_g = 3.05\,\text{eV}$ and $E_g = 3.21\,\text{eV}$ for the pure phases Rut and Ana, respectively, agree well with reports in literature.[233] Slightly lower E_g values were obtained for the mixed-phase supports than for pure anatase, which is plausible as rutile and brookite exhibit smaller band gaps than anatase.[231, 233]

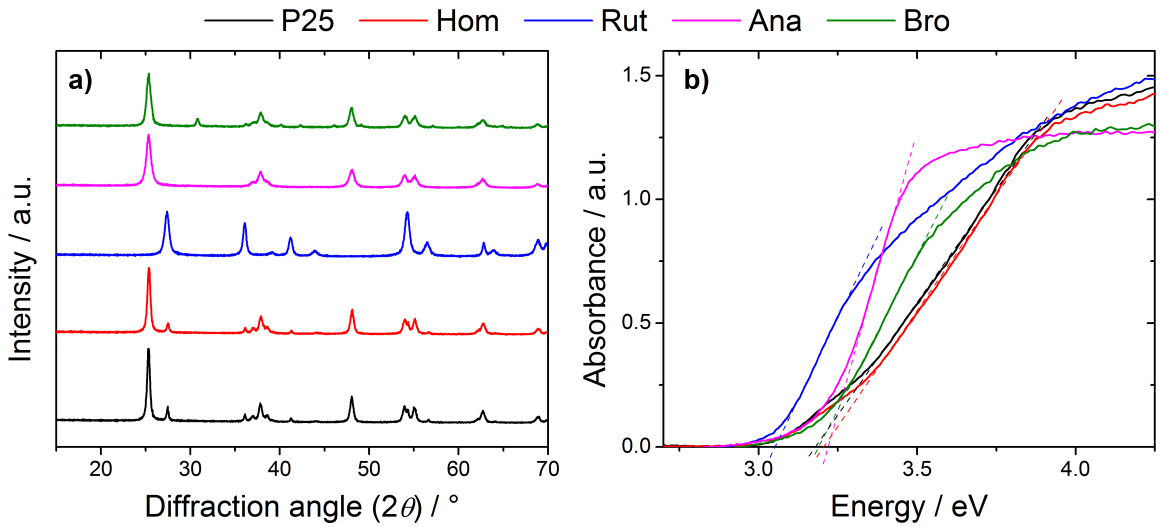

Figure 5.2: XRD patterns (a) and UV-vis-DR spectra (b) of the different TiO_2 supports.

5.1.1 Catalyst performance and the related formation of EPR-active charge carriers

Since the DP method revealed the most active AuP25 catalysts (see Chapter 4), this Au-deposition procedure was primarily applied to study the impact of different TiO_2-phase compositions as support materials. Selected Au-TiO_2 catalysts (based on P25, Ana and Rut as support material) were also synthesized *via* the SIM and DP12 methods in order to study the relation between the structure of the catalyst, its performance and the capability of generating light-active species. Table 5.2 summarizes the structural and catalytic

Table 5.2: Catalytic activities, mean Au diameters derived from TEM (Figure A.16), Au contents determined by ICP-OES, XPS Au $4f$ analysis, and detected EPR species at $T = 290\,\mathrm{K}$ under UV-vis irradiation in helium flow (Figure 5.4a) for $AuTiO_2$-DP catalysts with different support materials.

Catalyst	r_{H_2} / mmol g^{-1} h^{-1} UV-vis	vis	d_m(Au) / nm (TEM)	Au-wt.-% (ICP-OES)	Au-at.% (XPS)	E_b Au $4f$ / eV	EPR species
AuP25-DP	33	2.4	1.1	0.93	0.57	84.3	$O_2^{\bullet-}$
AuHom-DP	32	0.93	n.d.[a]	0.99	0.35	82.8 84.5	$O_2^{\bullet-}$
AuRut-DP	8.5	0.37	3.3	0.74	0.19	83.8 85.0	$O_2^{\bullet-}$, Ti_s^{3+}
AuAna-DP	17	0	5.1	0.80	0.11	85.3 88.7	Ti_b^{3+}
AuBro-DP	11	0	n.d.	0.85	0.16	83.2 85.6	Ti_b^{3+}

[a]Not determined.

characterization of Au-TiO_2 catalysts prepared with different TiO_2 support compositions *via* DP method. A similar overall Au content was observed in all $AuTiO_2$-DP samples (Table 5.2), which consequently led to a lower surface content of Au (derived from XPS) for catalysts with higher BET surface area and larger mean Au-particle sizes.

Anatase/rutile mixtures

Among all tested materials, the mixed anatase/rutile supports, P25 and Hom, led to catalysts with the highest photoactivities under UV-vis light (Table 5.2, Figure A.15), regardless of which Au-deposition method was applied (Figure 5.3a, black and red). As explained in Chapter 1.2, previous works provided evidence for a UV-light-induced improved charge-carrier separation in anatase/rutile mixtures due to either a hole-transfer from anatase to rutile,[234] and/or an electron transfer across an additional TiO_2 phase (recently proposed to occur from rutile to anatase)[83] prior to their injection into the metal particles.[32] This is widely accepted as explanation for the superior activity of the mixed phases compared to single rutile and anatase catalysts, which is confirmed by our study as well.

Rutile

AuRut-DP exhibited the lowest activity under UV-vis light (Table 5.2, Figure 5.3a, blue), although its surface area was higher than that of the other materials and should therefore favor low recombination rates as shown in Chapter 3 for $NaTaO_3$-based catalysts. On the other hand, using the SIM method for Au deposition could improve the H_2 evolution for the Rut support, whereas the DP method led to the best catalysts for P25 and Ana (Figure

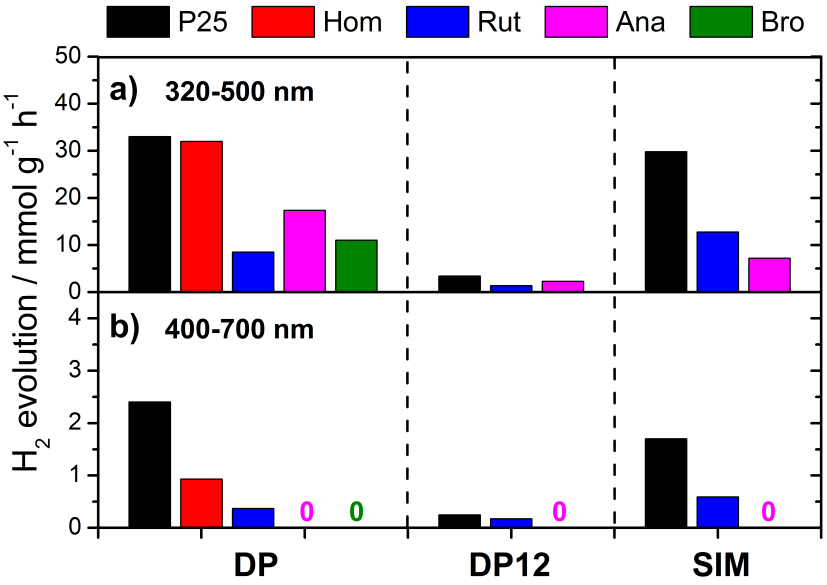

Figure 5.3: Photocatalytic H_2 evolution a) under UV-vis light (320–500 nm) and b) under visible light (400–700 nm) over Au-TiO_2 catalysts with different support compositions prepared by the Au-deposition methods DP, DP12 and SIM.

5.3a). The *in situ* EPR spectra of the AuTiO$_2$-DP catalysts displayed in Figure 5.4a may explain this behavior. A significant EPR signal corresponding to self-doped surface Ti^{3+} (similar to signal A1 in Chapter 4, Table 4.3) was detected for AuRut-DP (blue) already in the dark along with UV-vis-light-generated superoxide radicals, $O_2^{\bullet-}$ (signal A2 in Chapter 4, see Table 4.3 for parameters), while the latter was the only species observed in the highly active AuP25-DP (black) and AuHom-DP (red) catalysts with lower surface area. This suggests that pronounced self-doping is detrimental for the catalytic activity of Au-loaded TiO_2. An efficient electron transfer from Rut to the Au particle may thus be hindered in AuRut-DP, probably due to electron trapping at these surface defects, although the positive holes are efficiently trapped at hydroxyl radicals forming $O_2^{\bullet-}$ as described in Eq. 4.2–4.4.

Anatase

In the case of AuAna-DP, the H_2-evolution rate under UV-vis light was higher than that of AuRut-DP (Table 5.2, Figure 5.3a, pink). The characteristic Ti^{3+} signal of self-doped TiO_2 was detected for Ana only by use of the prolonged DP12 procedure (Figure 5.4b, pink) associated with strong activity loss (Figure 5.3b, pink), but not for AuAna-DP, which might be ascribed to its lower surface area compared to the Rut support. Instead, the EPR spectrum of AuAna-DP consists of an intense Ti^{3+} signal with characteristic g-values $g_{1,2} = 1.990$ and $g_3 = 1.962$ for the anatase phase (Figure 5.4a, pink). This signal was present in all Ana-based materials, even without Au loading (not shown). It was

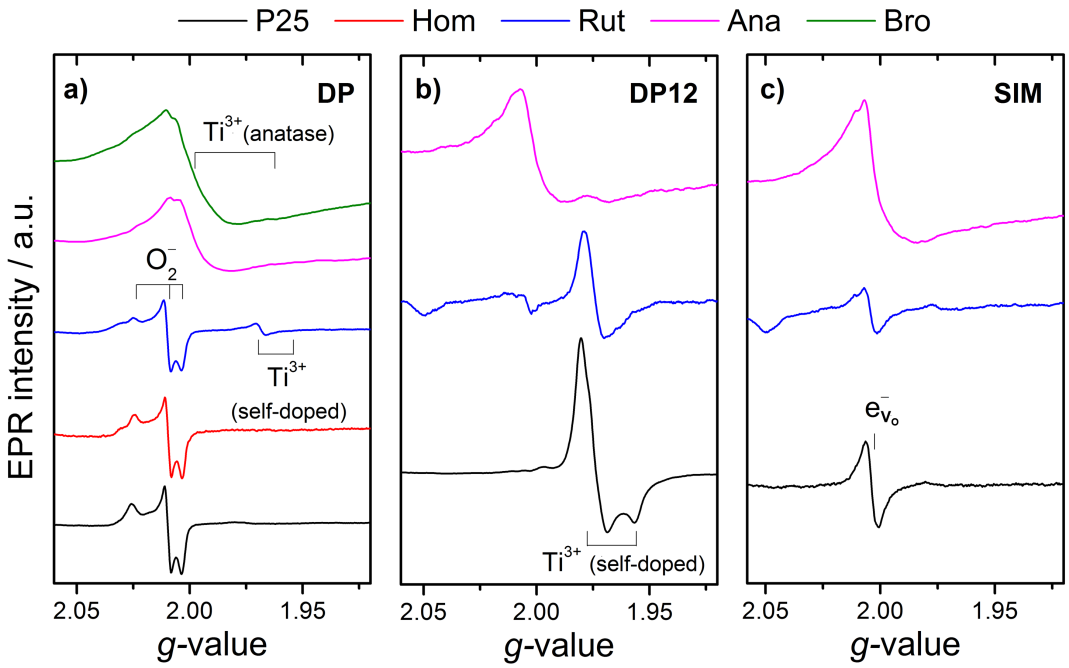

Figure 5.4: *In situ* EPR spectra of Au-TiO_2 catalysts with different support compositions prepared by the Au-deposition methods a) DP, b) DP12 and c) SIM. Spectra were recorded in helium flow after 10 min under UV-vis irradiation (Xe lamp, no filter).

already detected in the dark and showed neither light-response nor changes upon adding the reactants water and methanol. Furthermore, XPS on AuAna-DP did not indicate the presence of surface-located Ti^{3+} as in the case of self-doped TiO_2 materials. Therefore, this signal can be attributed to intrinsic bulk or subsurface-located defects, which were probably already created during the synthesis of this commercial TiO_2 support. Unlike the surface-Ti^{3+} species of the DP12-based catalysts, these bulk-located defect sites in Ana did not affect the activity under UV-vis light (Figure 5.3a). However, they might inhibit a sufficient SPR-induced electron transfer from Au into the conduction band of Ana, presumably due to an increased Schottky barrier. This is supported by the fact that also no $e^-_{V_O}$ signal (signal A3 in Chapter 4), corresponding to Au electrons trapped at oxygen vacancies, occurred when Au was deposited onto Ana using the SIM method (Figure 5.4c). As explained in Chapter 4, this signal may provide evidence for an effective transfer of Au electrons into the TiO_2-CB. The high bulk-Ti^{3+} concentration can thus lead to a weaker binding between Au and the Ana support, which is indicated by the XPS data as well (Table 5.2). For all $AuTiO_2$-DP catalysts, partly oxidized Au species were observed (E_b = 84.3–85.6 eV), consistent with the presence of very small $Au(OH)_x$ units in the as-prepared state as proposed in Chapter 4. However, TEM analysis revealed that AuAna-DP did not contain such small Au species (Figure A.16, mean particle diameter: 5.1 nm), although it exhibited the highest Au-binding energies followed by Bro. This points

either to a weaker binding of Au to the support as proposed by Tsukamoto *et al.*,[197] or to a different electronic environment of Au in Ana and Bro compared to the other supports, especially P25 and Hom, for which the maximum Au $4f$ binding energy was significantly lower. The suppressed electron transfer from Au to TiO_2, caused by a weak binding and/or an increased Schottky barrier due to intrinsic bulk defects, may thus explain the absence of visible-light activity for all Ana-based catalysts (Table 5.2, Figure 5.3).

Anatase/brookite composite

The EPR spectrum of the catalyst prepared with the anatase/brookite composite, AuBro-DP, exhibits a similarly intense Ti^{3+}-anatase signal (Figure 5.4a, green). Moreover, although its photoactivity under UV-vis light (320–500 nm) was appreciable (Figure 5.3a), no visible-light H_2 evolution was observed, neither under excitation with pure visible light ($>$ 420 nm filter, Table A.1) nor by applying the 400–700 nm filter (Table 5.2, Figure 5.3b). This strongly indicates that such a Ti^{3+}-enriched support material indeed hampers a transfer of SPR-excited Au electrons into the TiO_2 phase, which might be caused by a decreased electron affinity, due to the intrinsic bulk-Ti^{3+} charges, compared to non-defective TiO_2. As the conduction band of brookite ($E_{cb} = -0.46$ V *vs.* NHE at pH 7)[235] is more negative than those of rutile and anatase, a transfer into that phase is also not likely to occur.

5.2 Self-doping (reduction) of TiO_2

Self-doped TiO_2 recently gained high attention due to its enhanced visible-light response. The term expresses the modification of stoichiometric TiO_2 by reduction procedures, such as annealing in vacuum or in Ar/H_2 atmosphere, electrochemical reduction, or H_2-plasma treatment.[236] For example, Liu *et al.*[81] observed a significant activity increase for a commercial anatase TiO_2 catalyst (An) upon a specific hydrogen treatment, yet without providing unambiguous reasons for their findings. They reported that standard reduction in Ar or H_2/Ar mixtures poorly enhanced the photocatalytic H_2 evolution, while the activity of the catalyst treated with high-pressure hydrogen, Hy-An,

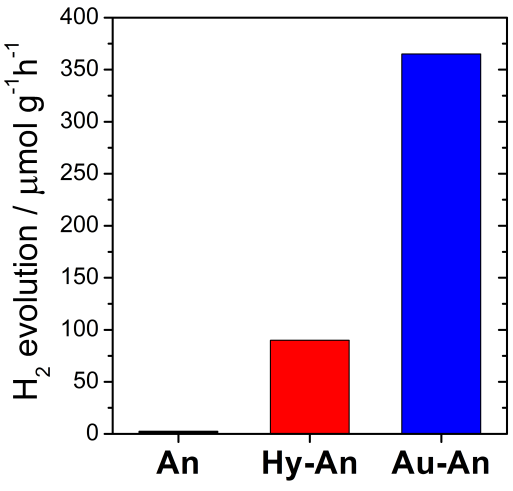

Figure 5.5: Photocatalytic H_2-evolution rates from H_2O/MeOH mixtures over anatase TiO_2 (An), H_2-treated anatase (Hy-An), and Au-loaded anatase (Au-An).[a]

[a]Conditions: 2 mg of catalyst in 10 mL H_2O/MeOH (vol. ratio 1:1), AM 1.5 solar-simulator illumination (100 mW cm^{-2}). Data taken from [81].

even without adding Au reached almost 30 % of that of the Au-loaded untreated anatase, Au-An, (Figure 5.5).[81] Comparison of the XRD patterns of An and Hy-An reveals a small growth in the anatase crystallite size upon H_2 reduction from 22 to 26 nm as well as a slight increase of the rutile phase (001) reflection (Figure 5.6a, enlarged inset). Although anatase/rutile phase composites generally show a better photocatalytic performance than their single-phase counterparts as demonstrated in Section 5.1, this small effect alone is not likely to explain the drastic activity increase observed for Hy-An. The UV-vis absorption spectra depicted in Figure 5.6 are quite similar for An (black) and Hy-An (red). However, Hy-An exhibits an increased absorption background as well as a slight shift of the threshold from $E_g = 3.15\,\text{eV}$ to 3.09 eV compared to the untreated catalyst, respectively. These optical changes upon the reduction process of the An catalyst can be attributed to the generation of intrinsic defects and an oxygen-deficient structure. Such a composition is represented by both stoichiometries, TiO_{2-x} or $Ti_{1+x}O_2$. The first case describes the presence of oxygen vacancies, $V_O^{\circ\circ}$, which are easily created upon mild reduction treatments. Their formation can be expressed by the following defect equation based on Kröger-Vink notation[a]:[237]

$$O_O^{\times} \rightleftharpoons V_O^{\circ\circ} + 2\,e' + \frac{1}{2}O_2(g) \tag{5.1}$$

Ionic compensation of the excess electrons is likely to occur by trapping at lattice Ti^{4+} ions:

$$Ti_{Ti}^{\times} + e' \rightleftharpoons Ti_{Ti}^{'} \tag{5.2}$$

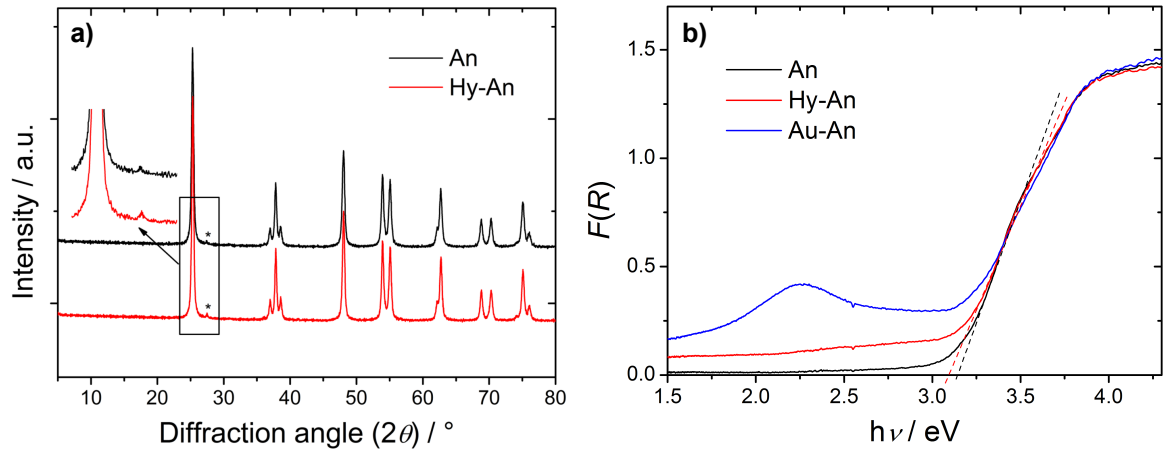

Figure 5.6: XRD patterns (a) and UV-vis absorbance spectra (b) of An (black), Hy-An (red), and Au-An (blue). The (001) reflection of the rutile phase (asterisk, enlarged inset) slightly increased after hydrogenation and the absorption edge was shifted to higher wavelengths.

[a]General form: M_S^C, where M corresponds to the species, *e.g.* atoms such as Ti, vacancies V or electrons e, S indicates the lattice site occupied by the species, *e.g.* i for an interstitial site, and C reflects the electronic charge of the species relative to the site it occupies. Zero charge is represented by ×, whereas ∘ and ′ indicate a single positive or negative charge, respectively.

On the other hand, excess of metal compared to oxygen ions can also exist in $Ti_{1+x}O_2$. It is formed by longer reduction treatments when oxygen is depleted from external layers, while Ti consequentially diffuses into the bulk, creating Ti interstitials, $Ti_i^{\circ\circ\circ\circ}$:

$$Ti_{Ti}^{\times} + 2\,O_O^{\times} \rightleftharpoons Ti_i^{\circ\circ\circ\circ} + 4\,e' + O_2(g) \tag{5.3}$$

At high concentration of Ti interstitials, the electrons are probably trapped by the Ti^{4+} ions:

$$Ti_i^{\circ\circ\circ\circ} + e' \rightleftharpoons Ti_i^{\circ\circ\circ} \tag{5.4}$$

It is likely that both defect species, Ti^{3+} and oxygen vacancies, are present in self-doped TiO_2, though their concentration can be different depending on the sample treatment. The created Ti^{3+} species, reflected by Ti'_{Ti} and $Ti_i^{\circ\circ\circ}$ in Eq. 5.1 and 5.4, may cause the increased absorption background of Hy-An due to the corresponding $d \rightarrow d$ transitions (Figure 5.6b). In order to confirm this attribution and to analyze the behavior of such paramagnetic species under irradiation, *in situ* EPR spectroscopic investigations were carried out.

5.2.1 *In situ* EPR investigations

Figure 5.7 depicts the low-temperature *in situ* EPR spectra of the commercial untreated anatase TiO_2, An (a), the Au-loaded catalyst, Au-An (b), and the H_2-treated anatase, Hy-An (c). The dark spectra of the untreated An catalyst and the Au-loaded Au-An exhibit very intense features characteristic for chemisorbed molecular nitric oxide, $NO^{\bullet}$, along with a small signal of Ti^{3+} located in the bulk (for parameters see Table 5.3).[226] Since these $NO^{\bullet}$ molecules were observed in untreated commercial TiO_2 without contact to air, they most likely arise from the synthesis procedure, in which NH_3 or ammonium salts might have been involved, whereby $NO^{\bullet}$ could be formed upon oxidation:

$$4\,NH_4Cl + 5\,O_2 \rightarrow 4\,NO + 5\,H_2O + 4\,HCl \tag{5.5}$$

It is assumed that these $NO^{\bullet}$ radicals are trapped in microvoids of the material and become weakly adsorbed at the TiO_2 surface by cooling the catalyst down to at least 190 K (the temperature dependence of the EPR spectrum is given in Figure A.17a).[68] When $NO^{\bullet}$ is adsorbed on surfaces, the electric field of the support may quench the orbital angular momentum, so that the magnetic moment is determined by the electronic spin only. This converts the $^2\Pi_{1/2}$ ground state of $NO^{\bullet}$ into a paramagnetic state, allowing its observation in the free-electron region of the EPR spectrum.[68,238] In the free state it has a zero angular momentum due to the antiparallel coupling of spin and orbital angular momentum.

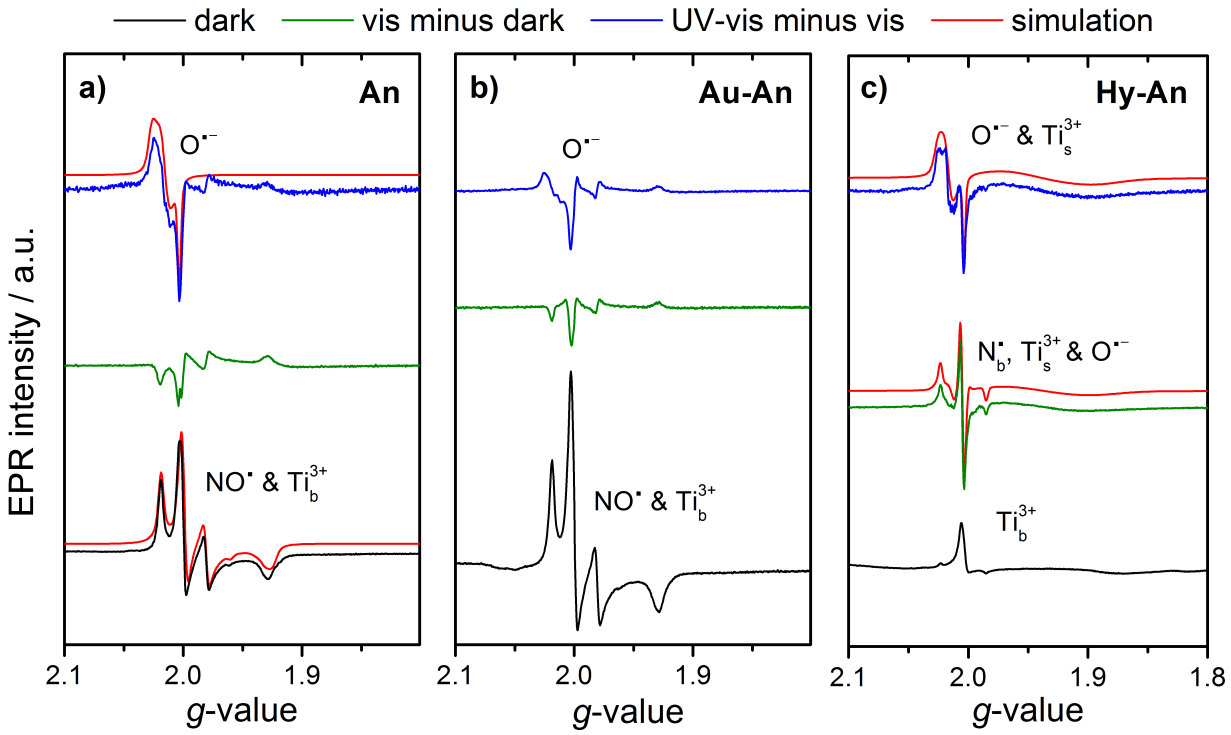

Figure 5.7: *In situ* EPR spectra of a) An, b) Au-An and c) Hy-An at $T = 90\,\mathrm{K}$. In order to visualize light-induced changes, the spectrum recorded in the dark (black) was subtracted from that under irradiation with visible light (Xe lamp, >420 nm filter), which produced the green lines. The blue curves reflect the subtraction of the spectrum under visible light from that under UV-vis light (Xe lamp, no filter). Red: spectrum simulations; parameters and the corresponding assignments are listed in Table 5.3.

Table 5.3: EPR parameters derived by simulation of the observed signals shown in Figure 5.7 for An, Au-An, and Hy-An as well as their assignment based on literature data.

EPR signal / assignment		g_z	g_y	g_x	A_z	A_y	A_x	Reference
$\mathbf{NO^{\bullet}}$	trapped in microvoids [a]	2.002	1.996	1.928	0.0	31.9	7.4	[68]
$\mathbf{Ti_b^{3+}}$	in bulk of N-containing TiO_2	2.003	2.003	1.961	--	--	--	[239]
$\mathbf{O^{\bullet -}}$	trapped holes at O^{2-} [a]	2.026	2.016	2.004	--	--	--	[204]
$\mathbf{Ti_s^{3+}}$	surface interstitials	1.956	1.956	1.895	--	--	--	[206]
$\mathbf{N_b^{\bullet}}$	in bulk of N-doped TiO_2	2.006	2.005	2.004	2.3	4.4	32.1	[227, 228]

[a]Detectable only at $T = 90\,\mathrm{K}$.

Interestingly, no such $NO^{\bullet}$ species was observed for the H_2-treated anatase, Hy-An, despite the fact that for Hy-An a similar surface-nitrogen species as for catalyst An was detected by XPS at *ca.* 400 eV (Figure 5.8a). Only a Ti_b^{3+} signal was recorded in the dark, which was found in all samples also at high temperature (Figure A.17b), supporting their attribution to intrinsic bulk-Ti^{3+} species of the commercial TiO_2 material as observed also for some anatase-containing Au-TiO_2 catalysts in Section 5.1. The Ti_b^{3+} signal intensity at 290 K for Hy-An, however, was twice as high as for the other catalysts, which may point

to the formation of oxygen vacancies and/or Ti interstitials upon the reduction treatment according to Eq. 5.1–5.4. This is also supported by the presence of a small shoulder corresponding to Ti^{3+} in the Ti 2*p* region of the XP spectrum (Figure 5.8b, red).

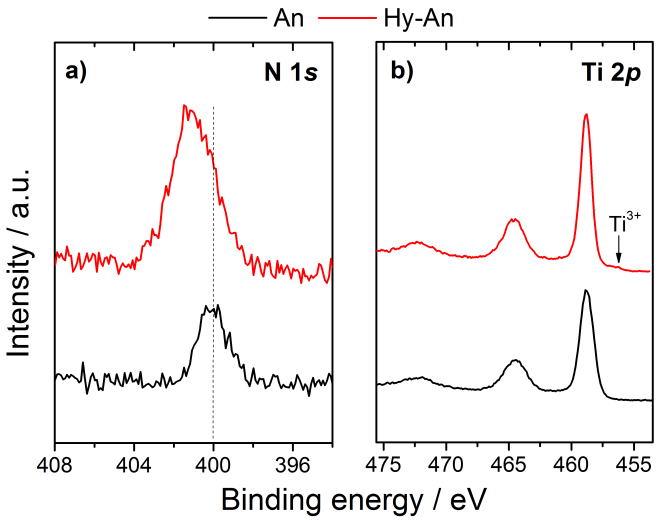

Figure 5.8: XP spectra of An (black) and Hy-An (red) in the N 1*s* (a) and Ti 2*p* (b) regions.

In order to visualize directly the EPR-spectrum changes under visible (Xe lamp, >420 nm filter) and subsequent UV-vis light (no filter), the corresponding difference spectra are depicted in Figure 5.7 (green and blue, respectively). Under visible light, the spectra of An and Au-An show only a slight decrease of the $NO^{\bullet}$ signal, which could result from light-induced temperature variations. In contrast, spectrum simulation for visible-light-irradiated Hy-An reveals the appearance of three new species. They can be assigned to bulk-located nitrogen radicals, $N_b^{\bullet}$, surface-located Ti_s^{3+} species and oxygen radicals, $O^{\bullet-}$ (Table 5.3), which were not formed in the other catalysts at any temperature under irradiation with visible wavelengths. The $N_b^{\bullet}$ species corresponds to either substitutional or interstitial nitrogen within the TiO_2 lattice.[229] The discrimination between the two forms will be further discussed below in Section 5.3. Hence, the high-pressure H_2 treatment apparently may have led to an incorporation of nitrogen into the TiO_2 matrix, originating from the enclosed NO molecules. This process seems likely to occur under these reductive conditions, as it has been shown by theoretical calculations that the energetic cost for the substitution of oxygen by nitrogen is strongly decreased in oxygen-deficient reduced TiO_{2-x} compared to stoichiometric TiO_2 ($\Delta E = 6.4$ and 10.0 eV, respectively).[229]

In the non-illuminated as-prepared Hy-An catalyst, diamagnetic N_b^- should be present as major fraction, because this form was proposed to be stabilized by trapping of the reduction-generated excess electrons (Ti^{3+}) at paramagnetic N species:[227]

$$N_b^{\bullet} + Ti^{3+} \rightarrow N_b^- + Ti^{4+} \tag{5.6}$$

As mentioned in Chapter 1.2, it has been shown previously that these N species tend to form localized N 2*p* states in the forbidden band of TiO_2, approximately 0.14–0.75 eV above the TiO_2 valence band.[229] Electrons can thus be excited from these occupied states into the conduction band of TiO_2 (N(2*p*) → Ti(3*d*) transition) by irradiation with visible light, forming both $N_b^{\bullet}$ and Ti_s^{3+} as observed in the EPR spectra (Figure 5.7c, green):[227]

$$N_b^- + Ti_s^{4+} \xrightarrow{h\nu_{vis}} N_b^\bullet + Ti_s^{3+} \quad (5.7)$$

Moreover, the IR part of the radiation source (Xe lamp, >420 nm) can excite electrons from the TiO_2-VB into these localized N 2*p* states (O(2*p*) → N(2*p*) transition), producing oxygen-trapped holes as demonstrated by Barolo *et al.*[228]:

$$N_b^\bullet + O^{2-} \xrightarrow{h\nu_{IR}} N_b^- + O^{\bullet-} \quad (5.8)$$

Since oxygen vacancies must be present in Hy-An, which can be described as F^{2+} centers creating localized states *ca.* 0.7 eV below the TiO_2 conduction band,[240] valence-band electrons can be also excited into these states by visible light:

$$F^{2+} + 2\,O^{2-} \xrightarrow{h\nu_{vis}} F^0 + 2\,O^{\bullet-} \quad (5.9)$$

The thus formed oxygen radicals, $O^{\bullet-}$, were also detected in Hy-An under irradiation with visible light (Table 5.4, Figure 5.7c, green) as evident from a weak shoulder at the low-field component of the $N_b^\bullet$ signal and from spectrum simulation. In contrast, UV-light irradiation was necessary to observe such $O^{\bullet-}$ signals in the spectra of the An and Au-An catalysts (Figure 5.7, blue) caused by interband excitation in TiO_2 (O(2*p*) → Ti(3*d*) transition). While UV-light-induced transitions are most likely the main contribution to the photoactivity of the An and Au-An catalysts, Eq. 5.7–5.9 show that Hy-An is moreover able to convert the major part of solar irradiation, *i.e.* visible light as well as IR light, into reactive charges.

Table 5.4: Summarized properties of An and Hy-An obtained from UV-vis, XPS, and EPR analyses.

Catalyst	Band gap / eV	E_b Ti 2*p* / eV	E_b N 1*s* / eV	N at.-% (XPS)	EPR species dark	vis. light	UV-vis light
An	3.15	458.8	400.0	0.94	$NO^\bullet$, Ti_b^{3+}	–	$O^{\bullet-}$
Hy-An	3.09	458.8 456.4	401.0	2.36	Ti_b^{3+}	$N_b^\bullet$, Ti_s^{3+}, $O^{\bullet-}$	$O^{\bullet-}$

Hoang *et al.* recently reported about a synergistic effect of hydrogen and nitridation co-treatment enhancing the photoactivity of TiO_2 in water oxidation.[241] Considering the structural and optical properties summarized in Table 5.4 for An and Hy-An, the present study strongly suggests that a similar effect may be responsible for the strong activation of the N-containing anatase catalysts by the high-pressure H_2-reduction procedure applied by Liu *et al.*[81] Milder procedures such as the standard reduction in (H_2/)Ar, which gave no activated catalysts, did apparently not lead to N incorporation as seen from the remaining

$NO^{\bullet}$ signal in the EPR spectra (see reference [81]). The detected visible-light-active $N_b^{\bullet}$ species in the activated Hy-An catalyst was previously discussed as main origin of the enhanced photoactivity of N-doped TiO_2 catalysts under visible light.[227] Therefore, its contribution to the increased H_2 evolution from H_2O/MeOH solutions over Hy-An is very likely, since it allows a more efficient utilization of solar light. However, recent reduction experiments on other TiO_2 samples conducted in the group of Prof. Schmuki, University of Erlangen, led also to activated catalysts even when no nitrogen was incorporated. On the other hand, synergistic effects of simultaneous N incorporation and reduction of TiO_2, which have been reported by several groups,[70, 241] cannot be excluded for Hy-An.

5.3 N doping of TiO_2

In order to investigate potential synergistic effects between such visible-light-responding nitrogen centers observed in the previous section and the optical properties of Au NPs, targeted N-doped TiO_2 supports for Au-TiO_2:N catalysts have been prepared and analyzed. Introducing nitrogen into the TiO_2 lattice can occur through a multitude of techniques. Annealing TiO_2 in ammonia atmosphere is a common procedure for generating visible-light-absorbing TiO_2:N catalysts.[242, 243] Furthermore, commercial TiO_2 materials such as P25 can be nitrided by this method, allowing comparisons to the catalysts investigated

Table 5.5: Sample colors, overall and surface N contents derived from EA and XPS, respectively, N 1*s* binding energies, and catalytic activities under UV-vis (320–500 nm) and visible light (400–700 nm) of pure and Au-loaded TiO_2:N catalysts compared to the undoped supports, Ana and P25.

Catalyst	Color	N wt.-% (EA)	N at.-% (XPS)	E_b N 1*s* / eV	r_{H_2} / mmol g^{-1} h^{-1} UV-vis	vis
Ana	white	n.d.[a]	n.d.	n.d.	0.25	--[b]
Ana:N10-500-6	pale yellow	0.22	n.d.	n.d.	n.d.	
Ana:N15-600-5	yellow	0.30	0.96	395–399	0.83	--
Ana:N15-650-5	deep yellow	0.36	n.d.	n.d.	n.d.	
Ana:N10-650-5	deep yellow	0.42	2.65	396–402	n.d.	
P25	white	n.d.	n.d.	n.d.	0.39	--
P25:N15-600-5	pale yellow / greenish	0.34	0.56	397.8	n.d.	
P25:N15-550-5	pale yellow / greenish	0.29	n.d	n.d.	n.d.	
P25:N15-550-3	pale yellow	0.22	0.65	399.8	0.66	--
TiO_2:N-Urea	pale yellow	0.25	1.53	399.5	n.d.	
Au-Ana:N	dark green	0.19	1.39	400.2	6.9	--
Au-P25:N	dark purple	0.21	1.42	399–402	18	0.27

[a]Not determined. [b]Volume below detection limit.

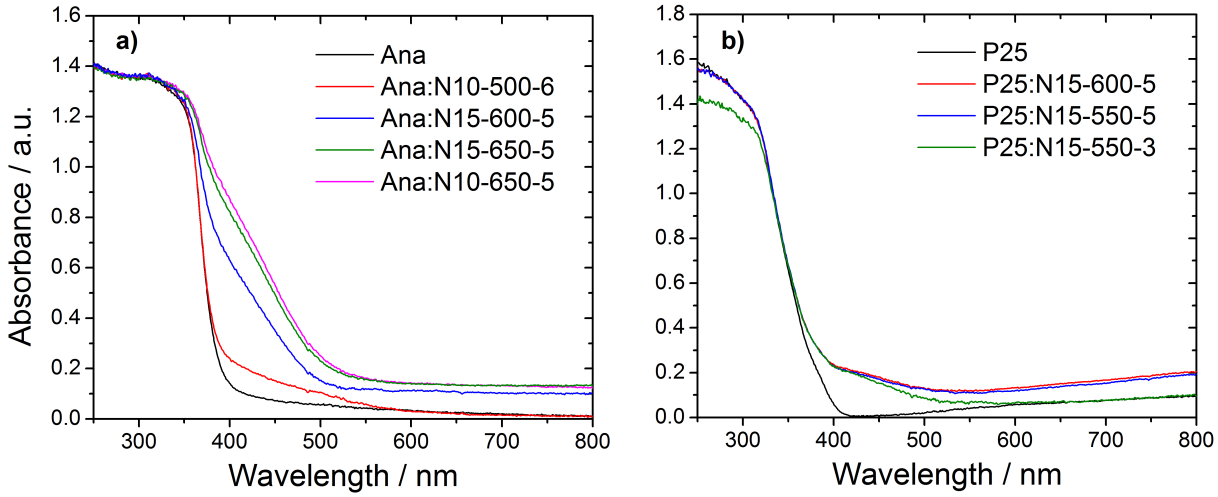

Figure 5.9: UV-vis absorbance spectra of various N-doped Ana (a) and P25 (b) catalysts.

in the previous chapters. A pure anatase phase (Ana, $70\,m^2\,g^{-1}$) and an anatase/rutile mixture (P25, $50\,m^2\,g^{-1}$) have been applied for N incorporation by thermal treatment in NH_3 at different ammonia flows, temperatures and nitridation times as listed in Table 2.1 (Section 2.1.3). For example, Ana:N10-500-6 denotes an Ana support that was nitrided in $10\,L\,h^{-1}$ NH_3 at 500 řC for 6 h. Given the results summarized in Table 5.5, the nitridation temperature seems to be the most affecting parameter for achieving high nitrogen contents. The best results (up to 0.42 wt.-% N) were obtained at 650 řC. At the same time, higher amounts of N in Ana led to a stronger absorption of visible wavelengths (400–500 nm) as shown in Figure 5.9a. In contrast, nitridation of P25 was less effective. Even at a nitridation temperature of 600 řC, absorption at high wavelengths corresponding to $d \rightarrow d$ transitions of Ti^{3+} appeared in the product rather than a further increase of absorption at 400–500 nm (Figure 5.9b). This could be due to the lower BET surface area of P25. Since a lower number of surface Ti and O sites was thus exposed to the NH_3 stream, reduction of TiO_2 or the undesired formation of TiN layers might have been occurred.

The photocatalytic H_2-production rate under UV-vis-light irradiation (320–500 nm) of P25:N15-550-3 was slightly improved compared to pristine P25 (Table 5.5). This effect was more significant for Ana:N15-600-5, which might be ascribed to the much stronger light absorption in the visible range (Figure 5.9a, blue). The Au-loaded catalysts, Au-P25:N and Au-Ana:N, both showed an unexpected decrease in activity under UV-vis- and visible-light conditions with respect to the undoped Au-TiO_2-DP catalysts investigated in Section 5.1 (for r_{H_2} values of AuAna-DP and AuP25-DP see Table 5.2). Reasons for these findings were therefore explored by structural analysis combined with *in situ* EPR spectroscopy.

5.3.1 Formation, structure and stability of N species under reaction conditions

The observed shift of the absorption edge by N doping can result from two main processes of nitrogen incorporation into the TiO_2 lattice. The first one occurs upon replacing lattice oxygen by nitrogen and produces substitutional nitrogen species (Figure 5.10a) as well as oxygen vacancies, $V_O^{\circ\circ}$. For using ammonia as nitrogen source, this process is expressed by Kröger-Vink notation as follows:

$$2\,NH_3(g) \;+\; 3\,O_O^{\times} \;\rightarrow\; 2\,N_O' \;+\; V_O^{\circ\circ} \;+\; 3\,H_2O(g) \tag{5.10}$$

Such a substitutional N species is also characterized by XPS with N 1*s* binding energies similar to that of anionic nitrogen in TiN, *i.e.* E_b = 396–397 eV.[229] The second photoactive nitrogen species is of interstitial nature (Figure 5.10b) and predominantly formed through wet-chemistry preparation methods.[244] Its generation can be written as:

$$2\,NH_3(g) \;+\; 3\,O_O^{\times} \;\rightarrow\; 2\,N_i''' \;+\; 3\,V_O^{\circ\circ} \;+\; 3\,H_2O(g) \tag{5.11}$$

Interstitial nitrogen is chemically bound to a lattice oxygen ion, which can be seen as a NO group in the bulk of the solid.[228] There exits, however, no clear consensus about the value of the corresponding binding energy in the XP spectrum. In many works, peaks in the range of 400–401 eV were attributed to interstitial N, though these values are also typical for chemisorbed N_2 molecules.[245] Due to the positive charge of interstitial N in the NO fragment, higher binding energies more close to those of nitrate (*e.g.* 408 eV in $NaNO_3$)[246] are expected.

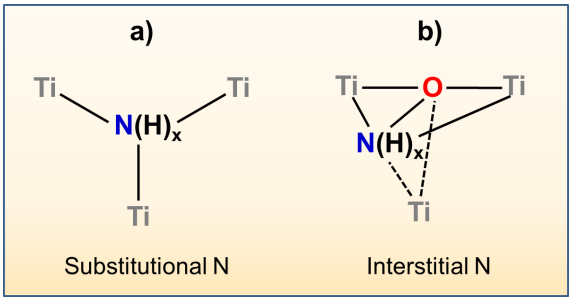

Figure 5.10: Schematic model structures for N dopants in substitutional (a) and interstitial (b) positions. Previous XPS and FTIR analyses support NH_x groups being possible N dopants depending on the synthesis conditions.[247–249]

Low-temperature *in situ* EPR spectroscopy on TiO_2:N catalysts

Spectroscopic techniques such as EXAFS combined with theoretical calculations have been previously applied in order to discriminate between interstitial and substitutional N species,[250] which, however, provided unequivocal results only at low dopant levels. Although EPR spectroscopy cannot clearly distinguish between these two dopant

forms as shown by theoretical calculations of the corresponding EPR parameters,[229] this technique provides valuable information about the nature of paramagnetic photoactive species, such as $N_b^\bullet$, their lifetimes and their consumption by the reactants. Figure 5.11 displays the EPR spectra of N-modified Ana (green) and P25 (blue) as well as the Au-loaded catalysts (red and black, respectively) in comparison to that of sol-gel-prepared TiO_2:N-Urea (pink) recorded at $T = 90\,K$ under visible-light excitation. The spectra of the NH_3-synthesized TiO_2:N catalysts contain signals of two N-based paramagnetic species. The dominant species is the well-known $N_b^\bullet$ radical, the generation of which has been already described in Section 5.2. The second signal shows a more complex hyperfine splitting, which has not been described in any of the previous works related to N-doped TiO_2 cited in the present thesis. Spectrum simulations (see Figure A.18, Table A.2) illustrate that two different radicals based on NH_x fragments can lead to such hfs splittings. The most prominent peaks of the weak complex signal can be fitted by assuming an $^\bullet$NH radical[a], which exhibits equal coupling constants for the interaction of the electron spin ($S = 1/2$) to one ^{14}N nucleus with $I = 1$ and one ^{1}H nucleus with $I = 1/2$ (Figure A.18a, green). However, small shoulders in the hfs pattern of the experimental spectrum may indicate the coupling to another ^{1}H nucleus in an $^\bullet NH_2$ group (Figure A.18a, blue) or a mixture of both radicals. Supported by FTIR spectroscopy, some authors attributed XPS peaks at $E_b \approx 400\,eV$ to NH_x species in interstitial position.[247, 249] However, XPS analysis of the reference sample, TiO_2:N-Urea, prepared *via* sol-gel method and urea as nitrogen source revealed exclusively an intense peak at $E_b = 399.5\,eV$ (Table 5.5, Figure A.19, blue), but only one weak EPR signal corresponding to $N_b^\bullet$ species appeared under irradiation (Figure 5.11, pink) and the complex signal of tentative NH_x is missing. In contrast to the catalyst prepared with urea, a broad XPS peak with maxima at 399.1 and 395.7 eV was observed for the Ana:N15-600-5 catalyst (Table 5.5, Figure A.19, green), which can be attributed to at least two different N species. This suggests that the prepa-

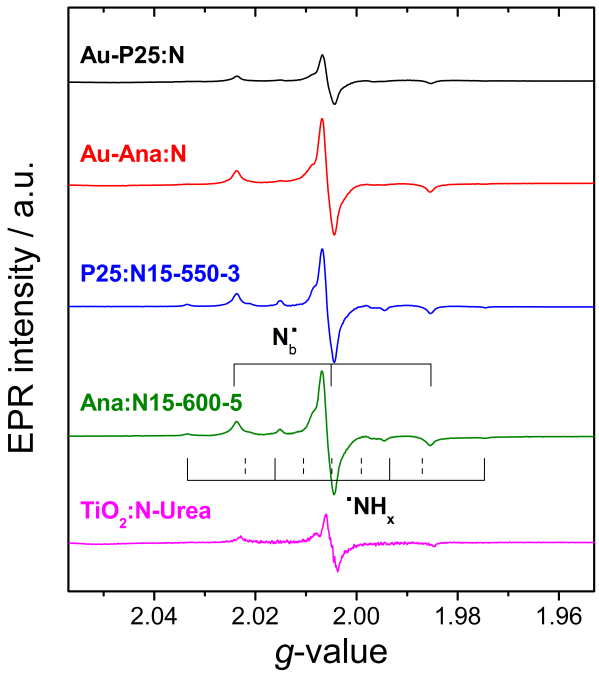

Figure 5.11: EPR spectra of pure and Au-loaded TiO_2:N catalysts under visible-light irradiation (Xe lamp, >420 nm filter) recorded at $T = 90\,K$.

[a]In agreement with common denotations in literature, incorporated N-radical species $N_b^\bullet$ and $^\bullet NH_x$ are considered here without any charges in the radical state.

ration method crucially determines the nature of incorporated N species. Teramura *et al.*[251, 252] previously reported about $^{\bullet}NH_2$ radicals generated under visible light on the surface of NH_3-treated TiO_2, which, however, gave rise to signals with different coupling constants, though the parameters of these surface-NH_2 groups might deviate from those in interstitial or substitutional positions. Unambiguous identification of NH_x species responsible for the observed signal would be only possible by isotope-exchange experiments using either $^{14}ND_3$ or $^{15}NH_3$ as nitrogen source and must be left a open question at present.

These two N-dopant forms, N_b and NH_x, create N $2p$ levels within the TiO_2-band gap, from which electrons can be excited under visible light leading the observed paramagnetic species (see Eq. 5.7). It must be stressed that no Ti^{3+} signal was detected under visible light at $T = 90\,K$, but only these two N-based radicals. This might suggest that the excited N $2p$ electrons are not transferred into the TiO_2-CB. Instead, it may be possible that they are quickly trapped at the adjacent oxygen vacancies. This assumption is supported by the work of Yamanaka *et al.* using femtosecond time-resolved diffuse reflectance spectroscopy.[253] The authors inferred from their experiments that in contrast to irradiation with UV light, visible-light excitation (450 nm) of N-doped TiO_2 led to a quick trapping of the excited N electrons by adjacent oxygen vacancies. The incorporation of two N species at substitutional sites, which is the favored state upon high-temperature-treatment in ammonia,[243] creates one oxygen vacancy in their vicinity (Eq. 5.10). Thus, the trapping of two N electrons in one vacancy, forming diamagnetic F^0 centers (oxygen vacancies filled with two electrons), may be more likely than that of a single electron leading to paramagnetic F^+, which was not observed in the EPR spectra.

At higher temperature, only the $N_b^{\bullet}$ radicals can be detected as seen from the temperature development of the EPR spectrum depicted in Figure A.18b. In order to draw conclusions for the stability and reactivity of this species in the different catalysts, its behavior under reaction-like conditions was analyzed by *in situ* EPR spectroscopy at room temperature with subsequent addition of the reactants water and methanol.

In situ EPR spectroscopy on Au-free TiO_2:N catalysts

For the Ana-based catalyst, N doping led to a more significant enhancement of the catalytic activity under UV-vis light than for P25 (Table 5.5). This finding might be also reflected by the corresponding *in situ* EPR spectra, which are depicted in Figure 5.12 for the Au-free TiO_2:N samples based on Ana (a) and P25 (b). In contrast to P25, the pure Ana support exhibits intrinsic bulk-Ti^{3+} species (see Figure A.20a, black) as already discussed in Section 5.1. This was observed in the dark spectrum of the nitrided Ana:N15-600-5 catalyst as well (Figure 5.12a, black), whereas an additional surface-Ti^{3+} signal at $g = 1.985$ was detected in the dark for P25:N15-550-3 (Figure 5.12b, black), evidently arising from the nitridation

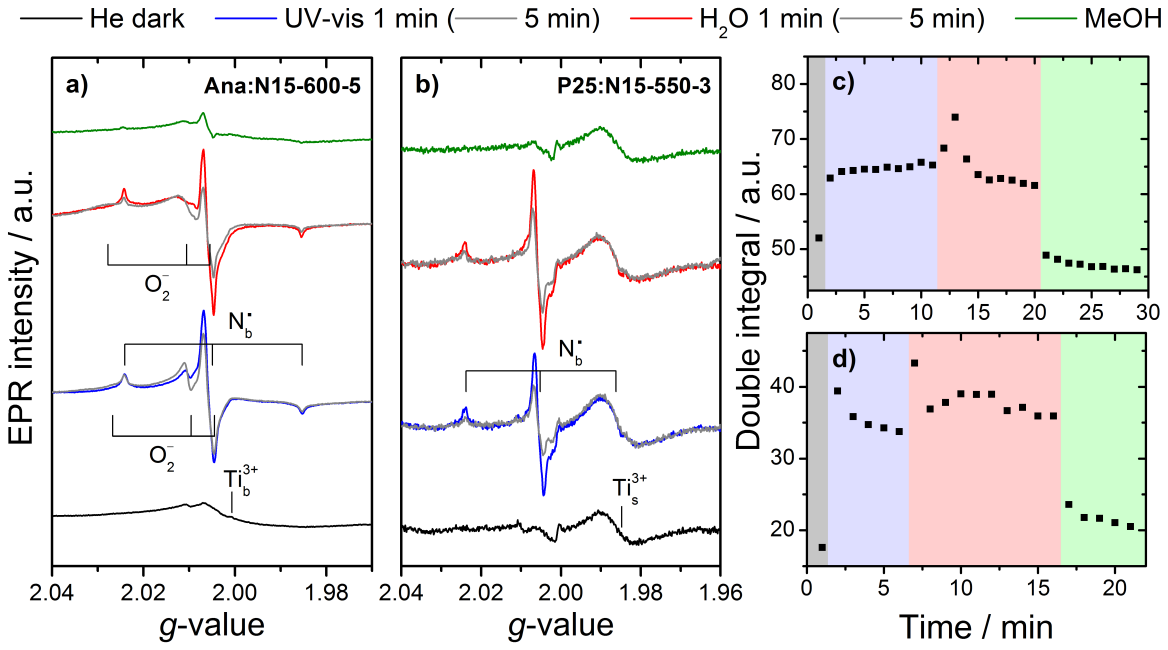

Figure 5.12: *In situ* EPR spectra and the corresponding double integrals of Ana:N15-600-5 (a, c) and P25:N15-550-3 (b, d). The experiment started in the dark under pure helium flow (black), followed by switching to UV-vis light (Xe lamp, no filter, blue) and adding subsequently water (red) and MeOH (green). Gray lines show the spectrum after five minutes under the specific conditions. Spectra were recorded at $T = 290\,\mathrm{K}$.

procedure since N-free P25 barely showed Ti^{3+} (Figure A.20b, black). This suggests that N doping in P25:N15-550-3 was accompanied with surface-TiO_2 reduction, possibly due to the reducing nature of NH_3 gas, which may partially decompose at high temperatures into H_2 and N_2.

For both catalysts, $N_b^\bullet$ signals appear upon UV-vis-light irradiation (Figure 5.12b & d, blue), but quickly lose intensity under ongoing light excitation (gray lines). Since UV-vis light also creates positive holes in the valence band, these reactive holes might further oxidize the visible-light-generated $N_b^\bullet$ radicals, leading to diamagnetic N_b^+:

$$N_b^\bullet \quad + \quad h_{vb}^+ \quad \rightarrow \quad N_b^+ \tag{5.12}$$

Unlike the behavior of P25:N15-550-3, the EPR spectra of Ana:N15-600-5 showed a constant double integral under irradiation with UV-vis light, *i.e.* no loss of excited charge carriers with time (Figure 5.12c, blue). However, signal $N_b^\bullet$ decreased in favor of increasing $O_2^{\bullet-}$ formation (compare blue and gray lines), which indicates the involvement of $N_b^\bullet$ in the generation of the latter. The following reaction might occur by trapping of $N_b^\bullet$ at HO_2^-, formed from surface-hydroxyl radicals similar as discussed in Chapter 4 (Eq. 4.3–4.4):

$$HO_2^- \quad + \quad N_b^\bullet \quad \rightarrow \quad H^+ \quad + \quad O_2^{\bullet-} \quad + \quad N_b^- \tag{5.13}$$

Such a hole-mediated formation of superoxide species has barely been observed for the pure Ana and P25 supports under identical conditions (Figure A.20). Upon addition of water to Ana:N15-600-5, the transformation into $O_2^{\bullet -}$ becomes even faster (Figure 5.12a, red and gray lines), probably due to an increased surface hydroxylation under these conditions, providing a higher number of trapping sites. Thus, Ana:N15-600-5 is apparently more capable of generating surface-bound reactive species than the P25:N15-550-3 catalyst. Both species, $^{\bullet}$OH (further reacting to $O_2^{\bullet -}$ in the absence of other reactants) and $N_b^{\bullet}$, act as oxidation sites for the sacrificial reactant MeOH as seen from the total disappearance of the signals upon adding MeOH (Figure 5.12, green). However, as explained in Chapter 4, the oxidation of MeOH occurs much faster *via* surface-bound hydroxyl radicals. This could explain the stronger activity enhancement for the Ana:N15-600-5 catalyst, because it allows the generation of $^{\bullet}$OH radicals from visible-light-generated $N_b^{\bullet}$ species.

In situ EPR spectroscopy on Au-loaded TiO_2:N catalysts

Loading Au onto Ana:N15-600-5 and P25:N15-550-3 by use of the DP method described in Chapter 4 results in a different development of the *in situ* EPR spectra compared to the Au-free catalysts as shown in Figure 5.13. In both samples, Au-Ana:N (a) and Au-P25:N (b), the $N_b^{\bullet}$ signal decreased much faster under ongoing irradiation compared to

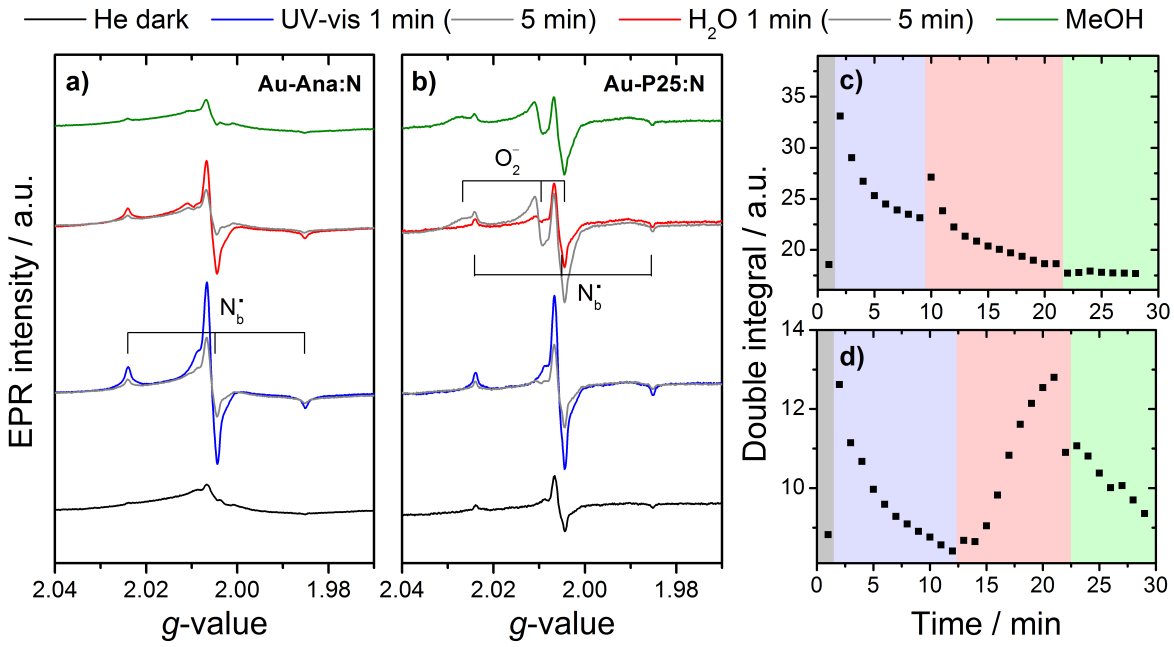

Figure 5.13: *In situ* EPR spectra and the corresponding double integrals of Au-Ana:N (a, c) and Au-P25:N (b, d). The experiment started in the dark under pure helium flow (black), followed by switching to UV-vis light (Xe lamp, no filter, blue) and adding subsequently water (red) and MeOH (green). Gray lines show the spectrum after five minutes under the specific conditions. Spectra were recorded at $T = 290\,\mathrm{K}$.

the Au-free catalysts, but without transformation into superoxide species (Figure 5.13, blue). This behavior might be explained by the longer lifetime and, thus, reactivity of UV-light-generated VB-holes due to the transfer of excited TiO_2 electrons to Au, which might accelerate the process expressed by Eq. 5.12. The slower signal decay in Au-Ana:N compared to Au-P25:N, without formation of new species may, thus, suggest a less efficient charge separation of UV-vis-light-generated holes and electrons in Au-Ana:N. This is in accordance with the catalytic results. Both Au-TiO_2:N catalysts show a loss of photoactivity under UV-vis light (320–500 nm) compared to the undoped Au-TiO_2 samples, AuAna-DP and AuP25-DP (Figure 5.14, blue). This loss was higher for Au-Ana:N (60 %) than for Au-P25:N (45 %). The better performance of Au-P25:N is also illustrated by the appearance of superoxide radicals, $O_2^{\bullet -}$, under addition of water (Figure 5.13b & d, red), which is indicative for the ability to generate highly reactive surface-hydroxyl radicals as discussed above.

It must be stressed that still no H_2 evolution was observed for Au-Ana:N under visible light (400–700 nm), despite the fact that N doping of Ana efficiently increased its light absorption in the visible range, which overlaps with the Au-SPR absorption as seen from Figure A.21. This fact indicates that the visible-light-responding N centers are apparently not able to transfer their electrons into the Au particle. However, this electron transfer is required for an efficient H_2 production since it suppresses the quick recombination of charge carriers. Instead, these electrons are most likely trapped by adjacent oxygen vacancies, whereby their mobility and transfer to Au are limited. This trapping may promote the UV-vis-light activity of metal-free TiO_2:N catalysts (Table 5.5) due to the associated longer lifetimes of charge carriers and an increased visible-light response as seen also for the Hy-An catalyst in the previous section. However, in Au-loaded TiO_2:N catalysts, trapping of visible-light-generated electrons by oxygen vacancies probably results in less reactive Au electrons under UV-vis light compared to the nitrogen-free Au-loaded materials. Since N doping leads to a highly defective surface structure, also less electrons can be transferred from the TiO_2-VB into the CB and finally to Au, leading to a lower amount of produced H_2.

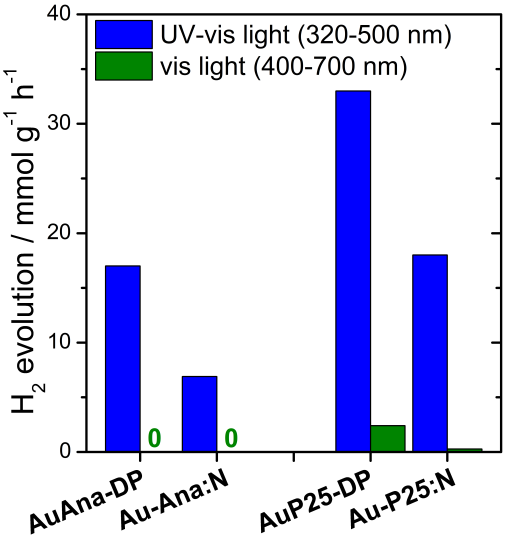

Figure 5.14: Photocatalytic H_2 evolution over Au-loaded TiO_2:N catalysts under UV-vis (blue) and visible light (green) compared to the undoped materials.

5.4 Conclusion

Among the different TiO_2-phase compositions as support material in Au-TiO_2 catalysts, anatase/rutile composites (P25 and Hom) led to the most active catalysts with UV-vis and visible light, which is probably caused by an improved charge-carrier separation due to electron excitation across the anatase/rutile interface in both directions, depending on the irradiation wavelength. Under pure visible light, no H_2 was detected at all for the Au-TiO_2 catalysts based on Ana and Bro. While for visible-light-active Au-TiO_2-DP catalysts based on P25, Hom and Rut, strong EPR signals corresponding to superoxide radicals appeared under UV and visible light, Ana and Bro exhibit intense features of intrinsic bulk-Ti^{3+} defects. This Ti^{3+} accumulation appears to increase the Schottky barrier at the Au/TiO_2 interface (Figure 5.15), presumably due to a variation of the electron affinity. Hence, SPR-excited Au electrons might not possess enough energy to overcome the increased energetic barrier or do not efficiently accumulate in the conduction band to reach the reductive power required for proton reduction.

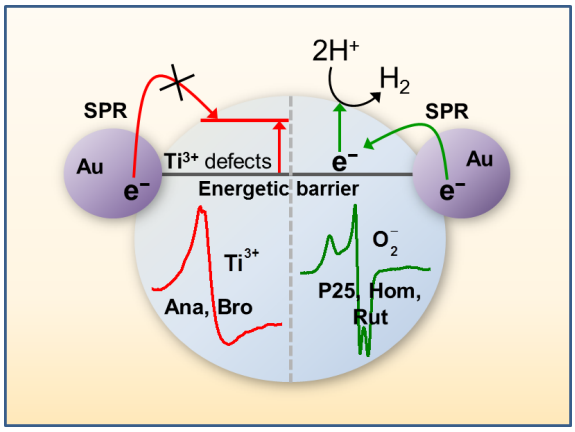

Figure 5.15: SPR-induced visible-light activity was observed in catalysts showing strong superoxide radicals when prepared by the DP method (right). In contrast, visible-light-inactive Ana- and Bro-based Au-TiO_2 gave rise to intense Ti^{3+} signals according to intrinsic defects, which might raise the energetic barrier for electron transfer from Au to TiO_2 by SPR excitation.

Modifying TiO_2 by reduction with H_2 at high pressure led to a significant increase of H_2 evolution from H_2O/MeOH even without Au under simulated solar irradiation. However, *in situ* EPR spectroscopic investigations provide evidence that the enhanced H_2 evolution might be not only caused by an increased number of intrinsic TiO_2 defects created upon the reduction treatment, but could also arise from additional extrinsic defects formed simultaneously by nitrogen incorporation. The nitrogen source appears to be nitric oxide molecules enclosed in microvoids of the material during the catalyst synthesis, which give rise to a characteristic EPR signal at low temperature in the dark. While for the untreated sample, no new paramagnetic species were formed under visible light, the activated Hy-An catalyst showed a visible-light-active paramagnetic center characteristic for lattice-incorporated $N_b^{\bullet}$ species along with Ti^{3+} and $O^{\bullet-}$ radical formation. The $N_b^{\bullet}$ radical was described to be one major origin for the visible-light activity of TiO_2:N catalysts[227] and might therefore contribute to the enhanced H_2 evolution over Hy-An.

On the other side, targeted N doping of TiO_2 by annealing in NH_3 led to the incorporation of two different N species. Besides the well-known EPR signal of $N_b^\bullet$ species, a more complex EPR signal was also observed under visible light, which has not yet been described in literature. Spectrum simulations helped to attribute it either to $^\bullet NH$ or $^\bullet NH_2$ groups, the existence of which in N-doped TiO_2 has been also suggested by previous XPS and FTIR studies. The EPR data indicate that both species contribute to the enhanced visible-light response of the TiO_2:N catalysts. This is in accordance with the slightly improved photoactivity under UV-vis light (320–500 nm) of the metal-free TiO_2:N catalysts compared to the pristine materials, probably due to increased absorption in the visible range. The *in situ* EPR studies demonstrate that the ability to convert these visible-light-generated charges into reactive surface sites such as OH radicals might be especially favorable to obtain higher photoactivities. In contrast, Au-TiO_2:N catalysts were significantly less active under the same conditions in comparison to undoped Au-TiO_2. Furthermore, no enhancement in H_2 evolution under pure visible light (400–700 nm) was observed for the Au-TiO_2:N samples, which is in accordance with observations in other studies.[254] Hence, against expectation and some recent mechanistic models,[227,228] the visible-light-active N species are probably not capable of injecting electrons efficiently into the conduction band of TiO_2, from which they could be quickly transferred to the Au NPs (Figure 5.16). Instead they are likely to be trapped and stabilized by oxygen vacancies in close vicinity. Due to the defective surface structure of the TiO_2:N support, UV-light-induced excitations of VB-electrons, needed for efficient H_2 generation by subsequent electron transfer to Au, are probably less compared to those in Au-TiO_2. This might explain the strongly decreased activity under UV-vis light of Au-TiO_2:N compared to their undoped counterparts.

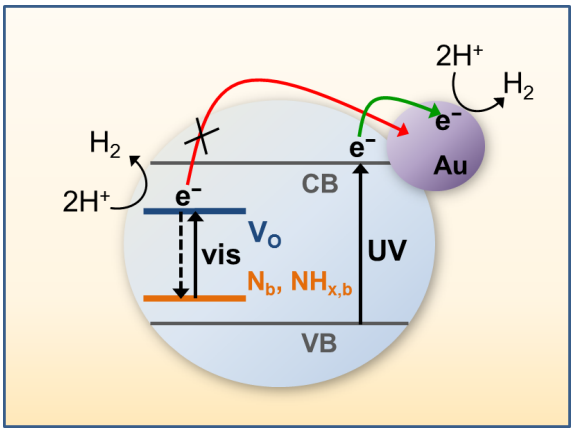

Figure 5.16: (Au-)TiO_2:N catalysts show increased visible-light absorption due to the formation of certain incorporated N species, forming localized states above the TiO_2-VB. However, electrons excited from these states are probably quickly trapped at adjacent oxygen vacancies rather than being transferred to Au NPs. While this trapping may contribute to the enhanced photoactivity of the metal-free TiO_2:N catalysts, a strongly decreased H_2 evolution was detected for Au-TiO_2:N compared to their undoped counterparts, which is likely due to a less effective interband excitation.

6 Effect of metal composition on the activity of Cu-based photocatalysts

The strong impact of the support structure on the photoactivity of Au-loaded semiconductors has been elucidated in Chapter 5. On the other hand, H_2-evolution rates should be crucially governed by the composition of the plasmonic metal component as well. As pointed out above, most works, dealing with plasmonic photocatalysts, focus on Au-based materials. This is probably due to its high stability and work function, which correlates with the height of the Schottky barrier at the metal/support interface.[255] Other coinage metals exhibiting SPR phenomena in the visible region as well, such as Ag and Cu, were rarely studied for that purpose, though their application would be a cheap alternative. In view of ecological and economic aspects, this chapter addresses the influence of metal composition on the photoactivity in hydrogen production. Especially Cu-based mono- and bimetallic catalysts with low metal contents were investigated in terms of their performance under visible and UV-vis light. Since the active species of $Cu(O_x)$-loaded semiconductors in photocatalytic reactions is controversially discussed due to its fast oxidation under ambient conditions,[256–261] in situ spectroscopic tools (XANES, UV-vis, EPR) were applied to shine light on the catalyst's specific behavior under reaction conditions. Moreover, structure-reactivity relationships were established by varying the metal-deposition techniques, which affected the structural composition of the resulting photocatalysts. This has been carried out for pure Cu-loaded TiO_2 in one part of the chapter, while the other part demonstrates how the behavior of Cu species changes upon the introduction of a second metal, i.e. Ag or Au.

6.1 Catalyst characterization and performance

All Cu-based mono- and bimetallic (Cu/Ag or Cu/Au) photocatalysts were prepared using P25 as TiO_2 support material. For exploring to what extend the deposition method also affects the performance of Cu-loaded TiO_2, two different methods were applied: impregnation (Cu-IM) and reductive precipitation (Cu-RP) as described in Section 2.1.2. Additionally, by using a stepwise reductive precipitation, bimetallic catalysts consisting of Cu and Ag (Cu/Ag-SP) or Cu and Au (Cu/Au-SP) were prepared. For comparison, a Cu/Au-CP mixed catalyst was synthesized through a simultaneous "co-precipitation" procedure. Table 6.1 summarizes the structural characteristics and photocatalytic performance in H_2 generation from H_2O/MeOH mixtures. Both pure Cu-loaded photocatalysts showed simi-

Table 6.1: Catalytic activities, metal contents and XPS data of mono- and bimetallic Cu-based TiO_2 catalysts.

Catalyst	r_{H_2}[a] / mmol g^{-1} h^{-1} UV-vis	vis	Cu(/Metal)-wt.-% (ICP-OES)	Cu(/Metal)-at.-% (XPS)	E_b Cu 2p / eV	Auger param. α'(Cu) / eV
Cu-IM	5.2	0.19	1.1	2.7	932.7	1848.2
Cu-RP	6.3	0.53	0.6	2.7	932.6	1848.1
Cu/Ag-SP	6.7	0.28	1.0/0.2[b]	3.2/0.2	932.7	1847.9
Cu/Au-SP	11	0.48	0.2/0.2	3.9/0.1	932.7	1848.3
Cu/Au-CP	7.5	1.6	0.2/0.2	1.2/0.1	932.5	1847.0

[a]Conditions: 25 mg cat., 10 mL H_2O/MeOH (1:1), 2.5 W output Lumatec irradiation.
[b]Nominal amount, Ag could not be determined by ICP-OES due to experimental reasons.

larly high H_2 productions under UV-vis light (320–500 nm), *i.e.* 5.2 and 6.3 mmol g^{-1} h^{-1} for Cu-IM and Cu-RP, respectively (Table 1). Given that only 60 % of the desired Cu content was yielded for Cu-RP, this sample is catalytically much more efficient than Cu-IM with 1.1 wt.-% Cu. Moreover, by excitation with visible light (400–700 nm) catalyst Cu-RP showed a markedly higher photoactivity compared to Cu-IM. Structural characteristics of these catalysts explaining their individual performance under both excitation wavelengths are discussed in Section 6.2.

The stepwise preparation of bimetallic catalysts led only to a significant positive effect under irradiation with UV-vis light for Cu/Au-SP, whereas the introduction of Ag barely affected the UV-vis activity (Table 6.1). Under visible light, however, both bimetallic SP catalysts exhibited a reduced H_2 evolution compared to the monometallic Cu-RP sample. In contrast, the co-precipitated Cu/Au-CP catalyst evolved more than three times the volume of H_2 as observed for Cu-RP (1.6 mmol g^{-1} h^{-1}, Table 6.1). Since always the same support material (P25) was used, which exhibits an absorption edge at *ca.* 400 nm (see Chapter 5), it seems not likely that the activities under visible light (400–70 nm) solely result from

a residual support absorption as proposed by Wei *et al.* for Au-TiO_2 catalysts.[132] Then one would expect more or less the same ratio between the activities under UV-vis (320–500 nm) and visible light. Therefore, other effects must be considered determining the rate of H_2 generation under visible light over these Cu-based bimetallic TiO_2 photocatalysts. These characteristics were analyzed in more detail by a combined *in situ* spectroscopic approach presented in Section 6.3. In general, without any protection of the reduced Cu particles, *e.g.* by graphene shells or other organic ligands,[262, 263] reduced Cu^0 NPs are quickly oxidized in ambient atmosphere and usually have to be activated in a reductive environment prior to the catalytic reaction.[264] However, the catalysts investigated in the present thesis showed H_2 production during the catalytic tests in argon atmosphere without an additional activation procedure.

6.2 *In situ* investigation of differently prepared monometallic Cu-TiO_2 catalysts

XPS analysis of the as-synthesized samples revealed a similar Cu surface coverage of the pure Cu catalysts, Cu-IM and Cu-RP, with a similar Cu $2p$ binding energy at around 932.7 eV (Table 6.1). This value corresponds rather to Cu^+ than to the fully oxidized Cu^{2+} state.[257, 265] This is, however, not in agreement with the UV-vis absorption bands of the as-synthesized catalysts (Figure 6.1, black) showing a typical absorbance at high wavelengths (>600 nm) corresponding to the $d \rightarrow d$ transitions of Cu^{2+}. As proposed by Irie *et al.*,[266] it might be plausible that a reduction of the small Cu(II)-oxide/hydroxide units on TiO_2 occurred upon introduction of the catalysts into the high-vacuum XPS chamber, whereby Cu_2O was formed at the surface, while probably mainly Cu^{2+} remained in the particle volume. Cu-oxide or Cu-hydroxide-loaded TiO_2 was previously reported to be active for H_2 generation from H_2O/MeOH under UV-vis light, which was proposed to result from an effective charge separation by a UV-light-induced electron transfer from TiO_2 e.g. into the CuO phase,[256] the conduction band of which is more positive than that of TiO_2. However, after addition of H_2O/MeOH, the Cu^{2+} absorption bands at wavelengths >600 nm were less prominent compared to the absorption background for both monometallic Cu catalysts investigated in the present study (Figure 6.1, red). For Cu-RP even a clear SPR-absorption band appeared with a maximum at 580 nm typical for Cu^0 NPs. In the Cu-IM sample, a weak Cu-SPR absorption band only appeared upon UV-light irradiation (Figure 6.1a, blue). Thus, in both samples, Cu-IM and Cu-RP, the H_2-evolution sites under UV light are likely the reduced Cu^0 particles, which are quickly formed *in situ*. Consequently, the inherent SPR properties of Cu^0 particles might be crucial for the visible-light performance of Cu-based catalysts as well. This is suggested by the fact that the

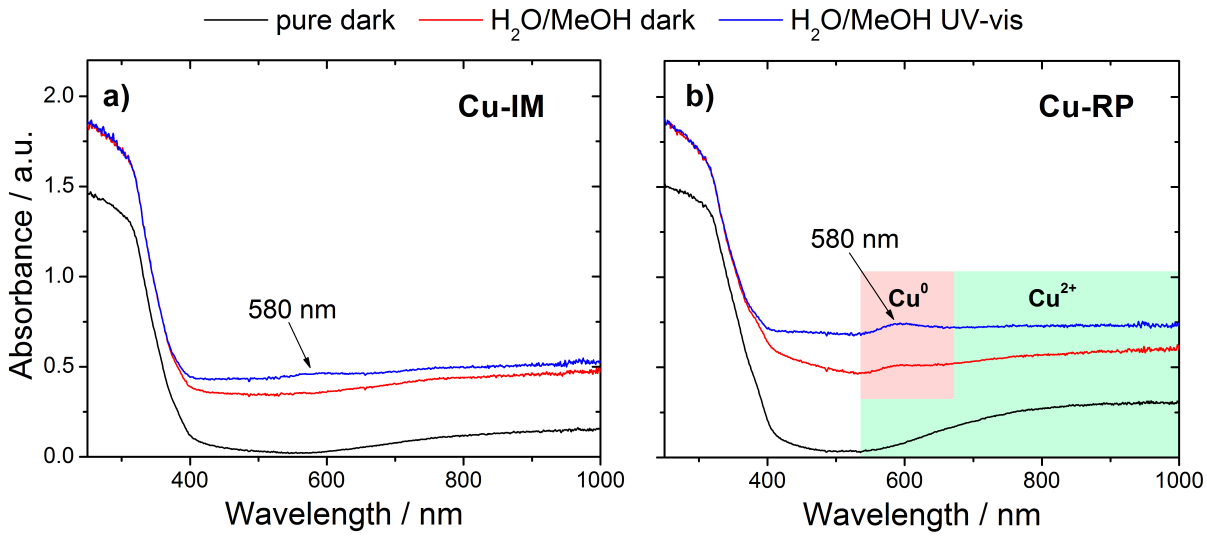

Figure 6.1: *In situ* UV-vis absorption spectra of the monometallic Cu-based catalysts prepared by a) impregnation (Cu-IM) and b) reductive precipitation (Cu-RP) in the as-synthesized state (black), in H_2O/MeOH (red) and under subsequent UV-vis-light irradiation for five minutes (blue). The typical absorption regions of Cu^{2+}, Cu^{+} and Cu^{0} are marked in green, yellow and red, respectively. Measurements in H_2O/MeOH led to an increased absorption background compared to those in air.

sole addition of H_2O/MeOH (without any irradiation) provoked no clear Cu^0-SPR-band formation for the Cu-IM catalyst, unlike the behavior of Cu-RP. This might be a reason for its poor activity under visible light. The different reactivity of the two investigated Cu catalysts is very likely due to different structural environments of the oxidized Cu(II) clusters in these two catalysts caused by the specific synthesis conditions. In fact, TEM analysis of the Cu-IM sample revealed equally distributed Cu species on the TiO_2 support without clear particle formation (Figure A.23), whereas catalyst Cu-RP contains additional small Cu agglomerations with diameters of 2–4 nm (Figure A.24). Hence, by using the IM method for Cu-TiO_2 preparation, an efficient *in situ* formation of Cu^0 agglomerates with optical properties inevitable for visible-light H_2 generation is apparently inhibited. In contrast, the pre-reduction with $NaBH_4$ during the RP method initially formed larger Cu units which more easily re-built their specific SPR-absorption properties upon addition of the electron-donating H_2O/MeOH mixture.

The *in situ* EPR spectra of the monometallic Cu-TiO_2 catalysts are depicted in Figure 6.2. They contain characteristic signals attributed to Cu^{2+}, which is paramagnetic due to one unpaired d electron of the $3d^9$ configuration ($S = 1/2$). The spectra exhibit poorly defined features of anisotropic hfs splitting corresponding to the coupling of the electron spin to the ^{63}Cu (natural abundance 69.09 %) and ^{65}Cu (natural abundance 30.91 %) nuclei with $I = 3/2$. Based on spectrum analysis for Cu/Au-SP (Figure A.27), different Cu^{2+} species can be also distinguished for the monometallic samples. Signal A exhibits g-values $g_{\parallel} = 2.38$ and $g_{\perp} = 2.05$, which are close to those that have been previously ascribed to Cu

single sites partly occupying Ti^{4+} vacancies at the TiO_2 surface.[267] Comparison of the EPR spectra in H_2O/MeOH (Figure 6.2, red) reveals a lower resolution of the respective hfs splitting ($A_{\parallel} \approx 80$ G) in Cu-IM, which suggests a larger dipolar interaction between the different Cu^{2+} sites leading to a broadening of the hfs lines. This is consistent with the observation of highly dispersed Cu^{2+} species in Cu-IM. In contrast, the few isolated Cu sites in Cu-RP might interact less with the larger Cu^{2+} units due to the longer distances between these different Cu^{2+} species. Moreover, as indicated by the *in situ* UV-vis measurements above (Figure 6.1) and the *in situ* XANES data shown below, Cu-RP quickly forms reduced SPR-active NPs by adding H_2O/MeOH. Thus, for Cu-RP suspended in H_2O/MeOH, the initial amount of Cu^{2+} relative to the reduced forms, Cu^{+} and Cu^{0}, should be lower than for Cu-IM. This means that less long-range dipolar interactions should occur in Cu-RP under these conditions, explaining the higher resolution of the hfs splitting.

The second Cu^{2+} species in both Cu-TiO_2 catalysts (signal B) with an estimated $g_{\parallel}$ at 2.25 shows a more pronounced line broadening, which is due to strong dipolar interactions between Cu^{2+} ions in oxidized Cu clusters.[267] This kind of Cu species constitutes the main part in both spectra. Its intensity, however, decreases upon irradiation with visible (Figure 6.2, green) and UV-vis light (blue). This light-induced reduction of Cu^{2+} occurred faster in Cu-IM (Figure 6.2, bottom inset), which might be due to the relatively higher initial concentration of non-reduced Cu^{2+} clusters in Cu-IM after addition of H_2O/MeOH compared to Cu-RP. The line shape of Cu-RP in H_2O/ MeOH indicates that less Cu^{2+} ions in the Cu clusters are available for reduction.

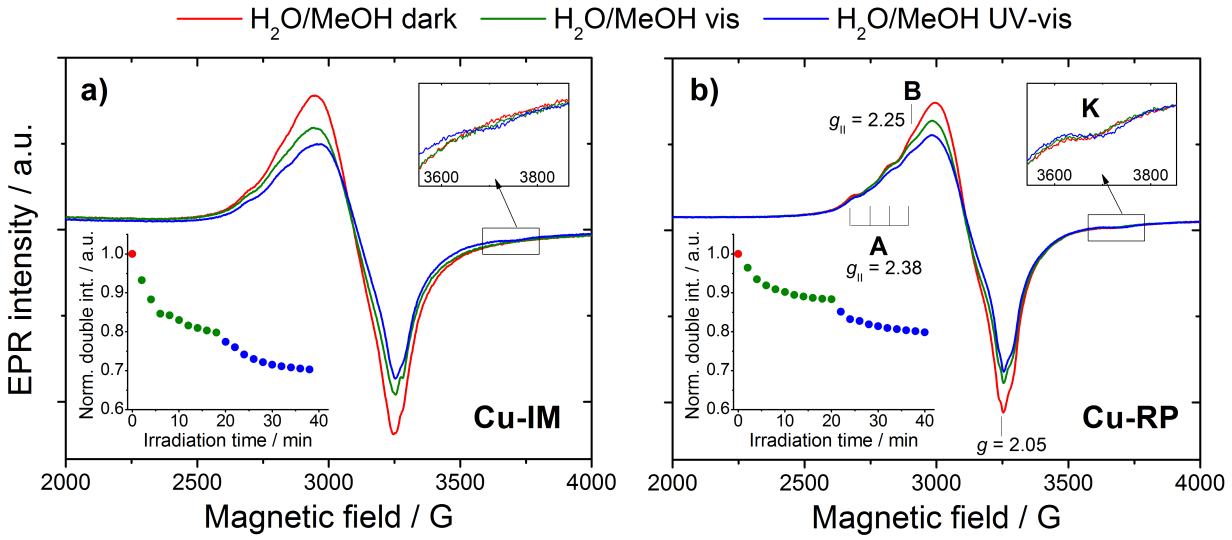

Figure 6.2: *In situ* EPR spectra of Cu-IM (a) and Cu-RP (b) in H_2O/MeOH (red) and under subsequent irradiation with visible (green) and UV-vis light (blue). In the spectra of Cu-RP, a small high-field feature at 3700 G appeared upon addition of H_2O/MeOH (top inset in (b)), which was only poorly observed for Cu-IM under UV-vis light. The bottom insets show the development of the normalized double integrals of the spectra from catalysts in H_2O/MeOH upon irradiation.

Interestingly, a new signal feature clearly appeared in the high-field region (3700 G) of the spectrum of Cu-RP after introduction of H_2O/MeOH, which was poorly observed, too, in Cu-IM upon irradiation with UV-vis light (Figure 6.2, top inset). From more detailed spectrum analysis of the Cu/Au-SP catalyst discussed in Figure A.27, this feature most likely arises from Cu^{2+} dimers (signal K).[268–270] It seems that these specific Cu-dimer species are either formed or appear in the EPR spectrum during the Cu^{2+} reduction to Cu^0 and stay stable along with the reduced Cu sites. For Cu in cerium oxide, such Cu^{2+} dimers were described to be localized at Ce^{4+} vacancies with oxygen as bridging units.[270] Hence, most likely these Cu^{2+} dimers are stabilized against reduction due to their incorporation into the TiO_2 lattice. The ongoing reduction of the surrounding oxidic Cu particles might weaken the long-range dipolar interaction between the different Cu^{2+} centers, so that the EPR signal of this dimer species becomes better resolved. In agreement with the above discussed results of UV-vis spectroscopy, a much easier reduction of the Cu species in Cu-RP is probably suggested by the early appearance of the Cu^{2+} dimers in the EPR spectrum of Cu-RP in H_2O/MeOH without any irradiation. The Cu^{2+} reduction might be facilitated due to the pre-agglomeration of small Cu units by reduction with $NaBH_4$ in the RP procedure, whereas the highly dispersed Cu oxide species in Cu-IM need to be treated with UV light for reduction, which then occurs probably mediated by TiO_2.

6.3 *In situ* spectroscopy on bimetallic Cu-based catalysts

In order to confirm that facilitated changes of the oxidation state in Cu-RP under reaction conditions are indeed essential for its improved visible-light activity, *in situ* XANES

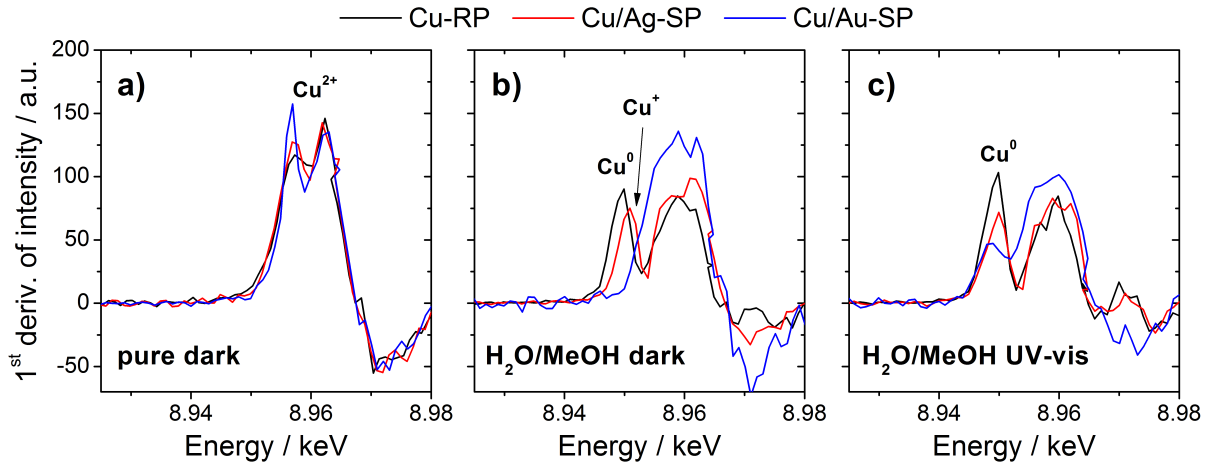

Figure 6.3: *In situ* XANES spectra at the Cu K-edge of monometallic (black: Cu-RP) and stepwise prepared bimetallic (red: Cu/Ag-SP, blue: Cu/Au-SP) catalysts a) as synthesized, b) after addition of H_2O/MeOH and c) under subsequent irradiation with UV-vis light. Depicted are the first derivatives of the absorption spectra.

measurements at the Cu K-edge were conducted on Cu-RP in comparison to the bimetallic stepwise prepared catalysts Cu/Ag-SP and Cu/Au-SP, which both showed a lower photocatalytic activity under visible light (Table 6.1). For a more precise distinction of the signal positions, Figure 6.3 displays the first derivative of the XANES spectra of the catalysts in the as-synthesized state (a), after addition of H_2O/MeOH (b) as well as under subsequent irradiation with UV-vis light (c). The spectra of Cu-RP (black) confirm that a fast reduction of Cu^{2+} to Cu^0 occurred upon adding H_2O/MeOH as discussed in Section 6.2. This Cu^{2+} reduction was retarded in case of the bimetallic catalysts Cu/Ag-SP and Cu/Au-SP. Apparently, the higher electron affinity of Au and Ag compared to Cu resulted in a lower reducibility of the Cu^{2+} species in the stepwise prepared bimetallic catalysts, since after H_2O/MeOH addition, no change in the Cu-oxidation state for Cu/Au-SP was observed, and only Cu^+ was formed in Cu/Ag-SP under the same conditions. However, the *in situ* Cu^+ formation was not accompanied with improved H_2 generation under visible light over Cu/Ag-SP (Table 6.1), although Cu_2O is a visible-light absorber.[261] This suggests that the Cu^0 state is the most reactive Cu species also for H_2 generation under visible light, probably due to its SPR properties.

Interestingly, the bimetallic Cu/Au-CP catalyst prepared by co-precipitation exhibited a strongly enhanced visible-light activity compared to Cu-RP (Table 6.1). This was not observed for Cu/Ag-SP and Cu/Au-SP, although the metal content of the latter was similar to that in Cu/Au-CP. Thus, different optical absorption properties resulting from structural differences are expected for the simultaneously precipitated sample compared to the stepwise prepared catalysts. The *in situ* UV-vis spectra of the bimetallic catalysts are shown in Figure 6.4. The spectra of the as-synthesized samples (black) contain the typical

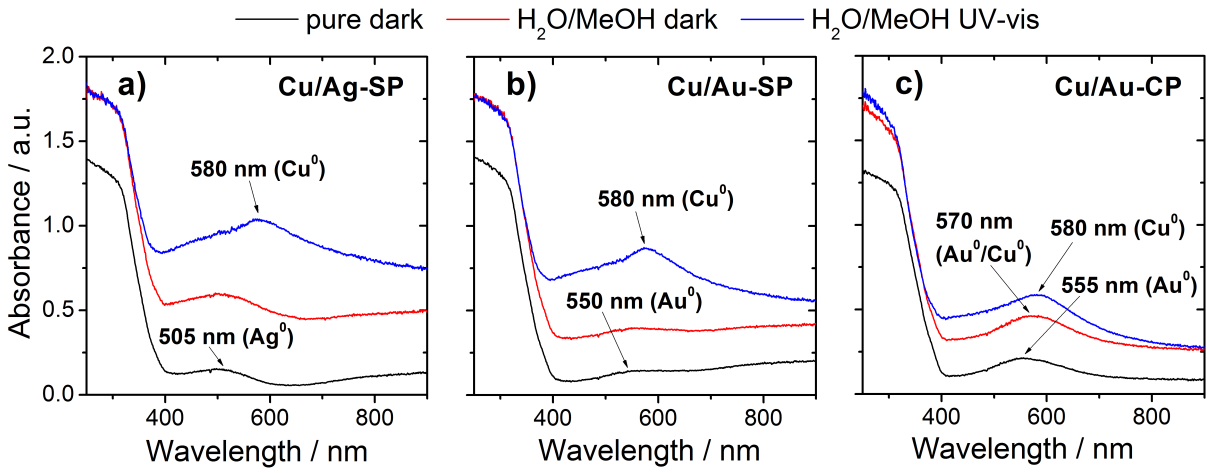

Figure 6.4: *In situ* UV-vis spectra of bimetallic Cu/Ag-SP (a), Cu/Au-SP (b) and Cu/Au-CP (c) as prepared (black), suspended in H_2O/MeOH (red) and under subsequent irradiation with UV-vis light (blue).

SPR-absorption bands of Ag (Figure 6.4a, $\lambda_{max} = 505\,nm$) and Au nanoparticles (Figure 6.4b & c, $\lambda_{max} = 550–555\,nm$). Upon addition of H_2O/MeOH (red), no significant change in absorption was observed for Cu/Au-SP and Cu/Ag-SP, except a small increase of the Ag-SPR absorption for the latter catalyst, indicating a reduction of partially oxidized Ag particles. In contrast, under the same conditions a clear red shift of the SPR-absorption maximum from 555 to 570 nm was detected for Cu/Au-CP (Figure 6.4c, red), suggesting an additional contribution of Cu^0 species to the SPR absorption being characteristic for Cu/Au-mixed particles.[271] Under subsequent irradiation with UV-vis light (blue), the SPR bands of the stepwise prepared samples, Cu/Ag-SP and Cu/Au-SP, show contributions of reduced Cu^0 as well.

6.3.1 Structure-reactivity relationships in Cu/Au-TiO_2 catalysts

The different behavior of Cu/Au-SP and Cu/Au-CP suggests that the precipitation sequence (stepwise or simultaneous) of Cu and Au plays a crucial role in determining specific structural characteristics for Cu/Au catalysts. These features obviously lead either to a strong enhancement of H_2 evolution under visible light (Cu/Au-CP) or only to a very good performance under predominant UV-light radiation (Cu/Au-SP, Table 6.1). Therefore, detailed structural and spectroscopic investigations have been performed on both Cu/Au catalysts in order to obtain information about structure-reactivity relationships in photocatalytic hydrogen generation over Cu/Au-TiO_2 catalysts. TEM analysis revealed highly dispersed Cu particles with mean Cu diameters of 1–2 nm for the stepwise prepared Cu/Au-SP catalysts (Figure 6.5a) similar to that of monometallic Cu-RP. As derived from EDX analysis of the Cu/Au-SP catalyst (Figure A.25), the Au particles of slightly larger size (2–5 nm) are separated from the Cu domains. The opposite was observed for the strongly visible-light-active Cu/Au-CP catalyst, in which Cu and Au were precipitated simultaneously forming mixed-metal particles mainly of sizes from 3–8 nm (Figure 6.5b, Figure A.26). Under ambient air, however, the Cu^0 component in such mixed-metal particles is probably quickly oxidized and re-appeared only under reaction conditions as seen from the shift of the SPR absorption maximum for Cu/Au-CP (Figure 6.4c, red).[272] Additionally, the XPS Auger parameters indicate a different structural environment of the Cu species in both samples (Table 6.1). Its lower value for Cu/Au-CP suggests a Cu species with a component of higher electron affinity in its vicinity, which is probably caused by the close proximity to Au in the mixed Cu/Au particles.

It seems unlikely that the difference in Au-particle sizes for Cu/Au-SP and Cu/Au-CP is the only crucial property determining the performance under visible light, although Wei *et al.* showed that larger Au particles were catalytically more active under visible light than smaller ones.[132] The Au size in both Cu/Au catalysts is still far below that of

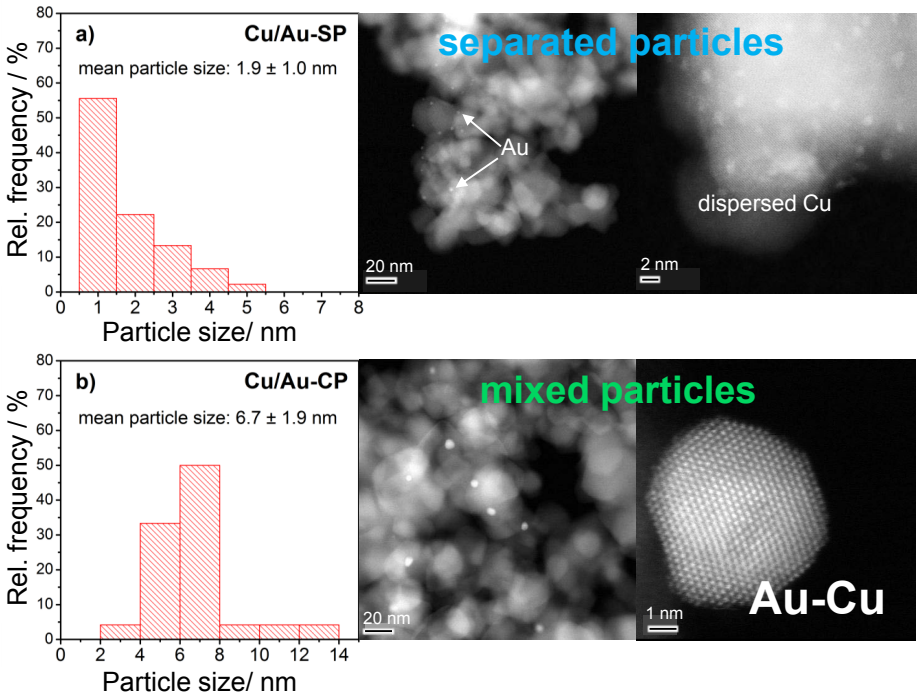

Figure 6.5: Particle-size distributions and HR-TEM images of Cu/Au-SP (a) and Cu/Au-CP (b).

the active catalysts (37 nm) in the study of Wei *et al.* As proven in Chapter 4 by using wavelength-dependent *in situ* EPR spectroscopy, not only the Au-intraband (SPR) transitions contribute to the activity of Au-TiO_2 catalysts under visible light, but also and more effectively $d \rightarrow sp$ interband excitations of electrons in the reduced nanoparticles. The latter are not dependent on the size and begin at the interband gap of $E_g = 2.5$ eV,[273] corresponding to 495 nm for Au. It was further shown above that there might be a synergistic effect between the overlap of both optical transitions, *i.e.* inter- and intraband excitations, which reached a maximum in the region of 400–500 nm for Au. It is therefore probable that especially light of this energy strongly contributes to the photoactivity of Au-catalysts. Working with optical filters >435 nm as done by Wei *et al.* might suppress this important effect. In case of Cu NPs, the plasmon absorption is in resonance with the interband transitions at energies *ca.* 2.1 eV.[273, 274] Hence, reaching the reduced state of Cu under reaction conditions is highly desired and of particular importance to utilize these absorption processes for converting high-wavelength light into chemical energy.

The two Cu/Au catalysts also exhibit different developments of the *in situ* EPR spectra depicted in Figure 6.6. The signal line width of Cu/Au-CP in H_2O/MeOH (red) is smaller than that of Cu/Au-SP, indicating less dipolar interactions between Cu^{2+} centers in Cu/Au-CP. This could be due to less remaining oxidized Cu species after addition of H_2O/MeOH, which is supported by the lower signal intensity in Cu/Au-CP as well. Moreover, the above mentioned Cu^{2+}-dimer signal already became visible for Cu/Au-CP in H_2O/MeOH

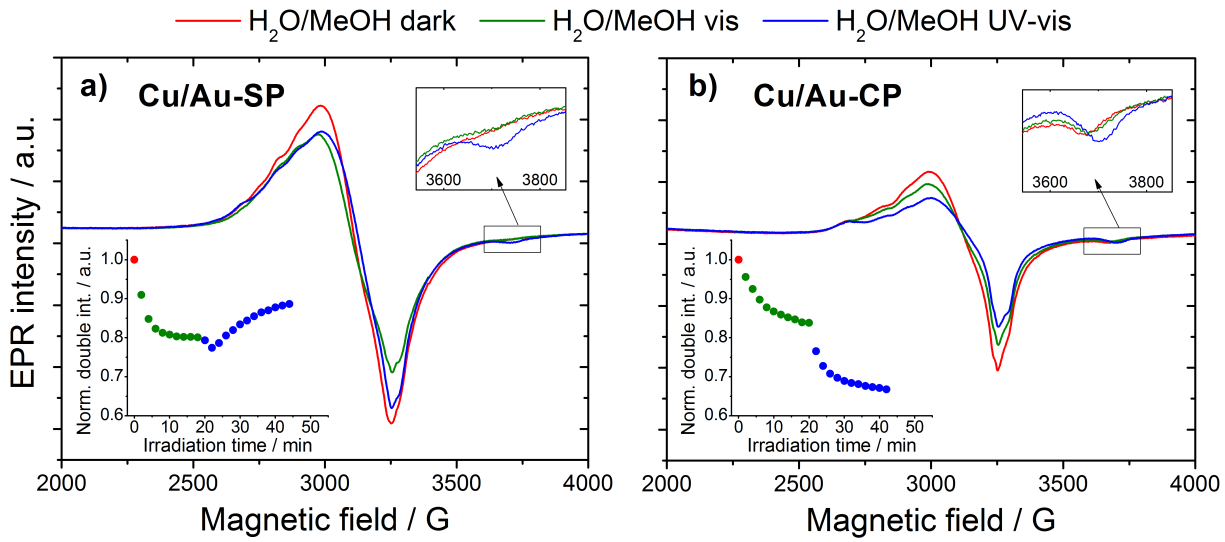

Figure 6.6: *In situ* EPR spectra of Cu/Au-SP (a) and Cu/Au-CP (b) in H_2O/MeOH (red) and under subsequent irradiation with visible (green) and UV-vis light (blue). The bottom insets show the development of the normalized double integrals of the spectra from catalysts treated with H_2O/MeOH upon irradiation. Contrary to Cu/Au-CP, the Cu^{2+}-dimer signal (enlarged top inset) in Cu/Au-SP appeared only under irradiation with UV-vis light, leading to an increase of the double integral (blue).

without any further irradiation, which is caused by a decreasing interaction with other Cu^{2+} in the surrounding, probably due to a lower number of remaining Cu^{2+} species. This is in accordance with the UV-vis results from Figure 6.4c, which showed that partly Cu^0 was formed by adding the reactants. It probably also explains the observation that the decrease of the Cu^{2+}-EPR signal under visible-light irradiation (Figure 6.6, green) was slower for Cu/Au-CP compared to Cu/Au-SP. In Cu/Au-SP, initially more Cu^{2+} species remained after addition of H_2O/MeOH, so that their light-induced reduction might occur faster. However, the Cu^{2+} reduction under visible light was poorly accompanied by the appearance of Cu^{2+} dimers in the EPR spectrum. Their characteristic features (enlarged top inset) were only clearly detectable under UV-vis light (Figure 6.6a, blue), which caused an increase of the EPR double integral under these conditions.

For directly monitoring the different changes of the Cu-oxidation state, *in situ* XANES measurements were conducted on both Cu/Au catalysts also under visible-light irradiation (Figure 6.7). Addition of H_2O/MeOH did not affect the position of the absorption edge in both catalysts (red). Subsequent visible-light irradiation (green lines), however, led to Cu^+ in the poorly visible-light-active Cu/Au-SP catalyst, while already SPR-active Cu^0 species were formed in the Cu/Au-CP catalyst. Hence, only these Cu^0 units that are in close contact to the electron-affine Au, *i.e.* in the Cu/Au-CP catalyst, are finally reduced to Cu^0 under visible light, probably under assistance of the electron-donating MeOH. The early Cu^0 formation in the mixed particles of Cu/Au-CP might cause its improved H_2 generation under pure visible light. This once again verifies that the plasmonic reduced

state of coinage metals is crucial for proton reduction under visible light rather than the oxidized Cu species. In contrast, for the separated Cu and Au particles in Cu/Au-SP, visible light is not sufficient for the reduction to Cu^0 since the electron affinity of Au probably attracts the electrons provided by the electron donator MeOH rather than the less noble Cu. The reduction to Cu^0 under UV-vis light (Figure 6.7, blue) then occurs by electron transfer to the Cu_2O or CuO units mediated by TiO_2, whereby well-dispersed Cu^0 particles are generated in Cu/Au-SP. This high dispersion of very small metal centers all over the support is especially beneficial for UV-light-mediated H_2 generation, since then the TiO_2-VB electrons are excited and transferred to the metal particles. The smaller the metal particles, the more active sites can trap electrons and reduce protons. This was confirmed by the markedly higher H_2 rate of Cu/Au-SP under UV-vis light.

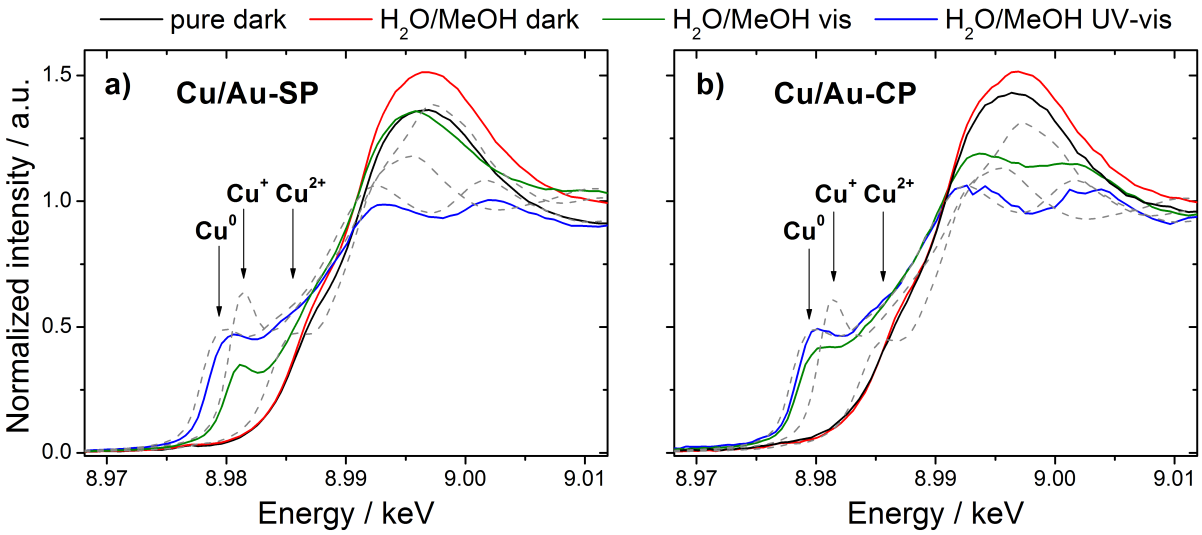

Figure 6.7: *In situ* XANES spectra of Cu/Au-SP (a) and Cu/Au-CP (b) as prepared (black), in H_2O/MeOH (red) and under subsequent irradiation with visible (green) and UV-vis light (blue). Reference spectra from CuO, Cu_2O and Cu foil are shown as gray dashed lines.

6.4 Conclusion

This chapter on the one hand demonstrated that Cu-based supported metal catalysts are also active in light-driven H_2 generation from H_2O/MeOH. However, the capability of generating active reduced Cu^0 particles under reaction conditions depends on the chosen Cu-deposition method. Impregnation led widely to finely spread oxidized Cu species, which were not sufficiently reduced to visible-light-active Cu^0 neither in H_2O/MeOH, nor under subsequent irradiation with visible light. Significant Cu^0 formation along with H_2 production occurred only in Cu-IM under UV light mediated by TiO_2. In contrast, a synthesis involving a pre-reduction step like the RP method led to a fast formation of SPR-active Cu^0

particles in the presence of electron-donating H_2O/MeOH even without irradiation. These Cu^0 particles act as active sites for H_2 evolution under visible- and UV-vis-light irradiation. Their inherent SPR properties might be also responsible for the enhanced photoactivity of Cu-RP under visible light (400–700 nm filter). It cannot be excluded that the small UV-light residue, still passing the visible-light filter, contributes to the corresponding H_2 evolution. However, this should not be the major reason for the catalytic activity, since then the ratio between the activities under visible and UV-vis light would be similar for all catalysts.

This applies to the bimetallic catalysts as well. A stepwise reductive precipitation of Cu and Au (or Ag) did not lead to an improved H_2 production under visible light, but to a strongly increased activity for Cu/Au-SP under UV-vis light. In contrast, simultaneous precipitation of Cu and Au led to a highly visible-light-active catalyst, though it exhibited a moderate activity under 320–500 nm excitation. It was inferred from TEM analysis combined with *in situ* UV-vis, EPR and XANES spectroscopy that the reason for this different behavior is probably the formation of mixed Cu/Au particles in Cu/Au-CP, which apparently allows a quick reduction to Cu^0 in H_2O/MeOH under pure visible light. Hence, H_2 was effectively evolved over Cu/Au-CP by using the visible-light filter (Figure 6.8). Contrary to this, the Cu/Au-SP catalyst contains very small Au particles that are separated from the Cu species, leading to a retarded reducibility of Cu and, thus, poor H_2 rates under visible light. However, since very small particles are efficient electron traps under UV-light excitation, this catalyst showed a markedly enhanced H_2 production under UV-vis light (320–500 nm).

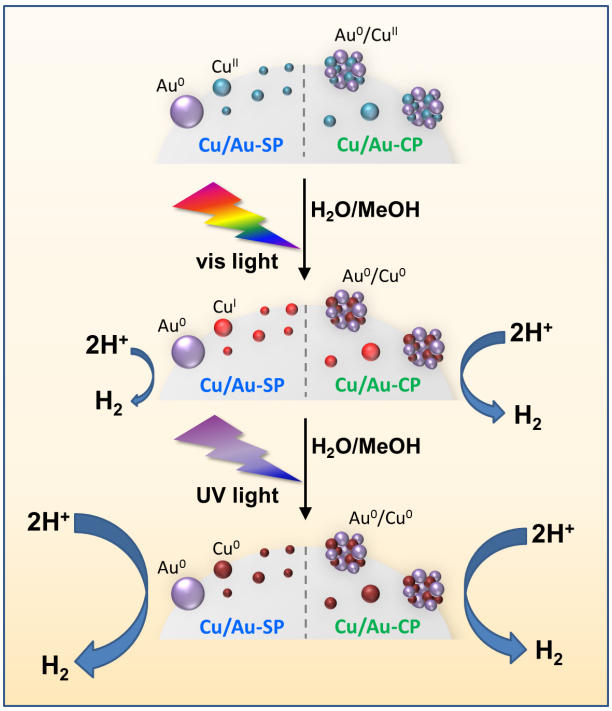

Figure 6.8: Illustration of the Cu/Au-TiO_2 catalyst structures (Cu/Au-SP: separated particles, Cu/Au-CP: mixed particles), which cause different *in situ* changes of the Cu-oxidation state. In H_2O/MeOH under visible light, Cu^{2+} (light blue) being in mixed particles of Cu/Au-CP is quickly reduced to Cu^0 (brown), leading to an improved H_2 evolution. For Cu/Au-SP, visible light only forms Cu^+ species (red), which is less active under 400–700 nm excitation. In contrast, UV light provokes the formation of highly dispersed Cu^0 along with small Au particles, resulting in a very high photoactivity under 320–500 nm light.

References

[1] British Petroleum. *Statistical Review of World Energy.* (2014).

[2] UNO. *World Population Prospects.* (2012).

[3] Lewis, N. S. and Nocera, D. G. *Proc. Natl. Acad. Sci.* **103**, 15729–15735 (2006).

[4] Smalley, R. E. *MRS Bull.* **30**, 412–417 (2005).

[5] Kalyanasundaram, K. and Grätzel, M. *Curr. Opin. Biotech.* **21**, 298–310 (2010).

[6] Roy, S. C., Varghese, O. K., Paulose, M., and Grimes, C. A. *ACS Nano* **4**, 1259–1278 (2010).

[7] Tachibana, Y., Vayssieres, L., and Durrant, J. R. *Nature Photon.* **6**, 511–518 (2012).

[8] Gust, D., Moore, T. A., and Moore, A. L. *Acc. Chem. Res.* **42**, 1890–1898 (2009).

[9] Imahori, H., Mori, Y., and Matano, Y. *J. Photochem. Photobiol. C* **4**, 51–83 (2003).

[10] Fujishima, A. *Nature* **238**, 37–38 (1972).

[11] Maeda, K. and Domen, K. *J. Phys. Chem. Lett.* **1**, 2655–2661 (2010).

[12] Pelaez, M., Nolan, N. T., Pillai, S. C., Seery, M. K., Falaras, P., Kontos, A. G., Dunlop, P. S., Hamilton, J. W., Byrne, J. A., O'Shea, K., Entezari, M. H., and Dionysiou, D. D. *Appl. Catal. B* **125**, 331–349 (2012).

[13] Serpone, N. and Emeline, A. V. *J. Phys. Chem. Lett.* **3**, 673–677 (2012).

[14] Shimura, K. and Yoshida, H. *Energy Environ. Sci.* **4**, 2467–2481 (2011).

[15] Kawai, T. and Sakata, T. *J. Chem. Soc., Chem. Commun.* , 694–695 (1980).

[16] Hoffmann, M. R., Martin, S. T., Choi, W., and Bahnemann, D. W. *Chem. Rev.* **95**, 69–96 (1995).

[17] Ward, M. D., White, J. R., and Bard, A. J. *J. Am. Chem. Soc.* **105**, 27–31 (1983).

[18] Dung, D., Ramsden, J., and Grätzel, M. *J. Am. Chem. Soc.* **104**, 2977–2985 (1982).

[19] Linsebigler, A. L., Lu, G., and Yates Jr, J. T. *Chem. Rev.* **95**, 735–758 (1995).

[20] Ni, M., Leung, M. K. H., Leung, D. Y. C., and Sumathy, K. *Renew. Sust. Energ. Rev.* **11**, 401–425 (2007).

[21] Chen, X., Shen, S., Guo, L., and Mao, S. S. *Chem. Rev.* **110**, 6503–6570 (2010).

[22] Ahmad, H., Kamarudin, S., Minggu, L., and Kassim, M. *Renew. Sust. Energ. Rev.* **43**, 599–610 (2015).

[23] Howe, R. F. and Grätzel, M. *J. Phys. Chem.* **89**, 4495–4499 (1985).

[24] Anpo, M. and Takeuchi, M. *J. Catal.* **216**, 505–516 (2003).

[25] Khan, M. R., Chuan, T. W., Yousuf, A., Chowdhury, M. N. K., and Cheng, C. K. *Catal. Sci. Technol.* , DOI:10.1039/C4CY01545B (2015).

[26] Lee, Y. K., Jung, C. H., Park, J., Seo, H., Somorjai, G. A., and Park, J. Y. *Nano Lett.* **11**, 4251–4255 (2011).

[27] Subramanian, V., Wolf, E., and Kamat, P. V. *J. Phys. Chem. B* **105**, 11439–11446 (2001).

[28] Wardman, P. *J. Phys. Chem. Ref. Data* **18**, 1637–1755 (1989).

[29] Wang, C.-Y., Groenzin, H., and Shultz, M. J. *J. Am. Chem. Soc.* **126**, 8094–8095 (2004).

[30] Asmus, K. D., Möckel, H., and Henglein, A. *J. Phys. Chem.* **77**, 1218–1221 (1973).

[31] Dvoranová, D., Barbieriková, Z., and Brezová, V. *Molecules* **19**, 17279–17304 (2014).

[32] Kho, Y. K., Iwase, A., Teoh, W. Y., Mädler, L., Kudo, A., and Amal, R. *J. Phys. Chem. C* **114**, 2821–2829 (2010).

[33] Lilie, V. J., Beck, G., and Henglein, A. *Ber. Bunsen-Ges. Phys. Chem.* **75**, 458 (1971).

[34] Hykaway, N., Sears, W. M., Morisaki, H., and Morrison, S. R. *J. Phys. Chem.* **90**, 6663–6667 (1986).

[35] Luca Chiarello, G. and Selli, E. *Recent Pat. Eng.* **4**, 155–169 (2010).

[36] Rossetti, I. *Int. Sch. Res. Not.* **2012**, DOI: 10.5402/2012/964936 (2012).

[37] Schneider, J. and Bahnemann, D. W. *J. Phys. Chem. Lett.* **4**, 3479–3483 (2013).

[38] Kandiel, T. A., Ivanova, I., and Bahnemann, D. W. *Energy Environ. Sci.* **7**, 1420–1425 (2014).

[39] Di Paola, A., Bellardita, M., Ceccato, R., Palmisano, L., and Parrino, F. *J. Phys. Chem. C* **113**, 15166–15174 (2009).

[40] Jaramillo, T. F., Baeck, S.-H., Kleiman-Shwarsctein, A., and McFarland, E. W. *Macromol. Rapid Commun.* **25**, 297–301 (2004).

[41] Wolcott, A., Smith, W. A., Kuykendall, T. R., Zhao, Y., and Zhang, J. Z. *Adv. Funct. Mater.* **19**, 1849–1856 (2009).

[42] Kato, H., Asakura, K., and Kudo, A. *J. Am. Chem. Soc.* **125**, 3082–3089 (2003).

[43] Kutty, T. R. N. and Avudaithai, M. *Catal. Rev.* **34**, 373–389 (1992).

[44] Sá, J., Fernández-García, M., and Anderson, J. A. *Catal. Commun.* **9**, 1991–1995 (2008).

[45] Zhang, N., Zhang, Y., and Xu, Y.-J. *Nanoscale* **4**, 5792–5813 (2012).

[46] Xie, G., Zhang, K., Guo, B., Liu, Q., Fang, L., and Gong, J. R. *Adv. Mater.* **25**, 3820–3839 (2013).

[47] Shearer, C. J., Cherevan, A., and Eder, D. *Adv. Mater.* **26**, 2295–2318 (2014).

[48] Zhang, Z., Wang, C.-C., Zakaria, R., and Ying, J. Y. *J. Phys. Chem. B* **102**, 10871–10878 (1998).

[49] Luttrell, T., Halpegamage, S., Tao, J., Kramer, A., Sutter, E., and Batzill, M. *Sci. Rep.* **4**, DOI: 10.1038/srep0404 (2014).

[50] Su, C., Hong, B.-Y., and Tseng, C.-M. *Catal. Today* **96**, 119–126 (2004).

[51] Li, X., Zhu, Z., Zhao, Q., and Wang, L. *J. Hazard. Mater.* **186**, 2089–2096 (2011).

[52] Grätzel, M. *Nature* **414**, 338–344 (2001).

[53] Kudo, A. and Miseki, Y. *Chem. Soc. Rev.* **38**, 253–278 (2009).

[54] Emeline, A. V., Kuznetsov, V. N., Ryabchuk, V. K., and Serpone, N. *Environ. Sci. Pollut. Res.* **19**, 3666–3675 (2012).

[55] Kubacka, A., Fernandez-Garcia, M., and Colon, G. *Chem. Rev.* **112**, 1555–1614 (2011).

[56] Choi, W., Termin, A., and Hoffmann, M. R. *J. Phys. Chem.* **98**, 13669–13679 (1994).

[57] Karakitsou, K. E. and Verykios, X. E. *J. Phys. Chem.* **97**, 1184–1189 (1993).

[58] Ishii, T., Kato, H., and Kudo, A. *J. Photochem. Photobiol. A* **163**, 181–186 (2004).

[59] Kato, H. and Kudo, A. *J. Phys. Chem. B* **106**, 5029–5034 (2002).

[60] Peng, S., Li, Y., Jiang, F., Lu, G., and Li, S. *Chem. Phys. Lett.* **398**, 235–239 (2004).

[61] Asahi, R., Morikawa, T., Ohwaki, T., Aoki, K., and Taga, Y. *Science* **293**, 269–271 (2001).

[62] Emeline, A. V., Kuznetsov, V. N., Rybchuk, V. K., and Serpone, N. *Int. J. Photoenergy* **2008** (2007).

[63] Gomathi Devi, L. and Kavitha, R. *RSC Adv.* **4**, 28265–28299 (2014).

[64] Hu, S., Li, F., and Fan, Z. *Appl. Surf. Sci.* **258**, 1249–1255 (2011).

[65] Yuan, J., Chen, M., Shi, J., and Shangguan, W. *Int. J. Hydrogen Energy* **31**, 1326–1331 (2006).

[66] Kuroda, Y., Mori, T., Yagi, K., Makihata, N., Kawahara, Y., Nagao, M., and Kittaka, S. *Langmuir* **21**, 8026–8034 (2005).

[67] Irie, H., Watanabe, Y., and Hashimoto, K. *J. Phys. Chem. B* **107**, 5483–5486 (2003).

[68] Di Valentin, C., Finazzi, E., Pacchioni, G., Selloni, A., Livraghi, S., Paganini, M. C., and Giamello, E. *Chem. Phys.* **339**, 44–56 (2007).

[69] Yang, K., Dai, Y., Huang, B., and Han, S. *J. Phys. Chem. B* **110**, 24011–24014 (2006).

[70] Sayed, F. N., Jayakumar, O. D., Sasikala, R., Kadam, R. M., Bharadwaj, S. R., Kienle, L., Schürmann, U., Kaps, S., Adelung, R., Mittal, J. P., and Tyagi, A. K. *J. Phys. Chem. C* **116**, 12462–12467 (2012).

[71] Cronemeyer, D. C. *Phys. Rev.* **113**, 1222–1226 (1959).

[72] Zuo, F., Wang, L., Wu, T., Zhang, Z., Borchardt, D., and Feng, P. *J. Am. Chem. Soc.* **132**, 11856–11857 (2010).

[73] Zhang, Z., Yang, X., Hedhili, M. N., Ahmed, E., Shi, L., and Wang, P. *ACS Appl. Mater. Interfaces* **6**, 691–696 (2013).

[74] Zhang, Z., Hedhili, M. N., Zhu, H., and Wang, P. *Phys. Chem. Chem. Phys.* **15**, 15637–15644 (2013).

[75] Guo, S., Wen, D., Zhai, Y., Dong, S., and Wang, E. *ACS Nano* **4**, 3959–3968 (2010).

[76] Zuo, F., Wang, L., and Feng, P. *Int. J. Hydrogen Energy* **39**, 711–717 (2014).

[77] Hu, Y. H. *Angew. Chem. Int. Ed.* **51**, 12410–12412 (2012).

[78] Wang, Z., Yang, C., Lin, T., Yin, H., Chen, P., Wan, D., Xu, F., Huang, F., Lin, J., Xie, X., and Jiang, M. *Energy Environ. Sci.* **6**, 3007–3014 (2013).

[79] Saputera, W. H., Mul, G., and Hamdy, M. S. *Catal. Today* **246**, 60–66 (2014).

[80] Liu, N., Schneider, C., Freitag, D., Hartmann, M., Venkatesan, U., Müller, J., Spiecker, E., and Schmuki, P. *Nano Lett.* (2014).

[81] Liu, N., Schneider, C., Freitag, D., Venkatesan, U., Marthala, V., Hartmann, M., Winter, B., Spiecker, E., Osvet, A., Zolnhofer, E. M., Meyer, K., Nakajima, T., Zhou, X., and Schmuki, P. *Angew. Chem. Int. Ed.* **53**, 14201–14205 (2014).

[82] Zhou, W., Li, W., Wang, J.-Q., Qu, Y., Yang, Y., Xie, Y., Zhang, K., Wang, L., Fu, H., and Zhao, D. *J. Am. Chem. Soc.* **136**, 9280–9283 (2014).

[83] Scanlon, D. O., Dunnill, C. W., Buckeridge, J., Shevlin, S. A., Logsdail, A. J., Woodley, S. M., Catlow, C. R. A., Powell, M. J., Palgrave, R. G., Parkin, I. P., Watson, G. W., Keal, T. W., Sherwood, P., Walsh, A., and Sokol, Alexey, A. *Nat. Mater.* **12**, 798–801 (2013).

[84] Kavan, L., Grätzel, M., Gilbert, S., Klemenz, C., and Scheel, H. *J. Am. Chem. Soc.* **118**, 6716–6723 (1996).

[85] Xiong, G., Shao, R., Droubay, T. C., Joly, A. G., Beck, K. M., Chambers, S. A., and Hess, W. P. *Adv. Funct. Mater.* **17**, 2133–2138 (2007).

[86] Hurum, D. C., Agrios, A. G., Gray, K. A., Rajh, T., and Thurnauer, M. C. *J. Phys. Chem. B* **107**, 4545–4549 (2003).

[87] Hurum, D. C., Gray, K. A., Rajh, T., and Thurnauer, M. C. *J. Phys. Chem. B* **109**, 977–980 (2005).

[88] Hurum, D. C., Agrios, A. G., Crist, S. E., Gray, K. A., Rajh, T., and Thurnauer, M. C. *J. Electron. Spectrosc. Relat. Phenom.* **150**, 155–163 (2006).

[89] Kandiel, T. A., Feldhoff, A., Robben, L., Dillert, R., and Bahnemann, D. W. *Chem. Mater.* **22**, 2050–2060 (2010).

[90] Tay, Q., Liu, X., Tang, Y., Jiang, Z., Sum, T. C., and Chen, Z. *J. Phys. Chem. C* **117**, 14973–14982 (2013).

[91] Marschall, R. *Adv. Funct. Mater.* **24**, 2421–2440 (2014).

[92] Serpone, N., Borgarello, E., and Grätzel, M. *J. Chem. Soc., Chem. Commun.* **6**, 342–344 (1984).

[93] Sun, W.-T., Yu, Y., Pan, H.-Y., Gao, X.-F., Chen, Q., and Peng, L.-M. *J. Am. Chem. Soc.* **130**, 1124–1125 (2008).

[94] Wang, H., Bai, Y., Zhang, H., Zhang, Z., Li, J., and Guo, L. *J. Phys. Chem. C* **114**, 16451–16455 (2010).

[95] Pang, S., Cheng, K., Yuan, Z., Xu, S., Cheng, G., and Du, Z. *Appl. Phys. Lett.* **104**, 201601 (2014).

[96] Yamada, K., Miyajima, K., and Mafuné, F. *J. Phys. Chem. C* **111**, 11246–11251 (2007).

[97] Zhang, X., Chen, Y. L., Liu, R.-S., and Tsai, D. P. *Rep. Prog. Phys.* **76**, 46401–46442 (2013).

[98] Wang, C. and Astruc, D. *Chem. Soc. Rev.* **43**, 7188–7216 (2014).

[99] Hallett-Tapley, G. L., Silvero, M. J., Bueno-Alejo, C. J., González-Béjar, M., McTiernan, C. D., Grenier, M., Netto-Ferreira, J. C., and Scaiano, J. C. *J. Phys. Chem. C* **117**, 12279–12288 (2013).

[100] Huang, X., Li, Y., Chen, Y., Zhou, E., Xu, Y., Zhou, H., Duan, X., and Huang, Y. *Angew. Chem. Int. Ed.* **52**, 2520–2524 (2013).

[101] Naya, S.-i., Kimura, K., and Tada, H. *ACS Catal.* **3**, 10–13 (2012).

[102] Sarina, S., Zhu, H., Jaatinen, E., Xiao, Q., Liu, H., Jia, J., Chen, C., and Zhao, J. *J. Am. Chem. Soc.* **135**, 5793–5801 (2013).

[103] Kochuveedu, S. T., Kim, D.-P., and Kim, D. H. *J. Phys. Chem. C* **116**, 2500–2506 (2012).

[104] Hou, W., Liu, Z., Pavaskar, P., Hung, W. H., and Cronin, S. B. *J. Catal.* **277**, 149–153 (2011).

[105] Lu, J., Zhang, P., Li, A., Su, F., Wang, T., Liu, Y., and Gong, J. *Chem. Commun.* **49**, 5817–5819 (2013).

[106] Hou, W., Hung, W. H., Pavaskar, P., Goeppert, A., Aykol, M., and Cronin, S. B. *ACS Catal.* **1**, 929–936 (2011).

[107] Thomann, I., Pinaud, B. A., Chen, Z., Clemens, B. M., Jaramillo, T. F., and Brongersma, M. L. *Nano Lett.* **11**, 3440–3446 (2011).

[108] Liu, Z., Hou, W., Pavaskar, P., Aykol, M., and Cronin, S. B. *Nano Lett.* **11**, 1111–1116 (2011).

[109] Warren, S. C. and Thimsen, E. *Energy Environ. Sci.* **5**, 5133–5146 (2012).

[110] Chen, J.-J., Wu, J. C., Wu, P. C., and Tsai, D. P. *J. Phys. Chem. C* **115**, 210–216 (2010).

[111] Gomes Silva, C., Juárez, R., Marino, T., Molinari, R., and García, H. *J. Am. Chem. Soc.* **133**, 595–602 (2010).

[112] Primo, A., Corma, A., and García, H. *Phys. Chem. Chem. Phys.* **13**, 886–910 (2011).

[113] Murdoch, M., Waterhouse, G., Nadeem, M., Metson, J., Keane, M., Howe, R., Llorca, J., and Idriss, H. *Nat. Chem.* **3**, 489–492 (2011).

[114] Tanaka, A., Sakaguchi, S., Hashimoto, K., and Kominami, H. *ACS Catal.* **3**, 79–85 (2012).

[115] Seh, Z. W., Liu, S., Low, M., Zhang, S.-Y., Liu, Z., Mlayah, A., and Han, M.-Y. *Adv. Mater.* **24**, 2310–2314 (2012).

[116] Yuzawa, H., Yoshida, T., and Yoshida, H. *Appl. Catal. B* **115**, 294–302 (2012).

[117] Fang, J., Cao, S.-W., Wang, Z., Shahjamali, M. M., Loo, S. C. J., Barber, J., and Xue, C. *Int. J. Hydrogen Energy* **37**, 17853–17861 (2012).

[118] Mie, G. *Ann. Phys.* **330**, 377–445 (1908).

[119] Kelly, K. L., Coronado, E., Zhao, L. L., and Schatz, G. C. *J. Phys. Chem. B* **107**, 668–677 (2003).

[120] Philip, R., Chantharasupawong, P., Qian, H., Jin, R., and Thomas, J. *Nano Lett.* **12**, 4661–4667 (2012).

[121] Klar, T., Perner, M., Grosse, S., von Plessen, G., Spirkl, W., and Feldmann, J. *Phys. Rev. Lett.* **80**, 4249–4252 (1998).

[122] Aeschlimann, M. In *Encycl. Nanosci. Nanotechnol.*, volume 3, 29–40. American Scientific Publishers (2004).

[123] Mubeen, S., Hernandez-Sosa, G., Moses, D., Lee, J., and Moskovits, M. *Nano Lett.* **11**, 5548–5552 (2011).

[124] Tian, Y. and Tatsuma, T. *J. Am. Chem. Soc.* **127**, 7632–7637 (2005).

[125] Zheng, Z., Huang, B., Qin, X., Zhang, X., Dai, Y., and Whangbo, M.-H. *J. Mater. Chem.* **21**, 9079–9087 (2011).

[126] Linic, S., Christopher, P., and Ingram, D. B. *Nat. Mater.* **10**, 911–921 (2011).

[127] Ingram, D. B. and Linic, S. *J. Am. Chem. Soc.* **133**, 5202–5205 (2011).

[128] Awazu, K., Fujimaki, M., Rockstuhl, C., Tominaga, J., Murakami, H., Ohki, Y., Yoshida, N., and Watanabe, T. *J. Am. Chem. Soc.* **130**, 1676–1680 (2008).

[129] Christopher, P., Xin, H., and Linic, S. *Nat. Chem.* **3**, 467–472 (2011).

[130] Adleman, J. R., Boyd, D. A., Goodwin, D. G., and Psaltis, D. *Nano Lett.* **9**, 4417–4423 (2009).

[131] Tanaka, A., Sakaguchi, S., Hashimoto, K., and Kominami, H. *Catal. Sci. Technol.* **2**, 907–909 (2012).

[132] Qian, K., Sweeny, B. C., Johnston-Peck, A. C., Niu, W., Graham, J. O., DuChene, J. S., Qiu, J., Wang, Y.-C., Engelhard, M. H., Su, D., Stach, E. A., and Wei, D. W. *J. Am. Chem. Soc.* **136**, 9842–9845 (2014).

[133] Nishijima, Y., Ueno, K., Yokota, Y., Murakoshi, K., and Misawa, H. *J. Phys. Chem. Lett.* **1**, 2031–2036 (2010).

[134] Hagfeldt, A. and Grätzel, M. *Chem. Rev.* **95**, 49–68 (1995).

[135] Solarska, R., Królikowska, A., and Augustyński, J. *Angew. Chem. Int. Ed.* **49**, 7980–7983 (2010).

[136] Furube, A., Du, L., Hara, K., Katoh, R., and Tachiya, M. *J. Am. Chem. Soc.* **129**, 14852–14853 (2007).

[137] Du, L., Furube, A., Hara, K., Katoh, R., and Tachiya, M. *Thin Solid Films* **518**, 861–864 (2009).

[138] Du, L., Furube, A., Yamamoto, K., Hara, K., Katoh, R., and Tachiya, M. *J. Phys. Chem. C* **113**, 6454–6462 (2009).

[139] Du, L., Furube, A., Hara, K., Katoh, R., and Tachiya, M. *J. Photochem. Photobiol. C* **15**, 21–30 (2013).

[140] McFarland, E. W. and Tang, J. *Nature* **421**, 616–618 (2003).

[141] Cushing, S. K., Li, J., Meng, F., Senty, T. R., Suri, S., Zhi, M., Li, M., Bristow, A. D., and Wu, N. *J. Am. Chem. Soc.* **134**, 15033–15041 (2012).

[142] Perner, M., Bost, P., Lemmer, U., von Plessen, G., Feldmann, J., Becker, U., Mennig, M., Schmitt, M., and Schmidt, H. *Phys. Rev. Lett.* **78**, 2192–2195 Mar (1997).

[143] Christopher, P., Ingram, D. B., and Linic, S. *J. Phys. Chem. C* **114**, 9173–9177 (2010).

[144] Rycenga, M., Cobley, C. M., Zeng, J., Li, W., Moran, C. H., Zhang, Q., Qin, D., and Xia, Y. *Chem. Rev.* **111**, 3669–3712 (2011).

[145] Yen, C.-W. and El-Sayed, M. A. *J. Phys. Chem. C* **113**, 19585–19590 (2009).

[146] Kato, H. and Kudo, A. *J. Phys. Chem. B* **105**, 4285–4292 (2001).

[147] Wohlrab, S., Weiss, M., Du, H., and Kaskel, S. *Chem. Mater.* **18**, 4227–4230 (2006).

[148] Dimitratos, N., Lopez-Sanchez, J. A., Morgan, D., Carley, A., Prati, L., and Hutchings, G. J. *Catal. Today* **122**, 317–324 (2007).

[149] Tomita, K., Petrykin, V., Kobayashi, M., Shiro, M., Yoshimura, M., and Kakihana, M. *Angew. Chem. Int. Ed.* **45**, 2378–2381 (2006).

[150] Gärtner, F., Losse, S., Boddien, A., Pohl, M.-M., Denurra, S., Junge, H., and Beller, M. *ChemSusChem* **5**, 530–533 (2012).

[151] Thompson, M. and Walsh, J. N. *A handbook of inductively coupled plasma spectrometry.* Blackie & Son Ltd., (1983).

[152] Brunauer, S., Emmett, P. H., and Teller, E. *J. Am. Chem. Soc.* **60**, 309–319 (1938).

[153] Wang, Z. L. *J. Phys. Chem. B* **104**, 1153–1175 (2000).

[154] Bragg, W. H. and Bragg, W. L. *Proc. R. Soc. A* **88**, 428–438 (1913).

[155] Scherrer, P. *Goett. Nachr.* **2**, 98–100 (1918).

[156] Howard, A., Clark, D. N. S., Mitchell, C. E. J., Egdell, R. G., and Dhanak, V. R. *Surf. Sci.* **518**, 210–224 (2002).

[157] Zwijnenburg, A., Goossens, A., Sloof, W. G., Crajé, M. W., van der Kraan, A. M., Jos de Jongh, L., Makkee, M., and Moulijn, J. A. *J. Phys. Chem. B* **106**, 9853–9862 (2002).

[158] Chergui, M. *Faraday Discuss.* **171**, 11–40 (2014).

[159] Ryczkowski, J. *Catal. Today* **68**, 263–381 (2001).

[160] López, R. and Gómez, R. *J. Sol-Gel Sci. Technol.* **61**, 1–7 (2012).

[161] Tauc, J., Grigorovici, R., and Vancu, A. *Phys. Status Solidi* **15**, 627–637 (1966).

[162] Gerlach, W. and Stern, O. *Z. Phys. A* **9**, 349–352 (1922).

[163] Abragam, A. and Pryce, M. H. L. *Proc. R. Soc. A* **205**, 135 (1951).

[164] Spalek, T., Pietrzyk, P., and Sojka, Z. *J. Chem. Inf. Model.* **24**, 18–29 (2005).

[165] Mabbs, F. E. and Collison, D. *Mol. Phys. Rep.* **26**, 39 (1999).

[166] Hu, C.-C. and Teng, H. *Appl. Catal. A* **331**, 44–50 (2007).

[167] Meyer, T., Priebe, J. B., da Silva, R. O., Peppel, T., Junge, H., Beller, M., Brückner, A., and Wohlrab, S. *Chem. Mater.* **26**, 4705–4711 (2014).

[168] Li, Z., Chen, G., and Liu, J. W. *Solid State Commun.* **143**, 295–299 (2007).

[169] Almquist, C. B. and Biswas, P. *J. Catal.* **212**, 145–156 (2002).

[170] Sun, Y., Egawa, T., Zhang, L., and Yao, X. *J. Mater. Sci. Lett.* **22**, 799–802 (2003).

[171] Laguta, V. V., Zaritskii, M. I., Glinchuk, M. D., Bykov, I. P., Rosa, J., and Jastrabik, L. *Phys. Rev. B* **58**, 156 (1998).

[172] Sweeney, K. L., Halliburton, L. E., and Kappers, L. A. *Phys. Lett. A* **116**, 81–84 (1986).

[173] Panich, A. M., Shames, A. I., Aleksenskii, A. E., and Dideikin, A. *Solid State Commun.* **152**, 466–468 (2012).

[174] Murphy, D. M., Griffiths, E. W., Rowlands, C. C., Hancock, F. E., and Giamello, E. *Chem. Commun.* , 2177–2178 (1997).

[175] Anpo, M., Che, M., Fubini, B., Garrone, E., Giamello, E., and Paganini, M. C. *Top. Catal.* **8**, 189–198 (1999).

[176] Coronado, J. M., Maira, A. J., Conesa, J. C., Yeung, K. L., Augugliaro, V., and Soria, J. *Langmuir* **17**, 5368–5374 (2001).

[177] Attwood, A. L., Murphy, D. M., Edwards, J. L., Egerton, T. A., and Harrison, R. W. *Res. Chem. Intermed.* **29**, 449–465 (2003).

[178] Claus, P., Brückner, A., Mohr, C., and Hofmeister, H. *J. Am. Chem. Soc.* **122**, 11430–11439 (2000).

[179] Akita, T., Lu, P., Ichikawa, S., Tanaka, K., and Haruta, M. *Surf. Interface Anal.* **31**, 73–78 (2001).

[180] Orlov, A., Jefferson, D. A., Macleod, N., and Lambert, R. M. *Catal. Lett.* **92**, 41–47 (2004).

[181] Bamwenda, G. R., Tsubota, S., Nakamura, T., and Haruta, M. *J. Photochem. Photobiol. A* **89**, 177–189 (1995).

[182] Haruta, M. *Gold Bull.* **37**, 27–36 (2004).

[183] Park, E. D. and Lee, J. S. *J. Catal.* **186**, 1–11 (1999).

[184] Subramanian, V., Wolf, E. E., and Kamat, P. V. *J. Am. Chem. Soc.* **126**, 4943–4950 (2004).

[185] Porta, F., Prati, L., Rossi, M., Coluccia, S., and Martra, G. *Catal. Today* **61**, 165–172 (2000).

[186] Satoh, N., Hasegawa, H., Tsujii, K., and Kimura, K. *J. Phys. Chem.* **98**, 2143–2147 (1994).

[187] Casaletto, M. P., Longo, A., Martorana, A., Prestianni, A., and Venezia, A. M. *Surf. Interface Anal.* **38**, 215–218 (2006).

[188] Soares, J. M. C., Morrall, P., Crossley, A., Harris, P., and Bowker, M. *J. Catal.* **219**, 17–24 (2003).

[189] Arrii, S., Morfin, F., Renouprez, A. J., and Rousset, J. L. *J. Am. Chem. Soc.* **126**, 1199–1205 (2004).

[190] Jiang, Z., Zhang, W., Jin, L., Yang, X., Xu, F., Zhu, J., and Huang, W. *J. Phys. Chem. C* **111**, 12434–12439 (2007).

[191] Dalacu, D., Klemberg-Sapieha, J. E., and Martinu, L. *Surf. Sci.* **472**, 33–40 (2001).

[192] Chang, F.-W., Yu, H.-Y., Roselin, L. S., Yang, H.-C., and Ou, T.-C. *Appl. Catal. A* **302**, 157–167 (2006).

[193] Zanella, R., Delannoy, L., and Louis, C. *Appl. Catal. A* **291**, 62–72 (2005).

[194] Yang, J. H., Henao, J. D., Raphulu, M. C., Wang, Y., Caputo, T., Groszek, A. J., Kung, M. C., Scurrell, M. S., Miller, J. T., and Kung, H. H. *J. Phys. Chem. B* **109**, 10319–10326 (2005).

[195] Fierro-Gonzalez, J. C., Guzman, J., and Gates, B. C. *Top. Catal.* **44**, 103–114 (2007).

[196] Tsubota, S., Cunningham, D. A. H., Bando, Y., and Haruta, M. *Stud. Surf. Sci. Catal.* **91**, 227–235 (1995).

[197] Tsukamoto, D., Shiraishi, Y., Sugano, Y., Ichikawa, S., Tanaka, S., and Hirai, T. *J. Am. Chem. Soc.* **134**, 6309–6315 (2012).

[198] Dimitrijevic, N. M., Saponjic, Z. V., Rabatic, B. M., Poluektov, O. G., and Rajh, T. *J. Phys. Chem. C* **111**, 14597–14601 (2007).

[199] Okumura, M., Coronado, J. M., Soria, J., Haruta, M., and Conesa, J. C. *J. Catal.* **203**, 168–174 (2001).

[200] Xing, M., Fang, W., Nasir, M., Ma, Y., Zhang, J., and Anpo, M. *J. Catal.* **297**, 236–243 (2013).

[201] Howe, R. F. and Grätzel, M. *J. Phys. Chem.* **91**, 3906–3909 (1987).

[202] Nakamura, I., Negishi, N., Kutsuna, S., Ihara, T., Sugihara, S., and Takeuchi, K. *J. Mol. Catal. A* **161**, 205–212 (2000).

[203] Baumann, S. O., Elser, M. J., Auer, M., Bernardi, J., Hu?sing, N., and Diwald, O. *Langmuir* **27**, 1946–1953 (2011).

[204] Kumar, C. P., Gopal, N. O., Wang, T. C., Wong, M.-S., and Ke, S. C. *J. Phys. Chem. B* **110**, 5223–5229 (2006).

[205] Micic, O. I., Zhang, Y., Cromack, K. R., Trifunac, A. D., and Thurnauer, M. C. *J. Phys. Chem.* **97**, 7277–7283 (1993).

[206] Livraghi, S., Chiesa, M., Paganini, M. C., and Giamello, E. *J. Phys. Chem. C* **115**, 25413–25421 (2011).

[207] Aono, M. and Hasiguti, R. R. *Phys. Rev. B* **48**, 12406 (1993).

[208] López-Muñoz, M. J., Soria, J., Conesa, J. C., and Augugliaro, V. *Stud. Surf. Sci. Catal.* **82**, 693–701 (1994).

[209] Li, Z., Dong, T., Zhang, Y., Wu, L., Li, J., Wang, X., and Fu, X. *J. Phys. Chem. C* **111**, 4727–4733 (2007).

[210] Sawyer, D. T. and Valentine, J. S. *Acc. Chem. Res.* **14**, 393–400 (1981).

[211] Villarreal, T. L., Gomez, R., Neumann-Spallart, M., Alonso-Vante, N., and Salvador, P. *J. Phys. Chem. B* **108**, 15172–15181 (2004).

[212] Sun, S., Ding, J., Bao, J., Gao, C., Qi, Z., and Li, C. *Catal. Lett.* **137**, 239–246 (2010).

[213] Enright, B. and Fitzmaurice, D. *J. Phys. Chem.* **100**, 1027–1035 (1996).

[214] Taylor, E. A. and L, G. G. *J. Phys. Chem.* **92**, 477 (1988).

[215] Hussein, G. A., Sheppard, N., Zaki, M. I., and Fahim, R. B. *J. Chem. Soc. Faraday Trans.* **87**, 2655–2659 (1991).

[216] Lee, G. D. and Falconer, J. L. *Catal. Lett.* **70**, 145–148 (2000).

[217] Chuang, C.-C., Chen, C.-C., and Lin, J.-L. *J. Phys. Chem. B* **103**, 2439–2444 (1999).

[218] Muggli, D. S. and Falconer, J. L. *J. Catal.* **191**, 318–325 (2000).

[219] Miller, K. L., Lee, C. W., Falconer, J. L., and Medlin, J. W. *J. Catal.* **275**, 294–299 (2010).

[220] Konstantinova, E. A., Kokorin, A. I., Sakthivel, S., Kisch, H., and Lips, K. *CHIMIA* **61**, 810–814 (2007).

[221] Beversluis, M., Bouhelier, A., and Novotny, L. *Phys. Rev. B* **68**, 115433 (2003).

[222] Xu, M., Gao, Y., Moreno, E. M., Kunst, M., Muhler, M., Wang, Y., Idriss, H., and Wöll, C. *Phys. Rev. Lett.* **106**, 138302 (2011).

[223] Zhao, W., Ai, Z., Dai, J., and Zhang, M. *PloS one* **9**, e103671 (2014).

[224] Wu, Y., Liu, H., Zhang, J., and Chen, F. *J. Phys. Chem. C* **113**, 14689–14695 (2009).

[225] Pany, S., Naik, B., Martha, S., and Parida, K. *ACS Appl. Mater. Interfaces* **6**, 839–846 (2014).

[226] Livraghi, S., Paganini, M. C., Chiesa, M., and Giamello, E. *Res. Chem. Intermed.* **33**, 739–747 (2007).

[227] Livraghi, S., Paganini, M. C., Giamello, E., Selloni, A., Di Valentin, C., and Pacchioni, G. *J. Am. Chem. Soc.* **128**, 15666–15671 (2006).

[228] Barolo, G., Livraghi, S., Chiesa, M., Paganini, M. C., and Giamello, E. *J. Phys. Chem. C* **116**, 20887–20894 (2012).

[229] Di Valentin, C., Pacchioni, G., Selloni, A., Livraghi, S., and Giamello, E. *J. Phys. Chem. B* **109**, 11414–11419 (2005).

[230] Kleber, W., Bautsch, H.-J., Bohm, J., and Klimm, D. *Einführung in die Kristallographie.* Munich, Oldenbourg Wissenschaftsverlag, (2010).

[231] Li, J.-G., Ishigaki, T., and Sun, X. *J. Phys. Chem. C* **111**, 4969–4976 (2007).

[232] Labat, F., Baranek, P., Domain, C., Minot, C., and Adamo, C. *J. Chem. Phys.* **126**, 154703 (2007).

[233] Reyes-Coronado, D., Rodriguez-Gattorno, G., Espinosa-Pesqueira, M. E., Cab, C., de Coss, R., and Oskam, G. *Nanotechnology* **19**, 145605 (2008).

[234] Sun, B., Vorontsov, A. V., and Smirniotis, P. G. *Langmuir* **19**, 3151–3156 (2003).

[235] Di Paola, A., Bellardita, M., and Palmisano, L. *Catalysts* **3**, 36–73 (2013).

[236] Yan, Y., Han, M., Konkin, A., Koppe, T., Wang, D., Andreu, T., Chen, G., Vetter, U., Morante, J. R., and Schaaf, P. *Journal of Materials Chemistry A* **2**(32), 12708–12716 (2014).

[237] Adepalli, K. K. *Influence of extended defects on the electrical properties of TiO_2 (rutile).* PhD thesis, University of Stuttgart, (2013).

[238] Van Faassen, E. and Vanin, A. *Radicals for Life: the various forms of nitric oxide.* Elsevier, (2011).

[239] Sun, H., Bai, Y., Jin, W., and Xu, N. *Sol. Energy Mater. Sol. Cells* **92**, 76–83 (2008).

[240] Di Valentin, C., Pacchioni, G., and Selloni, A. *J. Phys. Chem. C* **113**, 20543–20552 (2009).

[241] Hoang, S., Berglund, S. P., Hahn, N. T., Bard, A. J., and Mullins, C. B. *J. Am. Chem. Soc.* **134**, 3659–3662 (2012).

[242] Irie, H., Watanabe, Y., and Hashimoto, K. *J. Phys. Chem. B* **107**, 5483–5486 (2003).

[243] Wang, J., Tafen, D. N., Lewis, J. P., Hong, Z., Manivannan, A., Zhi, M., Li, M., and Wu, N. *J. Am. Chem. Soc.* **131**, 12290–12297 (2009).

[244] Napoli, F., Chiesa, M., Livraghi, S., Giamello, E., Agnoli, S., Granozzi, G., Pacchioni, G., and Di Valentin, C. *Chem. Phys. Lett.* **477**, 135–138 (2009).

[245] Fàbrega, C., Andreu, T., Güell, F., Prades, J. D., Estradé, S., Rebled, J. M., Peiró, F., and Morante, J. R. *Nanotechnology* **22**, 235403 (2011).

[246] Chen, X., Lou, Y.-B., Samia, A. C., Burda, C., and Gole, J. L. *Adv. Funct. Mater.* **15**, 41–49 (2005).

[247] Hu, Y., Liu, H., Kong, X., and Guo, X. *J. Nanosci. Nanotechnol.* **14**, 3532–3537 (2014).

[248] Zhao, Y., Qiu, X., and Burda, C. *Chem. Mater.* **20**, 2629–2636 (2008).

[249] Diwald, O., Thompson, T. L., Zubkov, T., Goralski, E. G., Walck, S. D., and Yates, J. T. *J. Phys. Chem. B* **108**, 6004–6008 (2004).

[250] Ceotto, M., Lo Presti, L., Cappelletti, G., Meroni, D., Spadavecchia, F., Zecca, R., Leoni, M., Scardi, P., Bianchi, C. L., and Ardizzone, S. *J. Phys. Chem. C* **116**, 1764–1771 (2012).

[251] Teramura, K., Tanaka, T., and Funabiki, T. *Chem. Lett.* **32**, 1184–1185 (2003).

[252] Yamazoe, S., Teramura, K., Hitomi, Y., Shishido, T., and Tanaka, T. *J. Phys. Chem. C* **111**, 14189–14197 (2007).

[253] Yamanaka, K.-i. and Morikawa, T. *J. Phys. Chem. C* **116**, 1286–1292 (2011).

[254] Zhou, H., Ding, L., Fan, T., Ding, J., Zhang, D., and Guo, Q. *Appl. Catal. B* **147**, 221–228 (2014).

[255] Chiarello, G. L., Aguirre, M. H., and Selli, E. *J. Catal.* **273**, 182–190 (2010).

[256] Bandara, J., Udawatta, C. P. K., and Rajapakse, C. S. K. *Photochem. Photobiol. Sci.* **4**, 857–861 (2005).

[257] Choi, H.-J. and Kang, M. *Int. J. Hydrogen Energy* **32**, 3841–3848 (2007).

[258] Lalitha, K., Sadanandam, G., Kumari, V. D., Subrahmanyam, M., Sreedhar, B., and Hebalkar, N. Y. *J. Phys. Chem. C* **114**, 22181–22189 (2010).

[259] Liu, Z., Bai, H., Xu, S., and Sun, D. D. *Int. J. Hydrogen Energy* **36**, 13473–13480 (2011).

[260] Gomathisankar, P., Hachisuka, K., Katsumata, H., Suzuki, T., Funasaka, K., and Kaneco, S. *Int. J. Hydrogen Energy* **38**, 11840–11846 (2013).

[261] Cheng, W.-Y., Yu, T.-H., Chao, K.-J., and Lu, S.-Y. *ChemCatChem* **6**, 293–300 (2014).

[262] Luechinger, N. A., Athanassiou, E. K., and Stark, W. J. *Nanotechnology* **19**, 445201 (2008).

[263] Kanninen, P., Johans, C., Merta, J., and Kontturi, K. *J. Colloid Interface Sci.* **318**, 88–95 (2008).

[264] Wu, N.-L. and Lee, M.-S. *Int. J. Hydrogen Energy* **29**, 1601–1605 (2004).

[265] Wu, Y., Lu, G., and Li, S. *Catal. Lett.* **133**, 97–105 (2009).

[266] Irie, H., Kamiya, K., Shibanuma, T., Miura, S., Tryk, D. A., Yokoyama, T., and Hashimoto, K. *J. Phys. Chem. C* **113**, 10761–10766 (2009).

[267] Li, G., Dimitrijevic, N. M., Chen, L., Rajh, T., and Gray, K. A. *J. Phys. Chem. C* **112**, 19040–19044 (2008).

[268] Aboukaïs, A., Bennani, A., Aïssi, C. F., Wrobel, G., Guelton, M., and Vedrine, J. C. *J. Chem. Soc. Faraday Trans.* **88**, 615–620 (1992).

[269] Soria, J., Conesa, J., Martinez-Arias, A., and Coronado, J. *Solid State Ionics* **63**, 755–761 (1993).

[270] Aboukaïs, A., Bennani, A., Lamonier-Dulongpont, C., Abi-Aad, E., and Wrobel, G. *Colloids Surf. A* **115**, 171–177 (1996).

[271] Kim, M.-J., Na, H.-J., Lee, K. C., Yoo, E. A., and Lee, M. *J. Mater. Chem.* **13**, 1789–1792 (2003).

[272] Bracey, C. L., Ellis, P. R., and Hutchings, G. J. *Chem. Soc. Rev.* **38**, 2231–2243 (2009).

[273] Johnson, P. B. and Christy, R.-W. *Phys. Rev. B* **6**, 4370 (1972).

[274] Pinchuk, A., Kreibig, U., and Hilger, A. *Surf. Sci.* **557**, 269–280 (2004).

Appendix

Further analyses on the $NaTaO_3$ catalysts from Chapter 3

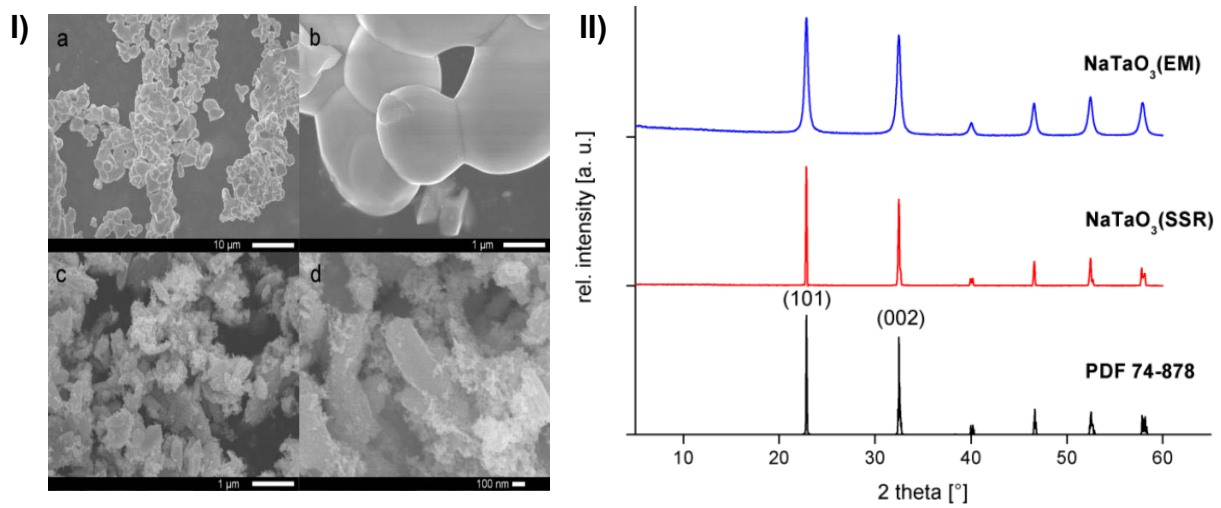

Figure A.1: I) SEM images of $NaTaO_3$(SSR) (a,b) and $NaTaO_3$(EM) (c,d). II) Powder XRD patterns of $NaTaO_3$ prepared by SSR and EM in comparison to ICDD PDF 73-878. Figures taken from [167].

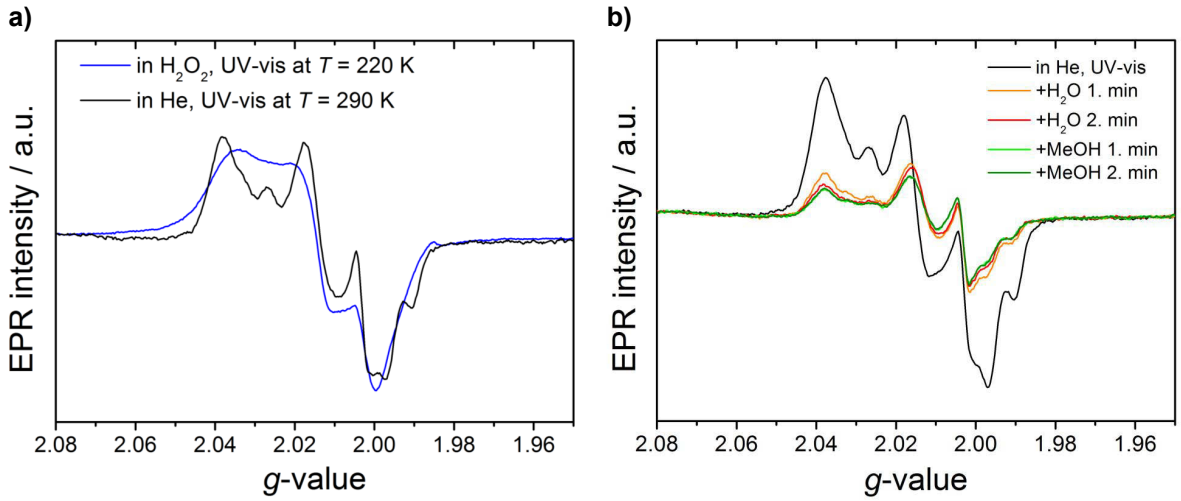

Figure A.2: a) Comparison of the EPR spectra of $NaTaO_3$(EM) under irradiation in 50 µL H_2O_2 at $T = 220$ K (blue) and in flowing He at $T = 290$ K (black). Signal C3 can thus be assigned to superoxide species, as the g-values observed for the H_2O_2-treated sample are similar. b) *In situ* EPR spectra of $NaTaO_3$(EM) in flowing He at $T = 290$ K (black) with subsequent addition of H_2O-saturated He (reddish lines) and H_2O/MeOH-saturated He (greenish lines). The main intensity loss of the surface-bound oxygen species C3–C5 was observed upon adding water (already after two minutes exposure), whereas the addition of methanol as hole scavenger caused a decrease of signal C2 (attributed to subsurface oxide radicals).

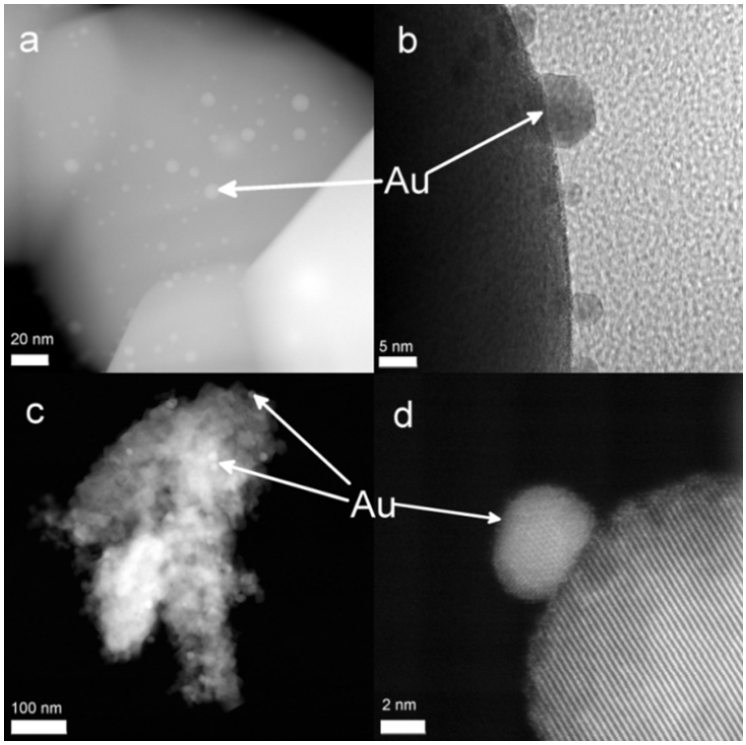

Figure A.3: TEM images of photodeposited 0.2 wt.% Au on $NaTaO_3$ prepared by SSR (a,b) and EM (c,d). Figure taken from [167].

Further analyses on the Au-TiO_2 catalysts from Chapter 4

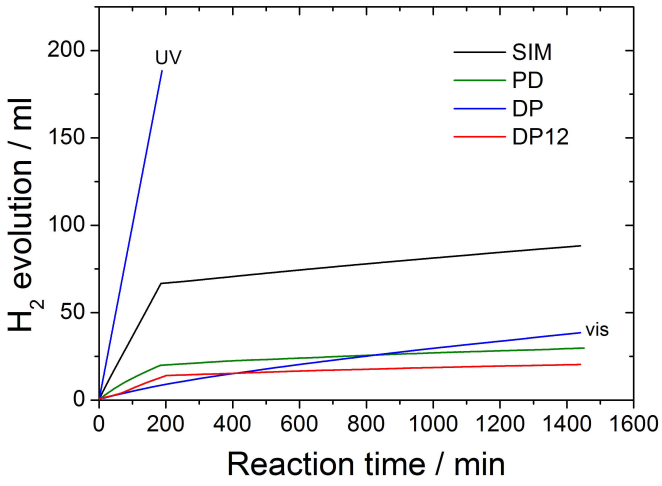

Figure A.4: Experimental photocatalytic H_2-evolution curves from H_2O/MeOH over AuP25 catalysts prepared by different Au-deposition methods. The hydrogen-evolution rate was constant over a period of 3 h under UV light (320–500 nm filter) and over subsequent 21 h under visible light (400–700 nm filter).

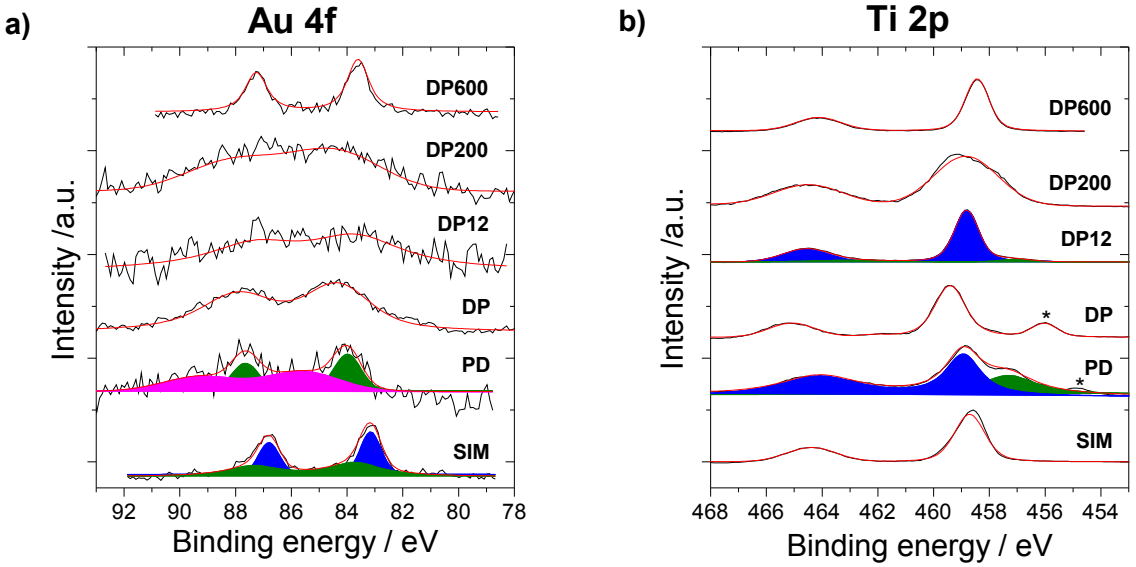

Figure A.5: Experimental (black) and fitted (red) XP spectra of AuP25 catalysts prepared by different Au-deposition techniques a) in the Au 4*f* region, where the green signal component refers to reduced Au^0 species, the blue component corresponds to Au^0-V_O sites and the pink one to oxidized Au^{3+}. b) XP spectra in the Ti 2*p* region, where the blue signal is attributed to Ti^{4+} and the green to Ti^{3+} species. The peaks at 456.0 eV (DP) and 454.9 eV (PD) are artifacts due to partial charging (asterisked).

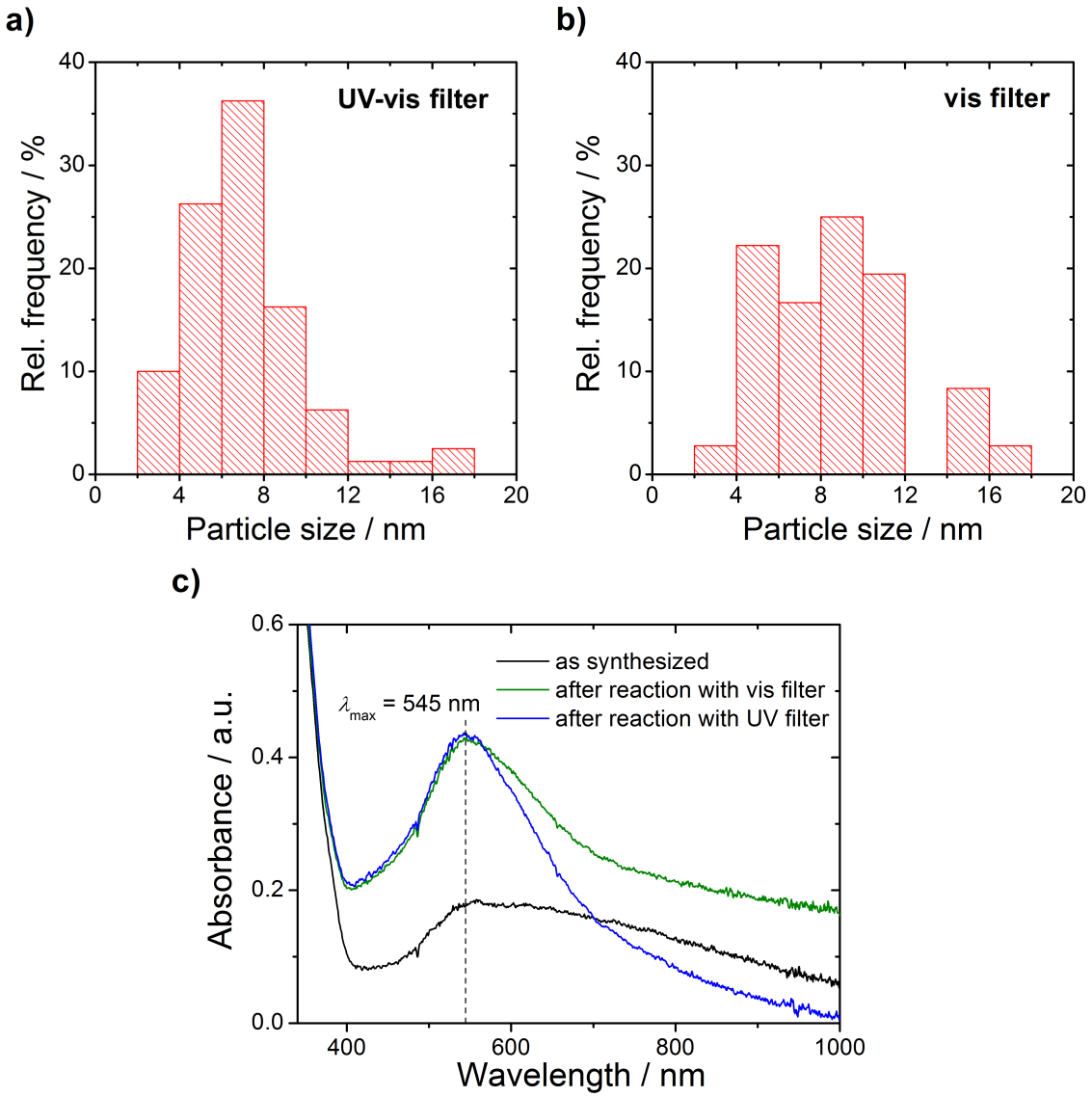

Figure A.6: Particle-size distributions obtained by TEM analysis of AuP25-DP catalysts a) after reaction with UV light for 3 h and b) after reaction with visible light for 21 h. c) UV-vis absorption spectra of the AuP25-DP catalysts as prepared (black), after reaction with UV light (blue) and after reaction with visible light (green).

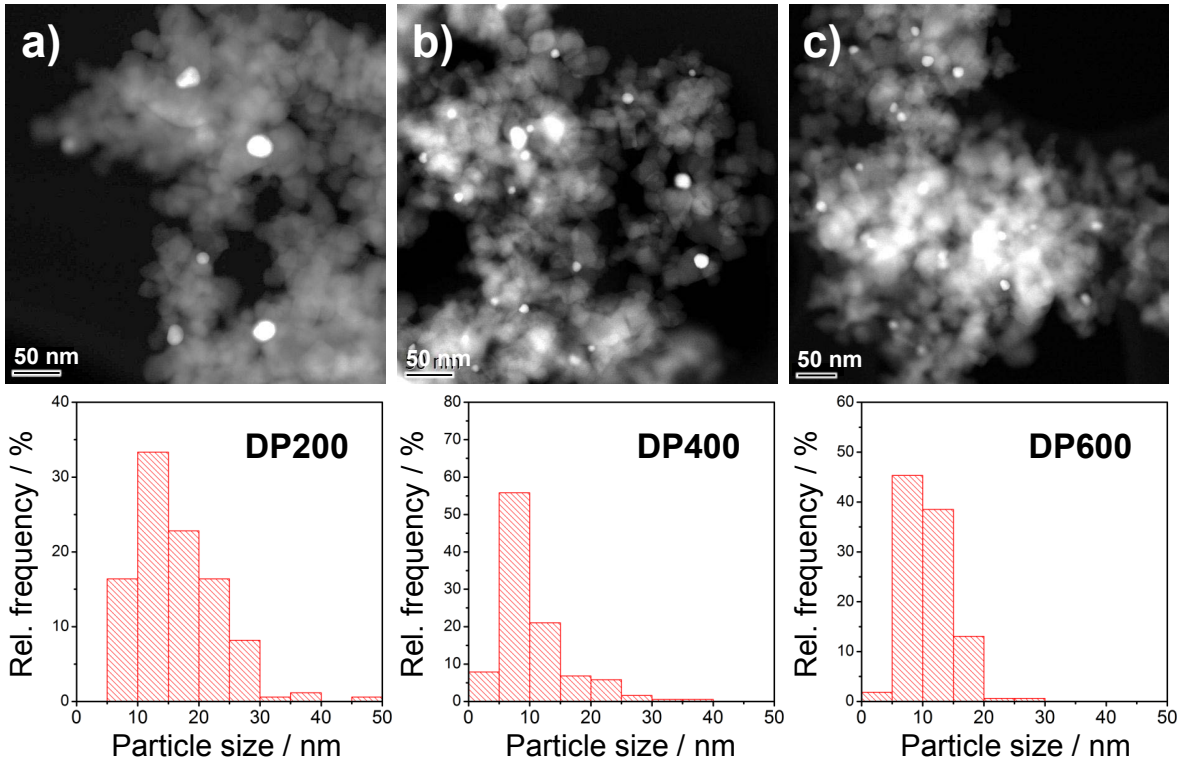

Figure A.7: TEM images and Au-particle size distributions of calcined AuP25-DP catalysts a) at 200 řC, b) at 400 řC, and c) 600 řC.

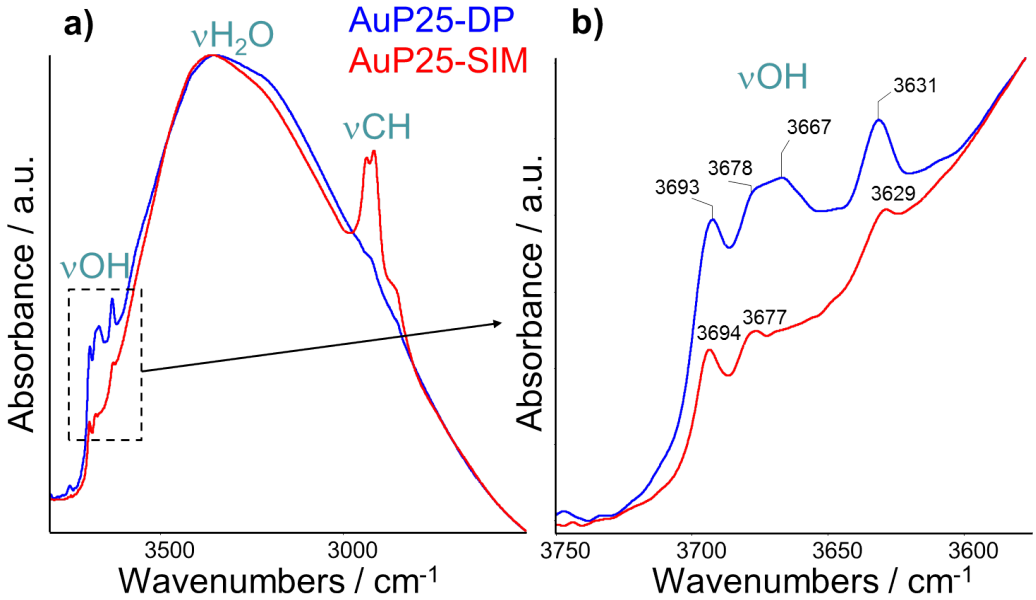

Figure A.8: FTIR spectra in transmission mode of AuP25-DP (blue) and AuP25-SIM (red) a) from 4000–2500 cm^{-1} and b) of the enlarged ν(OH) region. The spectra clearly demonstrate that DP procedure leads to a specific OH coverage, whereby superoxide radicals can be formed under irradiation through a hole-mediated process explained in Section 4.2.

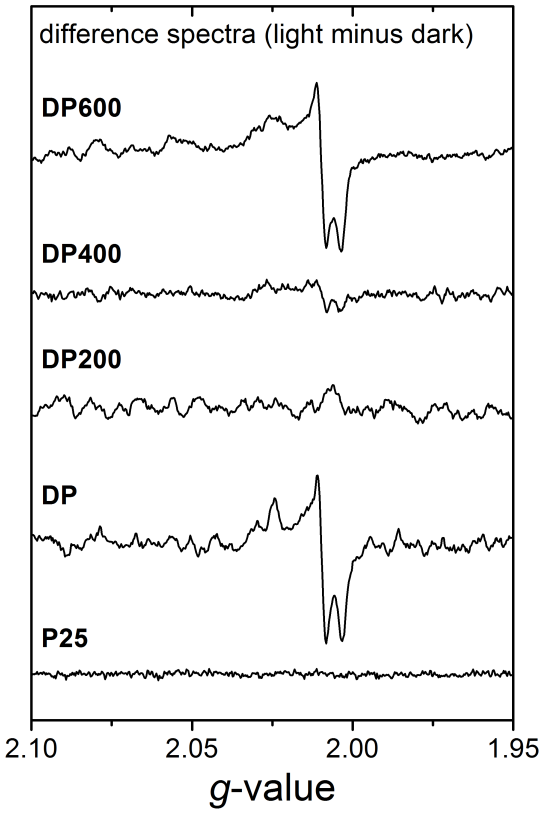

Figure A.9: *In situ* EPR spectra of AuP25-DP catalysts uncalcined and calcined at 200, 400 and 600 řC in comparison with P25. Displayed are the difference spectra obtained by subtracting the dark spectrum from that after 10 min UV-vis-light irradiation. The capability of forming stable superoxide radicals is apparently higher for catalysts that show higher H_2-evolution rates (AuP25-DP and AuP25-DP600) indicating a better charge separation by efficient electron transfer to Au in these catalysts, probably promoted by surface trapping of positive holes at OH groups.

Photocatalytic tests with pure visible light For selected catalysts of Chapters 4 and 5, investigations on the pure plasmonic Au activity were performed by removing the residual UV content of the Lumatec lamp's internal visible-light filter (Figure 2.1b) by use of an additional external filter (420 nm, Schott GG420), which was placed at a distance of 1 cm from the end of the optical fibre. Due to the low sensitivity of the H_2-detection set-up described in Section 2.2, these experiments were carried out as follows: The catalyst (50 mg) was added to a 10 mL Schlenk tube loaded with a magnetic stirrer bar and closed with a glass piece containing a tap and rubber sealant fitting. The whole system was purged with argon three times. A mixture of H_2O/MeOH (volume ratio 1 : 1, 10 mL) was added through the rubber sealed screw-fitted joint and both taps were closed. The Lumatec lamp equipped with the additional 420 nm filter was positioned with the end of the optical fibre cable 4.5 cm away from the Schlenk tube. The power measured after the filter was 3.05 W. The tube was submerged in a beaker of water, from which the side of the tube was positioned 0.5 cm away. The lamp was turned on and the solution was stirred for 24–26 hours before a sample (5 mL) of the gaseous head space was removed and analyzed by GC. Over time, the catalyst adhered to the inside side of the flask during reaction and thus occasionally this was cleared manually using an external magnetic stirrer bar to agitate the one internally. The results of these experiments are presented in Table A.1.

Table A.1: Pure visible-light (>420 nm) H_2 evolution of selected Au-TiO_2 catalysts.

Exp.-No.	Catalyst	Time / h	Integrated GC intensity[a] / 25 µVs	Area/h	$n(H_2)$[b] / µmol
I[c]	AuP25-SIM	6.75	54	8	
II	AuP25-SIM	26	270	10	15
III	AuP25-DP12	24	2	0	
IV	AuBro-DP	24	5	0	
V	AuP25-DP	24	34	1	
VI[d]	AuP25-DP	0.67	167	250	12
VII[e]	AuP25-DP	24.5	126	5	
VIII[f]	P25	24	28	1	

[a]Area taken from TCD2 B trace of a gas chromatogram. Note: area expected to be specific to the GC.
[b]Only amounts of H_2 above the calibration limit (1 % H_2 calibrated to 147 / 25 µVs) have been calculated.
[c]Power measured after filter was 2.95 W.
[d]No additional filter was applied. Reaction mixture from exp. V was used, conducted immediately after completion of exp. V.
[e]Reaction mixture from exp. V was used, conducted immediately after completion of exp. VI.
[f]Average of two experiments

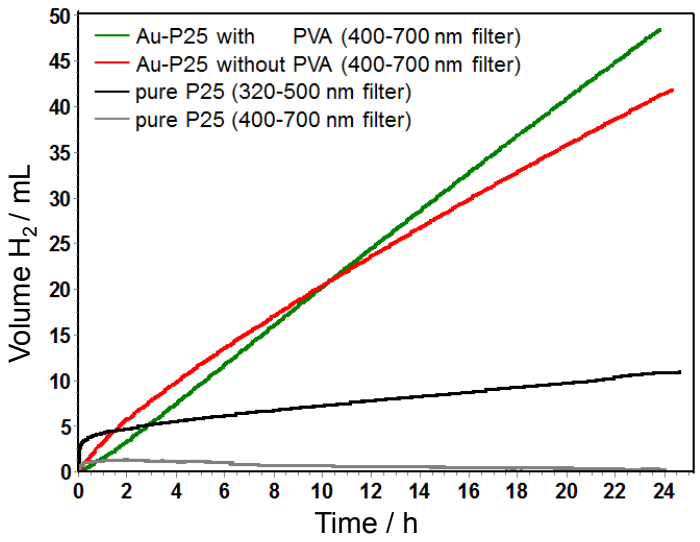

Figure A.10: H_2-evolution curves of P25 (black: 320–500 nm, gray: 400–700 nm) and AuP25-RP (red) in comparison to AuP25-SIM (green).

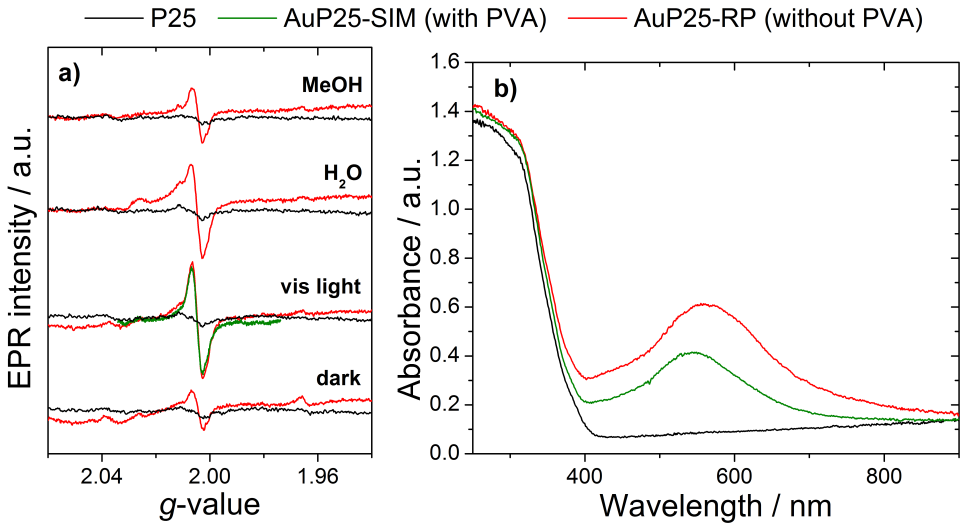

Figure A.11: a) Room-temperature *in situ* EPR spectra in the dark, under visible-light irradiation and with subsequent addition of H_2O and MeOH of P25 (black) and AuP25-RP (blue) in comparison to AuP25-SIM (green). b) The corresponding UV-vis spectra, respectively. AuP25-RP prepared without use of PVA showed the same signal A3 with similar intensity as AuP25-SIM. In contrast to AuP25-SIM, $O_2^{\bullet-}$ species (signal A2) is formed upon adding H_2O to AuP25-RP due to mechanisms according to Eq. 4.2–4.4. For bare P25, no significant EPR signal was observed under these conditions probably due to fast recombination of charge carriers.

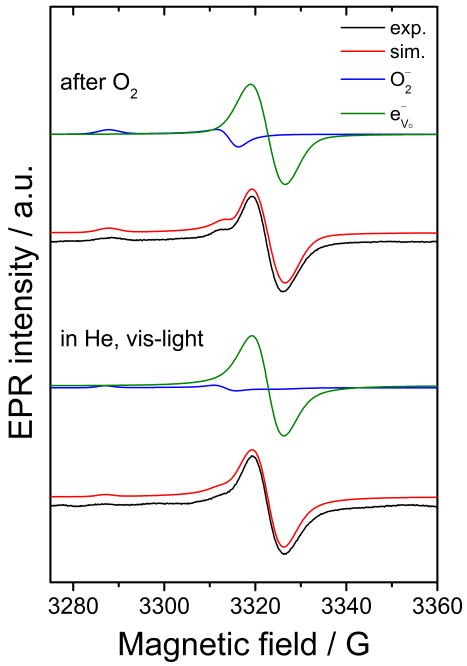

Figure A.12: Normalized EPR spectra and signal simulations of AuP25-SIM under visible-light irradiation in pure helium ($30\,\mathrm{mL\,min^{-1}}$) and after subsequent addition of $2\,\mathrm{mL\,min^{-1}}$ O_2. The contribution of $O_2^{\bullet-}$ increased significantly after addition of O_2, indicating an electron transfer from $e^-_{V_O}$ to O_2.

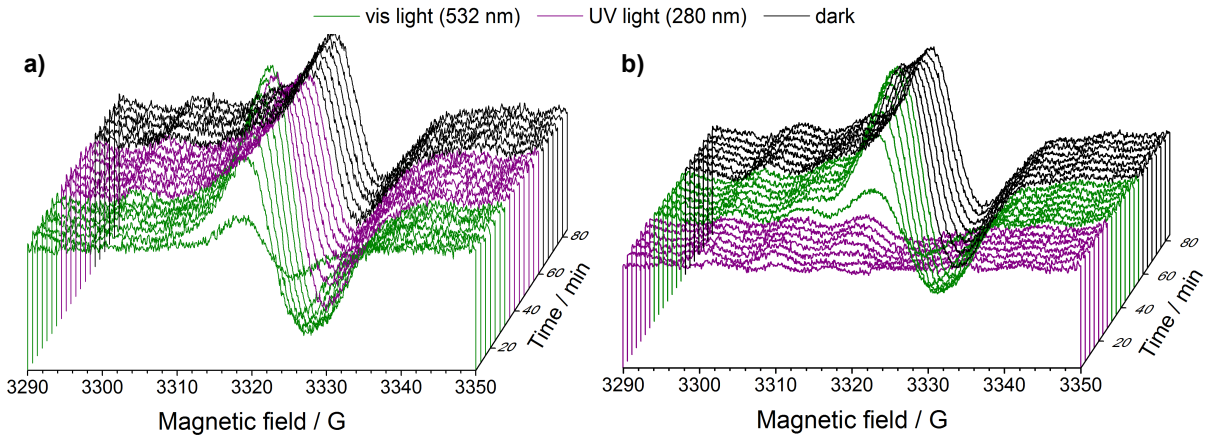

Figure A.13: *In situ* EPR spectra of AuP25-SIM during irradiation by a Xe lamp equipped with band-pass filters. The experiment started a) with visible light ($532 \pm 10\,\mathrm{nm}$) and was switched to UV light ($280 \pm 10\,\mathrm{nm}$) after 30 min before switching off the light and b) *vice versa*. Displayed are the difference spectra by subtracting the dark spectrum (before irradiation) from each spectrum under or after irradiation. The corresponding double integrals and kinetic fits are depicted in Figure 4.10

.

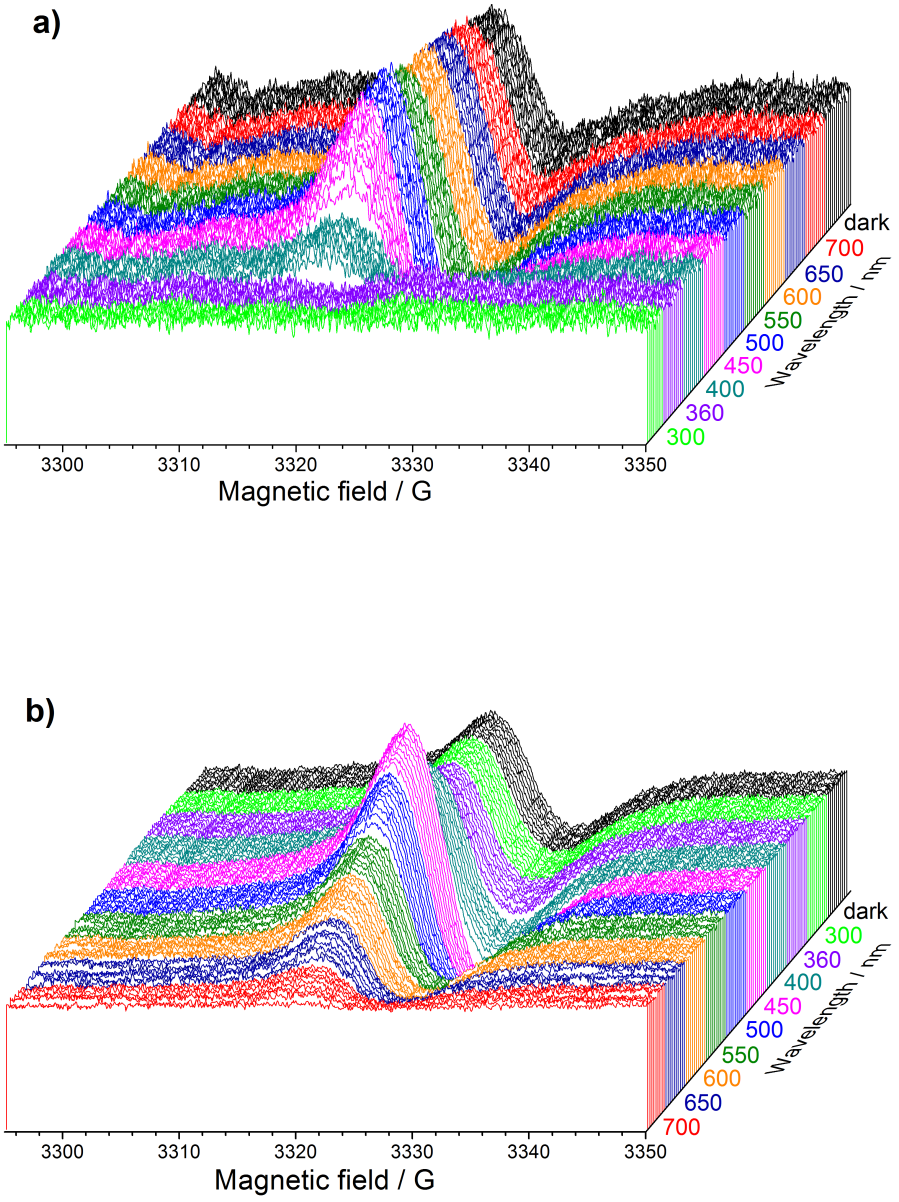

Figure A.14: *In situ* EPR spectra of AuP25-SIM during irradiation by a Xe lamp equipped with a set of band-pass filters to select distinct wavelengths with transmission widths of about 20 nm. The experiment was carried out in two different ways: a) starting at 300 nm to end at after 700 nm in the dark and b) *vice versa*. Each wavelength was hold for 10 min before switching to the next one. Displayed are the difference spectra by subtracting the dark spectrum (before irradiation) from each spectrum under or after irradiation. The corresponding double integrals are plotted together with the UV-vis absorption spectrum in Figure 4.11.

Further analyses on the Au-TiO_2(:N) catalysts from Chapter 5

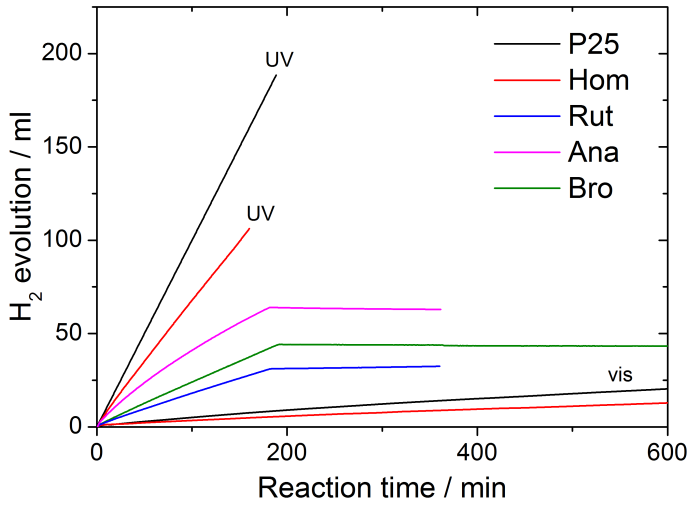

Figure A.15: Experimental photocatalytic H_2-evolution curves from H_2O/MeOH over AuTiO_2-DP catalysts prepared with different TiO_2-phase compositions. The hydrogen-evolution rate was constant over a period of 3 h under UV light (320–500 nm filter) and over subsequent 21 h (or 3 h) under visible light (400–700 nm filter).

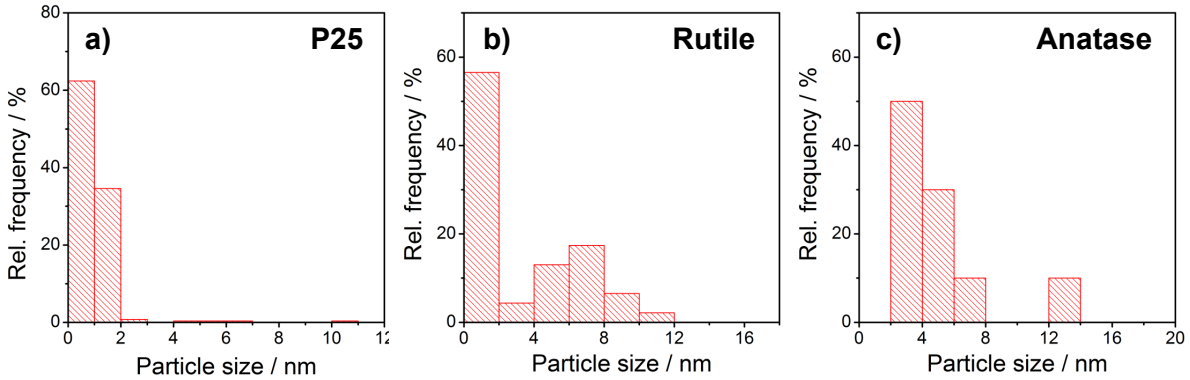

Figure A.16: Au-particle size distributions of a) AuP25-DP, b) AuRut-DP, and c) AuAna-DP. For the catalysts made of P25 and Rut a high number of very small Au species (<2 nm) was found, whereas the Ana sample contains exclusively Au particles larger than 2 nm.

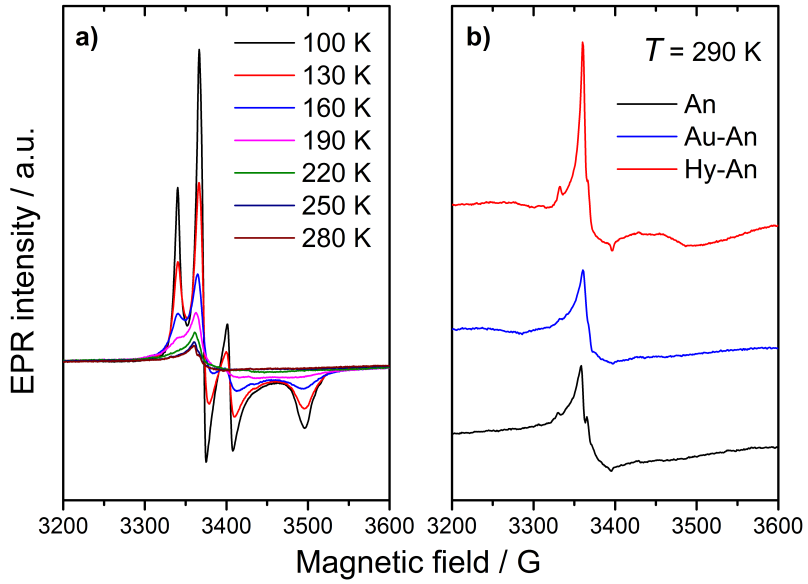

Figure A.17: a) Temperature dependence of the EPR signal intensity of $NO^{\bullet}$ for the untreated An catalyst. b) Comparison of the room-temperature EPR spectra of An (black), Au-An (red), and Hy-An (blue) recorded in the dark.

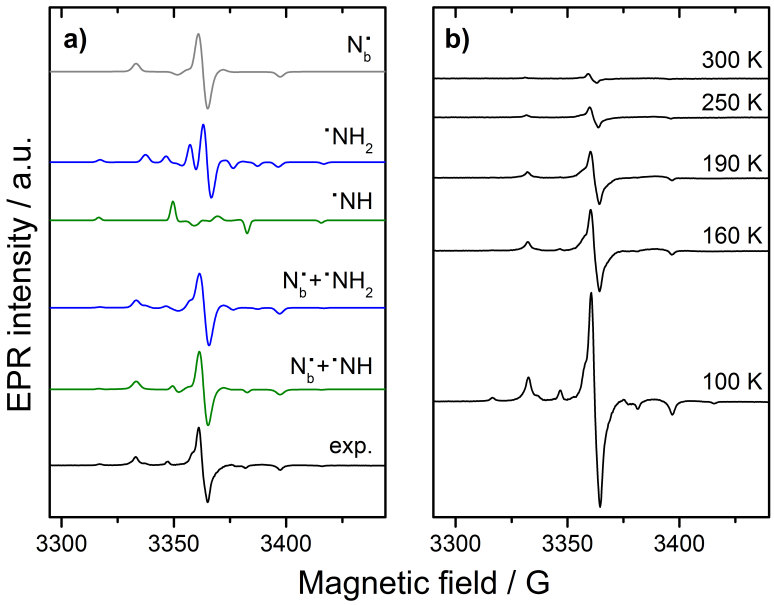

Figure A.18: a) EPR spectrum simulations of visible-light-irradiated (Xe lamp, >420 nm filter) P25:N15-550-3 recorded at $T = 90$ K (black). The spectrum can be simulated using combinations of the $N_b^{\bullet}$ (gray) with either an $^{\bullet}NH$ group ($I = 1$ and $I = 1/2$, green) or an $^{\bullet}NH_2$ radical species ($I = 1$ and $2 \times I = 1/2$, blue). b) Temperature dependence of the EPR signal intensity for P25:N15-550-3 under visible light.

Table A.2: Simulation parameters corresponding to Figure A.18a.

Center	Nuclear spins	g_z	g_y	g_x	A_z	A_y	A_x	A_{zz}	A_{yy}	A_{xx}	lw_z	lw_y	lw_x
$N_b^{\bullet}$	$I = 1$	2.0075	2.0060	2.0045	2.0	4.0	32.1	–			3.0	3.0	3.0
$^{\bullet}NH_2$	$I = 1$, $2 \times I = 0.5$	2.0056	2.0053	2.0035	0.0	0.0	29.5	0.0	0.0	19.5/21.0	3.0	3.0	2.5
$^{\bullet}NH$	$I = 1$, $I = 0.5$	2.0060	2.0040	2.0040	0.0	0.0	33.0	0.0	0.0	33.0	2.5	2.5	2.5

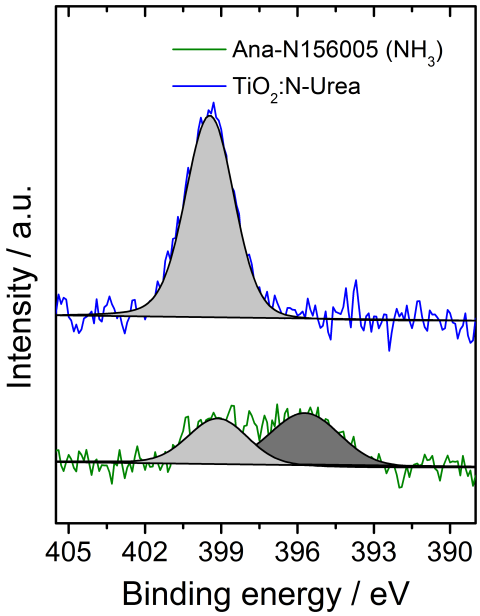

Figure A.19: Comparison of the XPS N 1*s* peaks of Ana:N15-600-5 (green) and TiO_2:N-Urea (blue).

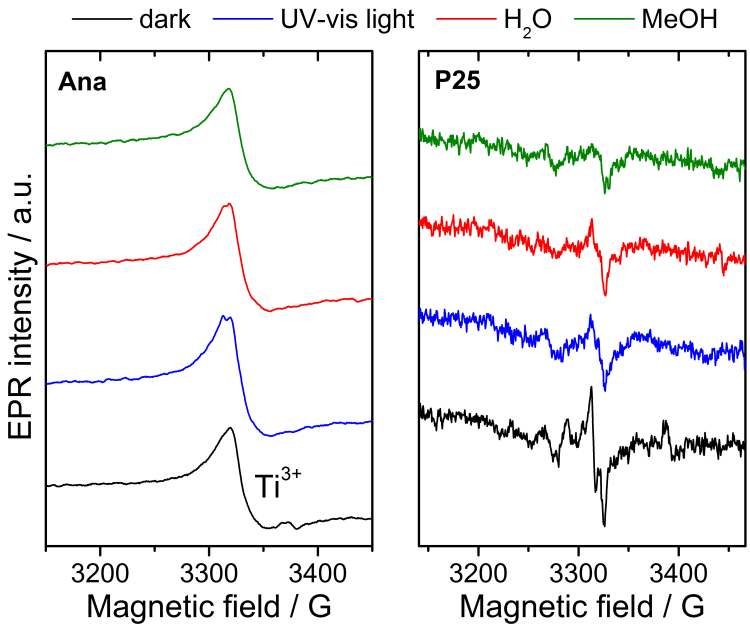

Figure A.20: *In situ* EPR spectra of the Au-free undoped Ana and P25 materials in the dark (black), under irradiation with UV-vis light (blue) and under subsequent addition of water (red) and MeOH (green).

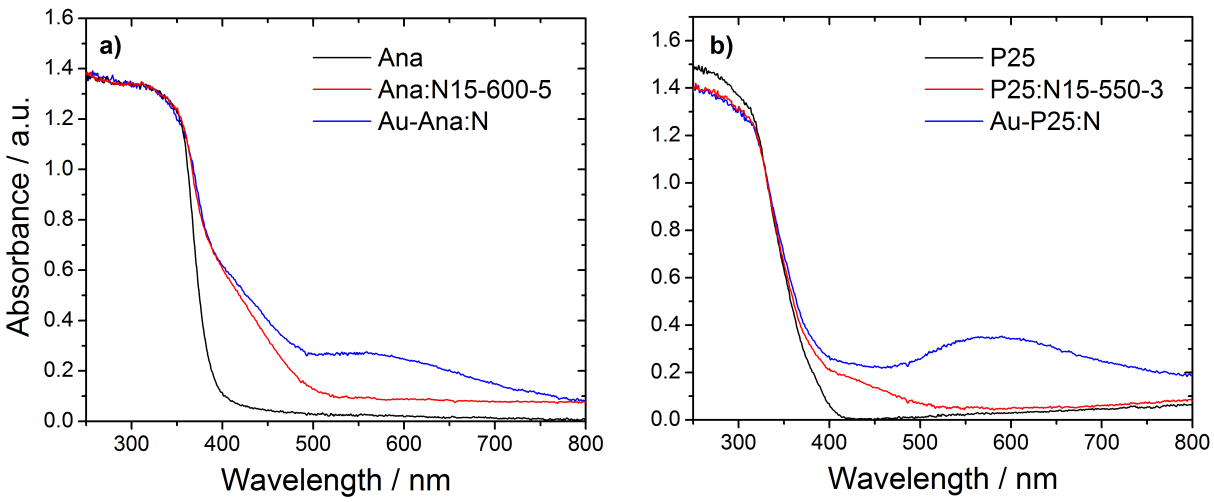

Figure A.21: UV-vis absorbance spectra of Au-loaded N-doped Ana (a) and P25 (b) catalysts.

Further analyses on the Cu-based catalysts from Chapter 6

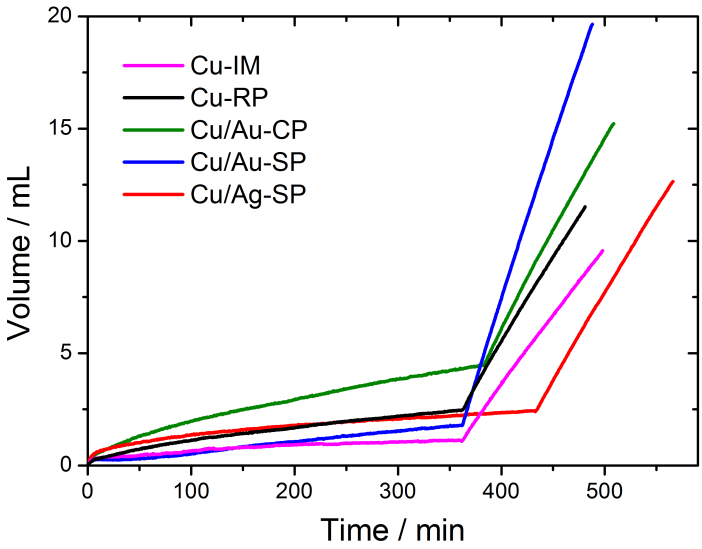

Figure A.22: Experimental photocatalytic H_2-evolution curves from H_2O/MeOH over mono- and bimetallic Cu-based TiO_2 catalysts using different filter settings of the Lumatec Hg lamp: *ca.* 6 h under visible light (400–700 nm filter) and subsequently *ca.* 2.5 h under UV light (320–500 nm filter).

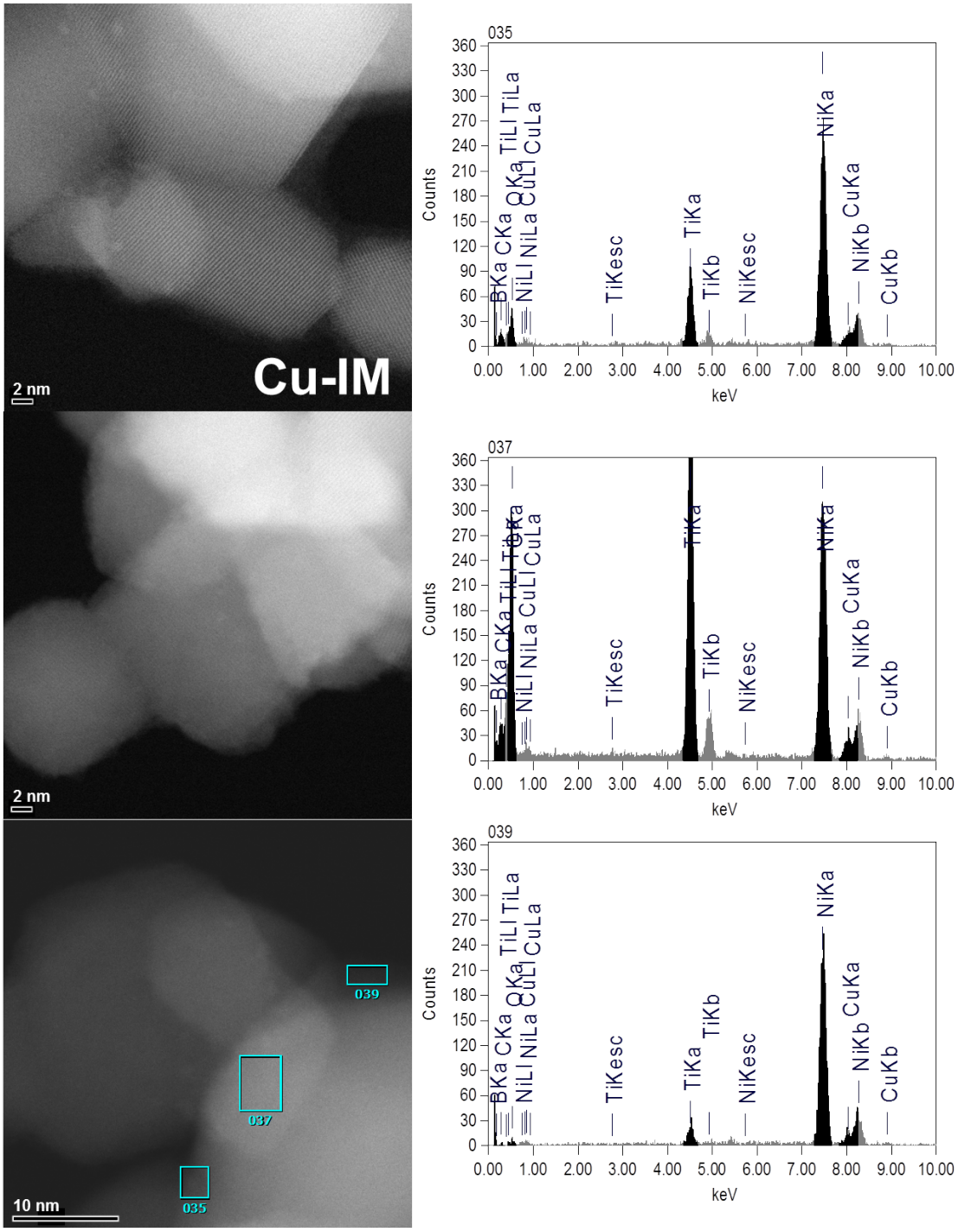

Figure A.23: HAADF-TEM images and EDX analysis of the poorly visible-light-active Cu-IM catalyst. Highly dispersed Cu species instead of clear Cu particle formation was observed.

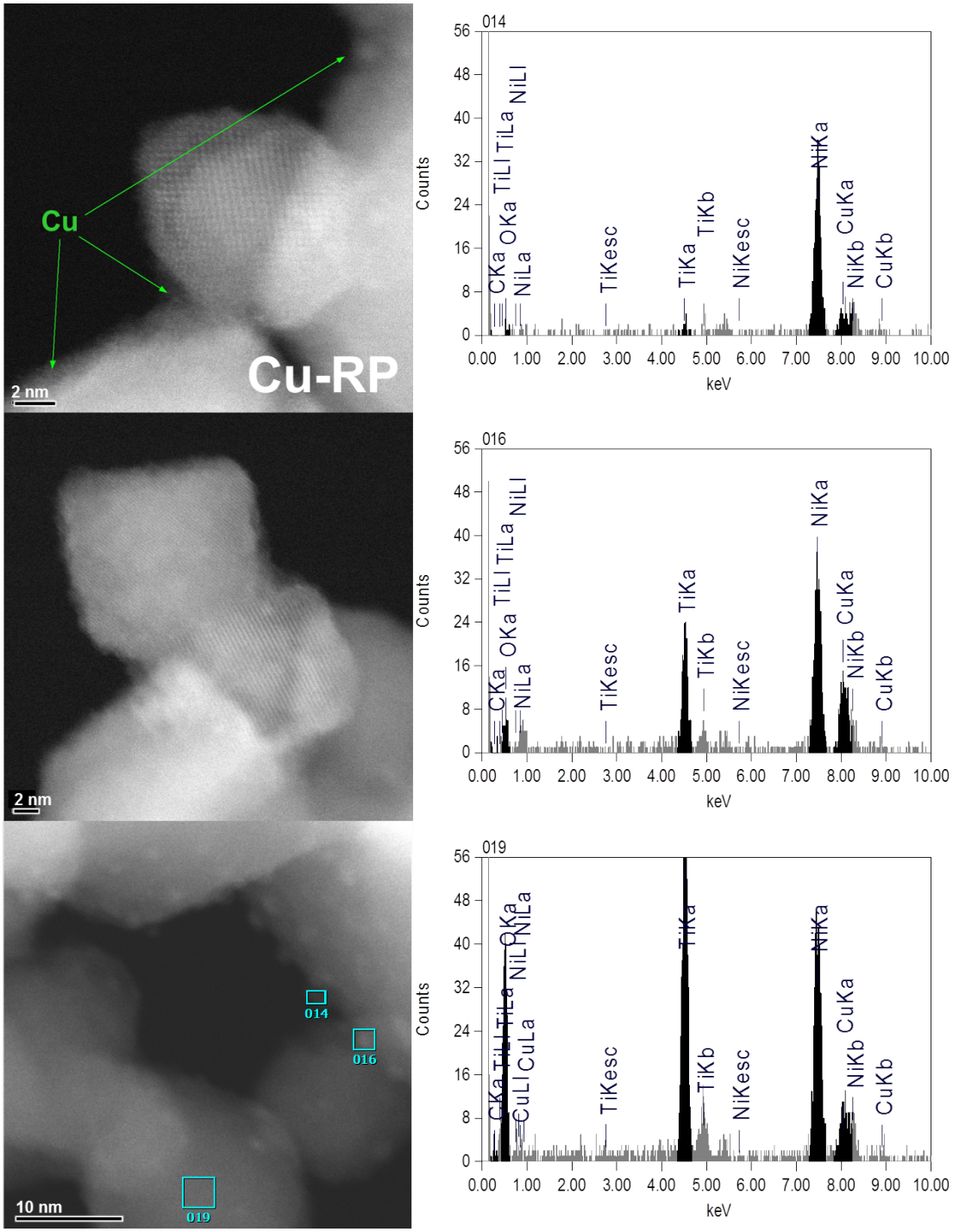

Figure A.24: HAADF-TEM images and EDX analysis of the Cu-RP catalyst. Along with Cu-spread areas, also small Cu agglomerates of 2–4 nm size were observed.

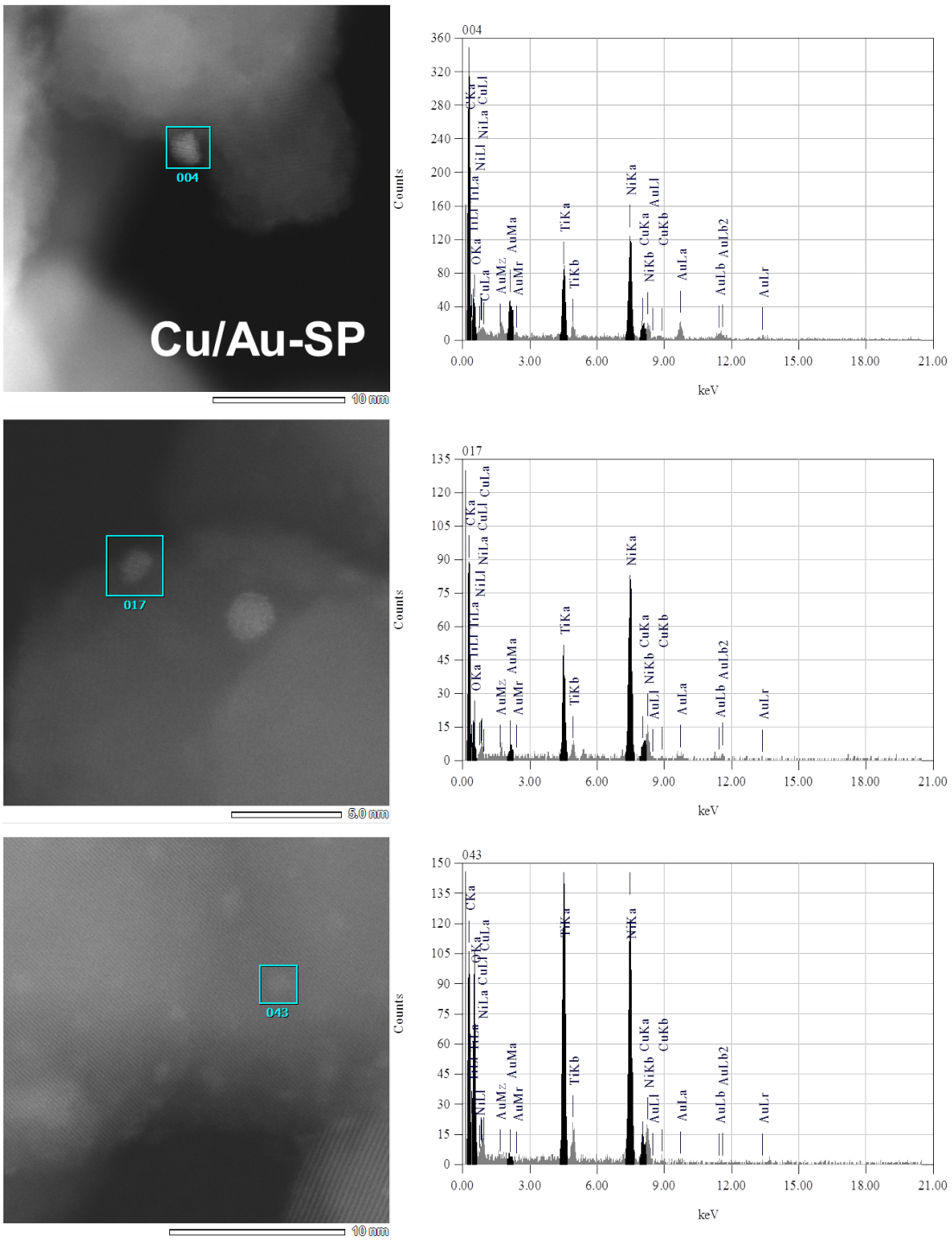

Figure A.25: HAADF-TEM images and EDX analysis of the poorly visible-light-active, but highly UV-vis-light-active Cu/Au-SP catalyst. Highly dispersed Cu areas are separated from the small Au particles of 2–5 nm size.

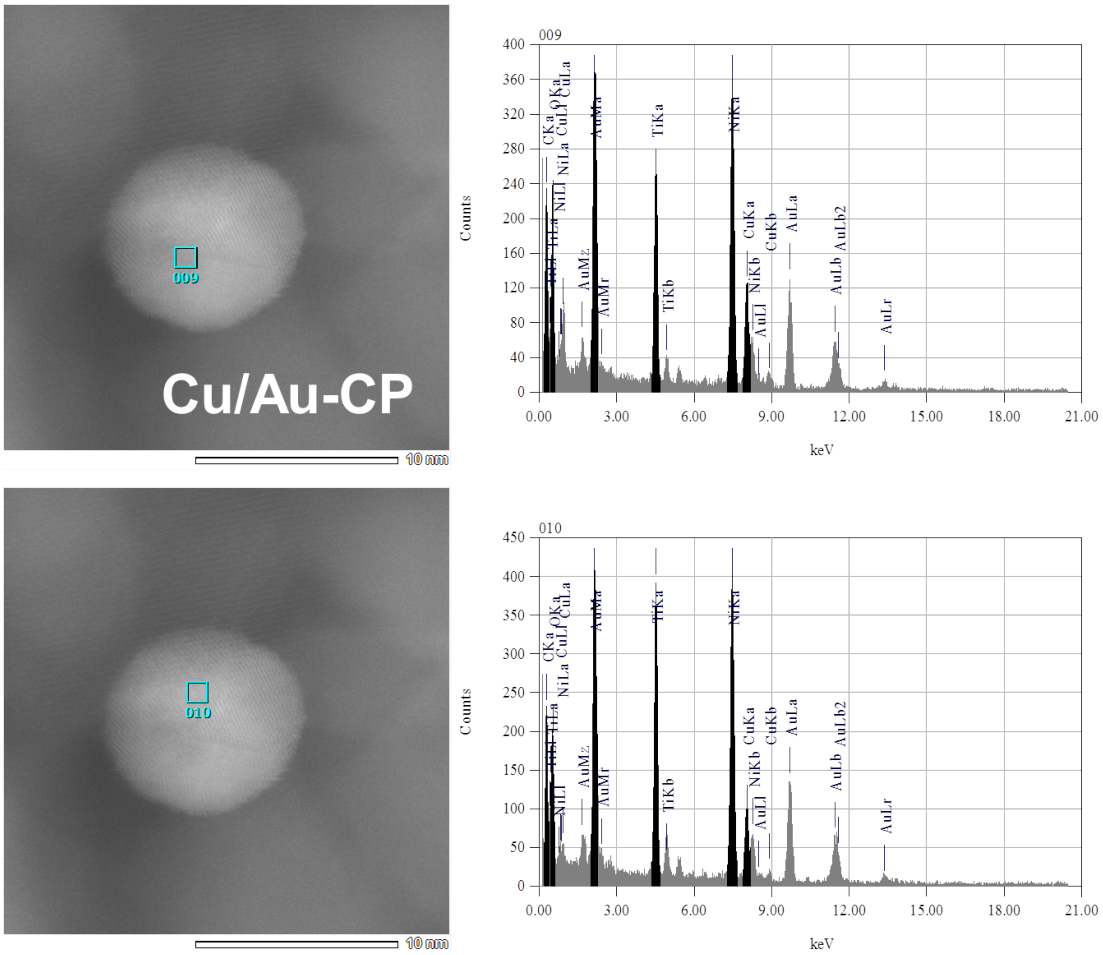

Figure A.26: HAADF-TEM images and EDX analysis of the highly visible-light-active Cu/Au-CP catalyst. 4–8 nm sized metal particles containing both Au and Cu were found.

EPR signal assignment of the Cu^{2+} species in Cu/Au-SP The difference spectra depicted in Figure A.27a show that at least four paramagnetic Cu^{2+} centers can be distinguished. Subtracting the spectrum under visible-light irradiation from that in the dark (pink) reveals that primarily the Cu^{2+} ions of oxidized Cu clusters (signal B, $g_{\parallel} = 2.25$) are reduced under these conditions and not species A ($g_{\parallel} = 2.38$), the latter of which shows defined hfs splitting and is probably arising from isolated Cu^{2+} sites occupying Ti^{4+} vacancies at the TiO_2 surface.[267]

The difference spectrum "UV-vis minus vis" (brown) exhibits two new signals, C and K, which are responsible for the increase of the double integral for Cu/Au-SP under these conditions (Figure 6.6a). Signal C exhibits a typical line shape of monomeric Cu^{2+} as well, whereas signal K is represented by two features split by *ca.* 1030 G. The latter is characteristic for Cu^{2+}-ion pairs, since the coupling between the two unpaired electrons becomes significant at a certain distance, resulting in a splitting of the spin system into a paramagnetic triplet state ($S = 1$) and a diamagnetic singlet state ($S = 0$).[268] At zero magnetic field, the former is again split by the anisotropic exchange interaction, which leads to one forbidden ($\Delta M_S = 2$) and two allowed ($\Delta M_S = 1$) transitions (Figure A.27b). In the spectrum, only the two perpendicular components of the allowed transitions of signal K appear, but with unresolved hyperfine splitting to the two Cu nuclei ($I = 3/2$), which would give rise to seven lines (1:2:3:4:3:2:1) for equivalent nuclei.

It is plausible that signals C and K appear due to line narrowing upon reduction of the other Cu^{2+} species causing decreased dipolar interactions. Hence, the appearance of signal K in the EPR spectra may indicate an efficient reduction of the oxidized Cu clusters. This happens in Cu/Au-SP only under UV-light irradiation in H_2O/MeOH.

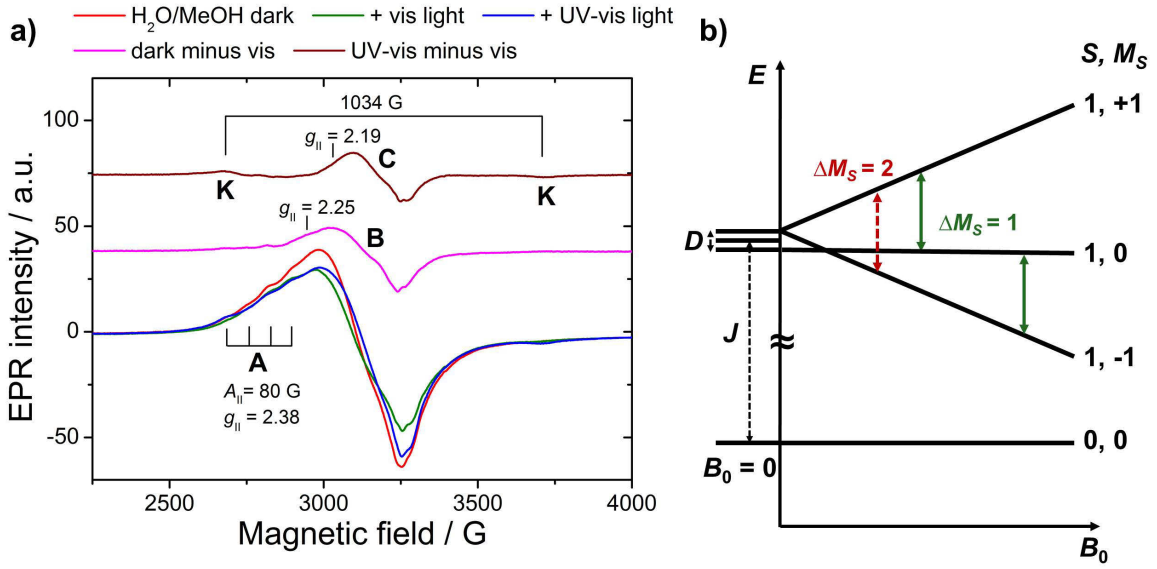

Figure A.27: a) *In situ* EPR spectra of Cu/Au-SP in H_2P/MeOH (red) and after subsequent irradiation with visible (green) and UV light (blue) for 20 min. To extract the different Cu^{2+} species, difference spectra are displayed resulting by subtracting the spectrum of the visible-light-irradiated catalyst from that in the dark (pink) or by subtracting the vis-spectrum from that under UV-vis light (brown). b) Energy-level diagram for the spin–spin interaction of Cu^{2+} dimers.

Acknowledgment

I would like to express my special appreciation and thanks to the following people:

- My advisor Prof. Dr. Angelika Brückner for providing me the opportunity to work on this interesting project and especially for encouraging my independent research. I am grateful for her constant support and trust in me, which strongly promoted my personal and scientific growth.
- Prof. Dr. Michael Wark and Prof. Dr. Matthias Bauer for kindly agreeing to take on the reviews of this thesis.
- The DFG and the Leibniz foundation for financial support.
- The groups of Dr. Sebastian Wohlrab, Prof. Dr. Patrik Schmuki, Prof. Dr. Adriana Zaleska and Dr. Matteo Cargnello for the fruitful collaborations in the field of semiconductor photocatalysis.
- Dr. Jabor Rabeah, Dr. Dirk Hollmann and Ulrich Marx for their lab support and helpful discussions.
- Dr. Henrik Junge and his co-workers for conducting the catalytic tests.
- Dr. Ursula Bentrup and Dr. Kathleen Grabow for the IR measurements.
- The service-analytical department for the plenty of catalyst characterizations.
- Michael Sebek, Stefanie Schüler, Dr. Hilal Wahab, Marta Paszkiewicz, Aleksandra Oryl and Anna Kuczynska for their help with catalyst synthesis.
- All the friendly and supporting colleagues at LIKAT.
- My family and friends – I highly appreciate their love, support and sacrifices over the past few years.